Mind The Gap: Tip Leakage Vortex Dynamics and Cavitation in Axial Turbines

THÈSE N^{O} 6611 (2015)

PRÉSENTÉE LE 12 JUIN 2015
À LA FACULTÉ DES SCIENCES ET TECHNIQUES DE L'INGÉNIEUR
LABORATOIRE DE MACHINES HYDRAULIQUES
PROGRAMME DOCTORAL EN MÉCANIQUE

ÉCOLE POLYTECHNIQUE FÉDÉRALE DE LAUSANNE

POUR L'OBTENTION DU GRADE DE DOCTEUR ÈS SCIENCES

PAR

Matthieu DREYER

acceptée sur proposition du jury:

Prof. C. Ancey, président du jury
Dr M. Farhat, directeur de thèse
Prof. J. A. Astolfi, rapporteur
Prof. J.-P. Franc, rapporteur
Prof. F. Gallaire, rapporteur

ÉCOLE POLYTECHNIQUE
FÉDÉRALE DE LAUSANNE

Suisse
2015

The one thing that scientists ought to be is humble,
because they, more than anyone, know how little they can explain.
— Steve Jones

Remerciements

Ce travail de thèse a été mené dans le cadre du projet HydroNet et n'aurait pas été possible sans le soutien financier du Centre de Compétences Energie et Mobilité (CCEM) et de swisselectric research, que je remercie. Un doctorat est une aventure qui ne peut se réaliser seul dans son coin. C'est pourquoi je tiens à remercier les nombreuses personnes qui, d'une manière ou d'une autre, ont contribué à l'accomplissement et à la réussite de ma thèse.

Tout d'abord je tiens à remercier sincèrement mon directeur de thèse, Dr. Mohamed Farhat, pour m'avoir accordé sa confiance tout au long de ce travail. Sa passion et son enthousiasme contagieux pour la science ont toujours été une source d'inspiration et de motivation. Lorsque le doctorant nage en eaux troubles, sa vision limpide de la mécanique des fluides est une aide indispensable pour retrouver le droit chemin. Je remercie également le directeur du Laboratoire des Machines Hydrauliques, Prof. François Avellan, pour l'opportunité qu'il m'a offerte de travailler dans son laboratoire, ainsi que pour ses conseils avisés dans les moments clés de ce travail.

Mes remerciements vont aux membres du jury: Prof. Christophe Ancey, Prof. François Gallaire, Prof. Jacques-André Astolfi et Prof. Jean-Pierre Franc, pour avoir pris le temps de lire et d'évaluer mon travail ainsi que pour leurs commentaires constructifs lors de la défense de thèse privée.

Je souhaite ensuite exprimer toute ma gratitude à tous les membres du laboratoire sans qui rien n'aurait été possible et avec qui j'ai eu beaucoup de plaisir à travailler. Merci à Isabelle Stoudmann-Schmutz pour son efficacité dans les tâches administratives ainsi que sa bonne humeur communicative. Merci également à Musliu Besard pour son professionnalisme et son indulgence alors que la guerre de bureau générait parfois de nombreux débris.

L'un des atouts majeurs de ce laboratoire est de pouvoir compter sur une équipe de professionnels, constituant l'atelier mécanique et le bureau d'étude, capable de transformer n'importe quel souhait en un mécanisme fiable et précis. Je me dois ainsi de remercier Philippe Faucherre et Raymond Fazan pour la conception, respectivement l'usinage, du support coulissant. Merci aussi à Alain Renaud et à Vincent Berruex (aka la machine) pour les divers coups de main lorsqu'il s'agissait d'apprivoiser *Catia*. Un énorme merci à l'équipe de choc des mécaniciens: Victor Rivas, David Buzzi, Louis Vina, dirigés successivement par

Louis Besançon et Maxime Raton. J'ai eu énormément de plaisir à partager avec ce dernier de la musique douce ainsi qu'à réaliser des projets hors du commun (le pedalboard est top et Big Body ne peut plus vivre sans catapulte). Je remercie également tous les ingénieurs des plateformes d'essai qui m'ont toujours bien aidé lorsque j'étais à la recherche d'un instrument qu'ils pouvaient me prêter. Un merci spécial doit être adressé à George Crittin pour son aide précieuse à chaque fois que le tunnel de cavitation partait en arrêt maladie.

Le second atout majeur de ce laboratoire est l'extraordinaire ambiance qui y règne entre collègues. Au cours des divers soupers raclette, weekend (périlleux) de ski, parties de beach volley et nombreux jeudredis, ces dernières années dédiées à la recherche m'ont surtout conduit à trouver de nouvelles et belles amitiés. Ces quelques lignes de remerciement ne pourront évidemment pas y rendre justice. Je remercie tout d'abord les personnes qui me supportent depuis le début de mes études à l'EPFL: Christian Vessaz et ma victime (souffrant du syndrome de Stockholm) Christian Landry. Leur choix de cours était au top, mais leur précision au tir d'élastiques laisse encore à désirer. Merci au Broyard pour tous ses bons petits plats ainsi que pour l'initiation (traumatisante) au tir de campagne et merci au Valaisan pour son grand sens de l'humour, ce fût un plaisir de partager le bureau avec toi. Merci aussi au génial Martino Reclari, le second locataire du bureau, avec qui j'ai tenté d'y instaurer un minimum de culture musicale. J'ai eu beaucoup de plaisir à collaborer avec toi et ton aide précieuse lors des nombreuses manips et discussions a été très enrichissante. Merci aussi de votre accueil avec Martina lors de notre visite au Japon. Un merci spécial, ou plutôt 1005 mercis, sont de rigueur à mon ami Andres Müller qui m'a fait prendre goût aux voyages et découvrir le Japon! Il aura suffi d'une cave intimiste pour qu'un début d'amitié s'installe et d'un panneau de circulation pour la sceller. Plus sérieusement, merci infiniment d'avoir contribué à l'amélioration de cette thèse par ta relecture et tes conseils avisés. Et promis on ne loupera plus de concert de Cake. Je ne saurai oublier de remercier le petit Arthur Favrel qui m'a bien fait rigoler, parfois malgré lui. Qui sait, peut-être qu'un jour ton rêve se réalisera et bon courage pour ta fin de thèse. Merci aussi à l'élégant Olivier Pacot qui continue à rendre Maude très jalouse. Les vacances aux Japon furent mémorables, surtout pour le mur du ryokan. Merci au philosophe Marc Tinguely, qui dispense actuellement sa sagesse à Londres (Mec, god save the queen!). Merci également à Steven Roth (Hey tonight ♪) pour son humour et sa complicité lors de nos aventures dans des contrées hostiles. Merci ensuite au fabuleux couple formé de Sebastien Alligné et Cécile Münch-Alligné. La recette du bonheur comporte apparemment du fenouil comme ingrédient. Merci également à Ebrahim Jahanbakhsh pour sa gentillesse ainsi qu'aux anciens Vlad Hasmatuchi et Amir Zobeiri pour les nombreux coups de mains et conseils et au (pas toujours) sage Christophe Nicolet. Merci aussi aux postdocs physiciens: le très savant Danail Obresechkov, le physicien des étoiles Philippe Kobel ainsi qu'à Pierre Bouillot, le théoricien devenu expérimentateur. Entre paradoxes et paires de Cooper, les discussions sont toujours passionnantes. Merci aussi à la nouvelle génération de post-docs et de doctorants grâce à qui cette bonne ambiance est garantie de continuer. Il y a ainsi les nouveaux locataires du haut: Audrey et Loïc et son humour vraiment « super »... Je souhaite bon courage pour la suite à Keita, Simon, Emmanuel, la carnassière Elena ainsi qu'à Outi.

Un grand merci est aussi de rigueur pour tous mes amis en dehors du laboratoire qui m'ont supporté et encouragé durant ces 4 ans. Merci ainsi au groupe de musique: Lucas Jaquet, Vincent Dougoud, Jérôme Cotting et Michel Yerly pour cette autre belle aventure, grâce à laquelle j'échappais au tracas de la thèse. Merci également à Yannis Orphanos et Augustin Quartenoud pour leur amitié, la relève musicale n'est pas loin. Merci à mes amis et anciens colloques, Pierre-Alain Blanc et Jérémy Binder, pour tous ces moments inoubliables, ainsi qu'à mon second frère, Axel Brunk, qui a encore beaucoup de choses à m'apprendre.

Un énorme merci à ma famille, et plus particulièrement à mes parents, Philippe et Christiane, qui m'ont soutenu inconditionnellement au cours de mes études, et tout au long de ma vie, ainsi qu'à Céline, Fanny et Arun, pour leurs encouragements et tout le reste... Je leur en suis infiniment reconnaissant.

Finalement, je tiens à remercier Maude pour tout ce qu'elle m'a apporté ces dernières années ainsi que pour son soutien, sa patience et son amour, maintes fois témoignés durant ce travail. Merci du fond du cœur.

Lausanne, 20 avril 2015 Matthieu

Abstract

The tip leakage vortex (TLV), which develops in the clearance between the blade tip and the casing of axial turbomachines, appears in many industrial applications, such as air transportation, space rockets and hydraulic machines. In the latter, cavitation may develop in the core of the TLV, often leading to severe erosion of the runner blades and the casing. Despite the progress achieved in understanding and controlling the dynamics of this particular flow, many associated phenomena are still not sufficiently explored. It remains, for instance, unclear how the clearance size is related to the occurrence of cavitation in the TLV. The present work contributes to this research by assessing the effect of the clearance size on the TLV intensity and dynamics in a simplified case study. The vortex is generated by a two dimensional generic blade in a water tunnel, while the clearance between the blade tip and the wall is varied. The properties of the TLV are established with the help of stereo-PIV and flow visualizations for a wide range of incidence angles, inlet velocities and tip clearances.

The measurements clearly reveal the existence of a specific tip clearance for which the vortex intensity is at its maximum and most prone to generate cavitation. By introducing a new dimensionless coefficient τ/Γ^*_∞, where τ is the normalized clearance and Γ^*_∞ is the normalized circulation in the unconfined case, it is established that the TLV circulation reaches a peak intensity for $\tau/\Gamma^*_\infty \approx 0.2$, the amplitude of which is in average 45 (±10) % higher than in the unconfined case, regardless of the operating conditions.

The change in the vortex structure due to cavitation occurrence is also investigated in a different case study by means of PIV using fluorescent seeding particles. A vortex is generated by an elliptical hydrofoil and the velocity field outside the vapor phase is compared with the one in cavitation-free conditions. It is found that the cavitation does not change the vortex circulation, since the tangential velocity distribution of the cavitating vortex is identical to the non-cavitating vortex far from the vapor core. The tangential velocity close to the vapor core is however lower than in cavitation-free conditions. Moreover, the fluid is in solid body rotation in the vicinity of the liquid-gas interface.

The alteration of the clearance geometry with shallow grooves to manipulate the gap flow and control the TLV intensity is evaluated in the simplified case study. The cavitation in the TLV and in the clearance region is significantly reduced with grooves located near the foil leading edge, oriented at 45° or 90° relative to the incoming flow. This result paves the way for further investigations, which may ultimately lead to TLV cavitation mitigation in axial turbines.

Keywords: Tip leakage vortex, axial turbine, cavitation, PIV, LDV, grooves, flow control

Résumé

Le tourbillon de jeu d'aubage, qui se développe dans l'espace entre l'aube et le carter des turbomachines axiales, apparaît dans de nombreuses applications industrielles, telles que le transport aérien, les fusées spatiales et les machines hydrauliques. Dans ces dernières, la cavitation qui peut se développer dans le cœur du tourbillon est souvent synonyme d'érosion sévère de la machine. Malgré les progrès réalisés dans la compréhension et la maîtrise de cet écoulement, de nombreux phénomènes associés restent insuffisamment explorés. Par exemple, on ne sait toujours pas de quelle manière la taille du jeu est liée à l'apparition de cavitation dans le tourbillon. Ce travail contribue à cette recherche en évaluant l'influence du jeu sur l'intensité et la dynamique du tourbillon dans un cas d'étude simplifié. Le tourbillon est généré par un profil générique dans un tunnel hydrodynamique et le jeu entre l'extrémité du profil et la paroi est varié. Les propriétés du tourbillon sont établies à l'aide de visualisations et de mesures par stéréo-PIV, pour une large gamme d'angles d'incidence, de vitesses et de jeux. Les mesures font clairement apparaître l'existence d'un jeu spécifique pour lequel l'intensité du tourbillon est maximale et le plus enclin à développer de la cavitation. En définissant un nouveau coefficient adimensionnel τ/Γ^*_∞, où τ représente le jeu normalisé et Γ^*_∞ la circulation normalisée dans le cas non-confiné, il est établi que la circulation du tourbillon atteint un pic d'intensité pour $\tau/\Gamma^*_\infty \approx 0.2$, dont l'amplitude est en moyenne 45 ($\pm$10) % plus élevée que dans le cas non-confiné, indépendamment des conditions de fonctionnement.

La modification de la structure d'un tourbillon suite à l'apparition de cavitation est également étudiée avec des mesures PIV utilisant des particules fluorescentes dans un cas d'étude distinct. Un tourbillon est généré par un profil elliptique et le champ de vitesse à l'extérieur de la phase vapeur est comparé à celui obtenu en l'absence de cavitation. On constate que la cavitation ne modifie pas la circulation du tourbillon, car la distribution de vitesse tangentielle est identique dans le cas cavitant et non-cavitant loin du noyau de vapeur. La vitesse tangentielle proche de la phase vapeur est toutefois plus faible avec la cavitation. De plus, le fluide est en rotation de corps solide au voisinage de l'interface liquide-gaz.

L'altération de la géométrie du jeu avec des rainures peu profondes pour contrôler l'intensité du tourbillon est aussi évaluée. La cavitation dans le tourbillon et dans le jeu est significativement réduite lorsque les rainures sont proches du bord d'attaque et orientées à 45° ou 90° par rapport à l'écoulement incident. Ce résultat ouvre la voie à d'autres études, qui pourraient aboutir à l'atténuation de la cavitation du tourbillon de jeu dans les turbines axiales.

Mots clefs : Tourbillon, turbine axiale, cavitation, PIV, LDV, rainures, contrôle d'écoulement

Contents

Remerciements **i**

Abstract (English/Français) **v**

List of figures **xiii**

List of tables **xix**

Nomenclature **xxi**

1 Introduction **1**
- 1.1 Problem overview 1
  - 1.1.1 Tip leakage vortex in axial turbomachines 1
  - 1.1.2 Reduced scale model testing and TLV cavitation prediction 3
  - 1.1.3 Vortex cavitation 4
- 1.2 State of the art 5
  - 1.2.1 Tip vortex formation 5
  - 1.2.2 Tip leakage vortex 7
- 1.3 Thesis objective 9
- 1.4 Document structure 9

2 Vortex models **11**
- 2.1 Structure of a tip vortex and governing equations 11
- 2.2 Non-cavitating vortex models 12
  - 2.2.1 Rankine vortex 12
  - 2.2.2 Lamb-Oseen vortex 12
  - 2.2.3 Vatistas vortex 13
  - 2.2.4 VM2 vortex 13
  - 2.2.5 Batchelor and Moore & Saffman vortex 14
  - 2.2.6 Key vortex parameters 15
- 2.3 Cavitating vortex models 16
  - 2.3.1 The modified Rankine vortex of Arndt & Keller 16
  - 2.3.2 The modified Lamb-Oseen vortex of Choi & Ceccio 17
  - 2.3.3 The cavitating Lamb-Oseen vortex of Bosschers 19

3 Experimental apparatus and procedure **21**

3.1 High-speed cavitation tunnel 21

3.1.1 Test section flow quality 22

3.1.2 Water quality and nuclei content 22

3.2 Hydrofoils 23

3.2.1 Rectangular planform hydrofoil 23

3.2.2 Elliptical planform hydrofoil 24

3.2.3 Leading edge roughness 25

3.3 Mounting supports 25

3.3.1 Sliding support 25

3.3.2 Hydrodynamic load cell 26

3.4 High-speed flow visualization 26

3.5 Laser Doppler Velocimetry 27

3.5.1 Measurement principle 27

3.5.2 Measurement deconvolution 28

3.6 Particle Image Velocimetry 31

3.6.1 Measurement principle 31

3.6.2 Fluorescent seeding particles 32

3.7 Post-processing of PIV data 33

3.7.1 Vortex identification 33

3.7.2 Wandering correction 36

4 Effect of cavitation on a tip vortex **39**

4.1 Case study 39

4.1.1 Motivation and context 39

4.1.2 Methodology 40

4.2 Experimental setup and data processing 41

4.2.1 Laser Doppler Velocimetry 41

4.2.2 Particle Image Velocimetry 44

4.2.3 Vortex cavity dimensions 51

4.3 Velocity field in cavitation-free conditions 52

4.3.1 Tangential velocity in cavitation-free conditions 52

4.3.2 Axial flow in cavitation-free conditions 53

4.3.3 Vortex characteristics 58

4.4 Cavitating vortex 63

4.4.1 Flow visualizations 63

4.4.2 Tangential velocity of the cavitating vortex 65

4.4.3 Axial flow of the cavitating vortex 67

4.4.4 Cavitating radius evolution 69

4.5 Discussion 70

5 Effect of gap width on the TLV 73
5.1 Motivation and context 73
5.2 Case study and experimental setup 73
5.2.1 Case study 73
5.2.2 Stereo Particle Image Velocimetry setup 74
5.3 Methodology 77
5.3.1 Flow parameters 77
5.3.2 Vortex parameters extraction 78
5.4 Flow visualizations 79
5.5 TLV characteristics 83
5.5.1 Incidence angle and Reynolds number effects 83
5.5.2 TLV axial flow 85
5.5.3 Influence of the tip geometry 88
5.6 TLV evolution with gap width 91
5.6.1 TLV intensity evolution 91
5.6.2 Gap width influence on the TLV axial flow 93
5.6.3 TLV position and wandering 95
5.6.4 Particular case at high incidence angles 98
5.6.5 Effect of the wall boundary layer thickness 100
5.6.6 New scaling of the TLV intensity 101
5.7 Summary and discussion 102

6 Towards a control of the TLV in hydraulic turbines 105
6.1 Motivation and context 105
6.2 Case study and experimental setup 106
6.3 Results 108
6.3.1 Flow visualizations 108
6.3.2 Hydrodynamic performances 114
6.4 Discussion 115

7 Conclusions and perspectives 117
7.1 Conclusions 117
7.2 Perspectives 118

A Appendices 121
A.1 Identification of the inclination angles between the vortex axis and the measurement plane 121
A.2 LDV measurement volume dimensions 123

Bibliography 133

Curriculum Vitae 135

List of Figures

1.1 Blade and casing arrangement in a Kaplan turbine [99]. 2

1.2 (a) Tip leakage vortex and clearance cavitation in a reduced scale model of a bulb turbine. (b) Example of anti-cavitation lips on a Kaplan turbine [1]. 2

1.3 Flow visualizations of the tip vortex formation. (a) Trailing vortices from a rectangular wing visualized in a smoke tunnel at $Re = 1 \times 10^5$, from Van Dyke [42]. (b) Trailing vortex from the tip of a rectangular wing visualized with colored fluid injection in water at $Re = 1 \times 10^5$, from Van Dyke [42]. (c) Cavitating tip vortex generated by a *NACA 0009* at $Re = 1.5 \times 10^6$ 6

2.1 Comparison of vortex models. The circulation Γ is the same for all vortices. . . 14

2.2 Value of β in eq. (2.12). The curve $\beta(n)$ for the Vatistas model is plotted along with the Rankine and Lamb-Oseen β value. 16

2.3 Cavitating and non-cavitating vortices from the model of Arndt & Keller [8]. . . 17

2.4 Choi & Ceccio [30] cavitating vortex for $r_{cv} = 0.5 r_c$ and different γ values. 18

2.5 Cavitating vortex of Bosschers [24] for various cavity radii. 20

3.1 EPFL high-speed cavitation tunnel. (a) Hydraulic circuit. (b) Test section. . . . 21

3.2 Streamwise mean velocity profile at the test section inlet, one chord upstream of the hydrofoil. W_∞=20 m/s. 22

3.3 Pictures illustrating the tip vortex generated by the *NACA 0009* (a) and the elliptical *NACA 16-020* (b). The flow is from right to left. 23

3.4 Sketch of the *NACA 0009* hydrofoil. 24

3.5 Sketch of the elliptical *NACA 16-020* hydrofoil. 25

3.6 Sketch of the sliding mounting support 26

3.7 Principle of LDV measurement from [14]. 28

3.8 (a) Tangential velocity profile measured by LDV. (b) Histograms of burst counts for two measurement locations. 29

3.9 (a) Deconvolution of a synthetic velocity profile. (b) Relative error between the original profile and the deconvolution of the mean profile. 31

3.10 (a) Büchner funnel for filtering of fluorescent particles from [88]. (b) Excitation and emission spectra of Rhodamine B in water. [110] 32

3.11 Comparison of the vortex identification methods. Flow conditions: W_∞=10 m/s, α=5°, z/c=1, rough *NACA 0009* hydrofoil. 35

3.12 (a) Wandering effect on the circumferential velocity. (b) Sketch of the parameters in eq. (3.16). (c) Correction of the wandering by aligning the velocity maps before averaging. 36
3.13 Example of a mean velocity map and the location of the instantaneous vortex centers. Flow conditions: W_∞=10 m/s, α=10°, z/c=1, rough *NACA 0009* hydrofoil. 38

4.1 (a) Top view of the experimental setup for the LDV measurements with the elliptical *NACA 16-020* hydrofoil. (b) Sketch of the method to find the mean vortex center. 42
4.2 (a) Example of the tangential velocity measured by LDV with (σ=1.7) and without (σ=2.8) vortex cavitation. W_∞=10 m/s, α=12° (b) Mesh of the measurement points surrounding the cavitating tip vortex. 43
4.3 Photograph of the cavitating tip vortex and the LDV laser beams. The laser beams are crossing slightly underneath the vortex cavity center. W_∞=10 m/s, α=12°, σ=1.7 44
4.4 Experimental setup for the PIV measurements with the elliptical *NACA 16-020* hydrofoil 45
4.5 Picture of the fluorescent particles and the cavitating tip vortex illuminated by the laser sheet. The camera is equipped with a long pass filter discarding the green laser light. 46
4.6 Relative orientation between the laser plane and the vortex axis. 46
4.7 Example of a raw and corrected PIV velocity fields in the case of a cavitating vortex. For readability, only 1 out of 4 vector is represented in the x-direction. . 48
4.8 Average tangential velocity profiles in cavitating-free conditions. (a) vector field with slicing cuts. (b) Average velocity (black curve) and individual velocity profiles (gray) 48
4.9 (a) Comparison on the PIV and LDV velocity profiles in cavitation-free regime. The grey area depicts the standard deviation.(b)-(d) Raw images from the PIV camera showing the local seeding in the vicinity of the cavitating vortex for the different seeding strategies. The vortex cavity edges are highlighted in yellow. . 50
4.10 (a) Sketch of the *NACA 16-020* with the tip injection channel. (b) LDV mean tangential velocity profiles one chord downstream of the hydrofoil, for various tip injection flow rates in cavitation-free conditions. W_∞=15 m/s, α=6° 51
4.11 Illustration of the image processing steps to determine the cavity radius 52
4.12 Mean tangential and axial velocity profiles measured by LDV along the x-axis for different incidence angles. Flow conditions: W_∞=10 m/s, cavitation-free, smooth hydrofoil. 54
4.13 Mean tangential and axial velocity profiles measured by LDV along the x-axis for different incidence angles. Flow conditions: W_∞=10 m/s, cavitation-free, rough hydrofoil. 55
4.14 Comparison of the tip vortex generated by the smooth and rough hydrofoils at W_∞=10 m/s, α=10°. 56

4.15 Average axial velocity for the smooth hydrofoil at α=12° and W_∞=10 m/s. (a) Raw LDV measurements. (b) Interpolated flow field 56

4.16 Evolution of the axial velocity in the vortex core for different incidence angles. Flow conditions: W_∞=10 m/s, smooth hydrofoil. 57

4.17 Axial velocity in the vortex core for an incidence angle of 12°. (a) Rough hydrofoil and W_∞=10 m/s. (b) Smooth hydrofoil and W_∞=15 m/s. 58

4.18 (a) Example the VM2 (black line) and Lamb-Oseen (dashed line) vortex model fitting on the LDV experimental data. (b) Curve fitting residual values. FLow conditions: W_∞=10 m/s, α=10°, smooth hydrofoil. 59

4.19 Wandering amplitude from PIV measurements. (a) 1000 instantaneous vortex centers at W_∞=10 m/s, α=12°. (b) Standard deviation of the mean vortex center position along the x and y axes as a function of α 60

4.20 Example of profile deconvolution at W_∞=10 m/s, α=12°. 60

4.21 Evolution of the lift and vortex characteristics with the foil incidence angle. . . 62

4.22 Computed pressure coefficient in tip vortex for the smooth hydrofoil at W_∞=10 m/s, α=12°. 63

4.23 Snapshots of the cavitating tip vortex generated by the elliptical *NACA 16-020* at different values of the cavitation number σ. Flow conditions: W_∞=10 m/s, α=12°, smooth hydrofoil. 64

4.24 Average velocity field ($u_v - \widetilde{w}\cot(\beta)$ and v_v) for the cavitating vortex at two different σ values. The cavity interface is marked by a white circle. For readability, only 1 out of 4 vectors is represented in the x-direction. 66

4.25 Isocontours of the velocity v_v for different σ values. $\sigma = 3$ corresponds to cavitation-free conditions, while $\sigma = 2$ and $\sigma = 1.5$ correspond to a small, respectively large, vortex cavity. Flow conditions: W_∞=10 m/s, α=12°. 66

4.26 Comparison of the tangential velocity for three values of sigma. $\sigma = 3$ corresponds to cavitation-free conditions, while $\sigma = 2$ and $\sigma = 1.5$ correspond to a small ($r_{cv} \approx 0.33 r_c$), respectively large ($r_{cv} \approx 0.8 r_c$) vortex cavity. The grey area represents the standard deviation. Flow conditions: W_∞=10 m/s, α=12°. 67

4.27 LDV axial velocity around a cavitating vortex. (a) Interpolated axial velocity map for the cavitating vortex at $\sigma = 1.5$. The measurement locations are depicted by the black dots and the cavity is represented by a white disk. (b) Axial velocity profile along the y-axis for the cavitation-free and cavitating vortex. Flow conditions: W_∞=10 m/s, α=12°. 68

4.28 Circulation and axial velocity profiles computed with eq. (4.3), for three Lamb-Oseen vortices with same circulation and arbitrary viscous core size radii. . . . 69

4.29 Non-dimensional cavity radius with the cavitation number for W_∞=10 m/s and 15 m/s, α=12°. Solid line: analytical predictions of Bosschers's model. Dashed lines: analytical predictions of Choi & Ceccio's model with varying parameter γ=0, 0.2, 0.4, 0.6, 0.8 and 1. 70

4.30 Comparison of the experimental tangential velocity and the prediction of the analytical models of Bosschers (red line) and Choi & Ceccio for γ=0.2 (green line), and γ=0.4 (blue line). The grey area depicts the standard deviation of the experimental data. 71

5.1 Sketch of the SPIV configuration used in the 3D measurement of the velocity field. 75
5.2 Comparison of the axial velocity profiles in the test section measured by PIV and LDV. No hydrofoil is mounted in the test section. 76
5.3 Example of an instantaneous velocity map over the complete common field of view of the SPIV cameras. The test section side wall is symbolized by the dashed line at x=0. 77
5.4 (a) Average tangential velocity $v_\theta(r)$ derived from 100 vectors fields. The measured velocity profile is fitted with a Lamb-Oseen and a Vatistas (n=2) velocity profile. (b) Corresponding circulation distribution. 79
5.5 Side view of the cavitating TLV generated by a *NACA 0009* at different p_∞. Flow conditions: W_∞=10 m/s, α=10°, τ=1. 80
5.6 See caption in Figure 5.7 81
5.7 (a) Snapshots of the cavitating TLV generated by a *NACA 0009* for different gap widths. The tip clearance is viewed from the side and is facing the observer. (b) Average TLV trajectory obtained from the superposition of the visualizations during 11 ms. The yellow crosses represent the position measured by SPIV in cavitation-free regime, in the planes z/c=1 and z/c=1.2. Flow conditions: W_∞=10 m/s, α=10°, p_∞=1 bar. 82
5.8 Vortex image system over and downstream of the hydrofoil according to potential flow theory [28]. The vortices b, c and d are the images of the actual vortex denoted by a. The induced velocities resulting from the image vortices b, c and d are sketched. 82
5.9 Evolution of the TLV circulation with incidence for the rough and smooth hydrofoil, W_∞= 10 m/s, τ=1.5, z/c=1. 83
5.10 Streamlines and norm of the streamwise vorticity, rough hydrofoil, W_∞= 10 m/s, τ=1.5, z/c=1. 84
5.11 Evolution of the TLV circulation with the inlet velocity for the rough and smooth hydrofoils, α=5°, τ=1.5, z/c=1. 85
5.12 Axial velocity in the vortex center vs incidence angle for both the rough and smooth hydrofoils. W_∞=10 m/s, τ=1.5, z/c=1 86
5.13 Isocontours of the axial flow, rough hydrofoil, W_∞= 10 m/s, τ=1.5, z/c=1. 87
5.14 3D streamlines with tracing particles in yellow showing the development of the TLV along the three measurement planes. The colors in the three measurement planes show the norm of the streamwise vorticity. Flow conditions: W_∞=10 m/s, τ=1.5, rough hydrofoil. 88
5.15 Cavitating TLV generated by a *NACA 0009* for the rounded tip and sharp tip geometry. Flow conditions: W_∞=15 m/s, α=5°, p_∞=0.9 bar, τ=0.5. 89

5.16 Evolution of the circulation and axial velocity vs incidence angle for the rounded tip and sharp tip hydrofoils. W_∞= 10 m/s, τ=1.5, z/c=1.2 90
5.17 Comparison of the TLV generated by the rounded tip and sharp tip hydrofoils at W_∞= 10 m/s, α=7°, τ=1.5 and z/c=1.2. Top: streamlines and norm of the streamwise vorticity. Bottom: isocontours of the axial flow velocity. 90
5.18 Evolution of the normalized circulation Γ^* with the normalized clearance τ. The dashed lines are the mean values for each incidence angle. 91
5.19 2D streamlines of the TLV with the norm of the streamwise vorticity (a) and isocontours of circumferential velocity (b) for various gap widths. Flow conditions: W_∞=10 m/s, α=10°, z/c=1, rough hydrofoil. 92
5.20 Evolution of axial velocity in the vortex core, normalized by the inlet velocity, with the normalized clearance τ. The dashed lines are the mean values for each incidence angle. 94
5.21 Isocontours of the axial velocity for different gap widths. Flow conditions: W_∞=10 m/s, α=10°, z/c=1, rough hydrofoil. 95
5.22 Evolution of the mean vortex center position (x_c, y_c) and standard deviation (std(x_c), std(y_c)) with the normalized clearance τ for the rough hydrofoil at z/c=1. The dashed lines are the mean values for each incidence angle. 96
5.23 x-y position of the TLV for the rough hydrofoil at W_∞=10 m/s and z/c=1. The x-coordinate represents the distance relative to the foil tip: x=$x_c - gap$. The numbers next to the data points indicate the corresponding value of τ. 97
5.24 Same caption as Figure 5.18 and Figure 5.20 but with the particular case of α=12°. Rough hydrofoil, z/c=1. 98
5.25 Instantaneous streamlines and axial velocity. Flow conditions: W_∞=10 m/s, α=12°, z/c=1, rough hydrofoil. 99
5.26 Instantaneous streamlines and axial velocity. Flow conditions: W_∞=10 m/s, α=10°, z/c=1, rough hydrofoil. 99
5.27 Comparison of the isocontours of the mean axial velocity for α=10° and α=12°. Rough hydrofoil, z/c=1. 100
5.28 (a) Boundary layer thickness vs inlet velocity at z/c=-1. (b) Boundary layer thickness vs downstream position at W_∞= 10 m/s. The dashed line is the best-fit of the theoretical law for a turbulent boundary layer on a flat plane [101]. No hydrofoil is mounted in the test section. 101
5.29 General TLV intensity evolution obtained by normalizing Γ^* and τ by Γ^*_∞ (the non-dimensional circulation at τ=2). Data measured at z/c=1, 1.2 and 1.5. . . . 102

6.1 Anti-cavitation lip and cavitating tip leakage vortex in a reduced scale model. . 105
6.2 Sketch of the grooves implementation. (a) Isometric view of the grooved cylinder and the hydrofoil. (b) Cross-section of the grooved cylinder. (c) Detail of the grooves geometry. 107
6.3 Different grooves configurations in the test section. 107

6.4 Comparison of the cavitating TLV without grooves in the clearance (top) and with the grooves oriented at 0° (bottom). (a) Snapshots of the cavitating TLV (b) Average TLV trajectory obtained from the superposition of the captured images during 11 ms at 20,000 FPS. Flow conditions: α=5° and $\tau = 0.1$, $\sigma = 1.2$. 108
6.5 Effect of the grooves at W_∞=10 m/s, α=5°, $\tau = 0.1$, $\sigma = 1.2$. (a) Snapshots of the cavitating TLV (b) Average TLV trajectory obtained from the superposition of the captured images during 11 ms at 20,000 FPS. 110
6.6 Same caption as Figure 6.5 but for α=5°, $\tau = 0.2$ and $\sigma = 1.2$. 111
6.7 Same caption as Figure 6.5 but for α=7°, $\tau = 0.1$ and $\sigma = 1.7$. 112
6.8 Same caption as Figure 6.5 but for α=7°, $\tau = 0.2$ and $\sigma = 1.7$. 113
6.9 Effect of the grooves on the lift and drag coefficients measured at $Re_c = 1 \times 10^6$ 115

A.1 Inclination of the vortex axis relative to the measurement plane. 121
A.2 (a) LDV configuration forming the measurement volume. (b) specification of the measurement volume size. 123

List of Tables

1.1 Permissible maximum deviations in geometrical similarity between prototype and model turbine, IEC 60193 standard [66]. 3

3.1 Technical specifications of the high-speed camera and lighting systems. 27
3.2 Technical specifications of the LDV equipment 28
3.3 Technical specifications of the PIV equipment. 32

4.1 Operating conditions for LDV and PIV measurements 41

5.1 Operating configurations for the SPIV measurements 78
5.2 Vortex core size for W_∞=10 m/s, α=7°, τ=1.5, z/c=1 84

Nomenclature

Latin letters

c	Hydrofoil chord	[m]
h	Maximum foil thickness	[m]
p	Static pressure	[Pa]
p_v	Saturation vapor pressure	[Pa]
p_∞	Static pressure at the test section inlet	[Pa]
r_c	Vortex viscous core radius	[m]
r_{cv}	Vortex cavity radius	[m]
x, y, z	Cartesian coordinates	[m]
r, θ, z	Cylindrical coordinates	[m], [rad], [m]
$x_\mathrm{c}, y_\mathrm{c}$	Vortex center coordinates	[m]
u, v, w	Spanwise, transverse and axial velocity	[m/s]
v_θ	Tangential velocity	[m/s]
$\tilde{w}$	Vortex induced axial velocity	[m/s]
L	Lift force	[kg·m/s^2]
D	Drag force	[kg·m/s^2]
S	Planform area	[m^2]
W_∞	Velocity at the test section inlet	[m/s]

Greek letters

α	Hydrofoil incidence angle	[°]
β	Laser plane inclination angle	[°]
Γ	Circulation	[m^2/s]
δ	Boundary layer thickness	[m]
ν	Kinematic viscosity	[m^2/s]
ρ	Density	[kg/m^3]
ω	Vorticity	[s^{-1}]

Non-dimensional variables

Re_c	Reynolds number	$Re_\mathrm{c} = \frac{W_\infty c}{\nu}$
σ	Cavitation number	$\sigma = \frac{p_\infty - p_v}{\frac{1}{2}\rho W_\infty^2}$
C_p	Pressure coefficient	$C_p = \frac{p - p_\infty}{\frac{1}{2}\rho W_\infty^2}$
C_L	Lift coefficient	$C_L = \frac{L}{\frac{1}{2}\rho W_\infty^2 S}$
C_D	Drag coefficient	$C_D = \frac{D}{\frac{1}{2}\rho W_\infty^2 S}$
τ	normalized tip clearance	$\tau = \frac{gap}{h}$
Γ^*	normalized circulation	$\Gamma^* = \frac{\Gamma}{W_\infty r_c}$
Γ^*_∞	Γ^* at τ=2	$\Gamma^* = \frac{\Gamma_{\tau=2}}{W_\infty r_c}$

Subscripts

cav	Cavitation
max	Maximum quantity
min	Minimum quantity
piv	PIV reference frame
p	Probe position
v	Vortex reference frame

Acronyms

EPFL	École Polytechnique Fédérale de Lausanne
IEC	International Electrotechnical Commission
LDV	Laser Doppler Velocimetry
PIV	Particle Image Velocimetry
RMS	Root Mean Square
SPIV	Stereo Particle Image Velocimetry
TLV	Tip leakage vortex

1 Introduction

1.1 Problem overview

1.1.1 Tip leakage vortex in axial turbomachines

Axial turbines and compressors require a small gap, or clearance, between the tip of the blades and the casing in order to ensure a rotor movement without rubbing, as illustrated in Figure 1.1. In an objective to minimize the energy losses, the tip clearance is usually kept as small as possible, within the limits of manufacturing constraints. Hence, the magnitudes of these clearances range from roughly one to several per cent of the blade chord in aircraft engines [116], while in hydraulic machines the tip clearance is typically 0.1 % of the blade chord [99]. The pressure difference between the blade pressure and suction sides provokes a leakage flow through the clearance region. The vorticity shed by this leakage flow rolls up into the so-called 'tip leakage vortex' (TLV), which is equivalent to a tip vortex developing in the vicinity of a wall. The adverse effects of tip leakage flows and the resulting TLV on the performance and efficiency of turbomachines have been extensively documented in the past. Examples include efficiency losses [37, 124], rotating instabilities [80, 106, 107], cavitation in pumps and inducers [49, 69, 74], as well as onset of stall in compressors [109].

The tendency of continuously increasing the output power of axial hydraulic machines, namely Kaplan, bulb and propeller turbines, is bringing the cavitation erosion issue to the front. Cavitation is likely to develop in the low pressure region that prevails in the core of TLVs as well as in the clearance region, as shown in Figure 1.2a. Depending on the trajectory of the cavitating vortex, severe erosion may be observed in the tip of the blades or in the discharge ring. Furthermore, the aggressiveness of the TLV cavitation may be amplified by a strong rotor-stator interaction: the wake of the distributor guide vanes produces a highly non-uniform pressure field, which leads to repetitive collapses and rebounds of the cavitating vortices [40, 91]. In this case, periodic inspections and repairs are required, leading to an increase of operational costs.

Despite the progress achieved so far in the understanding of tip vortex cavitation, mainly for marine propellers [7, 53, 85], it is still not possible to accurately predict the onset and development of TLV cavitation in axial turbines, neither from numerical simulations nor from reduced scale model tests. Design rules are still failing to avoid premature damage of the blades and the discharge ring. Besides the Reynolds number, such cavitation is very sensitive to the gap width and nuclei content in the water, as explained in Section 1.1.3. Obviously, these parameters are very hard to control during reduced scale model tests. As a consequence, it is possible to observe severe erosion on a turbine prototype while no cavitation was detected during model testing. In their attempt to mitigate the cavitation development in axial turbines, engineers commonly implement the so-called 'anti-cavitation lip', which is a metallic winglet attached to the tip of the blades shown in Figure 1.2b. Nevertheless, such a remedy often fails to reduce cavitation erosion, as reported by Roussopoulos & Monkewitz [99] in a simplified case study. Finally, it should be mentioned that in the case of Kaplan and bulb turbines, the blade pitch is adjustable in order to achieve an optimal efficiency over a wide range of flow and water head. The casing is therefore spherical or semi-spherical, as illustrated in Figure 1.1. The spherical casing yields greater efficiency, while the semi-spherical one facilitates the manufacture and maintenance, but also generates a stronger leakage flow [99].

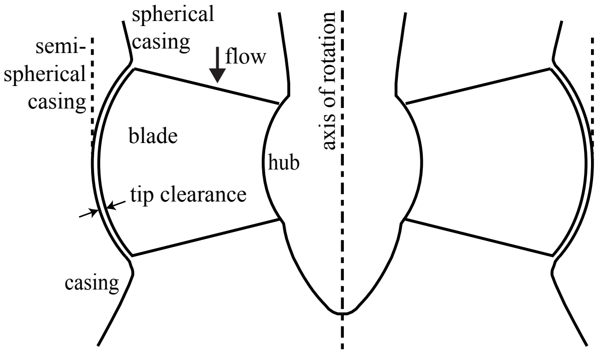

Figure 1.1: Blade and casing arrangement in a Kaplan turbine [99].

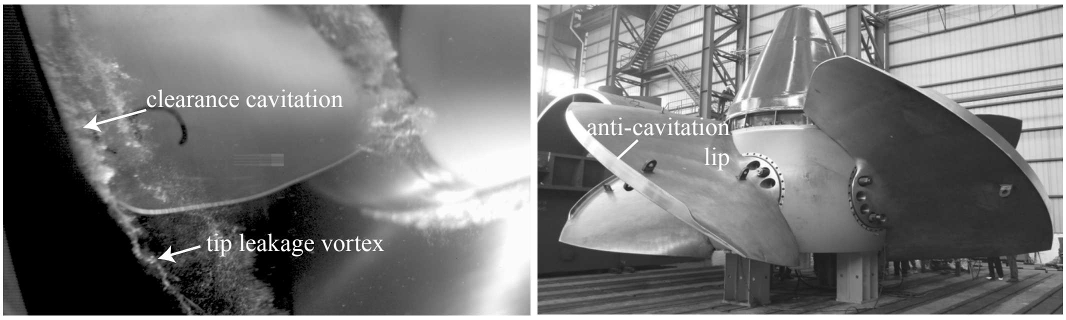

(a) TLV cavitation in a bulb turbine

(b) Anti-cavitation lip

Figure 1.2: (a) Tip leakage vortex and clearance cavitation in a reduced scale model of a bulb turbine. (b) Example of anti-cavitation lips on a Kaplan turbine [1].

1.1.2 Reduced scale model testing and TLV cavitation prediction

The rules for reduced scale model testing are stated by the International Electrotechnical Commission (IEC) 60193 standard [66]. The objective of the standard is to ensure that the hydraulic performance of the prototype can be predicted from model testing, considering scale effects. A basic requirement is to have geometrical similarity between model and prototype, i.e. all the water passages influencing the performance of the prototype should be as far as possible homologous to the prototype.

Concerning the blade tip clearances, the geometrical similarity requirements are met if the corresponding average clearance values of model and prototype are within the similarity tolerances given in Table 1.1. The IEC standard specifically asserts that the relative difference of the tip clearance between the average prototype value and the corresponding scaled model average value must be negative or zero, i.e. "*the prototype clearances shall not exceed the scaled model clearances*". Moreover, the uniformity tolerance, i.e. the relative deviation between the individual values of blade tip clearance and the corresponding average value, is set to ±50 %. This implies that locally, the deviation between the prototype and the scale model clearance can deviate up to a factor 3. Concerning the implication on hydraulic performances, the IEC states that as long as the deviations in geometric similarity of clearances are within the limits specified in Table 1.1, the scale-up of the hydraulic efficiency can be computed with the formula presented in the standard 60193 [66]. However, no directive is given regarding the influence of the clearance size on the prediction of TLV cavitation based on model testing.

From a practical point of view, the dimensions of the tip clearances during model testing depend on several factors. Mechanical considerations set the gap width to at least 0.2 mm in order to prevent any rubbing with the casing during the tests. Depending on the scaling factor between prototype and model, it is thus not always possible to respect the geometric similarity of the clearances. Moreover, the dimensions of the clearances are checked with the runner at rest and dewatered, i.e. no real time monitoring of the gap width is performed while the turbine is running. During a standard cavitation test, the pressure is varied at the runner

Table 1.1: Permissible maximum deviations in geometrical similarity between prototype and model turbine, IEC 60193 standard [66].

	Permissible maximum deviation		
	Uniformity tolerance		**Similarity tolerance**
	Model	**Prototype**	**Prototype/Model**
	Individual value to average value	**Individual value to average value**	**Prototype average value to scaled model average value $(L_P\text{-}\lambda_L L_M)$/(reference value) [1)]**
Clearances			
Seal and blade tip clearance	± 50 %	± 50 %	≤ 0
Seal clearance length	-	-	≥0
Guide vane end clearances	± 50 %	± 50 %	≤0

1) The reference value is taken to be the scaled model average value (λ_L L_M,) unless otherwise indicated. Angular tolerance is the difference between prototype and model angles.

exit in order to promote different cavitation patterns. The resulting pressure stresses on the runner casing and diffuser, often made of Plexiglas, may therefore affect the gap width. The thermal expansion and contraction due to the temperature difference between the assembly hall and the water, especially during winter, is another factor which potentially influences the clearance size. These aspects suggest that the clearance geometrical similarity is very hard to satisfy during model testing. But above all, there exists a considerable lack of knowledge of how the TLV cavitation is related to the gap width.

1.1.3 Vortex cavitation

Cavitation is commonly defined as the phase change process through which cavities form inside an initially homogeneous liquid when the pressure decreases [26, 51]. Since a region of concentrated vorticity, such as a tip vortex core, is accompanied by an intense pressure drop, it follows that cavitation inception often occurs in the vortex center. The fundamental parameter in the description of cavitation is the cavitation number σ, which is defined as:

$$\sigma = \frac{p_\infty - p_v}{\frac{1}{2}\rho W_\infty^2} \tag{1.1}$$

It is commonly admitted that cavitation occurs when the minimum pressure in a flow is equal to the vapor pressure, i.e. $p_{min} = p_v$. For steady flow, the pressure coefficient is given by

$$C_{p_{min}} = \frac{p_{min} - p_\infty}{\frac{1}{2}\rho W_\infty^2} \tag{1.2}$$

and the incipient value of σ is given by the condition $\sigma_i = -C_{p_{min}}$. As shown in a later section of this work, the minimum pressure coefficient at the vortex center varies with $\Gamma^2/W_\infty^2 r_c^2$, where Γ is the vortex circulation and r_c is the viscous core radius. In order to transpose the results from reduced scale model testing to the prototype, it is important to scale the experimental data for Γ and r_c by the flow conditions, such as the Reynolds number Re and the lift coefficient C_L [13]. Γ is related to the foil bound circulation Γ_0, which is linked to C_L according to the Kutta-Joukowski theorem ($\Gamma_0 = 0.5cW_\infty C_L$). Furthermore, McCormick [85] observed that the viscous core radius r_c is related to the thickness of the boundary layer δ on the pressure side surface of the foil tip, $r_c \sim \delta \sim Re^{-n}$, where $n = 0.2$ in the case of a turbulent boundary layer [13]. With these assumptions, the following inception scaling equation can be obtained [7]:

$$\sigma_i = K C_L^2 Re^m \tag{1.3}$$

where m is generally accepted to be approximately 0.4 and K is a positive constant that accounts for the differences in vortex roll up for different blade geometries, as reported by several authors [7, 13, 53, 82, 85].

The assumption that cavitation occurs at vapor pressure is generally inadequate [7]. Cavitation occurs in regions of flow where the pressure is low enough for nuclei to become unstable and grow into visual bubbles of vapor [11]. The process of vortex cavitation inception is therefore very sensitive to the water quality, i.e. the size and number density of nuclei [8]. These nuclei can be imbedded in the flow in the form of small gas bubbles, or find their origin in small cracks or crevices where the gas is trapped [7]. The critical pressure for cavitation inception approaches vapor pressure when there is a sufficient supply of nuclei greater than approximately 100 μm [11]. However, tip vortices can sustain large values of tension when there is a lack of nuclei [8]. Cavitation inception in tip vortices is a complicated physical process in which the details of how free-stream nuclei are ingested into the vortex plays a major role. As a consequence, the amount of sustainable tension and the size of the nuclei active in the cavitation are a function of the vortex strength. This can result in severe discrepancies in tip vortex cavitation occurrence between reduced scale models and prototypes, because the ratio of nuclei diameter to the vortex viscous core radius can vary by several orders of magnitude from experimental to prototype conditions [7]. It is therefore crucial to pay attention to the water quality when carrying out prediction experiments.

1.2 State of the art

Tip vortices are prevalent in many industrial applications (e.g., air transportation, marine propulsion, hydraulic machines, space rockets, etc.). The need to understand and control the dynamics of these flows has motivated numerous researches, producing an abundant literature. The references included in this section however merely represent a selection of contributions which were essential for the present work, and the bibliography is by no means an exhaustive summary of the problematic of tip vortex flows. The reader may refer to the book of Green [60] for a more comprehensive overview of all salient flows in which fluid vortices play a significant role. Concerning the adverse effects of tip leakage flows and TLV in turbomachines, an extensive literature review is given in the recent article of Wu et al. [122].

1.2.1 Tip vortex formation

The formation of tip vortices is an inherent characteristic of all lifting surfaces with finite wingspan [59]. Looking at the visualizations of the the flow in the vicinity of a rectangular wing in Figure 1.3, the rolling up of the streaklines at the wing tip into two concentrated vortices is striking. The vortex formation begins to occur almost at the leading edge of the wing, indicating a very rapid rolling up process, as illustrated in Figure 1.3c, which shows a cavitating tip vortex generated by a hydrofoil.

The formation of vorticity at the wing tip may be qualitatively understood in various ways. One of the simplest ways to understand the tip vortex formation is to consider the pressure field which exists near a wing tip [59]. The lift is generated by a net imbalance of the surface pressure distribution, i.e. the existence of a low static pressure above the wing and comparatively higher

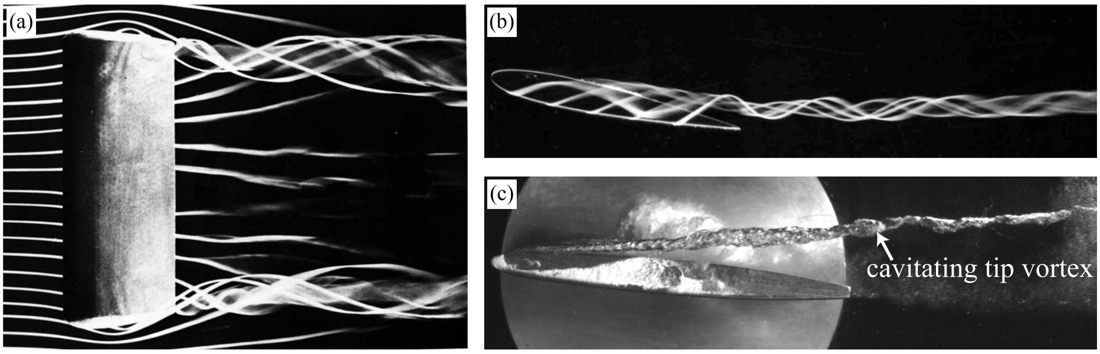

Figure 1.3: Flow visualizations of the tip vortex formation. (a) Trailing vortices from a rectangular wing visualized in a smoke tunnel at $Re = 1 \times 10^5$, from Van Dyke [42]. (b) Trailing vortex from the tip of a rectangular wing visualized with colored fluid injection in water at $Re = 1 \times 10^5$, from Van Dyke [42]. (c) Cavitating tip vortex generated by a *NACA 0009* at $Re = 1.5 \times 10^6$

pressures below it. As a consequence, the flow near the wing tips tends to curl around the tips, being forced from the high-pressure region just underneath the tips to the low-pressure region on the top side of the wing. This tendency for the flow to leak around the wing tips establishes a circulatory motion that trails downstream of the wing, creating a tip vortex at each wing tip [5]. Tip vortices may also be explained by considering Prandtl's classical lifting-line theory [5]. In order for the wing to generate lift, there must exist a net circulation around the wing (the 'bound vortex'). Kelvin's theorem furthermore implies that this circulation has to be matched by an equal and opposite shed circulation (the 'starting vortex') [61]. Helmholtz vortex laws (valid for inviscid and incompressible flows), however, state that a vortex filament cannot terminate in a fluid and the bound and starting vortices must hence be connected by tip vortices [59]. The formation of tip vortices is however more complex than presumed by the above mechanisms. In the near wake, the velocity field may be strongly asymmetric due to the interactions of multiple intertwined shear layer vortices, which are generated near the wing tip. Furthermore, the formation and development of tip vortices are strongly affected by several factors such as the wing geometry, the nature of the boundary layer on the wing, the viscosity and the turbulence intensity near the tip [60].

The tip vortices begin their existence as a sheet of vorticity which is shed by the wing, with a higher concentration of vorticity at each wing tip [59]. The self-induced motion of the vortex sheet causes it to roll-up near the wing tip into a strong single tip vortex. Kaden [123] made the first attempt to predict the vortex roll-up process analytically, in the specific case of an elliptical load distribution. Experiments suggest that this roll-up is essentially completed within 2-3 chords downstream of the wing trailing edge, independently of the wing geometry [59]. Assuming a laminar flow, Batchelor [18] derived an axisymmetric similarity solution for a steady incompressible isolated vortex, valid far downstream of the wing tip. This solution is often used to describe the structure of the tip vortex flow and is presented in Section 2.2.5. In the absence of viscosity, Batchelor predicted the existence of an axial velocity excess in the vortex core. However, Batchelor also suggested that the viscous diffusion of the vortex and the head losses arising from the wing boundary layer would eventually lead to an axial velocity deficit in the vortex core. Moore & Saffman [87] extended Batchelor's analysis and developed a more sophisticated model, valid in the intermediate region between the completion of the roll-up and the far field, where the solution of Batchelor holds. Recently, Pino et al. [35] used Stereo Particle Image Velocimetry (SPIV) to measure the 3D velocity field in the tip vortex behind a foil. Better agreement with the model of Moore & Saffman than with Batchelor's was observed.

Vortex measurements are complicated by the phenomenon of vortex wandering [38, 62], which is a random fluctuation of the vortex centerline whose origin remains unclear. It is presumed to arise from a resonant excitation triggered by the free stream turbulence, as reported by Fabre et al. [44]. Devenport et al. [38] studied the structure of the tip vortex in the wake of a rectangular wing using hot-wire probe and noted that the vortex wandering creates a smoothing effect that can make the vortex appear more diffuse than in reality. They also observed that the flow inside the vortex core is laminar. Recently, Giuni et al. [56] used SPIV to compare the tip vortex generated by a rectangular wing with a rounded and sharp tip geometry. Comparing the wandering of the vortex flow for the two wingtip geometries, they identified two sources of the vortex fluctuation: the interaction of secondary vortices moving around the primary vortex and the rolling-up of the vorticity sheet. The influence of the wingtip geometry (sharp or rounded) was also investigated by Lee & Pereira [77], who found that the tip shape may greatly influence the strength of the axial flow in the tip vortex core. The intensity of the axial flow in the vortex center plays a crucial role in the early evolution of the tip vortex [34, 56]. Moreover, the stability of tip vortices is strongly affected by the swirl parameter, which is proportional to the ratio between the maximum swirl velocity and the axial velocity at the center of the vortex [22, 46].

1.2.2 Tip leakage vortex

The earliest studies on tip leakage vortices were performed in the context of gas turbine or compressors and relate principally to the reduction of the accompanying losses. Many loss correlations and models have been proposed, see for instance Sieverding [104] for a review. Rains [97] proposed the application of slender body approximation to the tip leakage vortex. Following this approach, Chen [29] developed a vortex method to predict the position of the leakage vortex in an axial compressor. Song & Martinez-Sanchez [106, 107] proposed an analytical model for the position of the tip clearance vortex, based on the assumptions that the flow under the blade is a pressure-driven "sheet jet". The tip clearance flow in a compressor cascade was described by Kang et al. [70, 71, 72]. They observed that the TLV rapidly intensifies near the blade leading edge and that the TLV circulation grows with increasing tip clearances. The effect of different blade tip geometries on the tip leakage flow was investigated by Heyes et al. [65]. They found that the use of squealers (a recessed cavity at the blade tip), particulary on the suction side, may limit the efficiency losses compared to a conventional flat tip geometry.

More recently, several experimental and numerical studies of the flow field in the tip region of thermal turbomachines were carried out. Muthanna & Devenport [90] and Wang & Devenport [117] performed detailed measurements of the flow field downstream of a linear compressor cascade, with and without end wall motion. They found that the clearance region dynamics is dominated by the TLV, which produces a well-defined rotating flow and a region of streamwise mean-velocity deficit. They observed that the tip clearance size has a strong effect on the position, size and strength of the TLV: an increase of the gap width by a factor four leads to an increase of the TLV circulation by approximately three times. Moreover, they noted that the absence of end wall motion does not affect many of the characteristics of the TLV, including the mechanism that drives the vortex and turbulence structure. A change of the tip clearance modifies both the location and intensity of the TLV in the same way with and without end wall motion. For the same configuration, You et al. [125, 126] found with a large eddy simulation approach that the mechanisms for the generation of vorticity and turbulent kinetic energy are insensitive to tip-gap size variations.

The effect of the tip gap size on the tip leakage cavitation has first been investigated in axial-flow pumps by Farrell & Billet [49]. They have found that cavitation inception in an axial pump may be delayed if the tip clearance is set to an optimum value of about 0.2 times the maximum blade thickness. Laborde et al. [74] found that the clearance cavitation (but not the TLV cavitation) is strongly mitigated when the clearance edge is rounded on the blade pressure side. Boulon et al. [25] examined the effect of the clearance size on the tip vortex generated by an elliptical foil in a setup without relative motion between the end wall and the foil. They found, conversely, that the cavitation inception index increases as the gap is reduced, while no tip vortex cavitation was observed in the most confined cases. Similar observations were reported by Gopalan et al. [57] for the case of a cambered hydrofoil in a water tunnel. More recently, Wu et al. [122] and Miorini et al. [86] studied experimentally the internal structure of the TLV within the rotor of an axial waterjet pump, using both 2D and stereo-PIV. They observed that the instantaneous TLV structure is composed of unsteady vortex filaments that propagate into the tip region of the blade passage and roll up into the TLV. They also reported that vortex breakdown can occur when the TLV migrates towards the pressure side of the neighboring blade, which drastically changes the TLV characteristics [79].

Many phenomena associated with TLVs are still not understood. For instance, it remains unclear how the gap width is related to the occurrence of cavitation in the vortex, which can lead to severe erosion and premature cracks of impeller blades.

1.3 Thesis objective

The primary aim of this research project is to gain a better understanding of the underlying physics of vortex confinement as well as tip leakage vortex (TLV) cavitation. In particular, the clearance size effect on TLV strength and flow structure is assessed by performing systematic flow measurements in a simplified case study. The local properties of the TLV are established using stereo-PIV and flow visualizations for a wide range of incidence angles, inlet velocities and a large number of tip clearances. The experimental results form an extensive database for the validation and further development of analytical and numerical flow models. This shall allow proposing new avenues for the mitigation and control of TLV cavitation in axial turbines.

The change in the structure of a tip vortex due to cavitation occurrence is another central issue being addressed in the present work. The influence of a cavity inside a vortex on its key characteristics, such as the viscous core size and circulation, remains poorly investigated in the literature, despite the considerable importance for understanding and predicting the cavitation occurrence. It is intended to fill this gap by comparing the tip vortex velocity field with and without cavitation in its core.

Finally, specific techniques to mitigate the tip vortex cavitation are tested in the simplified case study. In particular, the alteration of the clearance geometry with shallow grooves to manipulate the gap flow and control the vortex intensity & trajectory is evaluated.

1.4 Document structure

Chapter 2 presents the vortex models which are used in the following sections to interpret the experimental data. After presenting the general equations governing vortex flows, the most common non-cavitating vortex models are introduced. Three cavitating vortex models found in the literature are also presented, along with their respective derivations.

Chapter 3 details the experimental apparatus and techniques used in the present work. The test facility and the hydrofoils are described as well as the velocity measurement techniques. Moreover, this chapter describes the specific post-processing strategies that are implemented in order to obtain accurate flow properties.

Chapter 4 is dedicated to the study of the effect of cavitation on the structure of a tip vortex. The results of this chapter are compared with the cavitating vortex models presented in Chapter 2.

Chapter 5 focuses on the effect of the gap width on the TLV strength and associated flow structures in a simplified case study. The potential benefit of the clearance geometry alteration with shallow grooves to mitigate TLV cavitation in the same simplified case study is finally discussed in Chapter 6.

2 Vortex models

2.1 Structure of a tip vortex and governing equations

Tip vortices are characterized by two zones: the core, close to the center of rotation where the viscous effects are dominant, and an outer region where the motion is mainly irrotational. In a cylindrical coordinate system, with the axes r, θ, z and the corresponding velocity components v_r, v_θ, v_z, the general Navier-Stokes equations of motion [19] for an axisymmetric ($\partial/\partial\theta$=0) and incompressible flow with no body force reduce to:

$$\frac{\partial v_r}{\partial t} + v_r \frac{\partial v_r}{\partial r} + v_z \frac{\partial v_r}{\partial z} - \frac{v_\theta^2}{r} = -\frac{1}{\rho}\frac{\partial p}{\partial r} + \nu\left(\nabla^2 v_r - \frac{v_r}{r^2}\right) \tag{2.1a}$$

$$\frac{\partial v_\theta}{\partial t} + v_r \frac{\partial v_\theta}{\partial r} + v_z \frac{\partial v_\theta}{\partial z} + \frac{v_\theta v_r}{r} = \nu\left(\nabla^2 v_\theta - \frac{v_\theta}{r^2}\right) \tag{2.1b}$$

$$\frac{\partial v_z}{\partial t} + v_r \frac{\partial v_z}{\partial r} + v_z \frac{\partial v_z}{\partial z} = -\frac{1}{\rho}\frac{\partial p}{\partial z} + \nu \nabla^2 v_z \tag{2.1c}$$

where the operator ∇^2 is given by: $\nabla^2 = \frac{\partial^2}{\partial r^2} + \frac{1}{r}\frac{\partial}{\partial r} + \frac{\partial^2}{\partial z^2}$. The continuity equation becomes:

$$\frac{1}{r}\frac{\partial (r v_r)}{\partial r} + \frac{\partial v_z}{\partial z} = 0 \tag{2.2}$$

The required boundary conditions in a plane perpendicular to the vortex axis can be formalized as:

- at r=0, $v_r = v_\theta = 0$, $\partial v_z/\partial r = \partial p/\partial r = 0$.
- as r→ ∞, $v_r \to 0$, $v_\theta \to 0$.

Since no general solution satisfying these equations is known, further assumptions and approximations have to be made to obtain an analytical description of a vortex, see for instance [19, 87, 92, 100]. Based on experimental measurements or heuristics arguments, several vortex models were developed over the years. This chapter reviews the most common vortex models, which are used in the following sections of this work to interpret the experimental data.

2.2 Non-cavitating vortex models

2.2.1 Rankine vortex

The tangential velocity in tip vortices can be approximated by simple vortex models that consider only the evolution of v_θ as a function of r, regardless of v_z and v_r, which are assumed to be zero. The simplest model of a vortex is the Rankine vortex, which assumes that the fluid in the vortex core ($r \le r_c$) is in solid body rotation, while the outer region ($r > r_c$) is irrotational:

$$v_\theta(r) = \begin{cases} \dfrac{\Gamma}{2\pi r_c^2} r & r \le r_c \\ \dfrac{\Gamma}{2\pi r} & r > r_c \end{cases} \tag{2.3}$$

where Γ is the vortex circulation and the core radius r_c is defined as the distance to the vortex axis where v_θ is maximal. However, this model is not realistic as the vorticity $\omega = (1/r)\partial(r v_\theta)/\partial r$, which is entirely contained within the vortex core, presents a discontinuity at $r = r_c$.

2.2.2 Lamb-Oseen vortex

Assuming that $v_r = v_z = 0$, and that v_θ is a function of r and t only, the Navier-Stokes eq. (2.1) reduce to [19]:

$$\frac{v_\theta^2}{r} = \frac{1}{\rho}\frac{\partial p}{\partial r} \tag{2.4a}$$

$$\frac{\partial v_\theta}{\partial t} = \nu\left(\frac{\partial^2 v_\theta}{\partial r^2} + \frac{1}{r}\frac{\partial v_\theta}{\partial r} - \frac{v_\theta}{r^2}\right) \tag{2.4b}$$

The Lamb-Oseen vortex [75] arises as an exact solution of eq. (2.4) for the initial condition $v_\theta(r,0) = \Gamma/2\pi r$ (the initial vorticity is $\omega(r,0) = \Gamma\delta(r)$ [100], where δ is Dirac's delta-function), and can be written as follows:

$$v_\theta(r,t) = \frac{\Gamma}{2\pi r}\left(1 - e^{-r^2/4\nu t}\right) \tag{2.5}$$

For any given time t, the term $4\nu t$ can be interpreted as the square of a distance [52], so that eq. (2.4) becomes:

$$v_\theta(r) = \frac{\Gamma}{2\pi r}\left(1 - e^{-\alpha r^2/r_c^2}\right) \tag{2.6}$$

where $r_c = \sqrt{4\nu\alpha t}$ is the location of peak tangential velocity and $\alpha \approx 1.25643$ (the exact value of α is solution of the equation: $\mathrm{e}^\alpha = 1 + 2\alpha$). It is worth mentioning that with this definition of r_c, only ~71 % of the total circulation Γ is contained within the vortex core, while 99 % of the circulation is reached at a distance $2r_c$,

2.2.3 Vatistas vortex

Vatistas [114] proposed a simplified empirical expression that encompasses a series of tangential velocity profiles for a vortex, which can be written in the form:

$$v_\theta(r) = \frac{\Gamma}{2\pi}\frac{r}{\left(r_c^{2n} + r^{2n}\right)^{1/n}} \tag{2.7}$$

By varying the shape parameter n in eq. (2.7), a wide range of velocity profiles can be defined. When $n = 1$, the Scully vortex is reproduced, the case $n \approx 2$ gives a close approximation to the Lamb-Oseen model, while $n \to \infty$ corresponds to the Rankine vortex [20]. It should be noted that with $v_\theta(r)$ given by the algebraic expression of Vatistas, the other velocity components v_r and v_z can be derived analytically from the equations of motion, see [20, 114].

2.2.4 VM2 vortex

The VM2 model was proposed by Fabre and Jacquin [45] in order to give a more realistic description of tip vortices. The model features two core scales r_1 and r_2, delimiting an intermediate region $r_1 < r < r_2$ within which $v_\theta(r) \sim r^{-\alpha}$, where α is a constant. The VM2 model is defined as follows:

$$v_\theta(r) = \frac{\Gamma}{2\pi}\frac{r_2^{\alpha-1}}{r_1^{\alpha+1}}\frac{r}{\left[1 + (r/r_1)^4\right]^{(1+\alpha)/4}\left[1 + (r/r_2)^4\right]^{(1-\alpha)/4}} \tag{2.8}$$

As an illustration, all the previously mentioned vortex models are plotted in Figure 2.1. The value of the circulation Γ is the same for all the vortices. Different values of the shape parameter

n are plotted for the Vatistas vortex, while for the VM2 model, the following parameters are chosen: $r_1 = 0.9r_c$, $r_2 = 3r_1$ and $\alpha = 0.9$. The VM2 and the Vatistas models can both approximate closely the Lamb-Oseen vortex, which has already been used successfully to fit experimental data of vortices, see for instance [30, 51].

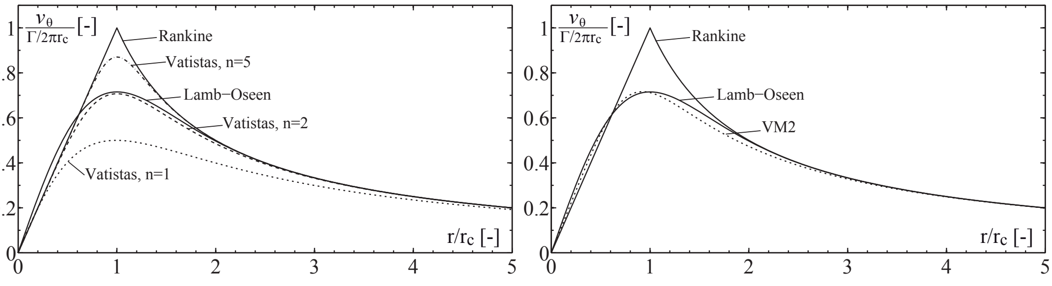

(a) Vatistas model (b) VM2 model

Figure 2.1: Comparison of vortex models. The circulation Γ is the same for all vortices.

2.2.5 Batchelor and Moore & Saffman vortex

This section would not be complete without mentioning the models of Batchelor and Moore & Saffman, which are widely used to describe the structure of the trailing vortex flow. Batchelor [18] published one of the first tip vortex models taking into account the axial velocity component. The author considered a boundary-layer-type approximation of the steady form of eq. (2.1), $\partial/\partial t = 0$, $\partial/\partial z \ll \partial/\partial r$ and $v_r \ll v_z$, valid far downstream of the hydrofoil, supplemented by the assumption that the axial velocity defect (or excess) is small compared to the freestream velocity W_∞. Batchelor found a self-similar solution whose tangential velocity $v_\theta(r,z)$ is equivalent to the Lamb-Oseen distribution given by eq. (2.5) (with the substitution of the time t by z/W_∞). The radial velocity $v_r(r,z)$ is zero and the axial velocity [35] is given by:

$$v_z(r,z) = W_\infty + \frac{\Gamma}{32\pi^2 \nu z} B\left(\frac{W_\infty r^2}{4\nu z}\right) - e^{-W_\infty r^2/4\nu z}\left[\frac{\Gamma}{32\pi^2 \nu z}\ln\left(\frac{W_\infty z}{\nu}\right) + \frac{W_\infty^2 L}{8\nu z}\right] \tag{2.9}$$

where L is an integration constant and B is a function given by:

$$B(\eta) = e^{-\eta}\left[\ln\eta + \mathrm{E}_1(\eta) - 0.807\right] + 2\mathrm{E}_1(\eta) - 2\mathrm{E}_1(2\eta) \tag{2.10}$$

where $\mathrm{E}_1(\eta) = \int_\eta^\infty (e^{-x}/x)\,dx$ is the exponential integral. A simplified version of Batchelor's model, referred to as the q-vortex, is commonly used in stability analyses [43]. This model is obtained by neglecting the variation of the velocity field along the z-axis and the term B in the function $v_z(r,z)$. After a few simplifications, this model can be written in the form [36]:

$$v_\theta(r) = \frac{q}{r}\left(1 - e^{-r^2}\right), \qquad v_z(r) = a + e^{-r^2} \tag{2.11}$$

where $a = W_\infty/\Delta W$, with $\Delta W = W_0 - W_\infty$, W_0 being the axial velocity at the vortex center. The swirl parameter q is defined as $\Omega r_c/\Delta W$, where Ω is the rotation rate at the vortex axis.

Moore & Saffman [87] developed a more sophisticated model valid in the intermediate region between the completion of roll-up and the far field. To this end, they solved the boundary-layer-type equations for the axial velocity induced by the viscous decay of the swirl, but, instead of assuming an external potential vortex like in Batchelor's solution, Moore & Saffman considered a more realistic solution for the external inviscid swirl that takes into account the roll-up process [35]. For an extensive presentation of the Moore & Saffman's solution, the reader may refer to [35, 50, 87]. It is worth mentioning that the VM2 model presented previously is essentially an approximation of the Moore & Saffman's solution without the axial flow [50].

2.2.6 Key vortex parameters

The minimum pressure coefficient in the vortex center $C_{p_{min}} = (p(r=0) - p_\infty)/0.5\rho W_\infty^2$ can be derived by integrating the radial equilibrium equation (2.4a). Independently of the considered vortex model, $C_{p_{min}}$ can be written in the form:

$$C_{p_{min}} = -\beta\left(\frac{\Gamma}{W_\infty r_c}\right)^2 \tag{2.12}$$

where β is a constant whose value depends on the choice of vortex model. For instance, it can be readily shown that $\beta = 1/2\pi^2 \approx 0.0506$ for the Rankine vortex whereas for the Lamb-Oseen vortex $\beta = 2\alpha log(2)/4\pi^2 \approx 0.044$. In the case of the Vatistas model, β is a function of the shape parameter n, as illustrated in Figure 2.2, defined by:

$$\beta(n) = \frac{1}{4\pi^2}\frac{\Gamma(1+1/n)\Gamma(1/n)}{\Gamma(2/n)} \tag{2.13}$$

It is stressed that $\Gamma(n)$ in eq. (2.13) denotes the Euler integral of the second kind (Gamma function), not to be confused with the circulation Γ. Equation (2.12) shows that the estimation of the minimum pressure in the vortex center, which is essential to predict the occurrence of cavitation, effectively reduces to the estimation of two key parameters, namely the vortex circulation Γ and the viscous core radius r_c.

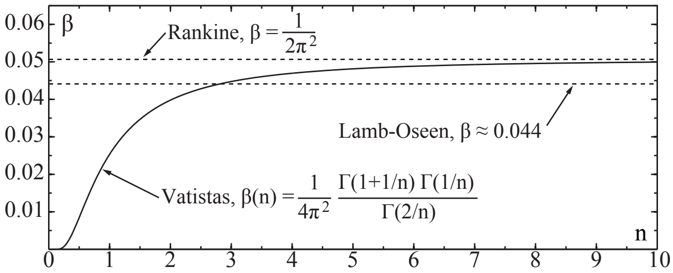

Figure 2.2: Value of β in eq. (2.12). The curve $\beta(n)$ for the Vatistas model is plotted along with the Rankine and Lamb-Oseen β value.

2.3 Cavitating vortex models

2.3.1 The modified Rankine vortex of Arndt & Keller

A simple model for cavitation inception in a vortex was derived by Arndt & Keller [8], based on the Rankine vortex in eq. (2.3). The total angular momentum per unit length contained within a radius $r_0 \to \infty$ for a Rankine vortex is given by:

$$\sum = \rho \int_0^{r_0} 2\pi r^2 v_\theta dr = \frac{1}{2}\rho\Gamma\left(r_0^2 - \frac{1}{2}r_c^2\right) \tag{2.14}$$

It should be noted that the total angular momentum is not bounded, but tends to infinity as $r_0 \to \infty$. Arndt & Keller then define a cavitating Rankine vortex such that $r \leq r_{cv}$ is vaporous, and its viscous core radius is r_{c2} $(r_{cv} < r_{c2})$:

$$v_{\theta,cav}(r) = \begin{cases} \dfrac{\Gamma}{2\pi r_{c2}^2} r & r_{cv} \leq r \leq r_{c2} \\ \dfrac{\Gamma}{2\pi r} & r > r_{c2} \end{cases} \tag{2.15}$$

where the subscript $'_{cav}'$ refers to the cavitating vortex. The radius r_{c2} is unknown and a priori different from r_c, the viscous core radius of a non-cavitating vortex. It should be noted that eq. (2.15) implies that the circulation Γ in the cavitating case is identical to the one of the non-cavitating vortex. The total angular momentum per unit length of the cavitating vortex (neglecting the vaporous part in comparison to the liquid phase) is:

$$\sum_{cav} = \rho \int_{r_{cv}}^{r_0} 2\pi r^2 v_{\theta,cav} dr = \frac{1}{2}\rho\Gamma\left(r_0^2 - \frac{1}{2}r_{c2}^2 - \frac{1}{2}\frac{r_{cv}^4}{r_{c2}^2}\right) \tag{2.16}$$

Assuming that the angular momentum is held constant, the equality $\sum = \sum_{cav}$ yields the following relation between r_c, r_{c2} and r_{cv}:

$$(r_c/r_{c2})^2 = 1 + (r_{cv}/r_{c2})^4 \tag{2.17}$$

Furthermore, by prescribing that the pressure at the cavity interface is equal to the vapor pressure, it can be shown [8] that:

$$r_{cv} = r_{c2}, \qquad r_{c2} = r_c/\sqrt{2} \tag{2.18}$$

The radius of the cavitating vortex core is equal to $1/\sqrt{2}$ times the non-cavitating viscous core radius and is completely filled with vapor. Moreover, using eq. (2.15), it is easy to show that the maximum velocity in the cavitating vortex is $\sqrt{2}$ times higher than in the non-cavitating vortex, as illustrated in Figure 2.3. It should be noted that the flow outside of the cavity is completely irrotational. According to Stokes's theorem [100], which states that the circulation is equal to the integral of the flux of vorticity, the vorticity must be entirely contained within the vaporous core. However, the physical relevance of this assumption has never been conclusively supported by experimental data.

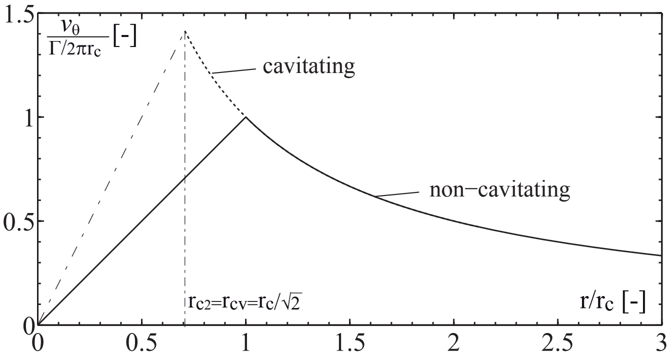

Figure 2.3: Cavitating and non-cavitating vortices from the model of Arndt & Keller [8].

2.3.2 The modified Lamb-Oseen vortex of Choi & Ceccio

A cavitating vortex model based on a heuristic modification of the Lamb-Oseen vortex, cf. eq. (2.6), was proposed by Choi & Ceccio [30]:

$$v_{\theta,cav}(r) = \frac{\Gamma_2}{2\pi\left(r-\gamma r_{cv}\right)}\left(1-e^{-\alpha\left(\frac{r-\gamma r_{cv}}{r_{c2}-\gamma r_{cv}}\right)^2}\right) \tag{2.19}$$

where r_{cv} is the cavity radius and Γ_2, r_{c2}, γ are parameters of the cavitating vortex. The circulation of the cavitating vortex Γ_2 is a priori different from Γ, the circulation of the non-cavitating vortex. The parameter γ can vary in the range of $0 < \gamma < 1$ and is related to the tangential velocity at the cavity interface. When $\gamma = 0$, the liquid velocity profile is the same as that of a non-cavitating Lamb-Oseen vortex (with radius r_{c2} and circulation Γ_2), with the vapor occupying the region $0 < r < r_{cv}$. Conversely, if $\gamma = 1$, the tangential velocity at the cavity interface is zero. The shear stress at the cavity interface is assumed to be zero [31].

In order to determine the parameters of the cavitating vortex (r_{cv}, Γ_2, r_{c2}, γ) as a function of the non-cavitating vortex parameters (Γ and r_c), four relationships are required to close the problem. One relationship is provided by the conservation of angular momentum $\sum$ per unit length, contained within a radius r_0:

$$\sum = \sum_{cav} = \rho \int_0^{r_0} 2\pi r^2 v_\theta dr = \rho \int_{r_{cv}}^{r_0} 2\pi r^2 v_{\theta,cav} dr \tag{2.20}$$

Since the integral of the angular momentum is not bounded as $r_0 \to \infty$, the upper limit of the integration r_0 is chosen large enough to not affect the solution (typically $r_0 = 10r_c$ [30]). Secondly, it is assumed that the kinetic energy per unit length KE is conserved:

$$KE = KE_{cav} = \rho \int_0^{r_0} \frac{1}{2} 2\pi r v_\theta^2 dr = \rho \int_{r_{cv}}^{r_0} \frac{1}{2} 2\pi r v_{\theta,cav}^2 dr \tag{2.21}$$

Thirdly, the pressure at the cavity interface must be equal to the vapor pressure p_v and is computed using the radial equilibrium specified in eq. (2.4a):

$$\frac{p(r = r_{cv}) - p_\infty}{\rho} = \frac{p_v - p_\infty}{\rho} = \int_\infty^{r_{cv}} \frac{v_{\theta,cav}^2}{r} dr \tag{2.22}$$

Finally, the fourth parameter γ is kept as a free parameter, to be determined by experiments. As an illustration, Figure 2.4 shows the Choi & Ceccio's cavitating vortex with a cavity radius $r_{cv} = 0.5r_c$, for different values of the γ parameter.

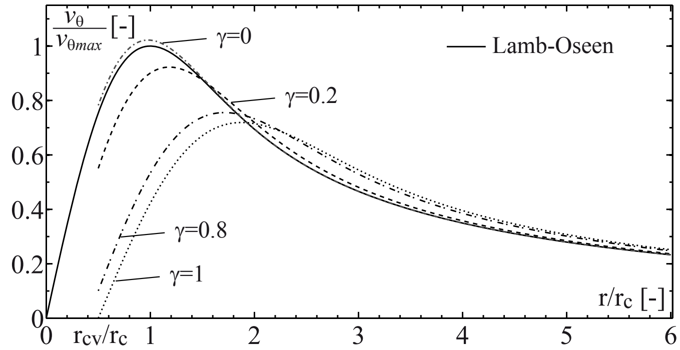

Figure 2.4: Choi & Ceccio [30] cavitating vortex for $r_{cv} = 0.5r_c$ and different γ values.

2.3.3 The cavitating Lamb-Oseen vortex of Bosschers

Bosschers [24] derived the analytical extension of the Lamb-Oseen vortex in the case of a cavitating vortex. Using jump relations at the cavity interface to obtain the appropriate boundary conditions, an exact solution to eq. (2.4) can be found. These jump relations are obtained using the Reynolds transport theorem for the conservation of mass and momentum for the total volume of fluid and vapor. Neglecting the surface tension and considering that the boundary of the interface moves with a relative velocity $\overrightarrow{u_s}$, the jump relations are given in vector format by [24]:

$$\text{mass}: \quad [[\rho\,(\vec{u}-\vec{u}_s)\cdot\vec{n}]] = 0 \tag{2.23}$$

$$\text{momentum}: \quad [[\rho\vec{u}\,[(\vec{u}-\vec{u}_s)\cdot\vec{n}] - \hat{\tau}\cdot\vec{n}]] = 0 \tag{2.24}$$

where $\vec{n}$ corresponds to the normal at the interface and $\hat{\tau}$ is the stress tensor given by:

$$\hat{\tau} = -p\hat{I} + \mu\left[\nabla\vec{u} + (\nabla\vec{u})^T\right] \tag{2.25}$$

Assuming that the contribution of the vaporous phase is negligible and the radial velocity v_r much smaller than v_θ, the projection of eq. (2.23) yields the following boundary conditions:

$$\text{r}: \quad p\,(r = r_{cv}) = p_v \tag{2.26}$$

$$\theta: \quad \frac{\partial v_\theta(r = r_{cv})}{\partial r} = \frac{v_\theta(r = r_{cv})}{r} \tag{2.27}$$

The pressure at the cavity interface is equal to the vapor pressure p_v. Equation (2.27) states that the shear stress at the cavity interface equals zero. The integration of this equation reveals that the tangential velocity at the cavity interface is a linear function of the type $v_\theta = \Omega{\cdot}r$, i.e. a solid body rotation. Bosschers [24] proposed the following general analytical solution for v_θ that satisfies eq. (2.4b):

$$v_\theta = \frac{\Gamma}{2\pi r}\left(1 - \beta e^{-\alpha r^2/{r_c}^2}\right) \tag{2.28}$$

where β is an arbitrary constant whose value depends on the boundary conditions. Substituting eq. (2.28) in eq. (2.27) yields:

$$\beta = \frac{r_c^2}{r_c^2 + \alpha r_{cv}^2} e^{\alpha r_{cv}^2/r_c^2} \tag{2.29}$$

The circumferential velocity v_θ of a cavitating vortex can then be written as:

$$v_{\theta,cav}(r) = \frac{\Gamma}{2\pi r}\left(1 - \frac{r_c^2}{r_c^2 + \alpha r_{cv}^2}\, e^{-\alpha(r^2 - r_{cv}^2)/{r_c}^2}\right) \tag{2.30}$$

Equation (2.30) implies that the circulation of the cavitating vortex Γ is identical to the one of the non-cavitating vortex given by eq. (2.6). The radius of the cavity r_{cv} can be determined using eq. (2.22) with the second boundary condition $p(r = r_{cv}) = p_v$, as shown in eq. (2.26). Figure 2.5 illustrates the circumferential velocity profiles obtained with eq. (2.30) for various cavity radii. Away from the cavity, the velocity distribution of the cavitating vortex is identical to the non-cavitating vortex. In contrast, near the liquid-gas interface, the tangential velocity field of a cavitating vortex is always smaller than in cavitation-free conditions. Using eq. (2.30), it is easy to show that the vorticity given by $\omega = (1/r)\partial(r v_\theta)/\partial r$ reaches its maximum at the cavity interface. Assuming that the vorticity in the vapor phase is constant and equal to the vorticity of the liquid phase at the cavity interface, it can be shown that the integral of the flux of vorticity, and hence the vortex circulation, are identical in the cavitating and non-cavitating cases.

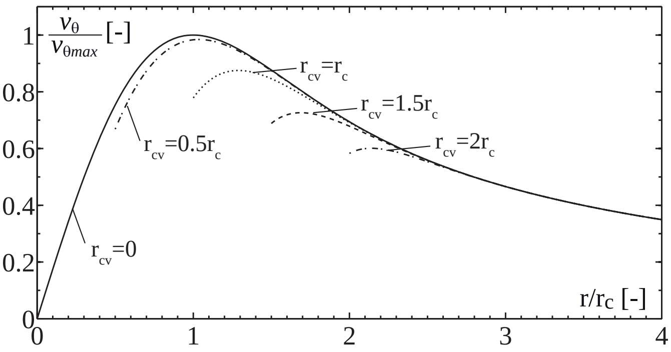

Figure 2.5: Cavitating vortex of Bosschers [24] for various cavity radii.

3 Experimental apparatus and procedure

3.1 High-speed cavitation tunnel

The experiments are carried out in the EPFL high-speed cavitation tunnel described by Avellan et al. [16] and illustrated in Figure 3.1. The test facility is a closed loop circuit holding approximately 100 m^3 of water. The inner dimensions of the rectangular test section are 150 x 150 x 750 mm. The test section walls are made of 80 mm thick Plexiglas, providing a good optical access to the flow. Upstream of the test section, a screen, a honeycomb and a convergent are installed to avoid macroscopic flow rotation and reduce the turbulence intensity. The contraction ratio of 46:1 results in a uniform velocity distribution in the test section. A double suction pump provides a total head of 36.5 m for 1.125 m^3/s at 885 rpm. The pump is driven by a 500 kW power DC-electric motor and the maximum flow velocity at the test section inlet is 50 m/s.

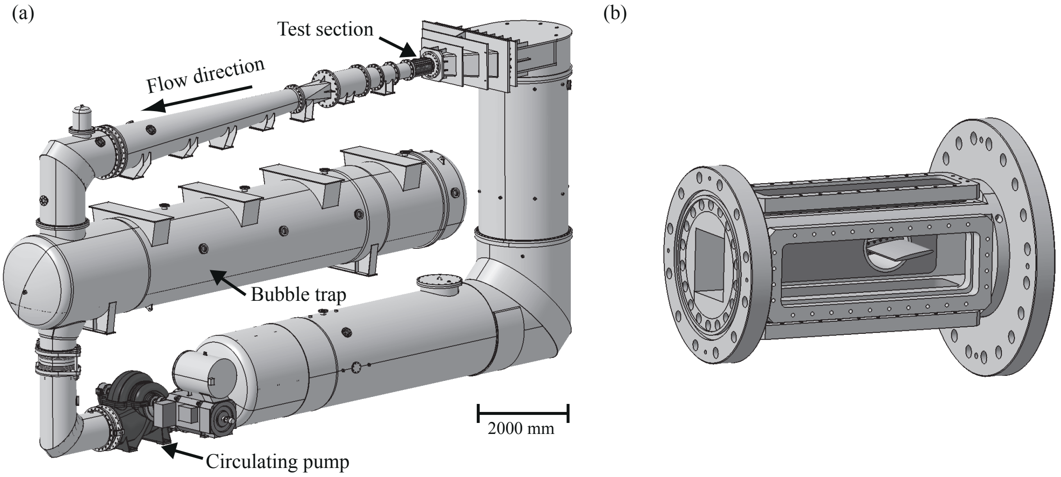

Figure 3.1: EPFL high-speed cavitation tunnel. (a) Hydraulic circuit. (b) Test section.

The operating flow parameters are the freestream velocity W_∞ at the test section inlet, and the cavitation number defined as $\sigma = 2(p_\infty - p_v)/\rho W_\infty^2$, where p_∞ and p_v are the reference pressure at the test section inlet and the vapor pressure, respectively. The mean flow velocity is derived from absolute pressure measurement at both ends of the convergent. The pressure can be varied by adjusting the air pressure on the free surface of a dedicated vessel.

3.1.1 Test section flow quality

The quality of the inlet flow is verified by performing a LDV velocity survey across the test section, cf. Section 3.5. The measurements are made at mid-height of the test section inlet, in the spanwise direction, while no hydrofoil was mounted. A typical example is illustrated in Figure 3.2 for W_∞=20 m/s. Apart from the boundary layer region, the velocity in the streamwise direction is constant within 2 % and the fluctuations are uniform within 0.4 %. Additional measurements at W_∞=10 m/s and 5 m/s did not reveal any significant Reynolds effects. The boundary layer thickness is estimated to be roughly 4 mm. It should be noted that the large standard deviation in the wall boundary layer measured by the LDV is due to the finite size of the control volume (about 1.3 mm) in a region of high velocity gradients.

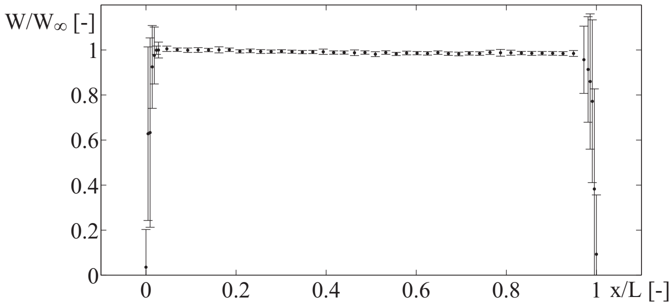

Figure 3.2: Streamwise mean velocity profile at the test section inlet, one chord upstream of the hydrofoil. W_∞=20 m/s.

3.1.2 Water quality and nuclei content

The intermediate stage of the cavitation tunnel is dedicated to the elimination of the free gas through a specific bubble trap system. It consists of a superposition of several roof-like plates, through which the flow passes. The bubbles larger than 100 μm tend to rise by gravity along the plates, where they are collected in a vertical pipe. The nuclei content is regulated by performing a degassing procedure before the measurements. The tunnel is operated in supercavitating conditions during approximately one hour, in order to activate the nuclei and facilitate their capture by the bubble trap. This degassing procedure allows to maintain the dissolved oxygen concentration below 3 ppm, with less than one active nuclei per cubic centimeter [48].

3.2 Hydrofoils

Two different kinds of hydrofoils are used throughout the experiments: a *NACA 0009* with a rectangular planform and a elliptical hydrofoil with a *NACA 16-020* cross section. The *NACA 0009* is used to investigate the gap width influence on the tip leakage vortex dynamics, since it creates a tip clearance geometry similar to an axial turbine. However, the generated cavitating vortex is disturbed by the interactions with the foil wake and the test section walls, resulting in a fluctuating non-cylindrical cavitating core, as illustrated in Figure 3.3. In addition, it is not possible to obtain a cavitating TLV without generating at the same time a partial cavitation on the foil leading edge. The *NACA 0009* hydrofoil is therefore not adapted to investigate the change in the vortex structure due to cavitation occurrence in its core. In contrast, the elliptical *NACA 16-020* hydrofoil spans only up to the middle of the test section and generates a very stable and coherent tip vortex that is almost free of perturbations, as shown in Figure 3.3b. Moreover, given that elliptical foils are used in numerous studies on tip vortex cavitation [7, 9, 25, 52, 53], the vortex generated by the *NACA 16-020* hydrofoil is an ideal case study to investigate the effect of cavitation on a vortex.

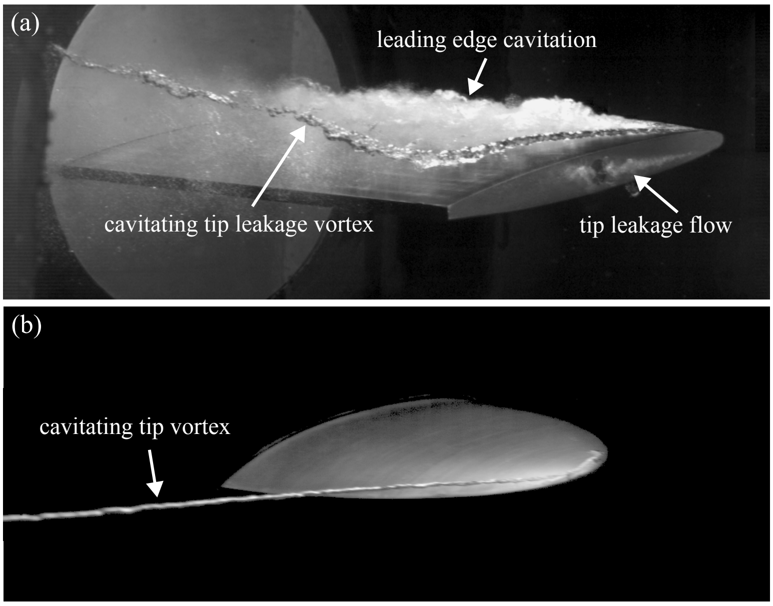

Figure 3.3: Pictures illustrating the tip vortex generated by the *NACA 0009* (a) and the elliptical *NACA 16-020* (b). The flow is from right to left.

3.2.1 Rectangular planform hydrofoil

The hydrofoil, sketched in Figure 3.4, is a stainless steel *NACA 0009* with a blunt trailing edge. The complete geometry designation is *NACA 0009 - 7.8 45/1.93* where the first number refers to the leading edge curvature, the second is the location of the maximum thickness and the third is the slope at the trailing edge. The foil chord length is originally c_0=110 mm. It is blunt

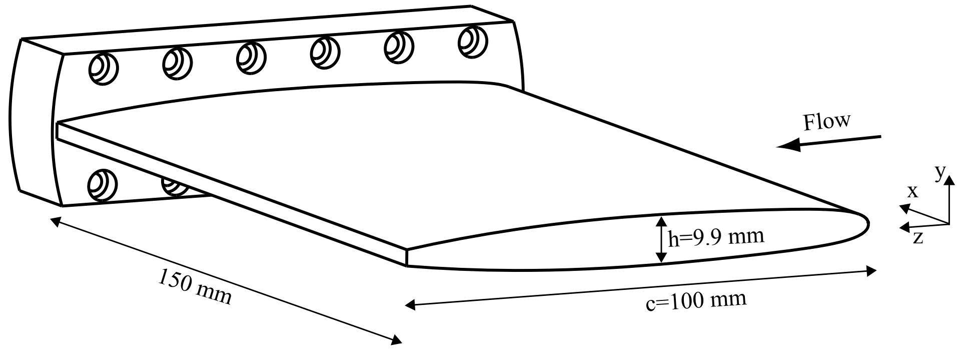

Figure 3.4: Sketch of the *NACA 0009* hydrofoil.

truncated at c=100 mm, resulting in a 3.22 mm trailing edge thickness. The foil span is 150 mm and its maximum thickness if h=9.9 mm. Two *NACA 0009* hydrofoils are used. The first one features two sharp edges on the tip pressure and suction side corners, while the second one is rounded with a small radius of 1 mm on the tip pressure side corner, in order to limit flow separation and cavitation in the clearance. The thickness distribution of the hydrofoil y_b is defined as:

$$\begin{aligned} 0 \le \frac{x}{c_0} \le 0.5 \qquad & \frac{y_b}{c_0} = a_0\left(\frac{x}{c_0}\right)^{1/2} + a_1\left(\frac{x}{c_0}\right) + a_2\left(\frac{x}{c_0}\right)^2 + a_3\left(\frac{x}{c_0}\right)^3 \\ 0.5 < \frac{x}{c_0} \le 1.0 \qquad & \frac{y_b}{c_0} = b_0 + b_1\left(1-\frac{x}{c_0}\right) + b_2\left(1-\frac{x}{c_0}\right)^2 + b_3\left(1-\frac{x}{c_0}\right)^3 \end{aligned} \tag{3.1}$$

with c_0 being the original chord length and :

$$\left\{\begin{array}{l} a_0 = +0.1737 \\ a_1 = -0.2422 \\ a_2 = +0.3046 \\ a_3 = -0.2657 \end{array}\right. \left\{\begin{array}{l} b_0 = +0.0004 \\ b_1 = +0.1737 \\ b_2 = -0.1898 \\ b_3 = +0.0387 \end{array}\right. \tag{3.2}$$

3.2.2 Elliptical planform hydrofoil

The elliptical *NACA 16-020* hydrofoil is sketched in Figure 3.5. The span is 90 mm and the chord length at the root is c_0=60 mm. The chord length changes accordingly to the position along the span, forming an elliptical planform. Its thickness distribution y_b is also defined by eq. (3.1), with the following coefficients [78]:

$$\begin{cases} a_0 = +0.197933 \\ a_1 = -0.04785 \\ a_2 = -0.0082 \\ a_3 = -0.11188 \end{cases} \begin{cases} b_0 = +0.002 \\ b_1 = +0.465 \\ b_2 = -0.684 \\ b_3 = +0.292 \end{cases} \tag{3.3}$$

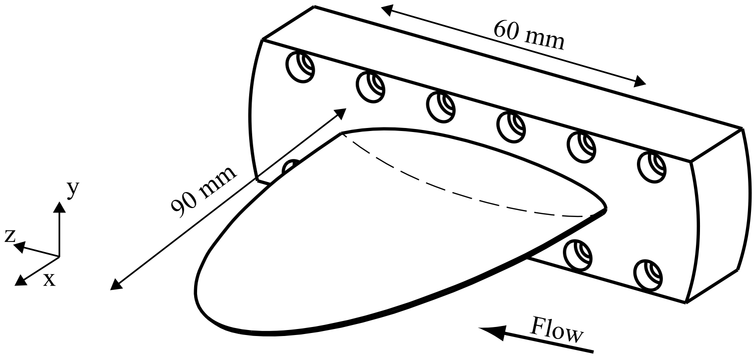

Figure 3.5: Sketch of the elliptical *NACA 16-020* hydrofoil.

3.2.3 Leading edge roughness

The influence of the foil boundary layer state is investigated by testing smooth and roughened leading edges. The turbulent boundary layer on the *NACA 0009* can be tripped with a 4 mm wide strip of distributed roughness, made of glue and 125 μm diameter sand. The roughness is placed on both sides of the hydrofoil, 4 mm downstream of the leading edge, as described by Ausoni et al. [15]. For the elliptical *NACA 16-020*, roughness is added on one twelfth of the chord length, e.g. at the maximum chord length (60 mm), 5 mm have been roughened.

3.3 Mounting supports

3.3.1 Sliding support

A sliding support of the hydrofoil was manufactured in order to easily adjust the clearance between the foil tip and the test section wall. The support is compatible with the existing hydrofoils and consists of an inner part, on which the hydrofoil is fixed, which slides into a fixed outer part, as sketched in Figure 3.6. The sealing between the two parts is ensured by an O-ring. The penetration of the hydrofoil in the test section is controlled via the rotation of a threaded rod, which is fixed to the sliding part with a bearing. The clearance size can be varied between 0-20 mm, corresponding to a penetration of the hydrofoil in the test section between 150 and 130 mm.

Since the clearance size can slightly change due to the deformation of the Plexiglas side windows when the test section is pressurized, the following methodology was adopted to measure the gap width. First, the test section is pressurized at the desired value. Then, the clearance is reduced down to zero, corresponding to the contact between the foil tip and the test section wall. Finally, the requested tip clearance is set by measuring the distance between the base of the support and a reference point on the threaded rod.

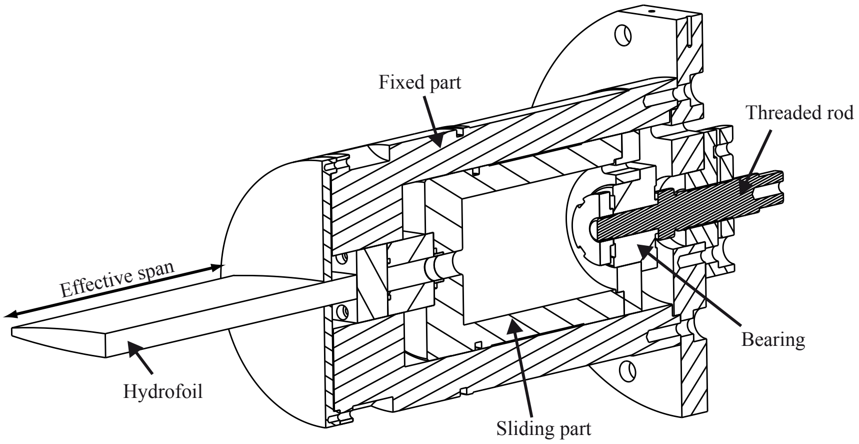

Figure 3.6: Sketch of the sliding mounting support

3.3.2 Hydrodynamic load cell

The measurement of the hydrodynamic forces on the hydrofoils is performed by a five component load cell. The load cell consists of a deformable H-beam on which the hydrofoils are mounted. The deformation of the H-beam is measured by several strain gauges forming five full bridge circuits. The maximum measurable lift force is 10^4 N and the precision is 1.5 N and 0.5 N for the lift and drag, respectively [41].

3.4 High-speed flow visualization

High-speed flow visualizations using cavitation as a tracer are performed in order to assess the vortex and leakage flow dynamics. For this purpose, a Photron Fastcam SA1.1 digital camera is employed with the appropriate lighting. The camera records images at full resolution (1024 x 1024 pixels) up to a frame rate of 5’400 fps. However, the resolution drops down to 64 x 16 pixels at the maximum frame rate of 675’000 fps. Two xenon flash lights (Cordin flash, model 359, 1.1 KJ energy) of 11 ms duration are used to illuminate the scene. Triggering and synchronization with the camera are achieved via a TTL signal. A highly uniform LED screen was also used as a back light, in order to enhance the contrast between the gaseous and liquid phases. The main technical specifications of the camera and the lighting source are given in Table 3.1.

Table 3.1: Technical specifications of the high-speed camera and lighting systems.

High-speed camera	
Model	Fastcam SA1.1
Max. resolution	1024 x 1024 pixels (up to 5'400 fps)
Max. frame rate	675'000 fps
Shutter speed	1 - 16'700 μs
Buffer memory	8 GB
Flash lamp	
Model	Cordin flash (model 359)
Max pulse duration	11 ms
Electric energy	1.1 KJ
LED backlight	
Model	PHLOX LEDW-BL-550X400-MSLLUB-Q-1R-24V
Dimension	550 x 400 mm
Luminance	7'000 CD/m^2

3.5 Laser Doppler Velocimetry

3.5.1 Measurement principle

Laser Doppler Velocimetry (LDV) is a non-intrusive flow velocity measurement technique. An overview of LDV principle and technique is given in [127]. The measurement principle, illustrated in Figure 3.7, is based on the analysis of the light scattered (Doppler burst) by seeding particles, which are supposed to follow the motion of the fluid without perturbing it. The intersection of two coherent and converging laser beams forms a tiny region, called measurement volume, where an interference fringe pattern of high and low light intensity is formed. The velocity of a particle crossing the measurement volume is measured by the spectral analysis of the scattered light signal, which is modulated by the spacing between the fringes. This spacing is imposed by the laser wavelength and beam intersection angle. The velocity component in the direction normal to the fringes is thus measured. Simultaneous measurements of the other velocity components can be achieved by combining couples of laser beams with different wavelengths and converging from different planes at the same location.

A two components Dantec FlowExplorer LDV system is used with a 300 mm focal length lens. The technical details of the LDV system are summarized in Table 3.2. It should be noted that due to light refractions, the dimensions of the measurement volume are not identical in water or air, see Appendix A.2 for the calculation of these dimensions. The seeding particles are 10 μm hollow glass spheres, with a density of 1100 kg/m^3. The LDV probe is usually mounted on a remotely controlled 2D traversing system to displace the measurement volume at the desired location.

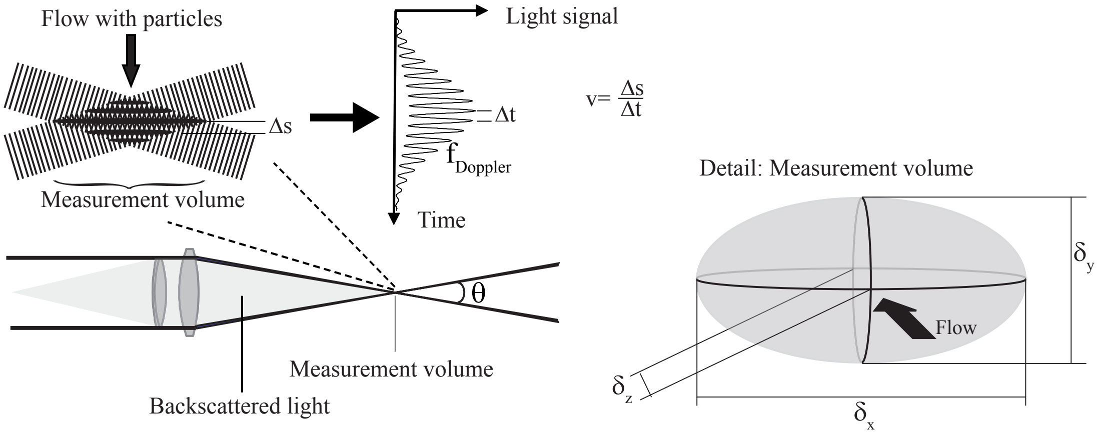

Figure 3.7: Principle of LDV measurement from [14].

Table 3.2: Technical specifications of the LDV equipment

Optical head	
Model	Dantec FlowExplorer
Wavelength	660 nm (Ch. 1) & 785 nm (Ch. 2)
Energy	35 mW per channel
Beam diameter	2.5 mm
Focal length in air	300 mm
Measurement volume in air	1.013 × 0.1013 × 0.1008 mm (Ch. 1)
($\delta_x \times \delta_y \times \delta_z$)	1.205 × 0.1205 × 0.1199 mm (Ch. 2)
Measurement volume in water	1.351 × 0.1013 × 0.1011 mm (Ch. 1)
($\delta_x \times \delta_y \times \delta_z$)	1.606 × 0.1205 × 0.1202 mm (Ch. 2)
Signal processor	
Model	BSA F60

3.5.2 Measurement deconvolution

Two phenomena are known to affect the measurement of a vortex by LDV. First, vortices are always subjected to the so-called wandering, which is a random fluctuation of the vortex centerline with an amplitude of the order of the vortex core size, cf. Section 3.7.2. In consequence, vortices measured by static measuring techniques, such as LDV, appear to be more diffuse than in reality [38, 67]. Secondly, the finite size of the LDV measurement volume, which is approximately of the same order as the viscous vortex core radius, leads to an additional smoothing effect of the velocities that must be accounted for [76]. The combination of these effects change any time-averaged point measurement into a weighted average in both space and time [62] such that a correction method is needed. Figure 3.8 shows a typical experimental tangential velocity profile with the histograms of the burst counts at two locations along the vortex radius. The viscous core radius is about 1 mm in this case. It can be observed that if the spatial velocity gradient is weak, such as at the position 1, the histogram features a tight distribution centered on the local mean velocity. On the other hand, in the central region with high spatial velocity gradients (position 2), the combined effect of vortex wandering and the finite dimension of the measurement volume cause the histogram to be spread over a wide velocity range.

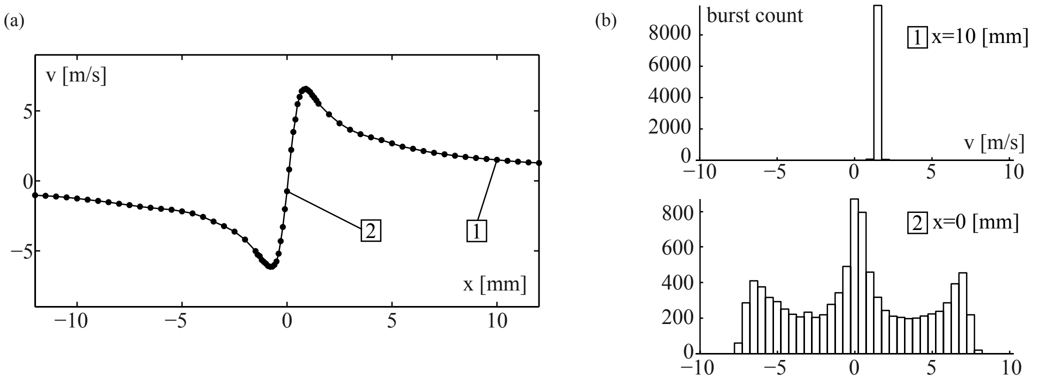

Figure 3.8: (a) Tangential velocity profile measured by LDV. (b) Histograms of burst counts for two measurement locations.

Following Devenport [38], a Gaussian isotropic wandering of RMS amplitude σ_w, can be modeled by attributing a probability density function (pdf) to the instantaneous vortex location x_v and y_v, in a Cartesian coordinate system whose origin is set at the mean vortex position:

$$Pdf_w\left(x_v, y_v\right) = \frac{1}{2\pi{\sigma_w}^2}\exp\left(-\frac{{x_v}^2 + {y_v}^2}{2{\sigma_w}^2}\right) \tag{3.4}$$

Note that eq. (3.4) can be easily adapted into a bivariate normal probability density function to model a non-isotropic wandering [67]. However, since an isotropic wandering is observed in our study, we will restrict our analysis to this particular case. The velocity field V_p measured over a long period by a static probe at the position x_p and y_p can thus be expressed by the convolution of the probability density function Pdf_w with the true velocity field:

$$V_p\left(x_p, y_p\right) = \int_{-\infty}^{\infty}\int_{-\infty}^{\infty} Pdf_w\left(x_v, y_v\right) V\left(x_p - x_v, y_p - y_v\right) dx_v dy_v = Pdf_w * V \tag{3.5}$$

where the symbol $*$ denotes the convolution operation. The effect of the finite size of the measurement volume is modelled in a similar manner. Since the measurement volume is formed at the intersection of two Gaussian laser beams, the light intensity distribution along its principal axes is also given by a Gaussian distribution [127]. The likeliness of detecting a particle passing through the measurement volume can thus be described by a bivariate probability density function:

$$Pdf_v\left(x_v, y_v\right) = \frac{1}{2\pi\sigma_{vx}\sigma_{vy}}\exp\left(-\frac{1}{2}\left(\frac{{x_v}^2}{{\sigma_{vx}}^2} + \frac{{y_v}^2}{{\sigma_{vy}}^2}\right)\right) \tag{3.6}$$

where, according to the properties of a gaussian beam [127], σ_{vx} and σ_{vx} correspond to $1/4$ of the dimensions of the measurement volume δ_x and δ_y, respectively. The velocity field measured by LDV V_m can finally be expressed as the successive convolution of Pdf_w and Pdf_v with the true velocity field V:

$$V_m = Pdf_v * Pdf_w * V = \overline{Pdf} * V \tag{3.7}$$

with

$$\overline{Pdf}\left(x_v, y_v\right) = \frac{1}{2\pi\sqrt{{\sigma_w}^2 + {\sigma_{vx}}^2}\sqrt{{\sigma_w}^2 + {\sigma_{vy}}^2}} \exp\left(-\frac{1}{2}\left(\frac{{x_v}^2}{{\sigma_w}^2 + {\sigma_{vx}}^2} + \frac{{y_v}^2}{{\sigma_w}^2 + {\sigma_{vy}}^2}\right)\right) \tag{3.8}$$

where we have taken advantage of the associativity of the convolution product and the fact that the convolution of two Gaussians is another Gaussian. Knowing the parameters of $\overline{Pdf}$, it is thus possible to inverse eq. (3.7), i.e. to perform a deconvolution of the measured velocity field to obtain the true velocity field.

Different strategies can be implemented to achieve this goal. One solution is to assume that the measured velocity profiles can be expressed by an analytical model, for instance the Lamb-Oseen model for the tangential velocity. Starting with an arbitrary analytical velocity profile, a profile that simulates the experimental data can be obtained through eq. (3.7). The parameters of the analytical model can then be determined by performing a best-fit, in least-square sense, of the convolved analytical model over the velocity profile measured by LDV. An alternative strategy is to take advantage of the numerous deconvolution techniques that have been used in the field of image processing and signal deblurring [67]. Using the convolution theorem, it is possible to express eq. (3.7) as a simple multiplication in the Fourier domain and the deconvolution can be directly computed as:

$$\mathscr{F}\left(V_m\right) = \mathscr{F}\left(\overline{Pdf}\right)\mathscr{F}\left(V\right) \qquad \rightarrow \qquad V = \mathscr{F}^{-1}\left(\frac{\mathscr{F}\left(V_m\right)}{\mathscr{F}\left(\overline{Pdf}\right)}\right) \tag{3.9}$$

where $\mathscr{F}$ denotes the Fourier transform. However, numerical problems arise when applying eq. (3.9) because the probability density function and the measurements are both band-limited due to the finite size of the measurement domain. To overcome this issue, iterative numerical processing can be used, such as the *Van Cittert* algorithm or *blind deconvolution* [67].

The wandering amplitude is a prori unknown. It is however possible to keep σ_w in eq. (3.8) as a free parameter and to adjust it by matching the standard deviation of the velocity in the vortex center with experimental data [93]. It should be noted that this procedure is valid only if the flow in the vortex center is laminar, i.e. all the velocity fluctuations are due to wandering and are not generated by turbulence. Recent measurements of Giuni et al.[56] indicate that this is indeed the case.

An example of deconvolution is illustrated in Figure 3.9(a). Starting with a synthetic velocity profile (red curve), an average velocity profile (black curve), which imitates experimental data acquired by LDV, is obtained using eq. (3.7). The wandering amplitude is set close to the one observed experimentally with the elliptical *NACA 16-020* hydrofoil, i.e. σ_w=0.2 mm, while σ_{vx} and σ_{vy} are computed from the dimensions of the measurement volume indicated in Table 3.2. The deconvolution of this average velocity profile is performed by solving eq. (3.9) with the *Van Cittert* algorithm and is represented by the dashed line. The deconvolution overlaps almost perfectly the original velocity profile and the relative error between the two curves is given in Figure 3.9(b). The maximum relative error is 0.006 %, demonstrating that the convolution procedure can be effectively inverted.

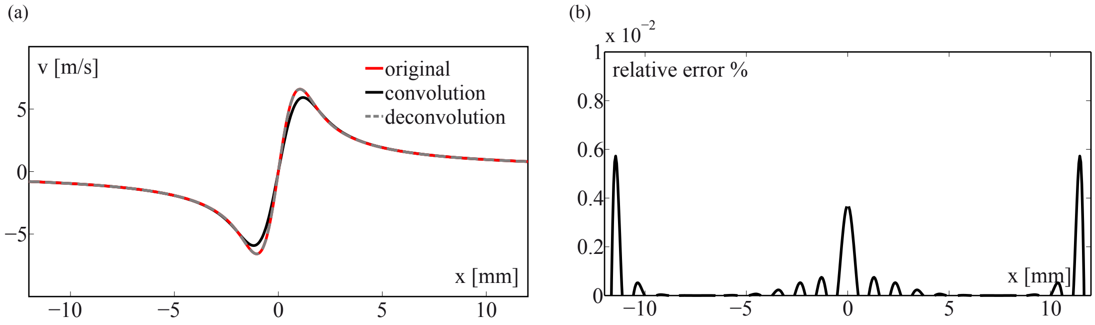

Figure 3.9: (a) Deconvolution of a synthetic velocity profile. (b) Relative error between the original profile and the deconvolution of the mean profile.

3.6 Particle Image Velocimetry

3.6.1 Measurement principle

Particle Image Velocimetry (PIV) is another non-intrusive optical flow velocity measurement technique. The measurement principle is based on the analysis of two successive images of seeding particles in the flow which are illuminated by a double pulsed laser sheet [2]. The images are divided into small portions, typically 32 × 32 pixels, called Interrogation Areas (IA). The average particle displacement vector of each IA is calculated by cross-correlation of the image pairs. Since the time between the two successive images is a precisely known parameter of the PIV acquisition, the velocity (in px/s) in each IA window can be evaluated. Using the appropriate scale factor between pixels and millimeters, the real physical flow velocity in m/s can be obtained. A two-velocity components vector map, which is the projection of the flow velocity in the plane of the laser sheet, is therefore available after data processing. By combining two cameras so that they observe the light-sheet plane from two different angles, it is possible to obtain the three velocity components by stereoscopy [94]. Each camera yields a slightly different two-velocity components vector map due to the parallax effect, the difference being from the out-of-plane velocity component. With the suitable calibration, this out-of-plane velocity component can be evaluated. In the stereoscopic arrangement, the lens plane is not parallel to the image plane. It is thus necessary to tilt the cameras in order to satisfy the Scheimpflug principle, which ensures that the focal plane is aligned with the laser sheet.

In the present study, a Litron Dual Power 200-15 laser (200 mJ/pulse, 532 nm wavelength) is used in combination with a cylindrical lens to generate a 2 mm-wide laser sheet. Image pairs are acquired using two CCD cameras (Dantec FlowSense E0 4M) with a resolution of 2048×2048 pixels. The technical details of the PIV equipment are summarized in Table 3.3.

Table 3.3: Technical specifications of the PIV equipment.

Laser	
Model	Litron Dual Power 200-15
Type	Frequency doubled Q-switched Nd:YAG
Wavelength	532 nm
Energy	200 mJ/pulse
Camera	
Model	Dantec FlowSense EO 4M
Resolution	2048 x 2048 pixels
Pixel Size	7.4 μm

3.6.2 Fluorescent seeding particles

Laser light reflections are problematic in PIV measurements as they can lead to erroneous velocities and may even damage the measurement equipment due to overexposure of the cameras CCD sensors. In a two-phase flow environment, it is thus not possible to perform conventional PIV measurement since the laser light is heavily reflected on the liquid-gas interfaces. The use of fluorescent seeding particles together with a suitable filter on the receiving optics is a way to circumvent this problem. Seeding particles can be marked with Rhodamine B dye, whose excitation and emission spectra is represented in Figure 3.10(b). Rhodamine B emits orange light at a wavelength of around 580 nm when excited with the 532 nm laser. By equipping the cameras with long pass filters, discarding wavelengths shorter than 570 nm, only the light scattered by the particles is recorded.

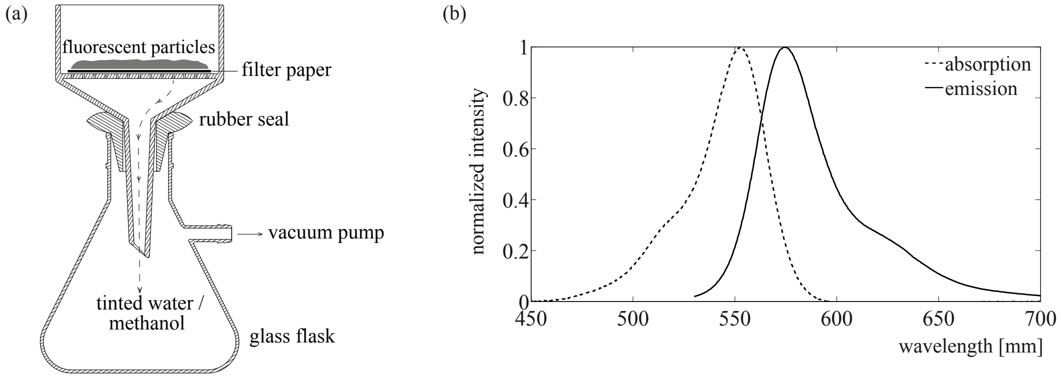

Figure 3.10: (a) Büchner funnel for filtering of fluorescent particles from [88]. (b) Excitation and emission spectra of Rhodamine B in water. [110]

Commercially available fluorescent particles tend to be too expensive in view of the considerable water volume (about 100 m^3) in the tunnel. An alternative procedure is thus introduced to obtain fluorescent particles from common polyamide particles and Rhodamine-B dye. Fluorescent seeding particles may be obtained from off-the-shelf 20 μm polyamide particles (density 1030 kg/m^3). The method is described in detail by Müller et al. [88] and a summary is presented hereafter. Approximately 100 g of polyamide particles are mixed with 1 l of water and 5 g of Rhodamine-B dye in a lockable glass container. To accelerate the diffusion of the dye in the particles, the container is placed in a heated incubator at 60°C for one month. Since the particles have the tendency to separate from the liquid phase and float on the surface, the solution is regularly agitated in order to ensure its homogeneity. Then, the particles are extracted by filtering the solution on a Büchner funnel, represented in Figure 3.10(a). It consists of a glass flask, a vacuum tight rubber seal and 4-12 μm filter papers. The side-arm of the glass flask is connected to a vacuum pump. The water traverses the perforated plate, drawn in by the vacuum in the glass flask, leaving the particles in form of a compressed powder on the filter paper. Once all the particles are on the filter paper, fresh water can be added several times to the funnel to rinse the particles from the excess of dye. The particles are then scraped off and decanted into another glass container. Finally, they are diluted in ethanol or methanol in order to wash off the remaining Rhodamine-B molecules which did not diffuse into the polyamide particles and are still stuck at the particles surface. The now fluorescent seeding particles are rinsed thoroughly one last time before they are ready to be used or stored. Rhodamine B can cause serious damage to the eyes, skin and respiratory ways. It is therefore recommended to wear protection gloves, safety goggles and dusk masks during the entire process and to work in a well-ventilated area.

3.7 Post-processing of PIV data

3.7.1 Vortex identification

The raw velocity fields obtained by PIV require further post-processing to extract important flow features. A vortex can be characterized by several parameters such as its swirl center location, viscous core radius, circulation, maximum vorticity etc. There are numerous ways to extract those features in a velocity field, a comparison of different methods is given in [3] and [115]. Some of the most commonly used vortex characterisation methods are briefly described hereafter, as well as their practical implementation to PIV measurements.

Vorticity computation

Vortices in a velocity field are usually revealed by concentrated regions of significant vorticity, corresponding to the vortex core. While the vorticity is a good vortex indicator in simple flow with minimal shear, this is not necessarily the case in complex flow fields [3]. Indeed, regions of high shear exhibit also a significant vorticity, without featuring a swirling motion.

A vortex can thus be improperly identified in region of high shear, e.g., in a boundary layer. Nevertheless, vorticity is widely used to identify the vortex location as it is expected to reach a local extremum in the vortex center.

Vorticity is a three-dimensional vector. However, PIV measurements - either 2D or 3D - are performed in a single plane such that only the gradients in that plane can be calculated. As a result, only the vorticity component normal to the laser sheet can be determined. When the laser plane is perpendicular to the free stream, the latter corresponds to the streamwise vorticity ω:

$$\omega = \frac{\partial v}{\partial x} - \frac{\partial u}{\partial y} \tag{3.10}$$

where u and v are the velocities along the x and y axis, respectively. The vorticity is computed by the numerical differentiation of the velocity field with a finite difference scheme. Several differentiation schemes exist, such as standard central difference, Richardson extrapolation, least squares operator, or methods based on the local circulation estimate (see [96] for more details). Even if the resulting streamwise vorticity is similar with each scheme, the following fourth-order Richardson extrapolation is selected:

$$\begin{aligned} \omega_{i,j} = & \frac{1}{12\Delta X}(-v_{i+2,j} + 8v_{i+1,j} - 8v_{i-1,j} + v_{i-2,j}) \\ & - \frac{1}{12\Delta Y}(-u_{i,j+2} + 8u_{i,j+1} - 8u_{i,j-1} + u_{i,j-2}) \end{aligned} \tag{3.11}$$

This scheme produces a small truncation error and tends less to smooth out gradients compared to second order least square schemes [102]. To minimize bias errors and avoid any undesirable effect of the differentiation of a noisy field, the spatial sampling resolution of the velocity field can be increased via a least-square cubic spline interpolation of the velocity prior to differentiation.

Q and λ_2 operator

Several studies have proposed vortex identification strategies based on the local velocity gradient tensor and its corresponding eigenvalues [33, 68, 27]. The underlying idea is that flow field patterns commonly accepted as vortices, i.e. spiral or close streamlines, correspond to singular values of the eigenvalues of the velocity gradient tensor $\nabla\vec{u}$ [112]. The latter is composed of the strain tensor **S** and the vorticity tensor $\mathbf{\Omega}$. The two-dimensional form of $\nabla\vec{u}$ is expressed as follows:

$$\begin{aligned} \nabla\vec{u} = & \begin{pmatrix} \frac{\partial u}{\partial x} & \frac{\partial u}{\partial y} \\ \frac{\partial v}{\partial x} & \frac{\partial v}{\partial y} \end{pmatrix} = \begin{pmatrix} \frac{\partial u}{\partial x} & \frac{1}{2}\left(\frac{\partial u}{\partial y} + \frac{\partial v}{\partial x}\right) \\ \frac{1}{2}\left(\frac{\partial u}{\partial y} + \frac{\partial v}{\partial x}\right) & \frac{\partial v}{\partial y} \end{pmatrix} + \begin{pmatrix} 0 & \frac{1}{2}\left(\frac{\partial u}{\partial y} - \frac{\partial v}{\partial x}\right) \\ \frac{1}{2}\left(\frac{\partial v}{\partial x} - \frac{\partial u}{\partial y}\right) & 0 \end{pmatrix} \\ = & \boldsymbol{S} + \boldsymbol{\Omega} = \boldsymbol{A} \end{aligned} \tag{3.12}$$

Chong et al. [33] proposed that a vortex core corresponds to the region with complex eigenvalues of $\nabla\vec{u}$. Complex eigenvalues are obtained if the discriminant Q of the characteristic equation is below zero, which can be expressed as:

$$Q=\frac{(\mathrm{trace}\,\boldsymbol{A})^2}{4}-\det\boldsymbol{A}=\frac{\left(\frac{\partial u}{\partial x}+\frac{\partial v}{\partial y}\right)^2}{4}-\frac{\partial u}{\partial x}\frac{\partial v}{\partial y}+\frac{\partial u}{\partial y}\frac{\partial v}{\partial x}<0 \tag{3.13}$$

Alternatively, Jeong and Hussain [68] proposed a definition of a vortex, known as the λ_2 criterion, that is based on the Hessian of pressure. A region corresponding to a vortex core is identified by negatives values of λ_2, which is the second largest eigenvalue of the tensor $\boldsymbol{S}^2+\boldsymbol{\Omega}^2$. This definition captures the pressure minimum in a plane perpendicular to the vortex axis. With the definition that the second and third eigenvalues of $\boldsymbol{S}^2+\boldsymbol{\Omega}^2$ must be below zero, it follows that either [112]

$$\lambda_2=\left(\frac{\partial u}{\partial x}\right)^2+\frac{\partial u}{\partial y}\frac{\partial v}{\partial x}<0 \qquad \text{or} \qquad \lambda_2=\left(\frac{\partial v}{\partial y}\right)^2+\frac{\partial u}{\partial y}\frac{\partial v}{\partial x}<0 \tag{3.14}$$

The vortex center corresponds thus to the local minimum of λ_2, which is defined as the mean value of eq. (3.14):

$$\lambda_2=\frac{\left(\frac{\partial u}{\partial x}\right)^2+\left(\frac{\partial v}{\partial y}\right)^2}{2}+\frac{\partial u}{\partial y}\frac{\partial v}{\partial x} \tag{3.15}$$

The Q and λ_2 operators are insensitive to vortex direction of rotation and are always negative in the swirling center. An example of the different operators indicating a vortex for a typical velocity field, representing a vortex near a solid boundary, is given in Figure 3.11. The vortex is generated by the *NACA 0009* hydrofoil and the solid wall is situated at $x=0$ mm. It is observed that the shear region in the boundary layer generates significant amount of vorticity. On the contrary, the Q and λ_2 operators are negative only in the region corresponding to the vortex core, correctly identifying the boundary layer as a region characterized by shear.

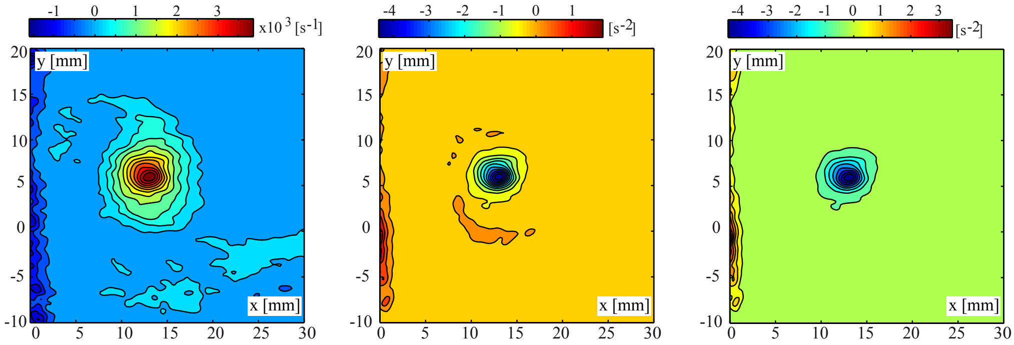

(a) vorticity (b) Q criterion (c) λ_2 criterion

Figure 3.11: Comparison of the vortex identification methods. Flow conditions: W_∞=10 m/s, α=5°, z/c=1, rough *NACA 0009* hydrofoil.

3.7.2 Wandering correction

The wandering is a random fluctuation of the vortex centerline with an amplitude of the order of the vortex core size. Although this phenomenon has been well referenced, its origin remains unclear. It is presumed to arise from a resonant excitation triggered by the free stream turbulence [44]. If not corrected, the wandering would yield a larger core size and a lower value of the maximum velocity in the mean vortex flow, as illustrated in Figure 3.12a. Birch [23] showed that for wandering amplitudes within the range of those usually observed experimentally, any axisymmetric flow field having zero velocity at $r = 0$ and r→ ∞ converge upon the circulation profile of a Batchelor q-vortex (cf. Section 2.2.5). Therefore, care must be taken in the interpretation of averaged swirl velocity profiles as a good agreement with a q-vortex may not necessarily imply that instantaneous profiles agree well with this model. Due to this wandering, single point measurement techniques, such as Laser Doppler Velocimetry (LDV) always result in a more diffuse velocity field than in reality, and correction methods must be applied to retrieve the true velocity field, as presented in Section 3.5.2.

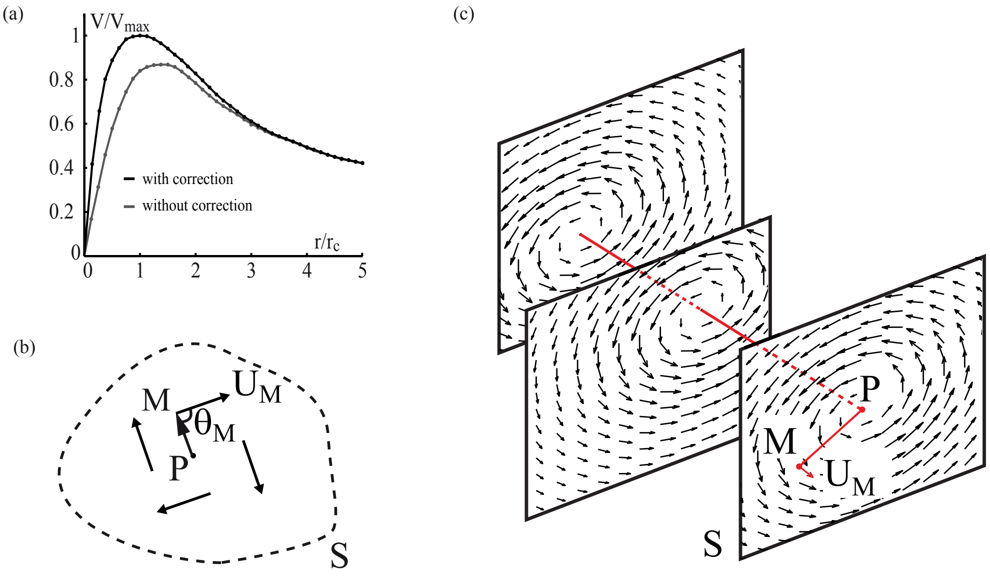

Figure 3.12: (a) Wandering effect on the circumferential velocity. (b) Sketch of the parameters in eq. (3.16). (c) Correction of the wandering by aligning the velocity maps before averaging.

The PIV technique leaves the possibility of accurately filtering out this vortex wandering in the averaging process because of its ability to capture the entire instantaneous velocity fields. Different strategies are available, see for instance Bhagwat et al. [21], but an efficient method consists in identifying the vortex swirl center and align the velocity maps before averaging, as illustrated in Figure 3.12c. The effectiveness of this method lies in the ability to accurately determine the instantaneous swirl center. Gradient-based vortex detection operators, such as the vorticity or Q and λ_2 criteria, are not well adapted since experimental noise and spatial resolution can greatly affect the accuracy of the vortex center identification. On the other hand, the method of Graftieaux [58] does not require any gradient evaluation and considers only the topology of the velocity field to identify the swirl center. It is a simple yet very robust way to identify the instantaneous swirl center location. The following dimensionless scalar function Π at the position P is introduced:

$$\Pi(P) = \frac{1}{S}\int_{M\in S}\frac{(PM \wedge U_M)\cdot z}{\|PM\|\cdot\|U_M\|}dS = \frac{1}{S}\int_S \sin(\theta_M)dS \tag{3.16}$$

where S is a two dimensional area surrounding P, M lies in S, z is the unit vector normal to the measurement plane. θ_M represents the angle between the velocity vector U_M and the radius vector PM, as sketched in Figure 3.12b. Π is a dimensionless scalar with the norm of bounded by 1. In the case of an axisymmetric vortex it can be shown that this bound is reached at the location of the vortex center. For an asymmetrical vortex, Π would however be slightly lower than 1. Equation (3.16) provides a way to identify the vortex swirl center. The application to PIV measurements, in which the velocity field is sampled at discrete spatial locations, is straightforward: S is defined as a rectangular domain of fixed size, centered on P, and Π is approximated by:

$$\Pi(P) = \frac{1}{N}\sum_S\frac{(PM \wedge U_M)\cdot z}{\|PM\|\cdot\|U_M\|} \tag{3.17}$$

where N is the number of velocity vectors inside S, c.f. Figure 3.12c. The vortex swirl center is identified by the local maximum detection of $\Pi(P)$. In general, the vortex center does not lie on a measurement grid node, and the realignment requires an interpolation of the measurement data. This is realized via a cubic spline interpolation of the velocity field.

Figure 3.13 illustrates an example of 100 instantaneous vortex centers superimposed on the mean velocity field, computed after alignment of the velocity maps. The vortex is generated by the rectangular *NACA 0009* hydrofoil at W_∞=10 m/s, α=10°. The wandering amplitude is indicated by the scattering of the vortex centers, which can be characterized by the standard deviation of the mean vortex center location. In this case, a value of 0.6 mm is obtained for the deviation along both the x and y directions, which represents about 12 % of the vortex viscous core radius.

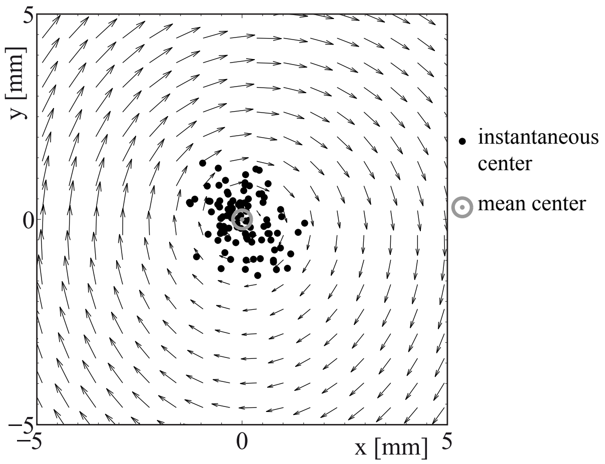

Figure 3.13: Example of a mean velocity map and the location of the instantaneous vortex centers. Flow conditions: W_{∞}=10 m/s, α=10°, z/c=1, rough *NACA 0009* hydrofoil.

4 Effect of cavitation on a tip vortex

4.1 Case study

4.1.1 Motivation and context

If the intensity of a vortex is large enough, the low pressure region that prevails in the vortex center can lead to the vaporization of its core. This phenomenon is called vortex cavitation and is a common, although complex problem in engineering applications. Possible consequences in hydraulic machines range from the generation of noise and vibrations, to the erosion and reduction of performances. The effect of cavitation on a vortex is both a fundamental and very practical question. Considerable attention has been given in the study of this phenomenon, see Arndt [7] for a review. However, the majority of studies focuses on the cavitation inception process and only limited results concern developed cavitation. Experimental evidences suggest that cavitation inception is controlled by complicated physical processes [7]. The cavitation inception in well-developed vortices is very sensitive to the water nuclei content, and the assumption that cavitation occurs at vapor pressure is generally inaccurate [8, 11].

Once cavitation occurs, the flow characteristics can be substantially altered. Based on the mass conservation balance, Franc & Michel [51] pointed out that for a vapor core of about one millimeter, liquid particles situated initially at 2 μm from the axis are ejected at 0.5 mm because of the cavitation. Hence, the structure of the velocity and pressure fields are changed when cavitation develops in a vortex. However, the cavitating core radius and vortex trajectory appears to be insensitive to the water quality once cavitation inception occurs, i.e. for developed cavitation [7, 12]. Therefore, investigations often focus on finding the relation between the radius of the cavitating core r_{cv} and cavitation number σ [81]. The redistribution of the vorticity around a cavitating vortex remains nevertheless an open question. Indeed, while the viscosity reduces the velocity towards zero in the core of a fully wetted vortex, no such limitation holds in the case of a cavitating core and the boundary conditions at the cavity interface are unknown.

Little information is available on the flow structure of a cavitating vortex, despite its considerable importance for understanding and predicting the cavitation occurrence. An accurate model of the cavitating vortex would provide a relation between the vortex strength, the cavity radius and the cavitation number, opening the possibility to develop scaling rules for cavitation inception. Arndt & Keller [8] suggested, using a simple Rankine model, that two types of vortices, having identical circulation and total angular momentum, can exist at the same cavitation inception number (cf. Section 2.3.1). The first is a fully wetted vortex and the second is a fully cavitating vortex with a vapor core equal to $1/\sqrt{2}$ times the non-cavitating viscous core radius and a maximum velocity that is $\sqrt{2}$ times higher than the maximum velocity in the non-cavitating case. According to Arndt & Keller, this model could explain the intermittent nature of cavitation inception but has yet to be experimentally confirmed. Other models based on a heuristic modification of a Lamb-Oseen vortex were proposed by Arakeri et al. [6] and Choi & Ceccio [30]. The boundary conditions of these models involve either zero shear stress or zero velocity at the cavity interface. For instance, the model of Choi & Ceccio [30] contains a free parameter γ that is related to the tangential velocity of the liquid phase at the cavity interface (cf. Section 2.3.2). Alternatively, Bosschers [24] used jump relations at the cavity interface to derive the appropriate boundary conditions and obtain the analytical extension of the Lamb-Oseen vortex in the case of a cavitating vortex (cf. Section 2.3.3). Unfortunately, due to the lack of experimental data, it is difficult to validate or refute a particular model.

The intrinsic experimental difficulties associated with velocity measurements in a two-phase flow environment are responsible for a general shortage of detailed experimental data on the flow structure around the vortex cavity. Falcão de Campos [47] used LDV to measure the velocity components of a vortex with and without cavitation. However, the velocity distribution near the cavity could not be measured in detail due to the unsteadiness of the vortex and the laser light reflections on the liquid-gas interface. Nevertheless, they concluded that further away from the cavity, the velocity distribution is identical for the cavitating and non-cavitating vortex.

The objective of this chapter is to fill this gap and give a description of the structure of a developed cavitating vortex, based on experimental velocity measurements. A special care is put to obtain the detailed flow in the vicinity of the cavity. To this end, a combination of state of the art LDV and fluorescent PIV techniques is used to investigate the flow field around a cavitating vortex.

4.1.2 Methodology

All the experiments are carried out in EPFL high-speed cavitation tunnel. The elliptical *NACA 16-020* foil is used to generate a rectilinear and remarkably stable tip vortex, which is suitable to investigate the potential changes related to the occurrence of cavitation in its core. The vortex is characterized by investigating the flow field in terms of tangential and axial velocity components. This is achieved by performing LDV as well as 2D fluorescent PIV measurements.

The LDV offers a local measurement of the axial and tangential velocity components, whereas the PIV provides the global velocity map in a cross section of the vortex. Measurements are performed in cavitation-free conditions as well as in the presence of a cavitating vortex. The amount of cavitation in the vortex is controlled by adjusting the inlet pressure between 0.7 and 4 bars. The corresponding cavitation number σ ranges from 1.2 to 2. The radius of the cavity at a given σ value is established by image processing based on high-speed visualizations and photographs of the vortex. For the cavitating-free conditions, the freestream velocity W_∞ is set between 10 m/s and 15 m/s and the foil incidence angle is varied between 4° and 16°. Measurements in cavitation conditions are performed with a highly stable vortex generated by the smooth hydrofoil at an incidence of 12°, and two inlet velocities (10 m/s and 15 m/s). This particular incidence allows to obtain a clearly-defined cavitating vortex, without excessive parasitic cavitation at the foil leading edge. The different operating conditions for the cavitation-free conditions and cavitating vortex are listed in Table 4.1.

Table 4.1: Operating conditions for LDV and PIV measurements

	W_∞(m/s)	α(°)	σ (-)	surface roughness
Cavitation-free				
LDV	10	4-6-8-10-12-14-16	4	smooth & rough
	15	12	2.5	smooth
PIV	5	4-6-8-10-12-14-16	4	smooth
	10			
	15			
Cavitating				
LDV	10	12	1.5-2	smooth
	15			
PIV	10	12	1.5-2	smooth
	15			

4.2 Experimental setup and data processing

4.2.1 Laser Doppler Velocimetry

LDV is used to measure the velocity field in cavitation-free regime as well as in the vicinity of the cavitating vortex. The position of the laser probe relatively to the test section is depicted in Figure 4.1a. A remotely controlled 2D traversing system is used to move the measurement volume at the desired location with 10 μm precision. A 100 mm diameter circular glass window with an anti-reflection coating adapted to the wavelength of the laser is fitted in the Plexiglas window to avoid unwanted laser beam deflections by residual stresses. In order to determine the position of the measurement volume, the successive refractions of the laser beams through the optical window and water have to be taken into account. It can easily be shown that the LDV probe displacement along the x-axis in air is proportional to the displacement of the measurement volume in water. The proportionality constant is independent of the optical window characteristics and is given by: $tan(\alpha_1)/tan(\alpha_2)$, where α_1 and α_2 are the half intersection angles between the two laser beams in air and in water, respectively [127]. The angle α_1 depends on the characteristics of the laser probe, while α_2 is determined via Snell's Law using the water refractive index (n=1.33). The ratio between the measurement volume displacement along the x-axis in water and in air is equal to 1.3359.

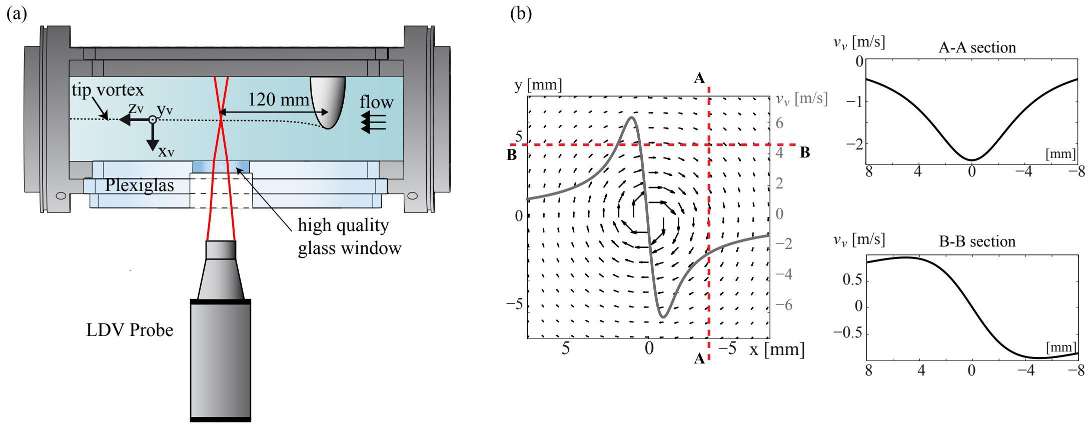

Figure 4.1: (a) Top view of the experimental setup for the LDV measurements with the elliptical *NACA 16-020* hydrofoil. (b) Sketch of the method to find the mean vortex center.

The vortex flow can be described either with a Cartesian or a cylindrical coordinate system, with the origin at the vortex center. The Cartesian coordinate system is characterized with the axes x_v and y_v pointing in the spanwise and vertical direction, respectively, while the axis z_v is aligned with the freestream velocity, as illustrated in Figure 4.1a. The corresponding velocities are referred to as u_v, v_v and w_v, where the subscript '$_v$' designates the vortex reference frame. In the cylindrical coordinate system, r is the radial coordinate with origin at the center of the vortex and θ is the angular coordinate, which is zero on the x_v axis. The corresponding azimuthal velocity is referred to as v_θ. The axis z_v is common to both coordinates systems.

LDV is a point-wise measurement technique, implying that a scan of the flow with successive displacements of the measurement volume must be performed in order to obtain a velocity profile. 5000 bursts are typically recorded at each point to compute the local statistic of the flow. However, experience shows that convergence can be reached with as few as 1000 bursts. The laser probe orientation is set in order to measure the streamwise velocity w_v with one channel, while the other channel measures the vertical velocity component v_v. To obtain an accurate tangential velocity profile (v_θ), it is necessary to identify the vortex center and align the laser beams in the plane $y_v = 0$, in which v_θ corresponds to v_v. The methodology to find the vortex center is sketched in Figure 4.1b. First, the inlet pressure is decreased in order to reveal the vortex position by a tiny cavitation filament. The measurement volume is then approximately aligned on the cavity. Secondly, the velocity v_v is measured along an arbitrary vertical (A-A) and horizontal (B-B) section in cavitation-free regime. The position of the velocity extremum along the A-A section in Figure 4.1b corresponds to the ordinate of the vortex center, while the position corresponding to $v_v = 0$ along the B-B section indicates the abscissa of the vortex center.

LDV in two-phase flow environment

The use of LDV in a two-phase environment is challenging since the laser beams may be reflected on the surface of the gaseous phase, resulting in significant measurement errors. Furthermore, when the measurement volume intersects with the gaseous cavity, inconsistent velocity signals are generated. An example is given in Figure 4.2a, which depicts two tangential velocity profiles, one in cavitation-free regime (σ=2.8) and the other with a cavitating vortex, as shown in Figure 4.3. The vortex cavity radius in this case is approximately 1 mm for a cavitation number of σ=1.7. Due to multiple reflections on the liquid-gas interface, the velocity profile in the cavitating case quickly becomes erroneous when approaching the cavity, even if the measurement volume does not intersect the cavity. To overcome this issue, point-wise measurements are performed on a mesh that surrounds the cavitating vortex core as closely as possible, see Figure 4.2b. The mesh resolution is 0.5 mm outside and 0.1 mm inside of the vortex core.

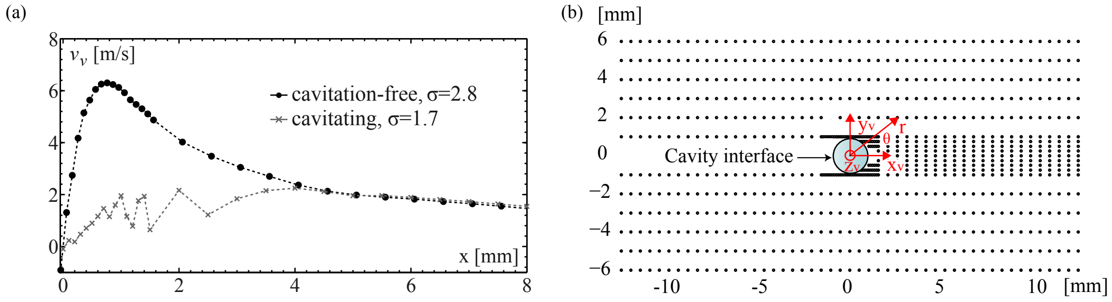

Figure 4.2: (a) Example of the tangential velocity measured by LDV with (σ=1.7) and without (σ=2.8) vortex cavitation. W_∞=10 m/s, α=12° (b) Mesh of the measurement points surrounding the cavitating tip vortex.

A picture of the LDV measurements around a cavitating vortex is given in Figure 4.3. The foil incidence angle is α = 12° and a steady cavitating tip vortex is generated when the cavitation number is σ=1.7. The two laser beams measuring the streamwise velocity component are clearly visible in red and the beams are crossing slightly underneath the vortex cavity, i.e. in the back of the image plane in Figure 4.3. When the laser beams intersect the cavity, they are reflected at the interface and their path is interrupted. This effect is also an efficient way to locate the position of the measurement volume with respect to the cavity interface.

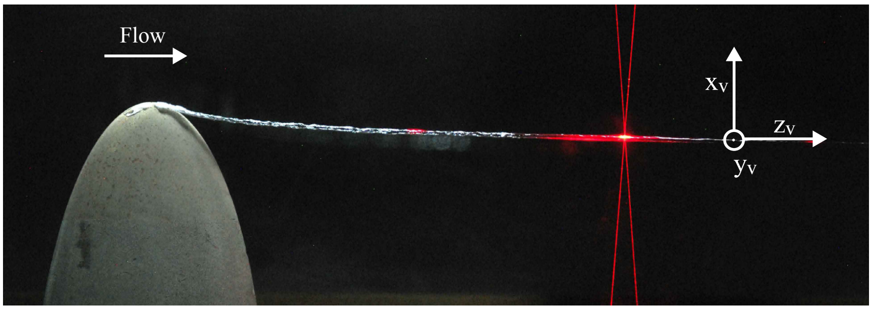

Figure 4.3: Photograph of the cavitating tip vortex and the LDV laser beams. The laser beams are crossing slightly underneath the vortex cavity center. W_∞=10 m/s, α=12°, σ=1.7

4.2.2 Particle Image Velocimetry

Fluorescent PIV is used to characterize the vortex velocity field in both cavitating and cavitation-free conditions. Given the locally high velocity gradients generated within the tip vortex, it is important to have a PIV configuration that yields the best possible spatial resolution and dynamic spatial range. Even though the use of a stereo-PIV setup such as the one used in Chapter 5 seems indicated, the resulting spatial resolution was found to be too low in preliminary tests. Therefore, an alternative 2D-PIV setup that achieves a high magnification of the area of interest with the smallest possible working distance is implemented, as illustrated in Figure 4.4. A 2 mm-wide laser sheet intersects the vortex axis with an angle β=30°, at a distance of two chords (120 mm) downstream of the hydrofoil pitch axis. An inclined mirror is used to adjust the orientation of the laser sheet. The angle between the laser sheet and the vortex axis allows to measure the vortex swirling velocity with a single camera, which is looking through the side window. The time interval between two laser pulses is set for each inlet velocity in order to limit the particle in-plane displacement to less than 30 % of the interrogation window size, while keeping a small out-of-plane displacement (e.g., 7.5 μs for W_∞=10 m/s). Image pairs are acquired using a CCD camera (Dantec FlowSense E0 4M) with a resolution of 2048×2048 pixels) and a 180 mm macro zoom lens. The camera focal plane is aligned with the laser sheet and a transparent water box is mounted on the lateral wall to minimize the optical distortions through the Plexiglas window. The lens aperture is set to a low f-number (f/16) to obtain sharp particle images. The laser is set to its maximum energy of 200 mJ/pulse, in order to get sufficient light from each individual particle. The final field of view covers an area of 22.5×22.5 mm. The conversion from the image plane (pixel coordinates) to the object plane (mm coordinates) is determined via the image of a dotted calibration target aligned with the light sheet. The seeding materials are fluorescent polyamide particles with an average diameter of 20 μm. The lens is equipped with a long pass filter, discarding wavelengths shorter than 570 nm. Therefore, only the light scattered by the particles is recorded, allowing velocity measurements in two-phase environments. Figure 4.5 (a color photograph taken with the same long pass filter as the PIV camera) shows the cavitating vortex crossing the measurement plane, in which the fluorescent particles are activated by the laser.

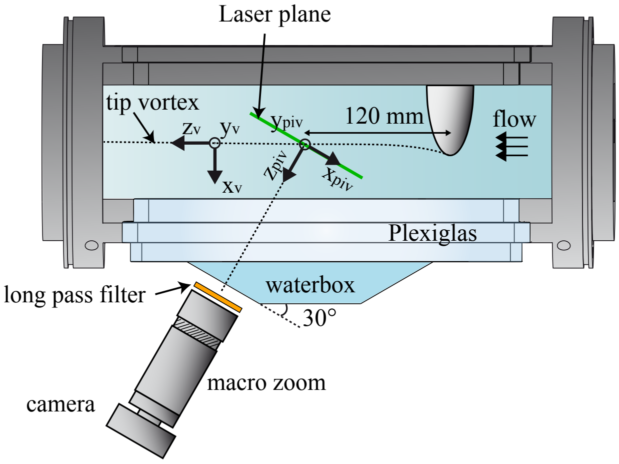
Laser plane
tip vortex
zv
yv
xv
ypiv
zpiv
xpiv
120 mm
flow
Plexiglas
waterbox
30°
long pass filter
macro zoom
camera

(a) Top view of the tunnel test section and optical instruments

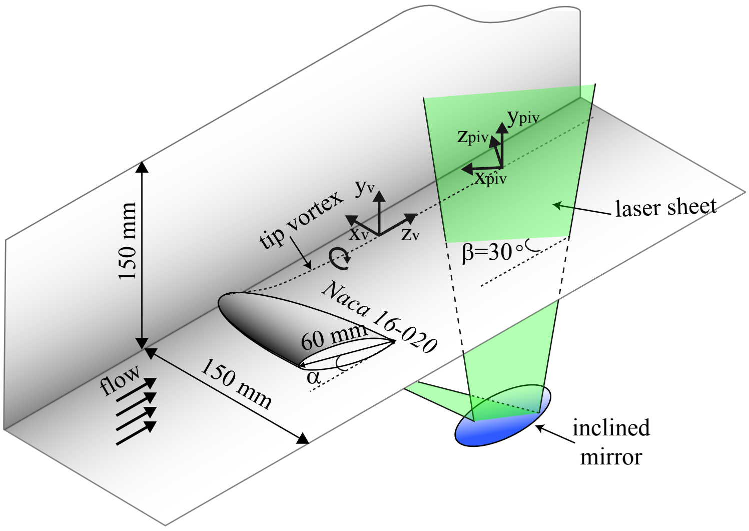
ypiv
zpiv
xpiv
laser sheet
yv
xv
zv
tip vortex
β=30°
150 mm
Naca 16-020
60 mm
α
flow
150 mm
inclined mirror

(b) Isometric view of the inlet test section and the inclined measurement plane

Figure 4.4: Experimental setup for the PIV measurements with the elliptical *NACA 16-020* hydrofoil

Post-processing of the PIV data

The velocity fields are derived by processing the acquired image pairs with an adaptive multi-pass correlation algorithm, which adjusts iteratively the size and shape of the individual Interrogation Areas (IAs) with the local seeding density and flow gradients [111, 121]. Starting from a mesh of initially large IAs, the adaptive PIV method determines iteratively an appropriate IA size for each grid node, according to a criterion ensuring a sufficient local particle density. This criterion is the presence of at least five particles in each IA and a minimum size of 16×16 pixels. The first iteration uses an IA of 128x128 pixels centered on each grid node and a total of 124×59 velocity vectors with a spatial resolution of 0.18 mm is finally obtained.

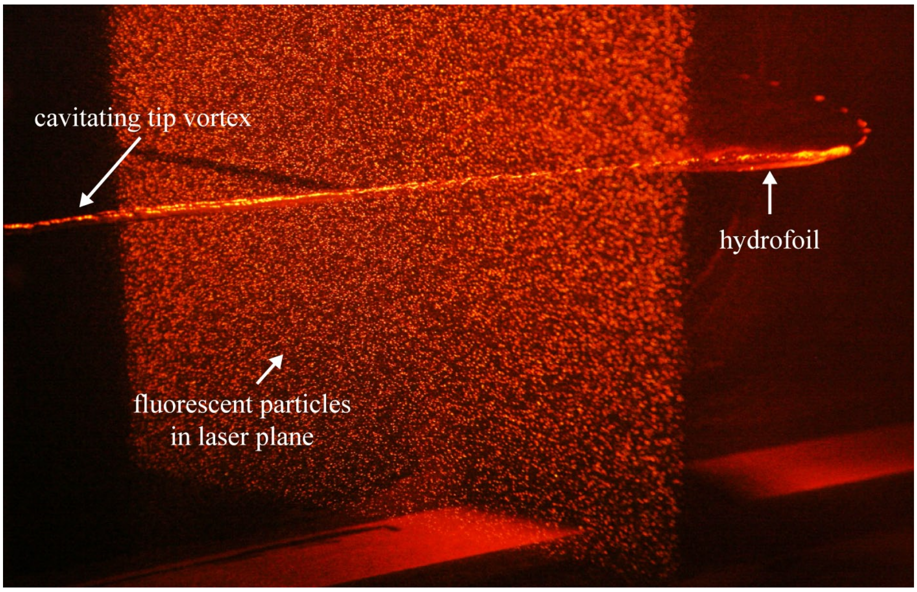
cavitating tip vortex
hydrofoil
fluorescent particles
in laser plane

Figure 4.5: Picture of the fluorescent particles and the cavitating tip vortex illuminated by the laser sheet. The camera is equipped with a long pass filter discarding the green laser light.

The vector fields are validated with an universal outlier test [120], and spurious vectors are replaced by the median value of the 5x5 neighboring vectors. The percentage of spurious vectors is typically below 1 %, indicating the good overall quality of the PIV correlations.

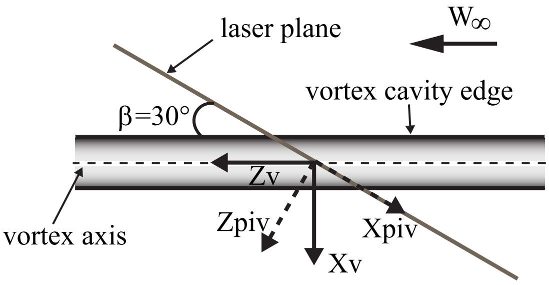
laser plane
W∞
vortex cavity edge
β=30°
Zv
vortex axis
Zpiv
Xpiv
Xv

Figure 4.6: Relative orientation between the laser plane and the vortex axis.

The plane of the PIV measurements is not normal to the vortex axis, as sketched in Figure 4.6. The transformation from the measurement coordinate system (x_{piv}, y_{piv}, z_{piv}) to the vortex coordinate system (x_v, y_v, z_v) is given by:

$$\begin{pmatrix} x_{piv} \\ y_{piv} \\ z_{piv} \end{pmatrix} = \begin{bmatrix} sin(\beta) & 0 & -cos(\beta) \\ 0 & 1 & 0 \\ cos(\beta) & 0 & sin(\beta) \end{bmatrix} \begin{pmatrix} x_v \\ y_v \\ z_v \end{pmatrix} \tag{4.1}$$

This projection multiplies the distances along the x_{piv}-axis by $sin(\beta)$ relatively to the vortex coordinate system. Given that the measured field of view covers a distance of $cos(\beta) \times 22.5$

mm = 19.5 mm along the z_v-axis, it is assumed that the vortex characteristics do not vary significantly over this interval. Due to the inclination of the laser plane relatively to the vortex axis, the spanwise u_v and streamwise w_v velocity components in the vortex coordinate system are combined in the laser plane to form the velocity u_{piv}, cf. eq. (4.1). The velocity component along the y-axis remains unaffected by the projection, or in other terms $v_{piv} = v_v$. It should be noted that w_v can be written as the sum of the freestream velocity W_∞, which is imposed, and the vortex induced axial velocity $\tilde{w}$, which is unknown, i.e. $w_v = W_\infty + \tilde{w}$. Using eq. (4.1), u_v can be expressed as:

$$u_v = \frac{u_{piv} + w_v \cos(\beta)}{\sin(\beta)} = \frac{u_{piv} + W_\infty \cos(\beta)}{\sin(\beta)} + \underbrace{\widetilde{w}\frac{\cos(\beta)}{\sin(\beta)}}_{unknown} \tag{4.2}$$

The measured velocity field u_{piv} can thus be corrected to obtain $u_v - \widetilde{w}\cot(\beta)$, which is close to the velocity u_v in the vortex reference frame if $\widetilde{w}$ is small compared to W_∞. The vortex center is then easily identified using Graftieaux's algorithm [58], and the vortex wandering can be filtered out during the averaging process, as described in Section 3.7.2. Figure 4.7a is an example of the mean velocity field $(u_{piv}\ v_{piv})$, obtained in the laser plane in the case of a cavitating vortex. It is interesting to note that the velocity vectors are computed in the entire field of view, despite the fact that the vortex cavity is obstructing part of the laser plane, as sketched in Figure 4.6. In fact, the light from the particles behind the vortex cavity is refracted through the liquid-gas interface, affecting the velocity computations and making apparent the cavity edges in Figure 4.7a. The same velocity field as in Figure 4.7a is shown in 4.7b, but with the corrected horizontal velocity $u_v - \widetilde{w}\cot(\beta)$. The swirling flow field and the vortex cavity edges are now clearly apparent. The average velocity field is determined after processing between 100 and 1000 individual vector fields, depending on the operating conditions.

Given that the velocity field along the y-axis is unaffected by the projection in the laser plane, i.e. $v_{piv} = v_v$, this latter is used to obtain an average swirl velocity profile. Sections every 5° across the vortex center are made and the velocity v_{piv} is extracted along these radii via a cubic spline interpolation of the velocity field. The corresponding tangential velocity along each radius is given by: $v_\theta = v_{piv}/cos(\phi)$, where ϕ is the angle between the radius and the x-axis. The average and standard deviation of v_θ is then computed as a function of the radial coordinate. Figure 4.8a illustrates this procedure for a vortex in cavitation-free conditions with a limited number of radii taken every 15° around the vortex center. The mean value of the velocity profile, as well as the individual velocity profiles are illustrated in Figure 4.8b. In the case of a cavitating vortex, the mean tangential velocity profile is computed by considering only the region unobstructed by the vortex cavity (positive x-values), as explained in Section 4.4.2.

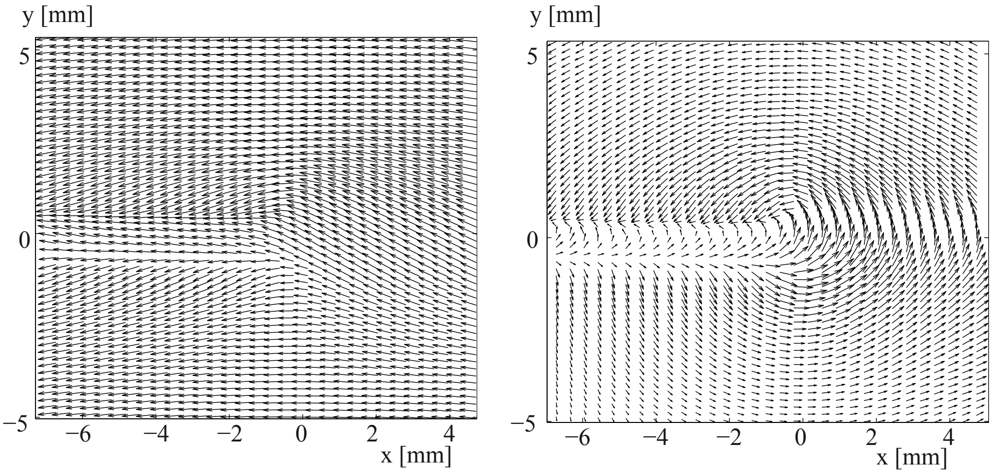

(a) Raw velocity field

(b) Corrected velocity field

Figure 4.7: Example of a raw and corrected PIV velocity fields in the case of a cavitating vortex. For readability, only 1 out of 4 vector is represented in the x-direction.

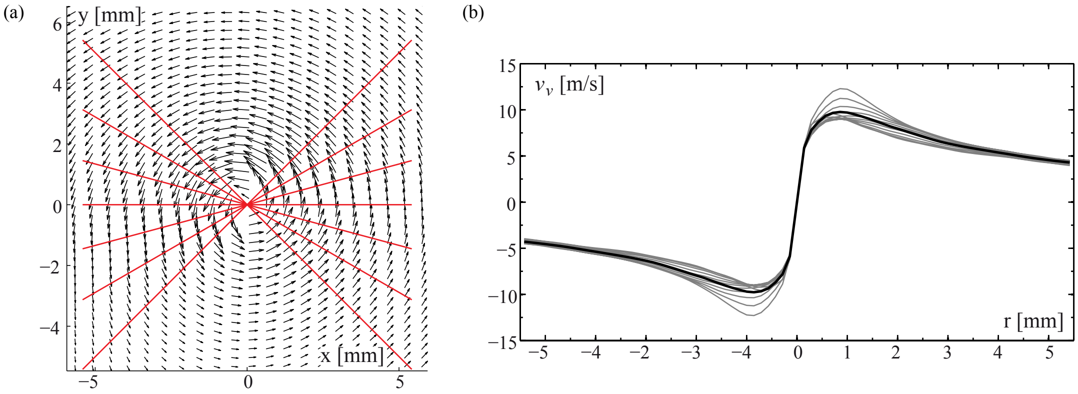

Figure 4.8: Average tangential velocity profiles in cavitating-free conditions. (a) vector field with slicing cuts. (b) Average velocity (black curve) and individual velocity profiles (gray)

Seeding problematic

Tip vortices feature strong gradients and high dynamic velocity range near their viscous cores, which are challenging to capture with PIV. For instance, variations from 0 to 10 m/s over a distance of 1 mm are common. As a reminder, the working principle of PIV is to measure the average displacement of tracer particles that are advected with the fluid in order to determine its velocity field. This displacement is evaluated via the computation of the cross-correlation between small Interrogation Areas (IAs) in two successive images. In order to have a sufficient spatial resolution to capture steep gradients, it is essential to have an IA as small as possible. As a basic rule, the ratio of the IA length to the vortex core radius should not be larger than 5 % [83]. On the other hand, errors in the measurements may arise if the IA is not populated with enough particles. In fact, the quality of the cross-correlation is directly linked to the number of particles in each IA [73, 118], and a minimum of 5 to 10 particles per IA is usually required [96]. To make up for a low seeding density, the adaptive PIV algorithm can increase locally the size of the IAs. However, this reduces also the effective spatial resolution and may bias the velocity measurements. Accurate measurements of vortices necessitate thus a high spatial resolution with a sufficient number of particles in the vicinity of the vortex core. Figure 4.9a shows a comparison of three tangential velocity profiles, two of which are obtained by PIV and one by LDV. All the measurements were obtained for the same flow conditions, hence the same tip vortex. The PIV setup featuring a low spatial resolution of ~0.6 mm obviously fails to resolve the velocity gradients in the vortex core. As a consequence, the peak tangential velocity appears much lower than in reality and the vortex core radius is increased dramatically. On the other hand, the velocity profile measured by the second PIV setup with a high spatial resolution of approximately 0.1 mm agrees well with the LDV measurements. It should be noted that the slope of the LDV measurement in the vortex core is slightly lower than for the high resolution PIV. This difference is due to the finite size of the LDV measurement volume and vortex wandering. A deconvolution of the LDV measurements can however be performed, as explained in Section 4.3.3.

In practice, an optimal seeding density is difficult to achieve in the cavitation tunnel, due to the considerable water volume of about 100 m^3. Indeed, with the assumption that a minimum of 5 particles per IA of 16×16 pixels is required within the volume generated by the 2-mm thick laser sheet, approximately 32 kg of seeding material would be necessary. Even if this represents a volume fraction of only approximately 0.03 % of the total water volume, the estimated cost for the in-house production of this amount of fluorescent particles is 35,000 CHF, which can hardly be justified. An alternative strategy is thus adopted: instead of the global seeding of the tunnel, only the stream tube passing through the observation area is seeded to obtain a high local concentration of particles.

Two distinct local seeding strategies are implemented. The first one, referred to as upstream injection, consists in injecting the fluorescent particles into the flow upstream of the test section, i.e. before the convergent, while performing the measurements simultaneously. To obtain a homogeneous seeding, it is necessary to inject the particles with a high pressure. Figure 4.9b shows a raw image from the PIV camera in the case of the upstream injection with a cavitating vortex, highlighted in yellow. The white dots represent the fluorescent particles, which are activated by the laser light. The particles are concentrated in a narrow stream tube, whose frontier is clearly visible on the image. By varying the injection pressure, the location of the seeded stream tube can be roughly control, but most of the time the particles do no pass through the region of interest. As a consequence, only about 20 image pairs could be acquired with a reasonable amount of seeding material. Nevertheless, the upstream injection proves to be effective in increasing the seeding density around the vortex. The seeding density may even be so high that the light emitted by the fluorescent particles is sufficient to illuminate the vortex cavity, making it clearly visible in Figure 4.9b. In this case, the dimension of the vortex cavity can be measured directly on those images.

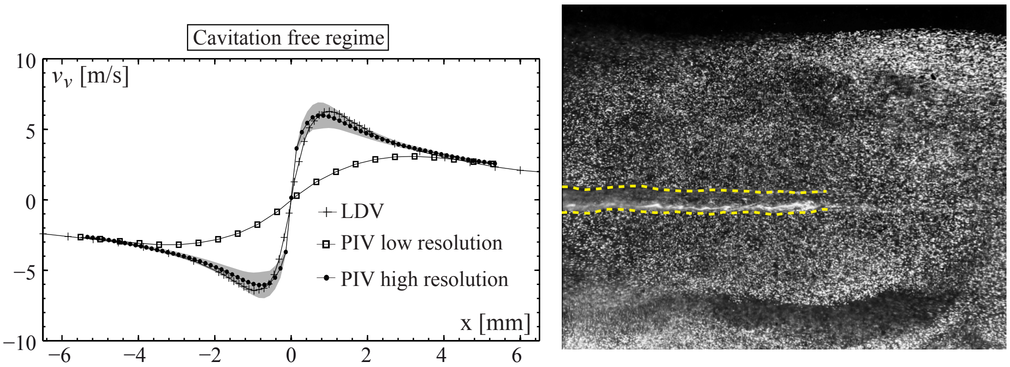

(a) Velocity profiles

(b) Upstream injection

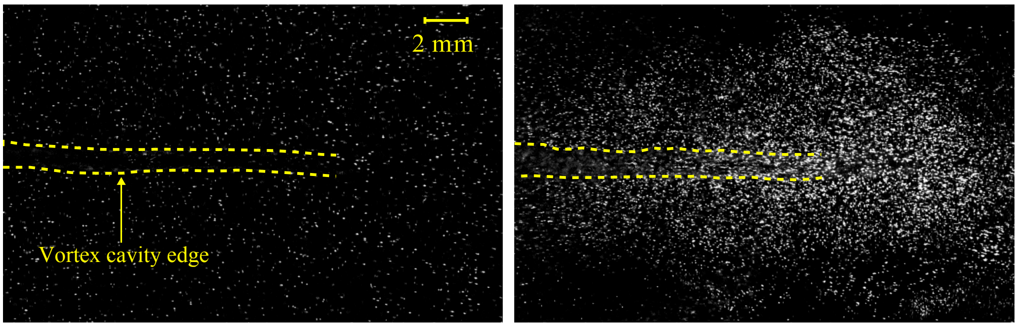

(c) No injection

(d) Tip injection

Figure 4.9: (a) Comparison on the PIV and LDV velocity profiles in cavitation-free regime. The grey area depicts the standard deviation.(b)-(d) Raw images from the PIV camera showing the local seeding in the vicinity of the cavitating vortex for the different seeding strategies. The vortex cavity edges are highlighted in yellow.

The second seeding strategy consists in injecting the fluorescent particles directly at the tip of the hydrofoil and is referred to as tip injection. The difficulty of matching the seeded stream tube with the vortex location is thereby eliminated. To this end, an injection channel with a diameter of 0.3 mm is drilled in the spanwise direction of the foil, see Figure 4.10a. This channel is connected to a pressurized container, filled with a highly concentrated mixture of particles and water. The injection flow rate is controlled with a needle valve. Figure 4.9c and 4.9d show the comparison of two raw images of a cavitating vortex from the PIV camera, with and without the injection of seeding particles. It can be observed that the tip injection effectively increases the seeding concentration in the vicinity of the vortex. Given the optimal seeding location, a relatively small amount of particles is necessary compared to the upstream injection and several hundreds of image pairs can be acquired. However, it is important to check that the injection does not alter significantly the vortex velocity field. To this end, LDV[1] measurements are performed at various water injection flow rates, in cavitation-free conditions. Figure 4.10b shows the mean tangential velocity profiles measured one chord downstream of the hydrofoil tip, for an incidence angle of 6° and a freestream velocity of 15 m/s. It can be observed that the velocity profiles remain unaltered for an injection flow rate up to Q$_{\text{inj}}$=3 cm^3/s, corresponding to ~5 % of the flow rate passing through the vortex core. As a precaution, the seeding flow rate during PIV measurements is however maintained at a value lower than 2 cm^3/s. The flow rate is estimated by measuring the time taken to empty the seeding container. Moreover, comparable velocity fields around a cavitating vortex are obtained with the two different seeding strategies, confirming that the vortex flow is not altered significantly by the tip injection. The effect of the cavitation on a tip vortex is finally assessed by taking advantage of the complementarity of the two seeding strategies.

---

[1] The measurements were performed by Martino Reclari [98]

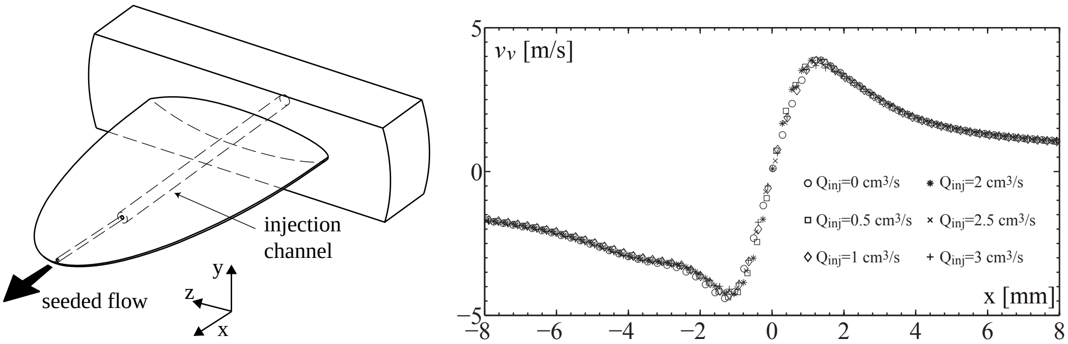

(a) Tip injection channel

(b) Velocity profiles with injection

Figure 4.10: (a) Sketch of the *NACA 16-020* with the tip injection channel. (b) LDV mean tangential velocity profiles one chord downstream of the hydrofoil, for various tip injection flow rates in cavitation-free conditions. W_∞=15 m/s, α=6°

4.2.3 Vortex cavity dimensions

The size of the mean cavity radius r_{cv} is determined by processing high-speed visualizations and digital photographs of the cavitating vortex. By varying the inlet pressure p_∞, the relationship between the cavity radius and the cavitation number σ can be established. It should be noted that even in a seemingly stable vortex, small disturbances in the cavitating vortex can be observed, as illustrated in Figure 4.11a. Therefore, several pictures, or video frames, are processed to obtain a spatial and temporal average of the cavity size. The images are taken from the side of the test section, at the same location as the velocity measurements (120 mm downstream of the hydrofoil). A 180 mm macro zoom lens is used to obtain a high magnification of the cavitating vortex in the field of view. The resulting resolution is 118 pixels per millimeter for the digital photographs and 35 pixels per millimeter for the high-speed visualization.

The cavity edges are identified through the changes in light intensity and contrast generated by an appropriate lighting of the vortex, as shown in Figure 4.11a. To compensate the illumination variations in the image background, a reference image, taken without the cavitating vortex, is subtracted to the raw image. The resulting image is then converted to a black and white

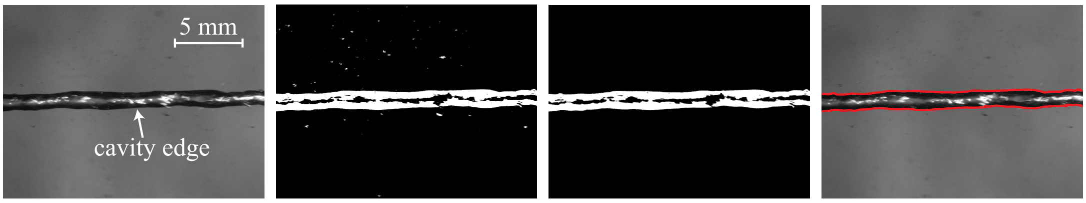

(a) Raw image (b) Binary image (c) Bubbles elimination (d) Edges detection

Figure 4.11: Illustration of the image processing steps to determine the cavity radius

(binary) form, so that the cavitating vortex appears in white, as illustrated in Figure 4.11b. At this stage, small traveling bubbles shed by parasitic cavitation on the hydrofoil may still be visible in the background. For an unambiguous cavity edge detection, those bubbles are eliminated by removing all objects that are smaller than a given amount of pixels. The resulting image is shown in Figure 4.11c. The cavity edges are identified as the location of the first and last white pixel in each column, see Figure 4.11d. The radius r_{cv} corresponds finally to the half distance between the upper and lower edges of the cavity. The spatial mean value of r_{cv} is obtained by measuring the cavity radius in each column of pixels, while a temporal mean value is obtained by analysing several distinct images.

4.3 Velocity field in cavitation-free conditions

In order to understand the effect of cavitation on a vortex, it is necessary to first understand the structure and characteristics of the vortex in cavitation-free conditions. The results presented hereafter are obtained by LDV and include the axial and tangential velocity profiles for different operating conditions of the vortex. The inlet pressure is set in order to avoid the formation of cavitation in the vortex, and the evolution of the vortex characteristics with variations of the foil incidence angle are discussed. Moreover, the influence of the foil boundary layer state is also investigated by testing smooth and roughened leading edges.

4.3.1 Tangential velocity in cavitation-free conditions

Figures 4.12a and 4.13a illustrate the variation of the mean tangential velocity for the smooth and rough leading edges, respectively. The measurements are performed by LDV along the x-axis with a resolution of 0.1 mm in the vortex core and 0.5 mm outside. The freestream velocity is fixed to 10 m/s. The data represent the average unprocessed velocities obtained by LDV, i.e. without deconvolution (cf. Section 3.5.2). The definition of the axes corresponds to the coordinate system in Figure 4.1a. Positive x-values correspond to the outboard side, i.e. the region which is normally not affected by the wake of the hydrofoil. This representation is identical to the point of view of an observer looking at the hydrofoil from a downstream position, with the swirl velocity taken positive in the anti-clockwise direction. For each incidence angle, the axes origin is centered on the mean vortex center.

The tangential velocity profiles are highly symmetrical with the same velocity extremum on either side of the vortex core. This shows that the vortex roll-up is already well advanced at the location of the measurement. The profile shape is typical of a tip vortex with a central region in solid body rotation, where the vorticity is concentrated, and an outer region where the flow is irrotational and the velocity decreases asymptotically towards zero. The tangential velocity reaches a maximum at a position that corresponds to the viscous core radius. The amplitude of this peak velocity increases monotonically with the incidence angle, for both the smooth and rough hydrofoils. For each incidence angle, the rough hydrofoil generates a peak tangential velocity which is systematically lower than the one generated by the smooth hydrofoil, see Figure 4.14a. The dimensions of the viscous core seem to vary with the incidence angle but its evolution is not easy to grasp in these figures and will be discussed in more detail in Section 4.3.3.

4.3.2 Axial flow in cavitation-free conditions

The axial velocity profile in tip vortices can either present a wake-like behavior, characterized by a velocity deficit in the vortex core, or a jet-like behavior, corresponding to a velocity excess compared to the freestream velocity [77, 108]. The axial velocity in a tip vortex is highly dependent on the wing geometry, the angle of attack, the Reynolds number, and the distance downstream of the wing tip [59]. The evolution of the axial flow velocity profile across the vortex for different incidence angles is represented in Figure 4.12b and Figure 4.13b, for the smooth and rough hydrofoils, respectively. The axial flow in the vortex core presents a very different behavior depending on whether the foil leading edge is smooth or rough. For the rough hydrofoil, a significant decrease of the axial velocity component w_v is observed in the center of the vortex. The magnitude of this velocity defect is directly linked to the incidence angle. For α=4°, the minimum velocity in the vortex is equal to approximately $0.9 \times W_\infty$, while this value drops to about $0.7 \times W_\infty$ for α=12°. Nevertheless, the shape of the axial velocity profiles is similar for all incidence angles and can be described by a bell-shaped or Gaussian profile, the width of which is slightly larger than the viscous core radius.

The axial flow profiles for the smooth hydrofoil shown in Figure 4.12b are characterized by a 'M' shape. The axial flow velocity presents two bumps with a velocity excess, on either side of the vortex center and a central region where the velocity drops abruptly. The nature of the axial flow in the vortex center and depends on the foil incidence angle. For instance at 4°, 6° and 16° the velocity in the vortex center is lower than the freestream velocity, whereas the jet-like behavior prevail at all the other incidences. The amplitude of the jet-like bumps is very similar between 14° and 16° and is approximately $1.1 \times W_\infty$. The velocity drop in the vortex center is however much more important in the case of α=16°. It should be mentioned that those incidence angles are close to the stall angle, which is situated around α=17°.

To better assess the axial flow pattern around the tip vortex, the velocity field is mapped with 1533 measurement points in a region of 30×20 mm around the vortex, as represented in

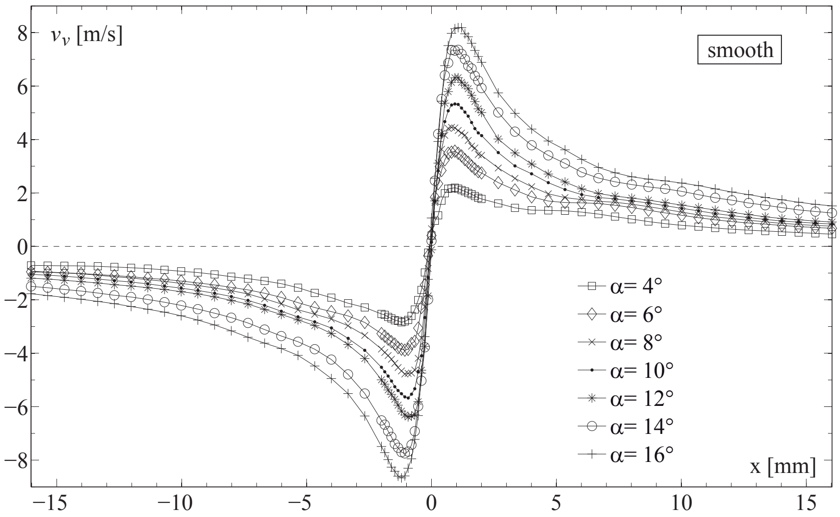

(a) Tangential velocity

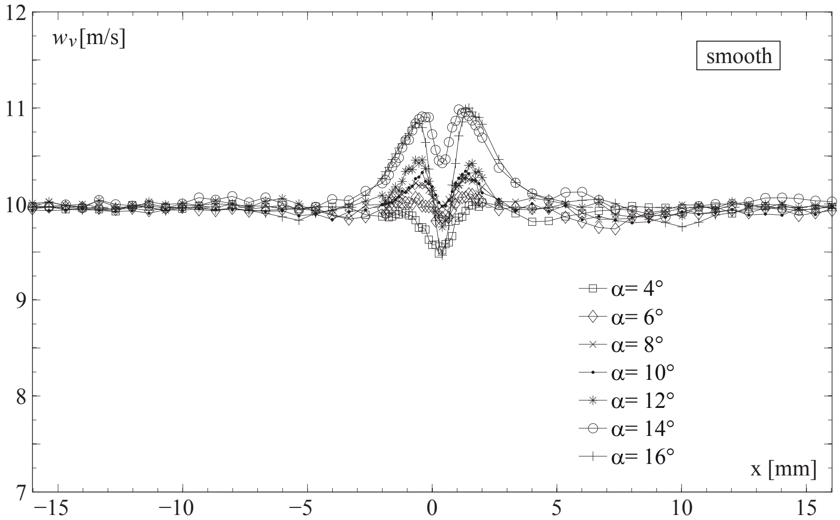

(b) Axial velocity

Figure 4.12: Mean tangential and axial velocity profiles measured by LDV along the x-axis for different incidence angles. Flow conditions: W_∞=10 m/s, cavitation-free, smooth hydrofoil.

Figure 4.2 (but without the empty region behind the vortex). To capture the details of the flow in the vortex core, the spatial resolution is 0.1 mm in the central region -2≤x≤2 mm, whereas a coarser grid with a resolution of 0.5 mm is adopted elsewhere. A cubic spline interpolation of the data is then performed to obtain an uniform mesh. The resulting average axial velocity fields in the case of W_∞=10 m/s and α=12° are represented in Figure 4.15. An anti-clockwise spiral structure with a velocity deficit around the core is clearly visible. This region of velocity deficit is the remainder of the wake sheet: the vortex tends to roll up the fluid layers in its vicinity, entraining the hydrofoil wake. The velocity survey across the x-axis in Figure 4.12a passes necessarily though this wake sheet between x=5 mm and x=10 mm, which disturbs

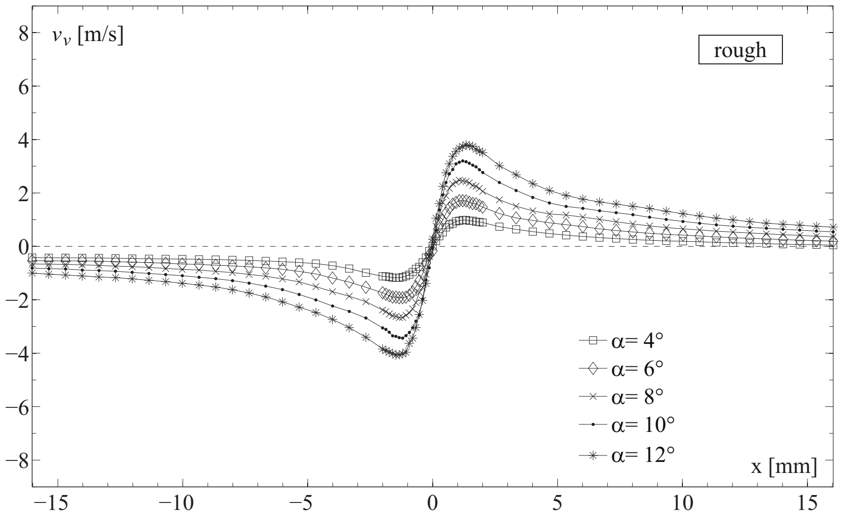

(a) Tangential velocity

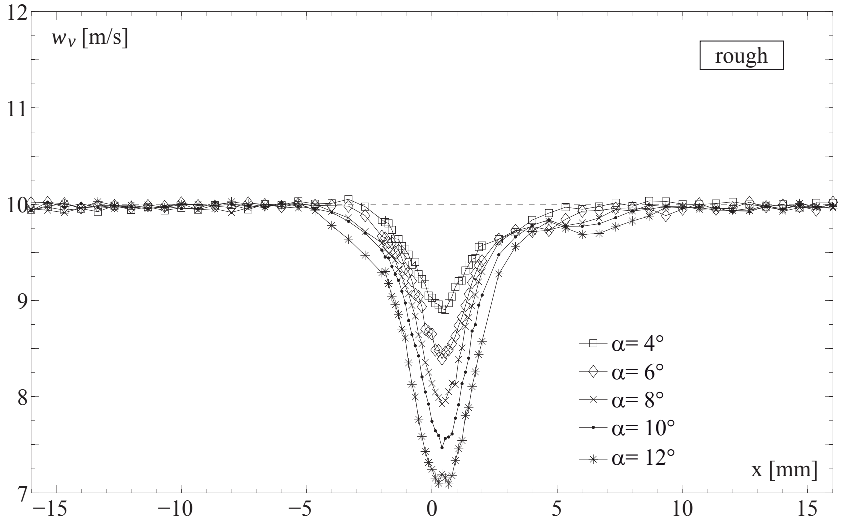

(b) Axial velocity

Figure 4.13: Mean tangential and axial velocity profiles measured by LDV along the x-axis for different incidence angles. Flow conditions: W_∞=10 m/s, cavitation-free, rough hydrofoil.

slightly the tangential velocity resulting in a small slope change of the velocity profiles. The two side bumps of velocity excess in Figure 4.12b correspond to an annular jet-like region surrounding the vortex center. This jet-like region is not axisymmetric and the highest velocity is reached at around y=-1 mm. In the vortex center, a circular region of lower axial velocity prevails, in accordance with the velocity drop in the vortex center illustrated in Figure 4.12b. The final axial velocity field is thus a complex structure resulting from the roll-up of several fluid layers with different velocities.

Figure 4.16 shows the evolution of the axial flow in a region of 4×4 mm around the vortex center for different incidence angles. The flow pattern is similar for each incidence angle

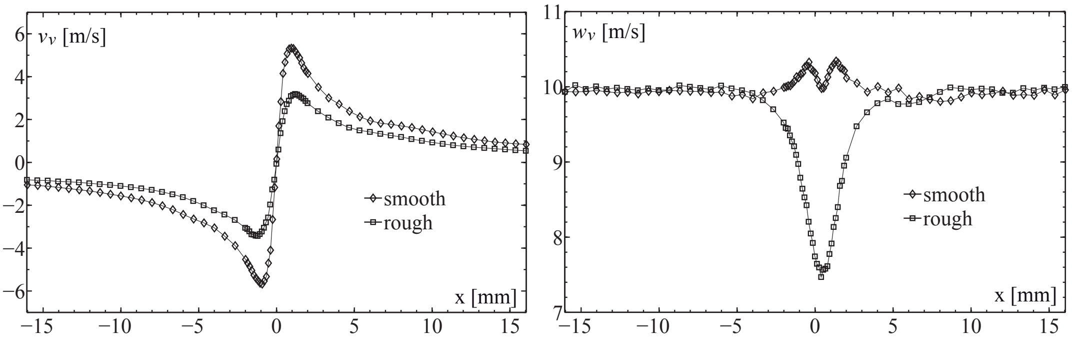

(a) Tangential velocity

(b) Axial velocity

Figure 4.14: Comparison of the tip vortex generated by the smooth and rough hydrofoils at W_∞=10 m/s, α=10°.

with a central region of low velocity surrounded by a annular region of velocity excess. It is worth noting that the vortex center, determined with the tangential velocity and situated at the axes origin, does not always correspond to the location of the axial velocity minimum. The dimensions and the amplitude of the region with a velocity excess increase with the incidence angle. For each incidence angle, the asymmetry of the annular excess velocity region is observed, although it is more pronounced at high incidence angles. Its origin is certainly found in the rolling up process of the wake sheet. If the vortex rotation direction is inverted (negative incidence angle), the bump of excess velocity is turned upside down, as illustrated in Figure 4.16e and Figure 4.16f, for α=12° and α=-12°, respectively. This asymmetric axial flow is likely to disappear as the vortex progresses downstream, due to the viscous diffusion that tends to homogenize the velocity field.

The axial flow in the vortex center generated by the rough hydrofoil is shown in Figure 4.17a. It features a circular bell-shaped region of velocity deficit, in accordance with the velocity profile in Figure 4.13b. For the smooth hydrofoil, the influence of the Reynolds number on the axial

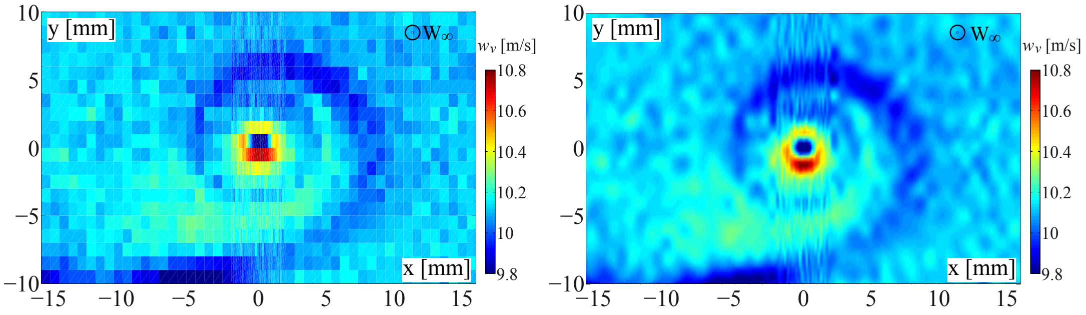

(a) Raw LDV

(b) Interpolated

Figure 4.15: Average axial velocity for the smooth hydrofoil at α=12° and W_∞=10 m/s. (a) Raw LDV measurements. (b) Interpolated flow field

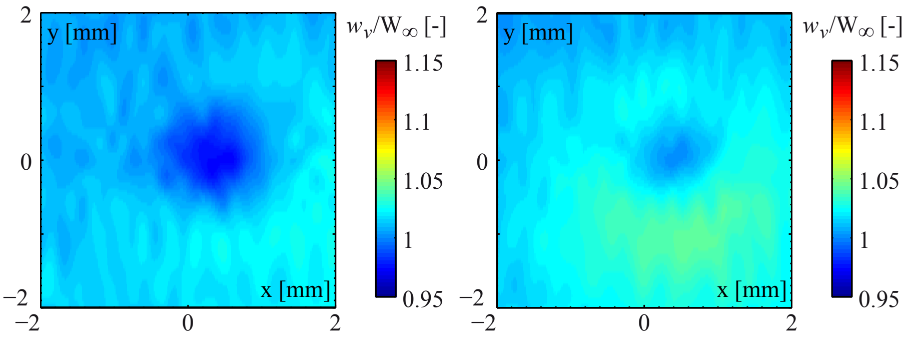

(a) α=4° (b) α=6°

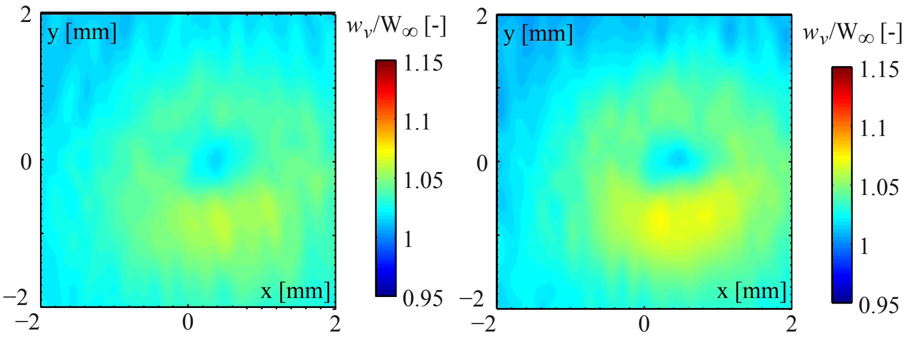

(c) α=8° (d) α=10°

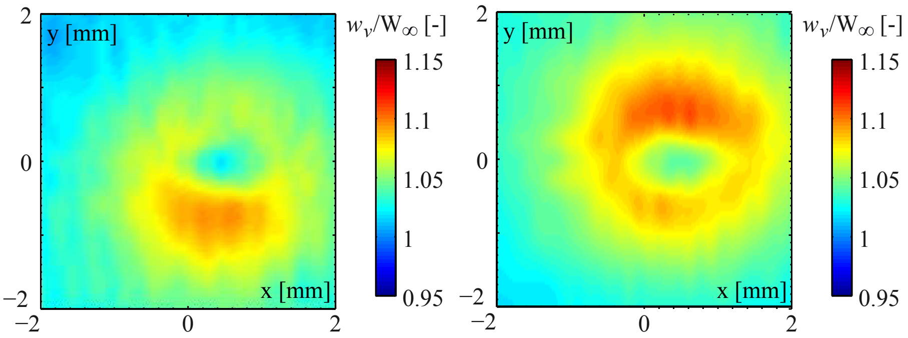

(e) α=12° (f) α=-12°

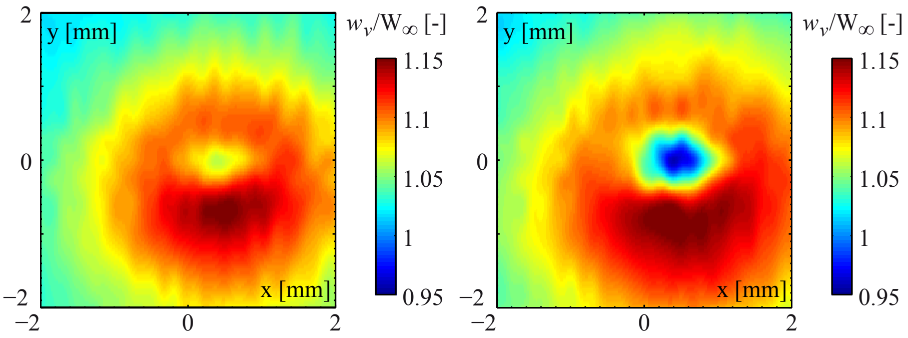

(g) α=14° (h) α=16°

Figure 4.16: Evolution of the axial velocity in the vortex core for different incidence angles. Flow conditions: W_∞=10 m/s, smooth hydrofoil.

velocity is assessed by comparing the flow at W_∞=15 m/s, represented in Figure 4.17b, with the case of W_∞=10 m/s in Figure 4.16e. When the axial velocity is scaled by the freestream velocity, the two Reynolds numbers generate a very similar pattern. In the case of W_∞=15 m/s, the annular jet-like region is slightly smaller than for W_∞=10 m/s, but the velocity excess or deficit amplitudes are comparable in both cases. The axial flow for the smooth and rough hydrofoils should nevertheless become identical at higher Reynolds number, since the boundary layer will be fully turbulent in both cases.

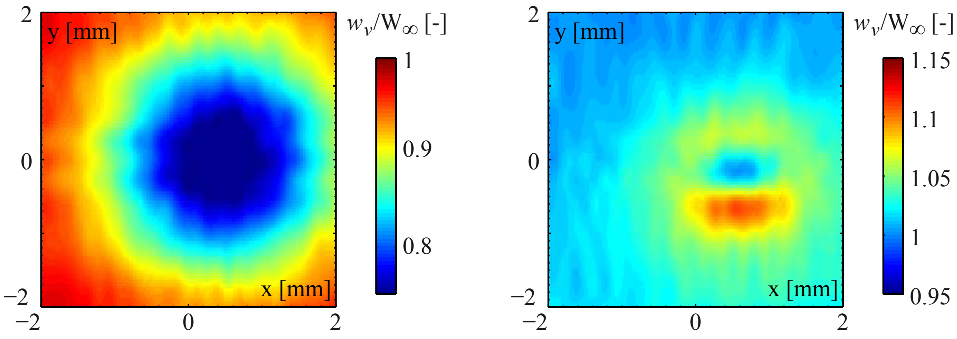

(a) W_∞=10 m/s, α=12°, rough

(b) W_∞=15 m/s, α=12°, smooth

Figure 4.17: Axial velocity in the vortex core for an incidence angle of 12°. (a) Rough hydrofoil and W_∞=10 m/s. (b) Smooth hydrofoil and W_∞=15 m/s.

4.3.3 Vortex characteristics

Vortex model fit

In order to extract the key vortex characteristics or to perform the deconvolution of the LDV measurements (cf. Section 3.5.2), it it useful to fit the experimental data with an analytical vortex model. Figure 4.18 shows a typical example with the fitting of two common vortex models on the experimental tangential velocity, measured with the smooth hydrofoil at W_∞=10 m/s and α=10°. The full black line corresponds to the best fit of the VM2 model on the experimental data while the dashed line corresponds to the best fit of a Lamb-Oseen model, as introduced in Section 2.2. The parameters of each model are adjusted using a least-square method, with a Levenberg-Marquardt algorithm built in *Matlab*. As highlighted in Figure 4.18b, which displays the value of the residuals between the analytical model and the experimental data, the VM2 model presents an overall better fit of the experimental data than the Lamb-Oseen model. The VM2 model is indeed more flexible since it involves four parameters while the Lamb-Oseen model features only two degrees of freedom, given by the circulation and the viscous core size. As a reminder, the Lamb-Oseen velocity distribution is identical to the azimuthal velocity of the Batchelor's vortex, which is only valid far downstream of the hydrofoil, while the VM2 model is essentially an approximation of the vortex model of Moore & Saffman [50], which is supposedly valid in the intermediate region between the completion of roll-up and the far field (cf. Section 2.2.5). Whenever a model fit is required, the VM2 model is therefore chosen since it is able to capture accurately the position of the peak velocity and the evolution of the velocity away from the center, which gives the overall vortex circulation.

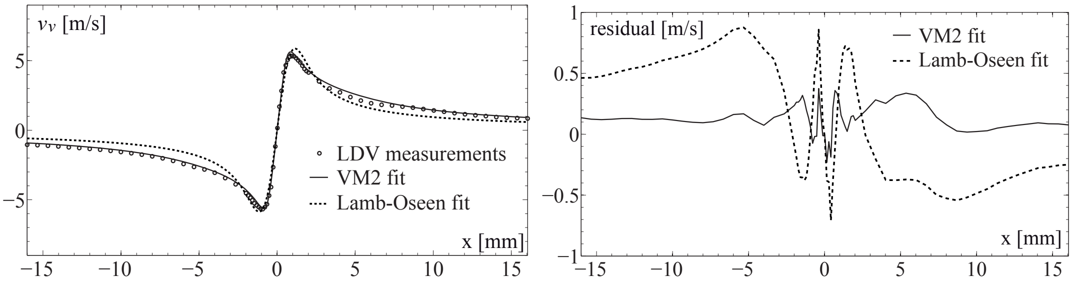

(a) Tangential velocity profiles

(b) Residuals

Figure 4.18: (a) Example the VM2 (black line) and Lamb-Oseen (dashed line) vortex model fitting on the LDV experimental data. (b) Curve fitting residual values. FLow conditions: W_∞=10 m/s, α=10°, smooth hydrofoil.

Velocity deconvolution

The LDV measurements are used to extract the vortex characteristics such as the circulation, the viscous core dimension and the axial velocity peak. In order to retrieve the real vortex characteristics from the LDV measurements, it is necessary to compensate the smoothing effect inherent to the vortex wandering and the size of the measurement volume. A deconvolution of the data is therefore performed, as explained in Section 3.5.2. LDV measurements are preferred over those obtained by PIV since the axial velocity is not directly measured with the latter, as discussed in Section 4.2.2. The PIV measurements are however used to asses the contribution of the vortex wandering in eq. (3.8), representing the probability density function used for the deconvolution. For each angle of incidence, the mean vortex center location and its standard deviation are determined from the analysis of 1000 PIV vector fields. Figure 4.19a illustrates the repartition of the instantaneous vortex centers at W_∞=10 m/s and α=12°, while Figure 4.19b shows the evolution of the standard deviation of the mean vortex center position along the x and y axes with the foil incidence angle. It is observed that the wandering is practically isotropic for every incidence angle, with an amplitude around 0.2 mm, except at α=4° and 6° where its value increases to 0.3 mm.

The deconvolution of the tangential velocity in the case of W_∞=10 m/s and α=12° is illustrated in Figure 4.20. The deconvolution is achieved by performing a best-fit, in least-square sense, of the convolution of a VM2 model over the actually measured velocity profile. The resulting profile is shown in Figure 4.20a along with the raw experimental profile. The deconvolution does not change the overall vortex circulation since the velocity distribution is unaffected outside the vortex core. However, larger velocity extrema and a smaller viscous core are obtained. To assess the accuracy of this new profile compared to the reality, the histogram of the experimental velocity distribution at the vortex center is shown in Figure 4.20b. It is

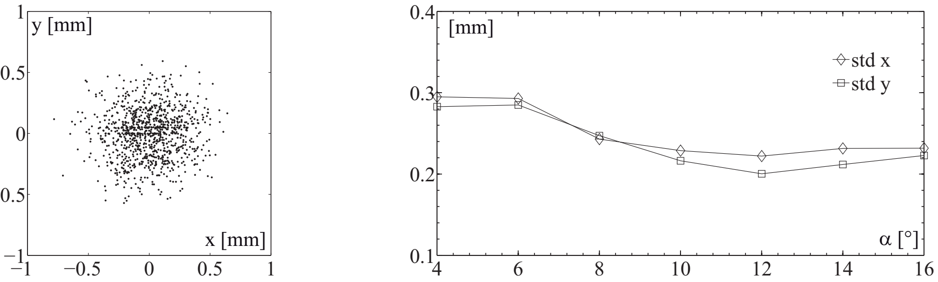

(a) Instantaneous vortex center position (b) standard deviation

Figure 4.19: Wandering amplitude from PIV measurements. (a) 1000 instantaneous vortex centers at W_∞=10 m/s, α=12°. (b) Standard deviation of the mean vortex center position along the x and y axes as a function of α

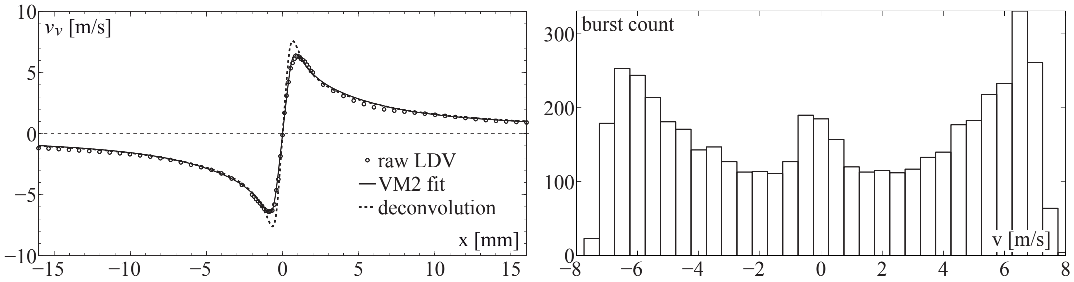

(a) Tangential velocity profiles (b) histogram

Figure 4.20: Example of profile deconvolution at W_∞=10 m/s, α=12°.

observed that the maximum velocity measured is 7.5 m/s, in adequacy with the maximum velocity of the deconvoluted profile.

Vortex characteristics versus angle of incidence

The evolution of the main vortex characteristics with the foil incidence angle is summarized in Figure 4.21. The lift coefficient C_L for the smooth and rough hydrofoils at $Re_c = 9 \times 10^5$ is represented in Figure 4.21a. For the smooth hydrofoil, both the lift produced in cavitation-free conditions and with a cavitating tip vortex are represented. In cavitating conditions, the pressure is adapted for each incidence angle in order to obtain a cavitating tip vortex, while avoiding the formation of a leading edge cavity. It is observed that the cavitation in the tip vortex core does not affect the lift coefficient. The lift of the rough hydrofoil increases linearly up to the stall angle, while the lift evolution of the smooth hydrofoil is more irregular at low incidence angles. The lift coefficient is systematically higher for the smooth hydrofoil than for the rough one. A slope change is however observed between α=6° and 8°, after which the lift of the two hydrofoils are comparable until the stall angle is reached. The differences between the two hydrofoils are related to the development of the boundary layer. For the rough hydrofoil, the boundary layer is fully turbulent from the foil leading edge, while for the smooth hydrofoil the transition to turbulence is probably not uniform across the wingspan [25], resulting in a complex flow field. The stall angle occurs sooner for the rough hydrofoil (16°) than for the smooth hydrofoil (18°).

Figure 4.21b illustrates the evolution of the vortex viscous core radius r_c, before and after the velocity deconvolution. For the smooth hydrofoil, the deconvolution yields a viscous core radius ~25 % smaller than the unprocessed LDV measurements, and ~15 % smaller for the rough case. Moreover, the viscous core radius generated by the rough hydrofoil is around twice as large as the one of the smooth hydrofoil. This is in line with the work of McCormick [85], who observed that the viscous core radius grows with the thickness of the boundary layer on the pressure side surface, near the foil tip. In either case, the viscous core radius does not change monotonically with the foil incidence angle, but a minimum is reached at α=8°. This evolution of r_c indicates that the development of the boundary layer thickness near the hydrofoil tip is highly dependent on the incidence angle.

The normalized circulation Γ^* is defined as the vortex circulation Γ scaled by the viscous core radius r_c and the inlet velocity W_∞. Γ^* is linked to the pressure drop at the vortex center, as explained in Section 2.2.6. The evolution of Γ^* with the incidence angle is shown in Figure 4.21c, before and after the velocity deconvolution. The vortex circulation Γ is directly proportional to the foil bound circulation Γ_0, which is linked to the lift coefficient C_L according to the Kutta-Joukowski theorem ($\Gamma_0 = 0.5 c W_\infty C_L$) [5]. Therefore, the vortex circulation increases monotonically with the hydrofoil incidence angle. Because of its larger viscous core, the rough hydrofoil generates a lower Γ^* than the smooth one.

Finally, the evolution of the axial velocity peaks within the vortex core, normalized by the freestream velocity, is shown in Figure 4.21d. For the smooth hydrofoil, the maximum value of w_v ($w_{v\max}$), corresponding to the two maxima on either side of the vortex center in Figure 4.12b, and the minimum value of w_v ($w_{v\min}$) reached at the vortex center, are both represented. It is observed that the two velocity maxima increase slightly with the incidence angle, switching from a wake-like to jet-like profile in the vortex center around α=8°. However at α=16° the axial flow at the vortex center changes again from jet-like to wake-like. In contrast, for the rough hydrofoil, the axial velocity at the vortex center exhibits a constant decline with the incidence angle. The nature of the axial flow, i.e. wake-like or jet-like, results from the balance between an inviscid effect, which tends to accelerate the flow, and the momentum defect originating in the foil boundary layer that rolls up into the vortex core, resulting in a velocity deficit [60, 108]. From the application of energy conservation (Bernoulli's principle), Batchelor [18] derived the following expression for the axial velocity in an idealized axisymmetric vortex:

$$w(r)^2 = W_\infty^2 + \int_r^\infty \frac{1}{4\pi^2 r'^2} \frac{\partial \Gamma^2}{\partial r'} \,\mathrm{d}r' - 2\Delta H \tag{4.3}$$

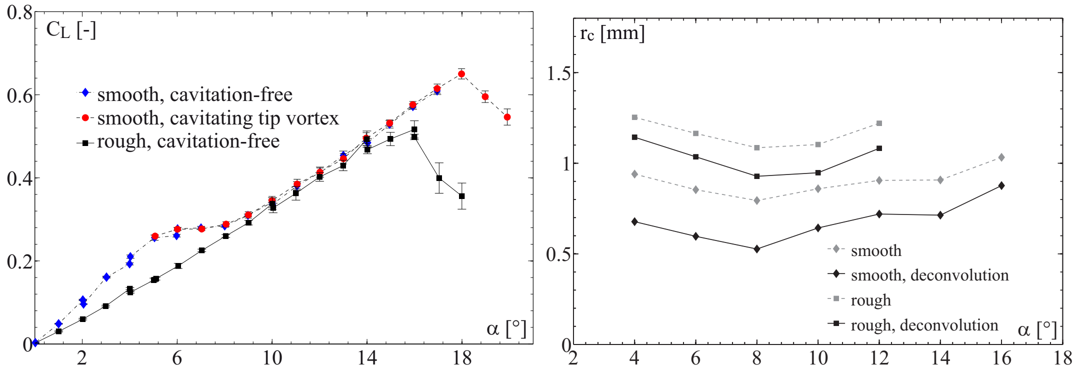

(a) Lift coefficient at $Re_c = 9 \times 10^5$

(b) Viscous core radius

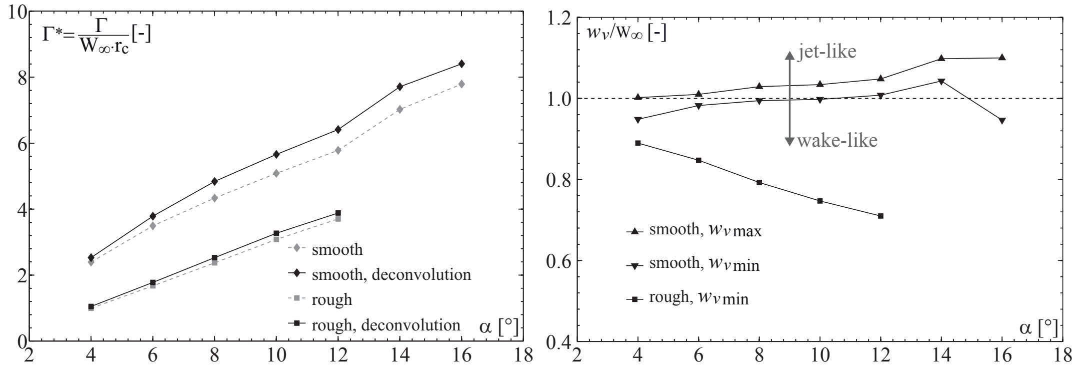

(c) Normalized circulation

(d) Axial velocity peak

Figure 4.21: Evolution of the lift and vortex characteristics with the foil incidence angle.

where the circulation Γ is a function of the radius r and ΔH is an arbitrary function that accounts for the viscous losses along a streamline passing through the boundary layer of the hydrofoil. Since the vorticity in the vortex is one-signed, it can be shown that the second term on the right-hand side of eq. (4.3) is strictly positive [18]. An axial velocity excess in the vortex center, or a jet-like profile, is predicted in the absence of viscosity. Given that the vortex circulation increases in proportion to the lift produced, i.e. to the incidence angle as illustrated in Figure 4.21c, this axial velocity excess is expected to increase monotonically with the foil incidence angle, as has been observed in several studies [4, 55, 77]. However, the dissipation term ΔH competes with the inviscid acceleration mechanism to determine the final nature of the resulting core axial flow. The decreasing axial velocity observed in Figure 4.21d implies thus that the dissipation term ΔH increases with the foil incidence angle and is prevailing over the second term on the right-hand side of eq. (4.3). Moreover, Arndt et al. [12] reported that elliptic planform wings may experience laminar separation and reattachment. This separation is expected to produce large head losses (ΔH) and therefore a reduced axial velocity in the vortex core [59].

Pressure distribution

The distribution of the pressure coefficient C_p in the vortex can be determined by integrating the radial equilibrium equation $\partial p / \partial r = \rho v_\theta^2 / r$. Figure 4.22 shows the C_p distribution obtained for the smooth hydrofoil in the case of W_∞=10 m/s and α=12°, which corresponds to the selected operating condition to study the cavitating vortex. The pressure integration is performed for the velocity distribution resulting from the raw and deconvoluted LDV velocity profiles shown in Figure 4.20a. At the vortex center, the minimum pressure coefficient is $C_{p_{min}} = -1.6$ for the raw LDV data and $C_{p_{min}} = -2.1$ for the deconvoluted profile. Experimentally, the incipient cavitation number is between $\sigma_i \approx$2-2.2, which is in good accordance with the predicted value ($\sigma_i = -C_{p_{min}}$) for the deconvoluted profile. This validates the deconvolution procedure and confirms its importance to obtain the true vortex characteristics.

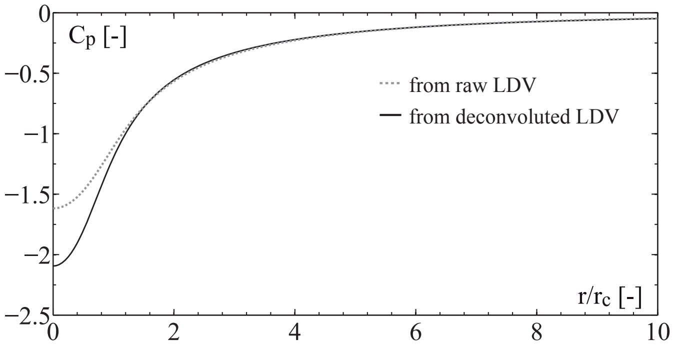

Figure 4.22: Computed pressure coefficient in tip vortex for the smooth hydrofoil at W_∞=10 m/s, α=12°.

4.4 Cavitating vortex

4.4.1 Flow visualizations

Figure 4.23 shows the visualizations of the cavitation in the tip vortex at different values of the cavitation number σ, for the smooth hydrofoil. The freestream velocity is fixed to W_∞=10 m/s and the incidence angle is $\alpha = 12°$. At $\sigma = 2$, the conditions are very close to cavitation inception and the vortex is only partially and intermittently cavitating. High-speed visualizations indicate that the vortex cavitation is triggered by the capture and growth of small bubbles in the vortex core. The source of these bubbles could not be clearly determined, but they seem to originate from small surface defects on the foil suction side. A small cavitation strip attached to a surface irregularity near the foil tip can actually be distinguished in Figure 4.23 at $\sigma = 2$. The growth of these bubbles in the radial direction rapidly stabilises at an equilibrium radius, while they continue to elongate in the axial direction, forming a cylindrical bubble shape, as also reported by Arndt and Maines [10].

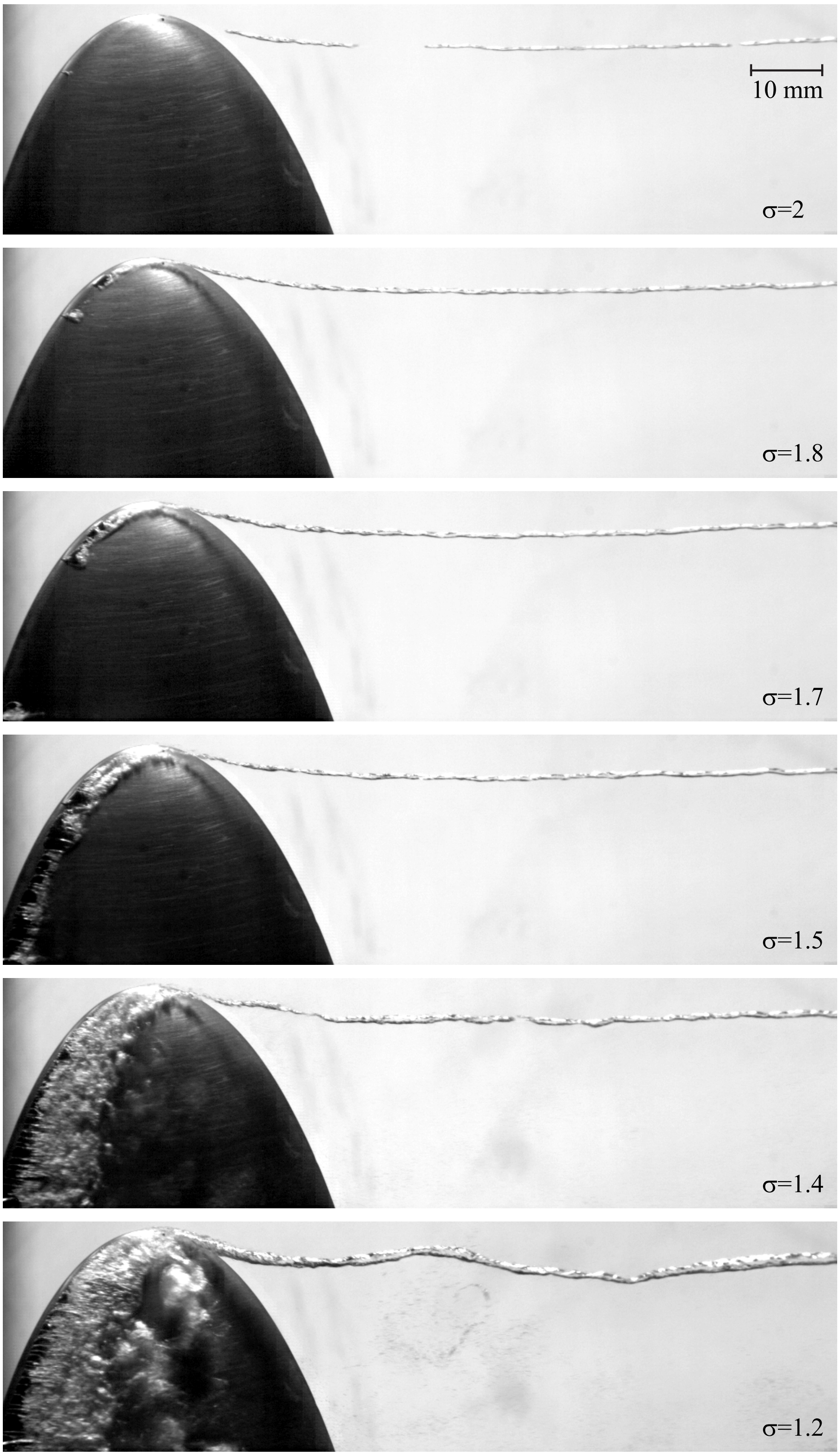

Figure 4.23: Snapshots of the cavitating tip vortex generated by the elliptical *NACA 16-020* at different values of the cavitation number σ. Flow conditions: W_∞=10 m/s, α=12°, smooth hydrofoil.

At $\sigma = 1.8$, the vortex vapor core attaches to the foil tip permanently. Such a cavity is very stable both spatially and temporally and extends far downstream of the test section. In addition to the vortex cavitation, a leading edge cavity develops in the area of attachment between the vortex and the foil tip. This leading edge cavity grows towards the foil root as σ decreases, while new spots of leading edge cavitation appear along the wingspan, see for instance at $\sigma = 1.7$. Between $1.5 \leq \sigma \leq 2$, the leading edge cavity dimensions steadily increase, extending to the whole wingspan. The size of the vortex vapor core remains however remarkably constant as it evolves downstream of the foil. A further decrease of the cavitation number leads to the shedding of horseshoe vortices [7] behind the leading edge sheet cavitation. These structures induce some disturbances on the cavitating vortex, resulting in a highly unsteady trajectory, cf. at $\sigma = 1.2$. The vortex vapor core is also affected by the flow unsteadiness and its size can vary spatially, yielding sometimes to a local collapse of the cavity, see for instance at $\sigma = 1.4$. In order to obtain relevant average quantities of the velocity field, the investigation of the cavitation effect on a tip vortex is limited to the case of a steady vortex with an uniform cavity.

4.4.2 Tangential velocity of the cavitating vortex

In the case of a cavitating vortex, the velocity field is characterized using 2D fluorescent PIV, cf. Figure 4.4. In order to obtain a stable cavitating vortex without excessive parasitic cavitation at the foil leading edge, the measurements are limited to the smooth hydrofoil at the flow conditions W_∞=10 m/s and α=12°. The cavity size is varied by changing the cavitation number σ. The measurements are performed at three different σ values: $\sigma = 3$ corresponding to cavitation-free conditions, $\sigma = 2$ representing the onset of vortex cavitation, and $\sigma = 1.5$ corresponding to a well established cavitating vortex, as shown in Figure 4.23. For each case, the average velocity field is obtained from 500 individual vector fields, following the procedure described in Section 4.2.2. It is verified that increasing the number of velocity fields does not change the mean flow characteristics.

Figure 4.24 shows the average velocity fields of the cavitating vortices with the velocity components $u_v - \tilde{w}\cot(\beta)$ and v_v, where β is the angle between the laser plane and the vortex axis and $\tilde{w}$ is the vortex induced axial velocity, cf. eq. (4.2). As explained in Section 4.2.2, the actual velocity field in the vortex reference frame $(u_v,\ v_v)$ is close to the one in Figure 4.24 if $\tilde{w}$ is small. For readability reasons, only 1 out of 4 vectors is represented in the x-direction. The origin of the axes is taken at the vortex swirling center. The radius of the cavity r_{cv} is derived directly from the raw PIV images using the faint light reflections on the cavity interface. At $\sigma = 2$, $r_{cv} \approx 0.25$ mm and is represented by the plain white circle at the origin. No distortion of the mean velocity field is observed for negative x-values despite the presence of the cavitating vortex. In contrast, the distortions of the vector field due to the passage of the cavitating vortex are well visible if the cavitating vortex is large, as illustrated in Figure 4.24b. At $\sigma = 1.5$, the corresponding vortex cavity radius is approximately 0.7 mm and is represented by the plain white circle.

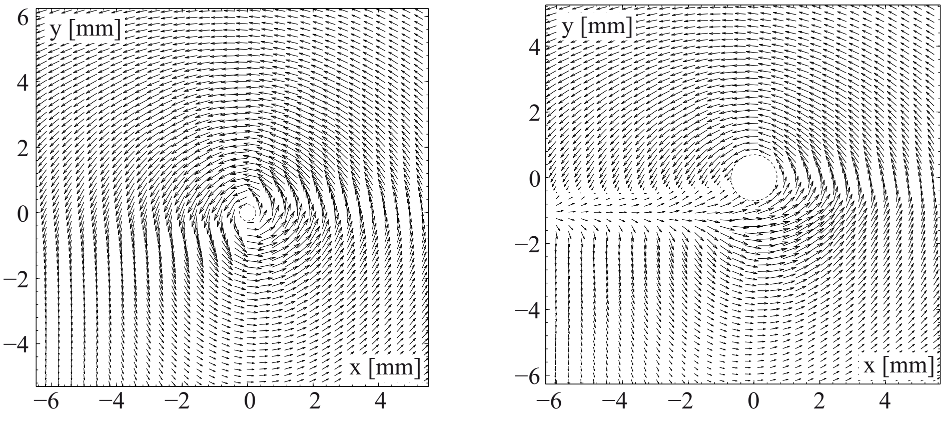

(a) $\sigma = 2$ (b) $\sigma = 1.5$

Figure 4.24: Average velocity field ($u_v - \widetilde{w}\cot(\beta)$ and v_v) for the cavitating vortex at two different σ values. The cavity interface is marked by a white circle. For readability, only 1 out of 4 vectors is represented in the x-direction.

The velocity along the y-axis is the same in the reference frame of the vortex and the PIV, i.e. $v_{piv} = v_v$ (cf. Section 4.2.2). This latter is therefore used to obtain the average swirl velocity profile. A comparison of the isocontours of the velocity v_v for the three selected σ values is given in Figure 4.25. The footprint of the cavitating vortex is again clearly visible for negative x-values in the case of $\sigma = 1.5$. While the differences between the cases $\sigma = 3$ and $\sigma = 2$ are subtle, the velocity maxima are smaller in the case of $\sigma = 1.5$, corresponding to the large cavitating vortex. Since the velocity field at negative x-values is affected by the passage of the cavity, the mean tangential velocity profile is computed by considering only the right-hand side of the velocity field, i.e. the positive x-values.

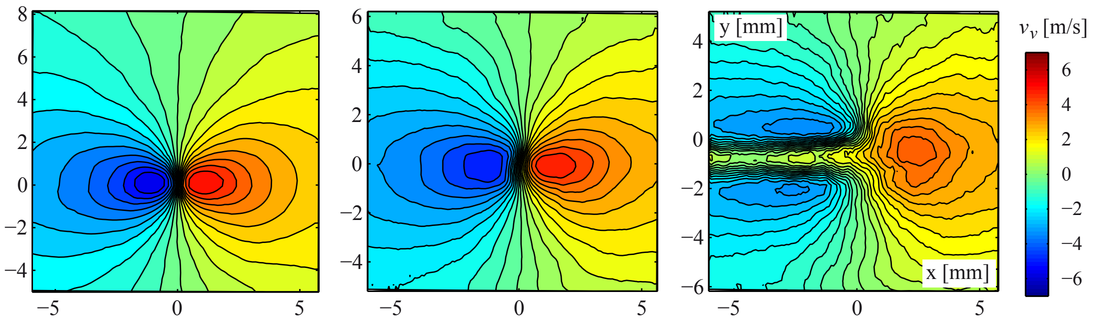

(a) σ = 3, cavitation-free (b) σ = 2 (c) σ = 1.5

Figure 4.25: Isocontours of the velocity v_v for different σ values. $\sigma = 3$ corresponds to cavitation-free conditions, while $\sigma = 2$ and $\sigma = 1.5$ correspond to a small, respectively large, vortex cavity. Flow conditions: W_∞=10 m/s, α=12°.

The mean tangential velocity profiles for the three selected σ values are represented in Figure 4.26. The tangential velocities are scaled by the maximum velocity of the non-cavitating vortex $v_{\theta_{max}}$ and the abscissa is made non-dimensional using r_c, the viscous core size of the non-cavitating vortex. In the case of a cavitating vortex, the first value corresponds to the velocity at the cavity interface. The cavity size at $\sigma = 2$ corresponds to 33 % of r_c while, at $\sigma = 1.5$ the cavity size is 80 % of r_c. Outside the cavity, the three tangential velocity profiles merge together beyond the distance $r/r_c = 3$, which implies that the overall circulation $\Gamma = 2\pi r v_\theta$ is equal for the three vortices. In contrast, the tangential velocity changes drastically near the cavity interface and the velocity is always smaller for a cavitating vortex than in the cavitation-free regime. The peak tangential velocity at $\sigma = 2$ amounts to 90 % of $v_{\theta_{max}}$ and only to 70 % at $\sigma = 1.5$. Interestingly, a region where the velocity increases linearly with the radius, i.e. a solid body rotation, persists just outside of the cavity. Furthermore, the peak velocity of the cavitating vortex occurs at a larger radius than for the non-cavitating vortex: at $\sigma = 2$ the maximum velocity is reached at $r/r_c = 1.05$ while at $\sigma = 1.5$ this value increases to $r/r_c \approx 2$. Finally, the velocity at the cavity interface is approximately $0.5 \times v_{\theta_{max}}$ for the small cavity and approximately $0.4 \times v_{\theta_{max}}$ in the case of the large cavity.

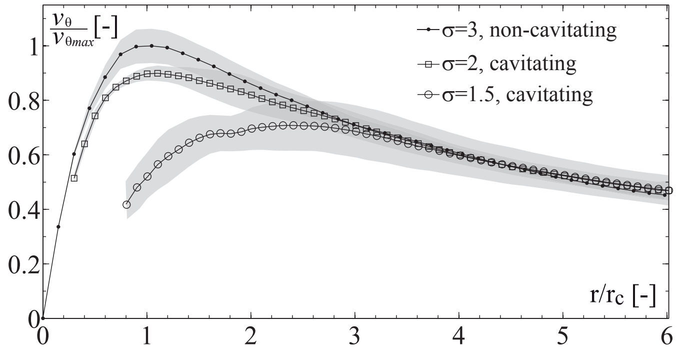

Figure 4.26: Comparison of the tangential velocity for three values of sigma. $\sigma = 3$ corresponds to cavitation-free conditions, while $\sigma = 2$ and $\sigma = 1.5$ correspond to a small ($r_{cv} \approx 0.33 r_c$), respectively large ($r_{cv} \approx 0.8 r_c$) vortex cavity. The grey area represents the standard deviation. Flow conditions: W_∞=10 m/s, α=12°.

4.4.3 Axial flow of the cavitating vortex

In addition to the tangential velocity modifications, the cavitation within a vortex is likely to have an influence on the surrounding axial flow as well. The axial flow of the non-cavitating vortex is presented in Section 4.3.2, where LDV measurements are mapped in a region of 30×20 mm around the vortex. In the case of a cavitating vortex, a similar approach is adopted, except that the measurement mesh has to be adapted to the presence of the cavity. This is evidenced by the black dots in Figure 4.27a, representing the measurement locations, together with the axial velocity for the conditions W_∞=10 m/s, α=12° and $\sigma = 1.5$, corresponding to the large vortex cavity. The axial velocity is scaled by the freestream velocity W_∞ and the flow field is interpolated with a cubic spline between the measurement location in order to obtain

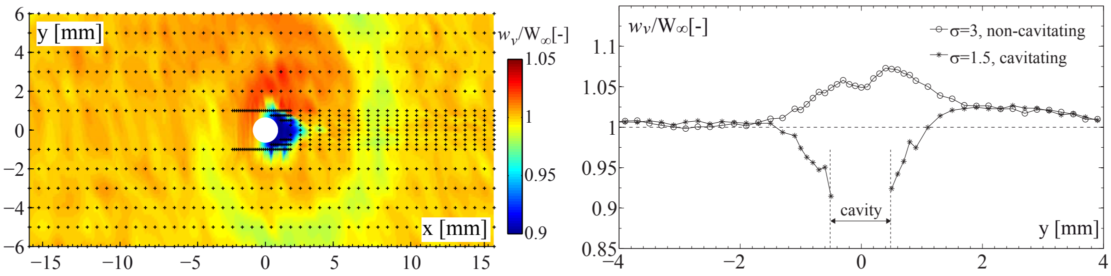

(a) Axial velocity map

(b) Axial velocity profile

Figure 4.27: LDV axial velocity around a cavitating vortex. (a) Interpolated axial velocity map for the cavitating vortex at $\sigma = 1.5$. The measurement locations are depicted by the black dots and the cavity is represented by a white disk. (b) Axial velocity profile along the y-axis for the cavitation-free and cavitating vortex. Flow conditions: W_∞=10 m/s, α=12°.

the complete map. The origin of the axes is at the vortex center and the cavity interface is represented by the white disk.

Similarly to the non-cavitating case, a fluid layer with a velocity deficit emanates from the foil wake and winds around the vortex. However, unlike the non-cavitating vortex, a region of velocity deficit is visible just outside of the cavity. Due to the lack of measurements for negative x-values, this wake-like region appears only for $x > 0$. This asymmetry is however likely to be an artifact of the interpolation. A comparison of the axial velocity profile for the cavitating and non-cavitating vortex is presented in Figure 4.27b. The LDV velocity survey is made along the y-axis, taking advantage of the small dimensions of the measurement volume in this direction (~0.1 mm, see Table 3.2), which allows to approach the cavity very closely. The cavitation in the vortex core changes the jet-like velocity profile of the non-cavitating vortex into a region of velocity deficit, such that the axial velocity is equal to $0.92 \times W_\infty$ at the cavity interface.

The cavitation in a vortex reduces both the maximum tangential velocity and the axial velocity near the vortex center. However, the swirl number defined as the ratio of the maximum tangential velocity to the axial velocity at the vortex center, $S = v_{\theta_{max}} / w_v(0)$ [46], is not the same for the cavitating and non-cavitating vortex. In cavitation-free conditions, the swirl number is $S = 0.71$, while $S = 0.57$ for the cavitating vortex if $w_v(0)$ is replaced by the axial velocity at the cavity interface. The reason for this axial velocity change is difficult to identify. The relation of Batchelor eq. (4.3) presents however two possible interpretations. First, the viscous losses ΔH may increase due to the occurrence of cavitation at the foil tip, in the vortex formation region. A fluid particle just outside the vortex cavity is likely to have passed through a leading edge cavity near the foil tip, see Figure 4.23, affecting its momentum. Secondly, since the peak of axial velocity occurs at a position $r > r_c$, the second term on the right-hand side of eq. (4.3) is smaller for a cavitating vortex than in cavitation-free conditions and a lower axial flow is hence expected. This phenomenon is illustrated in Figure 4.28 by considering a non-cavitating Lamb-Oseen velocity profile and ignoring the viscous losses for the sake of simplicity. By definition, the circulation distribution of this vortex is given by:

$$\Gamma(r) = \Gamma_C\left(1 - e^{-1.2345\cdot\frac{r^2}{r_c{}^2}}\right) \tag{4.4}$$

where Γ_C is the overall vortex circulation. For a fixed value of Γ_C, the evolution of the circulation with the radial distance is flattened and features lower gradients if the size of the viscous core radius r_c increases, as sketched in Figure 4.28a. Replacing these circulation profiles in the second term on the right-hand side of eq. (4.3) leads to the axial velocity profiles, which are represented in Figure 4.28b. If the viscous core size is doubled, the Batchelor's equation predicts that the maximum axial velocity at the vortex center is approximately 25 % of the velocity of the original vortex. While this result is not directly transposable to the case of a cavitating vortex, the flattened tangential velocity profile shown in Figure 4.26 induces nevertheless a lower axial velocity than in the cavitation-free regime.

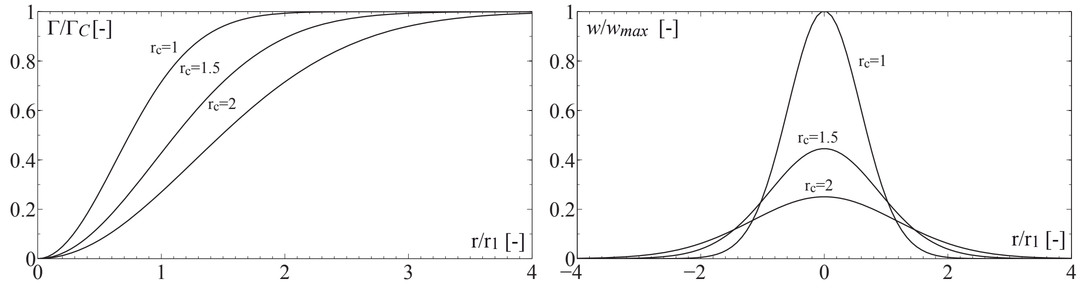

(a) Circulation distribution

(b) Axial velocity profile

Figure 4.28: Circulation and axial velocity profiles computed with eq. (4.3), for three Lamb-Oseen vortices with same circulation and arbitrary viscous core size radii.

4.4.4 Cavitating radius evolution

The relation between the vortex cavity size r_{cv} and the cavitation number σ is investigated by analyzing high-speed visualizations and digital photographs of the cavitating vortex. The tests are performed at W_∞=10 m/s and 15 m/s, while the incidence of the hydrofoil is fixed at 12°. The cavitation number is varied in a range between the inception index, $\sigma_i = 2.2$, and $\sigma = 1.3$. Lower σ values result indeed in an unsteady vortex, which is destabilized by the leading edge cavitation, cf. Figure 4.23. The results are presented in Figure 4.29, where r_{cv} is scaled by the viscous core size of the non-cavitating vortex, determined from the LDV measurements, and σ is divided by σ_i. It can be observed that close to the cavitation inception, the cavity rapidly expands to a significant r_{cv}/rc ratio. This phenomenon is also visible in Figure 4.23 at $\sigma = 2$, where the vortex is either cavitation-free or cavitating with a radius of $r_{cv} \approx 0.25$ mm.

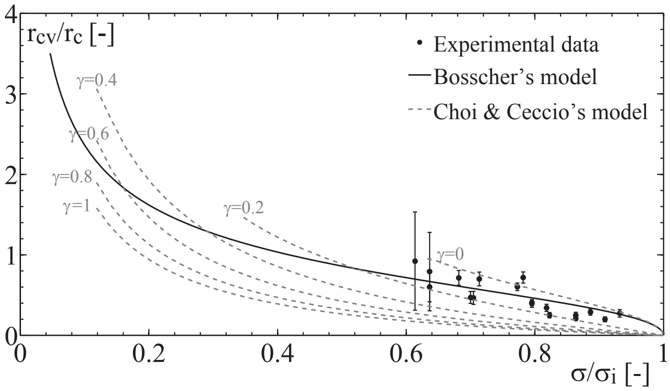

Figure 4.29: Non-dimensional cavity radius with the cavitation number for W_∞=10 m/s and 15 m/s, α=12°. Solid line: analytical predictions of Bosschers's model. Dashed lines: analytical predictions of Choi & Ceccio's model with varying parameter γ=0, 0.2, 0.4, 0.6, 0.8 and 1.

The analytical prediction for the cavitating vortex models by Choi & Ceccio [30] and Bosschers [24], cf. Section 2.3, are also represented. As a reminder, both models are based on a modified Lamb-Oseen velocity profile. The parameter γ in the model of Choi and Ceccio can vary in a range of $0 < \gamma < 1$. When $\gamma = 0$, the velocity profile of the cavitating vortex is the same as that of a non-cavitating Lamb-Oseen vortex, with the vapor occupying the region $0 < r < r_{cv}$. Conversely, if $\gamma = 1$, the tangential velocity at the cavity interface is zero.

Interestingly, the experimental results are in fairly good agreement with the models of Bosschers and Choi & Ceccio for $0 < \gamma < 0.4$, even though the non-cavitating velocity profile is not perfectly described by a Lamb-Oseen vortex, as discussed in Section 4.3.3. This suggests that certain characteristics of the cavitating vortex are nonetheless properly predicted by these models, as further discussed in the next Section.

4.5 Discussion

The main effects of the cavitation on a tip vortex can be summarized in the following way. Far from the cavity, the tangential velocity distribution of the cavitating vortex is identical to the non-cavitating vortex, implying that the vortex circulation Γ is not affected by the cavitation. In contrast, near the cavity, the tangential velocity is lower than in cavitation-free conditions, see Figure 4.26. Furthermore, the location of the peak tangential velocity, which is occurring at $r = r_c$ for the non-cavitating vortex, is shifted to a position $r > r_c$ when the vortex is cavitating. Just outside the cavity, the fluid is in solid body rotation, with the tangential velocity increasing linearly with the radius. Finally, the cavitating vortex features an axial velocity deficit near the cavity, compared to the jet-like axial flow in cavitation-free regime. To the author's knowledge, these are the first detailed experimental data on the flow structure around a cavitating vortex.

These findings demonstrate that the cavitating vortex model of Arndt & Keller [8] (cf. Section 2.3.1), which predicts a maximum velocity for the cavitating vortex that is $\sqrt{2}$ times higher than the maximum velocity in the non-cavitating case, is not physically accurate. It is however interesting to compare the experimental results with the prediction of Bosschers's and Choi & Ceccio's models for a cavitating vortex, see Section 2.3. The results are shown in Figure 4.30 for the case of the large cavity ($r_{cv} \approx 0.8 r_c$). First, it should be noted that both models assume that the non-cavitating vortex is described by a Lamb-Oseen vortex. As discussed in Section 4.3.3, this assumption is not valid in our case since the non-cavitating vortex is best described by a VM2 vortex. It is thus likely that better results would be obtained with a model based on a modified VM2 velocity distribution. An extension of the VM2 model for cavitating vortices was however unavailable at the time of the present analysis and will be the object of a future work. In Figure 4.30, the Lamb-Oseen velocity profile corresponding to the best fit of the experimentally measured non-cavitating vortex is represented by the black curve. The velocity profiles are normalized by the maximum tangential velocity of the non-cavitating vortex $v_{\theta_{max}}$ and the abscissa is made non-dimensional using r_c, the viscous core size of the non-cavitating vortex. The peak tangential velocity of the Lamb-Oseen vortex occurs at the abscissa $r_{L-O} = 1.3 r_c$. The agreement with the experimental profile is fairly poor in the region $1 < r/r_c \leq 5$, but becomes better at larger distance from the core (cf. Figure 4.18). The parameters of this Lamb-Oseen vortex are used to determine the parameters of the analytical cavitating vortices that match the size of the experimental cavity radius $r_{cv} = 0.8 r_c$. Bosscher's solution is represented by the red curve, while Choi & Ceccio's solution is calculated for two γ values (γ=0.2 in green and γ=0.4 in blue). A reduction of the peak tangential velocity with the appearance of a cavitating core is predicted by all the analytical models. However, the velocity decline is underestimated by the model of Bosschers and Choi & Ceccio for γ=0.2, while for γ=0.4 the peak velocity equals to 75 % of the maximum velocity of the Lamb-Oseen vortex, which is fairly close to the experimental velocity decline ($0.7 v_{\theta_{max}}$). The velocity at the cavity interface is also in close agreement with the experimental profile. However, the shift of the location of the peak tangential velocity is not well predicted by the three models ($1.15 r_{L-O}$

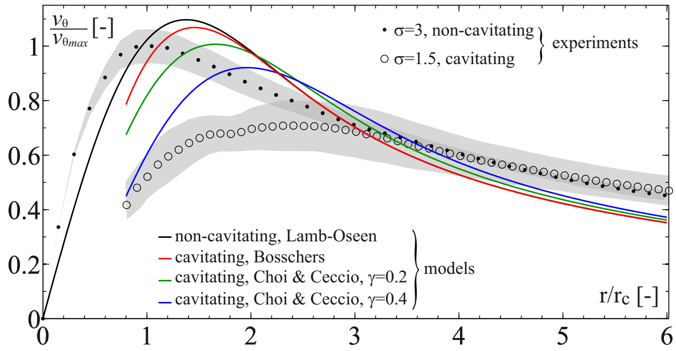

Figure 4.30: Comparison of the experimental tangential velocity and the prediction of the analytical models of Bosschers (red line) and Choi & Ceccio for γ=0.2 (green line), and γ=0.4 (blue line). The grey area depicts the standard deviation of the experimental data.

for the red curve, $1.2r_{L-O}$ for the green curve and $1.4r_{L-O}$ for the blue curve) compared to the experiment ($\sim 2r_c$). Finally, the three analytical curves feature a region where the fluid is in solid body rotation just outside the cavity, in accordance with the experiments.

For the cavitating vortex, it may be surprising that the maximum tangential velocity is not reached at the cavity interface, but that the tangential velocity decreases when approaching the cavity. The following considerations suggest that this is however a general characteristic of cavitating vortices. As demonstrated in Figure 4.30, the tangential velocity v_θ decreases following a 1/r-law beyond a distance of approximately 3 times the viscous core radius. This is the case for both non-cavitating and cavitating vortices and corresponds to an outer region of irrotational fluid motion. Furthermore, the overall vortex circulation remains constant for both cavitating and non-cavitating cases, implying that the vorticity flux is conserved according to Stokes's theorem:

$$\Gamma = \int_A \vec{\omega} \cdot \vec{n} \cdot dS \tag{4.5}$$

Assuming that the vorticity is not contained entirely within the vaporous core, a region of concentrated vorticity needs to exist in the liquid phase close to the cavity interface. Furthermore, if the sign of the streamwise vorticity $\omega = (1/r)\partial(r v_\theta)/\partial r$ is to match the one of a non-cavitating vortex, the tangential velocity v_θ has to decrease towards the cavity interface. Finally, assuming that the shear stress at the cavity interface equals zero, which is expressed by eq. (2.27), the fluid at the cavity interface is in solid body rotation, as explained in Section 2.3.3. The combination of these arguments explains the shape of the measured tangential velocity profile for a cavitating tip vortex.

5 Effect of gap width on the TLV

5.1 Motivation and context

The tip leakage vortex (TLV), which develops in the clearance between the rotor and the stator of axial hydro turbines, compressors and ducted marine propellers, has been studied for decades. Yet, many associated phenomena are still not understood. For instance, it remains unclear how the clearance size is related to the occurrence of cavitation in the vortex, which can lead to severe erosion. The objective of this chapter is to provide accurate measurements of the velocity field in a simplified case study, in order to gain a better understanding of the underlying physics of vortex confinement and provide an extensive experimental database for further developments.

5.2 Case study and experimental setup

5.2.1 Case study

The structure and trajectory of a TLV generated at the tip of a fixed 2D hydrofoil is investigated experimentally for different confinements and flow parameters. The experiments are carried out in the EPFL high-speed cavitation tunnel and the TLV is generated by a stainless steel *NACA 0009* hydrofoil, featuring a chord length of c=100 mm and a maximum thickness of h=9.9 mm. The hydrofoil is mounted on a sliding support, allowing for an adjustable clearance (or gap) between the foil tip and the test section lateral wall. The gap can be varied smoothly between 0 and 20 mm. The influence of the foil boundary layer state is investigated by testing smooth (natural transition) and roughened (tripped boundary layer) leading edges. The impact of the wall boundary layer thickness on the TLV intensity evolution is evaluated indirectly by varying the inlet velocity W_∞.

Velocity measurements in vortical structures are subject to uncertainty due to the wandering phenomenon, which is a random displacement of the vortex centerline with an amplitude of the order of the vortex core size. Although this phenomenon has been well referenced, its origin remains unclear. It is presumed to arise from a resonant excitation triggered by the free stream turbulence [44]. As a consequence, single point measurement techniques, such as Laser Doppler Velocimetry (LDV), always result in a more diffuse velocity field than in reality, and correction methods must be applied to retrieve the true velocity field, cf. Section 3.5.2. Furthermore, the size of the LDV measurement volume introduces another smoothing effect that must be taken into account as well. Given that only two velocity components can be measured simultaneously with a common LDV setup, we have selected the Stereo Particle Image Velocimetry (SPIV) technique for the measurement of the 3D velocity field of the TLV. Moreover, SPIV leaves the possibility of accurately filtering out the vortex wandering in the averaging process, as explained in Section 3.7.2.

In this simplified approach, the effect of relative motion between the rotating blades and the casing of an axial turbine is not taken into account. It is assumed that the mean vortex flow is not fundamentally altered by the end wall motion, as already shown by [117]. The results are represented in the Cartesian x, y, z coordinate system and the corresponding velocities are referred to as u, v and w. The origin of the coordinate system is located on the test section lateral wall, corresponding to the plane $x = 0$, while the foil axis of rotation is on the intersection of the planes $y = 0$ and $z = 0$. The orientation of the coordinate system is illustrated in Figure 5.1.

5.2.2 Stereo Particle Image Velocimetry setup

SPIV is used to measure the 3D velocity field in three cross-sections of the tip vortex at different downstream locations (see Figure 5.1). A 2 mm-wide laser sheet is generated by a double pulsed YAG laser (Litron DualPower, 200 mJ/pulse, 532 nm wavelength) and a cylindrical lens. The time interval between laser pulses is set for each inlet velocity in order to limit the maximum out-of-plane displacement of the seeding particles to one tenth of the laser sheet thickness (e.g., 30 μs for W_∞=5 m/s). Image pairs are acquired using two CCD cameras (Dantec FlowSense E0 4M) with a resolution of 2048×2048 pixels. The cameras are installed on both sides of the laser sheet with an orientation of 30° with respect to the latter. To minimize the optical distortions, a transparent water box is mounted on the lateral wall. Its fixation is ensured by creating a partial vacuum, allowing for a simple positioning procedure. Two 60 mm lenses are used in combination with Scheimpflug mounts to align the focal plane with the laser sheet. The laser and the cameras are mounted on a joint support and moved to different downstream positions with a 2D traversing system.

Fluorescent and regular polyamide particles (20 μm average diameter) are used as seeding material. The out-of-plane velocity component is obtained by combining the 2D velocity fields derived for each camera. A third-order polynomial calibration ensures the conversion between the camera reference frame and the real physical dimensions. To this end, a 100×100 mm double-faced doted target (dots separated by 2.5 mm) is immersed in the test section and is imaged at several positions within the width of the laser sheet. The accuracy of the

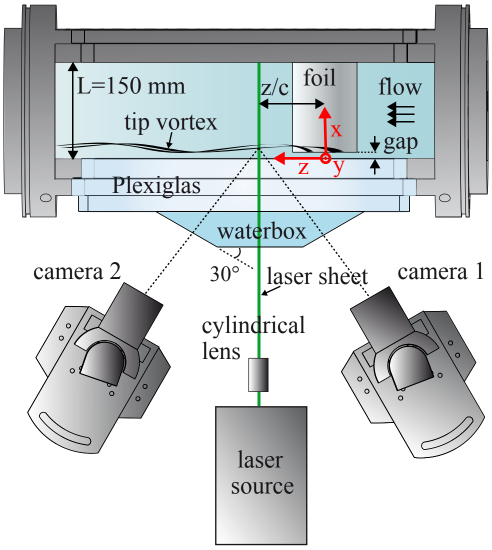
L=150 mm
z/c
foil
flow
tip vortex
x
gap
z
y
Plexiglas
waterbox
camera 2
30°
laser sheet
camera 1
cylindrical
lens
laser
source

(a) Top view of the tunnel test section and optical instruments

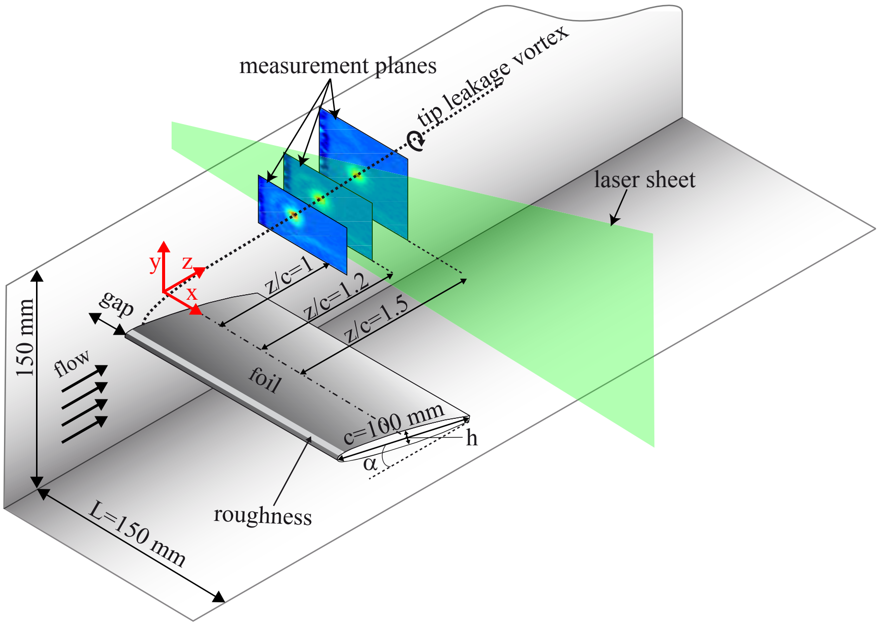
measurement planes
tip leakage vortex
laser sheet
y
z
x
gap
z/c=1
z/c=1.2
z/c=1.5
150 mm
flow
foil
c=100 mm
h
α
roughness
L=150 mm

(b) Isometric view of the inlet test section with the three measurement planes

Figure 5.1: Sketch of the SPIV configuration used in the 3D measurement of the velocity field.

calibration is verified by comparing the streamwise velocity profiles (corresponding to the out-of-plane component) measured by SPIV with the one measured by LDV, while no hydrofoil was mounted in the test section, see Figure 5.2. An excellent agreement in the velocity data outside the boundary-layer is observed. The mean values measured by the LDV near the wall seem however higher than the mean values obtained by PIV. This can be interpreted as the combination of two phenomena. First, as the LDV measurement volume has a length of about 1.3 mm, part of the measurement volume intersects with the test section wall in the boundary layer region, leading sometimes to inconsistent velocity signals. Secondly, the LDV measurements are performed at the position z/c= -1, i.e. upstream of the hydrofoil, whereas the PIV measurements are performed downstream of the hydrofoil. Different values of the boundary layer thickness are thus expected, as discussed in Section 5.6.5.

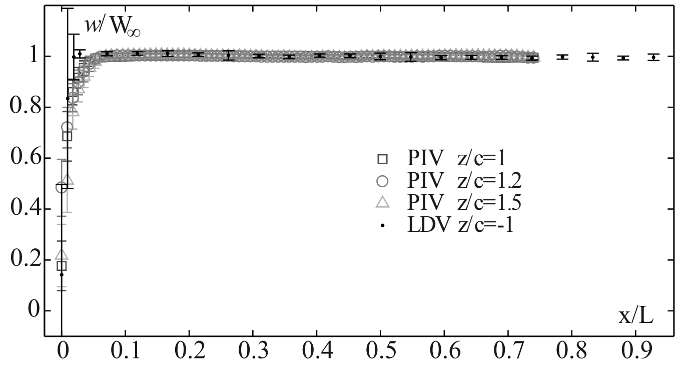

Figure 5.2: Comparison of the axial velocity profiles in the test section measured by PIV and LDV. No hydrofoil is mounted in the test section.

PIV post-processing

The velocity fields are derived by processing the acquired image pairs with an adaptive multi-pass correlation algorithm, which adjusts the size and shape of the each Interrogation Area (IA) with the local seeding densities and flow gradients [111, 121]. The commonly adopted criterion for the IA size is the presence of at least eight particles in each IA and a minimum of 16×16 pixels. A total of 182×120 velocity vectors with a spatial resolution of 0.6 mm is finally obtained. The distance from the wall to the first measured velocity vector is approximately 0.2 mm. The vector fields are validated with an universal outlier test and spurious vectors are replaced by the median value of the 5x5 neighboring vectors. The percentage of spurious vectors is typically around 5 %. Figure 5.3 shows a typical instantaneous velocity map for the two in-plane (u and v) velocity components. The TLV is easily identified as the dominating vortical structure but smaller vortices are also visible in the foil wake.

The measurement errors are estimated assuming a 0.1 pixel uncertainty on the measurement of particle displacements [119]. Since both cameras contribute symmetrically to the measurement, the in-plane errors are smaller by a factor $1/\sqrt{2}$ than the value for a single camera arrangement and the error of the out-of-plane component equals the in-plane error multiplied by $1/\tan(\phi)$ [94], where ϕ is the angle between the light sheet normal and the camera viewing direction. Given an average particle displacement of 5 pixels, the uncertainties are estimated to be 1.4 % for the in-plane components and 0.8 % for the out-of plane component. This is in accordance with Figure 5.2, which shows less than 1 % difference between the the axial velocity (out-of plane component) measured by LDV and PIV. The average velocity field is determined after processing 100 individual vector fields for each operating condition. It is verified that increasing this number does not affect the flow statistics. This is in line with the findings of Giuni [54], who noted in a similar case study that the statistical convergence of most of the quantities characterizing the tip vortex is achieved after processing a 100 PIV snapshots.

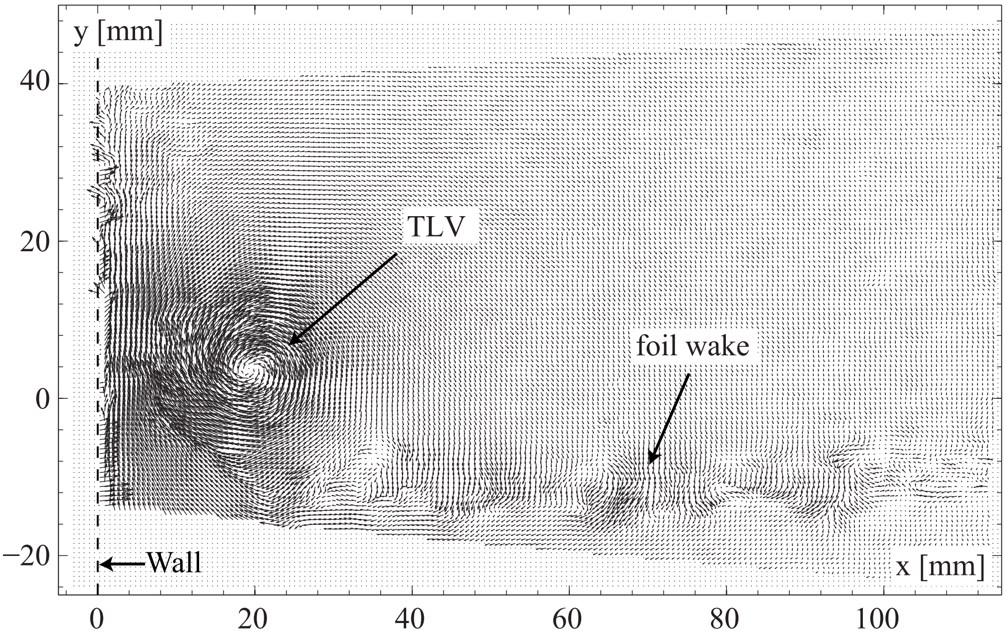

Figure 5.3: Example of an instantaneous velocity map over the complete common field of view of the SPIV cameras. The test section side wall is symbolized by the dashed line at x=0.

5.3 Methodology

5.3.1 Flow parameters

The velocity field is measured at three streamwise positions (z/c=1, 1.2 and 1.5) downstream of the hydrofoil in cavitation-free conditions. Measurements closer to the hydrofoil, i.e. at positions z/c<1, are not feasible because of the space required for the PIV cameras. At each position, five incidence angles (3°, 5°, 7°, 10°, 12°) are tested in combination with up to four inlet velocities (5, 10, 15 and 20 m/s). The Reynolds number based on the foil chord $Re_c = W_\infty c/\nu$ varies between 5×10^5 and 2×10^6. Additional incidence angles and inlet velocities are nevertheless tested at the position z/c=1, for a deeper analysis of the vortex evolution. It should be noted that the inlet velocity is limited by the occurrence of cavitation, which cannot be avoided at high incidence angles without exceeding the maximum admissible pressure in the test section. Therefore, the foil tip pressure side corner was rounded with a small radius of 1 mm, since this is known to limit the cavitation in the clearance region [74]. Obviously, such geometry alteration may have an influence on the vortex formation, as reported in different studies [56, 77]. To assess the potential effect of the rounded tip, additional measurements are performed at the position z/c=1.2 with a second hydrofoil featuring two sharp edges on the tip pressure and suction side corners. The first hydrofoil is hereafter designated as *rounded tip*, while the the second one is designated as *sharp tip*. Unless explicitly stated otherwise, all the results refer to the rounded tip hydrofoil. For each of these configurations, the tip clearance is varied between 0 and 20 mm, corresponding to a normalized tip clearance $\tau = gap/h$ between 0 and 2. Moreover, measurements are performed both with and without the turbulent boundary layer tripping on the hydrofoil leading edge. A total of 1,235 distinct configurations are investigated, as reported in Table 5.1.

Table 5.1: Operating configurations for the SPIV measurements

	$\alpha(°)$	W_∞(m/s)	z/c [-]	$\tau = gap/h$ [-]	surface roughness
Rounded tip					
	3	5, 10, 15, 20	1, 1.2, 1.5	0-2*	rough & smooth
	5	5, 10, 15, 20	1, 1.2, 1.5	0-2	rough & smooth
	7	5, 10, 15	1, 1.2, 1.5	0-2	rough & smooth
	10	5, 10	1, 1.2, 1.5	0-2	rough & smooth
	12	5, 10	1, 1.2, 1.5	0-2	rough & smooth
Sharp tip					
	3	10	1.2	0-2	rough
	5	10	1.2	0-2	rough
	7	10	1.2	0-2	rough
	10	10	1.2	0-2	rough
	12	10	1.2	0-2	rough

$^*\tau$=2, 1.5, 1, 0.7, 0.5, 0.4, 0.3, 0.2, 0.15, 0.1, 0.06, 0.03, 0

5.3.2 Vortex parameters extraction

The streamwise vorticity $\omega = \partial v/\partial x - \partial u/\partial y$ is computed by the numerical differentiation of the velocity field. To minimize bias errors and avoid any undesirable effect from the differentiation of a noisy field, the spatial sampling resolution is increased via a least-square cubic spline interpolation of the velocity. The derivatives are then estimated with a fourth-order Richardson numerical scheme, as described in Section 3.7.1.

The average vortex flow field is computed after filtering out the vortex wandering (cf. Section 3.7.2). The algorithm of Graftieaux et al. [58] is implemented to identify the instantaneous vortex center and align the velocity maps before averaging. To speed up the computations, the swirl center is sought in a small region centered on the vorticity peak that prevails near the TLV center. In general, the vortex center does not lie on a measurement grid node, and the realignment requires an interpolation of the measurement data. This is realized via the cubic spline interpolation of the velocity field mentioned above.

As discussed in Section 2.2.6, the prediction of the minimum pressure in the vortex center effectively reduces to the estimation of two key parameters, namely the vortex circulation Γ

and the viscous core radius r_c. The viscous core radius is estimated through a best fit of the Lamb-Oseen or the Vatistas model, over the average tangential velocity. The Vatistas model has the advantage of being more flexible, since it offers a wide range of velocity profiles with the help of the shape parameter n. The setting $n = 1$ reproduces the Scully vortex, whereas the case $n \approx 2$ gives a close approximation of the Lamb-Oseen model and $n \rightarrow \infty$ corresponds to the Rankine vortex, see Section 2.2.3. The model providing the best fit of the experimental data is retained to estimate the core size. Figure 5.4a illustrates a typical example of the best fit of the tangential velocity profile, which is accurately described by a Lamb-Oseen vortex in this case. In order to account for a possible asymmetry of the vortex, the circulation is not determined from a model fit but is rather calculated by integrating the vorticity contained within the TLV. In the case of a Lamb-Oseen vortex, only approximately 71 % of the total circulation is contained within the vortex core, while 99 % of the circulation is reached at a distance $2r_c$, as illustrated in Figure 5.4b. Hence, the circulation of the TLV is computed by integrating the vorticity encompassed in a disk of radius $2r_c$ centered on the vortex.

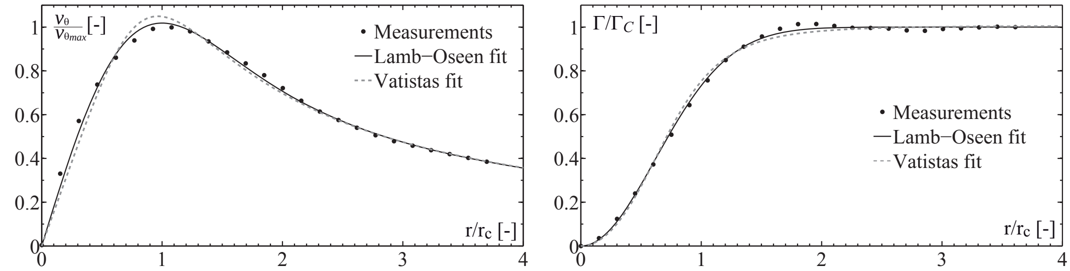

(a) Tangential velocity profiles

(b) Circulation distribution

Figure 5.4: (a) Average tangential velocity $v_\theta(r)$ derived from 100 vectors fields. The measured velocity profile is fitted with a Lamb-Oseen and a Vatistas (n=2) velocity profile. (b) Corresponding circulation distribution.

5.4 Flow visualizations

Cavitation is a convenient way to visualize the trajectory of vortices, as reported by Ausoni et al. [15]. A reduction of the static pressure in the test section leads to the vaporization within the vortex core, which makes it visible. However, this is not a strictly passive means of flow visualization, as vapor can completely fill the vortex core, leading to vorticity redistribution and possible alterations of the flow dynamics, as discussed in Chapter 4. Nevertheless, if the vaporous core represents only a small fraction of the non-cavitating vortex viscous core, it was shown that the average flow field outside of the cavity is very close to the cavitation-free regime.

Figure 5.5 illustrates the cavitating TLV obtained at two different inlet pressures and highlights the topology of the clearance flow. The inlet velocity is 10 m/s, the incidence angle is 10° and the normalized tip clearance is $\tau = 1$. At $p_\infty = 1$ bar, the cavitation indicates that the

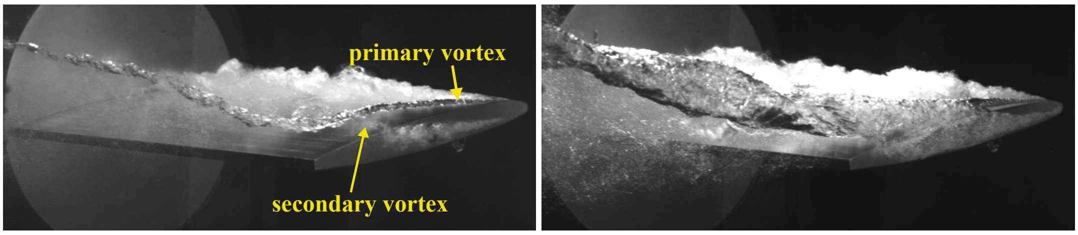

(a) p_∞=1 bar (b) p_∞=0.7 bar

Figure 5.5: Side view of the cavitating TLV generated by a *NACA 0009* at different p_∞. Flow conditions: W_∞=10 m/s, α=10°, τ=1.

TLV is formed by an intense primary vortex that originates near the foil leading edge, while a weaker secondary vortex that merges with the primary vortex can be distinguished near the trailing edge. Secondary vortices arise from the flow separation in the clearance that produces a multitude of vortex filaments that roll up into the TLV [54, 86]. This phenomenon becomes clearly visible when the pressure is further decreased, as shown in Figure 5.5b where a cavitating vortex sheet that wraps around the TLV is apparent. Downstream of the hydrofoil, the substantial amount of cavitation also changes the TLV into a large cavitating helical structure, which seems to be the result of two merging vortices. No evidence of a secondary vortex could however be seen in the cavitation-free SPIV measurements one chord downstream of the hydrofoil.

The effect of the gap width on the cavitating TLV is illustrated in Figure 5.6 and 5.7. The inlet velocity is 10 m/s, the incidence angle is 10° and p_∞ is kept to 1 bar for all clearances. The left column depicts an instantaneous realization of the TLV flow, extracted from the high-speed visualizations, while the right column represents the summation of all the images captured during 11 ms at 20,000 FPS, in order to assess the mean TLV trajectory. The scattering of the cavitation bubbles in the vortex core unveils the wandering amplitude, which is quite small in these cases. Moreover, comparisons with the TLV position in cavitation free regime, obtained by SPIV and represented by the yellow crosses in Figure 5.6 and 5.7, indicate that neither the vortex trajectory nor the wandering amplitude are altered by the cavitation.

The trajectory of the TLV strongly depends on the clearance size: the smaller the gap, the more the vortex is pulled away from the hydrofoil. This is due to a purely potential effect and can be understood through the consideration of a simple model consisting of a 2D vortex above a wall, as explained by Doligalski et al. [39] and sketched in Figure 5.8b. To ensure zero flow across the wall, an image vortex is placed symmetrically to the actual TLV with respect to the confinement wall. This image vortex induces an upward velocity on the actual vortex. Another feature is the change in slope of the vortex trajectory at the foil trailing edge. This is particularly visible if the TLV remains relatively close to the foil along the chord, i.e. at large clearance values like τ=2. Again, this phenomenon can be explained with reference to the image system of the tip clearance flow. Over the foil, one must consider three images of the TLV to satisfy the relevant kinematic constraints, as reported by Chen et al. [28] and sketched in Figure 5.8a.

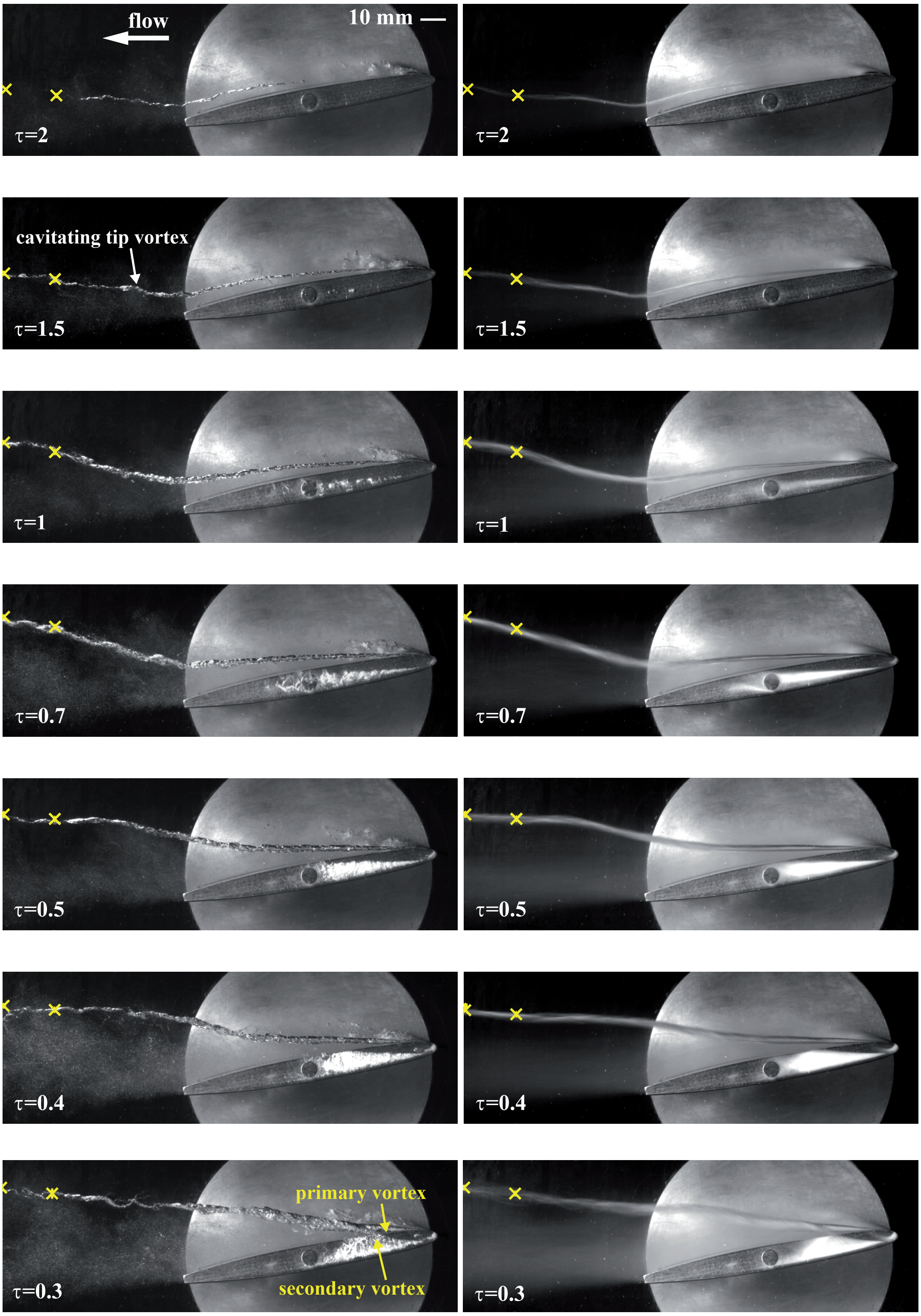
flow
10 mm
τ=2
τ=2
cavitating tip vortex
τ=1.5
τ=1.5
τ=1
τ=1
τ=0.7
τ=0.7
τ=0.5
τ=0.5
τ=0.4
τ=0.4
primary vortex
secondary vortex
τ=0.3
τ=0.3

(a) Instantaneous (b) Average

Figure 5.6: See caption in Figure 5.7

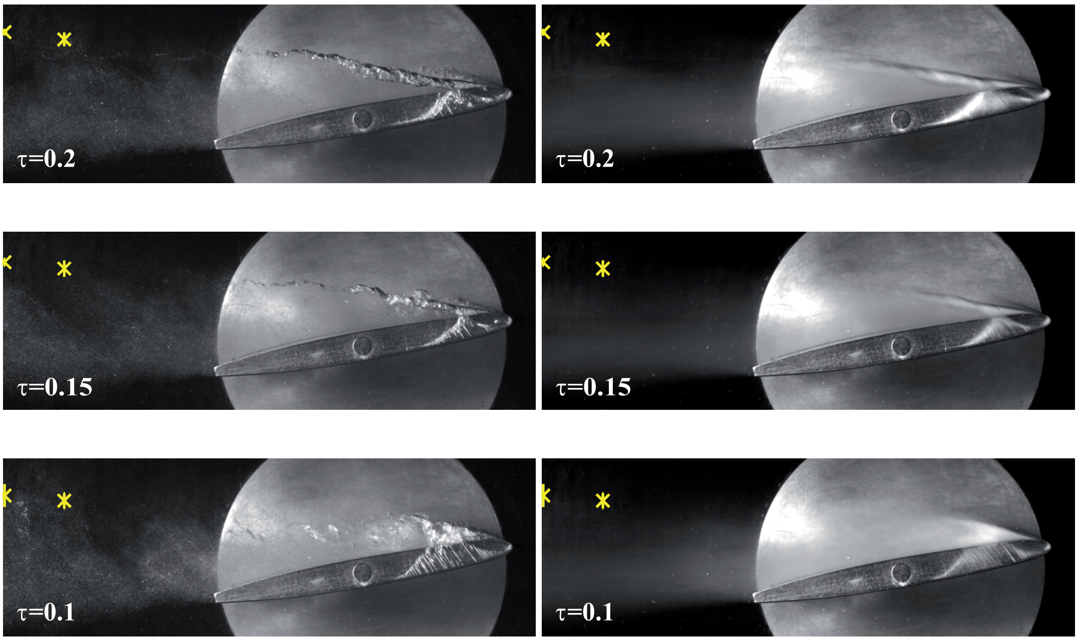
τ=0.2
τ=0.2
τ=0.15
τ=0.15
τ=0.1
τ=0.1

(a) Instantaneous

(b) Average

Figure 5.7: (a) Snapshots of the cavitating TLV generated by a *NACA 0009* for different gap widths. The tip clearance is viewed from the side and is facing the observer. (b) Average TLV trajectory obtained from the superposition of the visualizations during 11 ms. The yellow crosses represent the position measured by SPIV in cavitation-free regime, in the planes z/c=1 and z/c=1.2. Flow conditions: W_{∞}=10 m/s, α=10°, p_{∞}=1 bar.

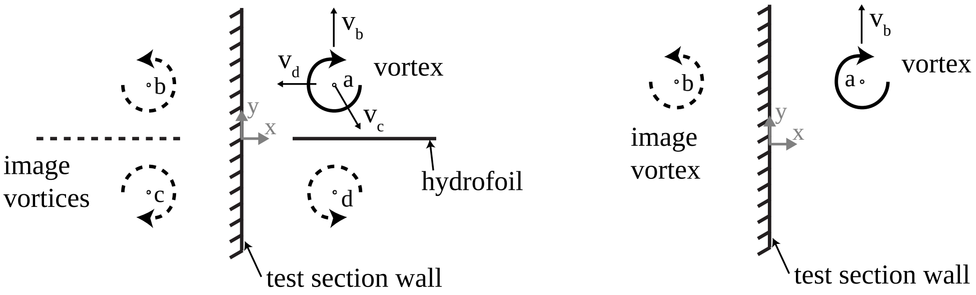
V_b
V_d
vortex
a
b
V_c
y
x
image
vortices
c
d
hydrofoil
test section wall
V_b
vortex
a
b
image
vortex
y
x
test section wall

(a) Over the hydrofoil

(b) Downstream of the hydrofoil

Figure 5.8: Vortex image system over and downstream of the hydrofoil according to potential flow theory [28]. The vortices b, c and d are the images of the actual vortex denoted by a. The induced velocities resulting from the image vortices b, c and d are sketched.

Two of the image vortices induce vertical velocities on the actual vortex that partially cancel out. After the blade, there is only one image vortex needed to satisfy the boundary conditions, and the resulting induced upward velocity is thus larger.

The amount of cavitation in the vortex core reveals the changes of the vortex strength along the chord. As the clearance is reduced, the cavitation becomes more intense and the vortex is less coherent. For the most confined configuration, the vortex rapidly loses its coherence until practically vanishing, indicating a vorticity redistribution, as seen in Figure 5.7. Cavitation in the clearance region indicates that the gap flow turns into a vertical wall jet as the gap is reduced, entraining vorticity filaments into the TLV. In the cases τ=0.3 and 0.2, the merging of a primary vortex, originating at the leading edge, and a secondary vortex that develops in the clearance is visible. Flow visualizations at low inlet pressure showed that the secondary vortex exists for all clearances. However, as it is weaker than the primary vortex, the secondary vortex is not visible in Figure 5.6 for large clearances. The secondary and primary vortices systematically merge together and the merging location moves towards the foil leading edge as the clearance is reduced.

5.5 TLV characteristics

The TLV is formed by the rolling up of the vorticity transported by the leakage flow, which is driven by the pressure gradient across the clearance. Its characteristics depend on the foil incidence angle, the inlet velocity and the wall proximity. This section investigates the evolution of the mean TLV characteristics for a fixed normalized clearance τ=1.5. This clearance allows to study the TLV structure without an excessive influence of the wall. Unless explicitly stated otherwise, all the results are the average values of the flow.

5.5.1 Incidence angle and Reynolds number effects

The evolution of the vortex circulation Γ with the incidence is plotted in Figure 5.9 for the smooth and rough hydrofoils. The circulation increases monotonically with the hydrofoil incidence angle. This behavior is expected, since the vortex circulation Γ is proportional to the foil bound circulation Γ_0, which is linked to the lift coefficient C_L according to the

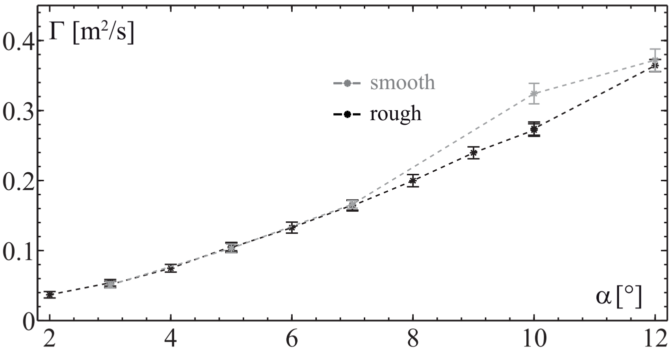

Figure 5.9: Evolution of the TLV circulation with incidence for the rough and smooth hydrofoil, W_∞= 10 m/s, τ=1.5, z/c=1.

Kutta-Joukowski theorem ($\Gamma_0 = 0.5 c W_\infty C_L$). The vortex circulation follows therefore the linear dependence of the lift coefficient with the incidence angle. Rough and smooth hydrofoils generate a nearly equal vortex circulation while the standard deviation increases steadily with the vortex intensity. However, the viscous core radius is larger with the rough foil, as reported in Table 5.2 for the incidence α=7°. Indeed, McCormick [85] observed that the viscous core radius is related to the thickness of the boundary layer on the pressure side surface near the foil tip, which is larger when the turbulent boundary layer is tripped.

Figure 5.10 show the vorticity maps with 2D streamlines for four incidences (3°, 5°, 7° and 10°) in a region of 50×50 mm surrounding the TLV generated by the rough hydrofoil. It can be observed that the vorticity is concentrated around the vortex axis, within the viscous core,

Table 5.2: Vortex core size for W_∞=10 m/s, α=7°, τ=1.5, z/c=1

surface roughness	core size [mm]	circulation [m^2/s]
smooth	3.8	0.166
rough	4.2	0.168

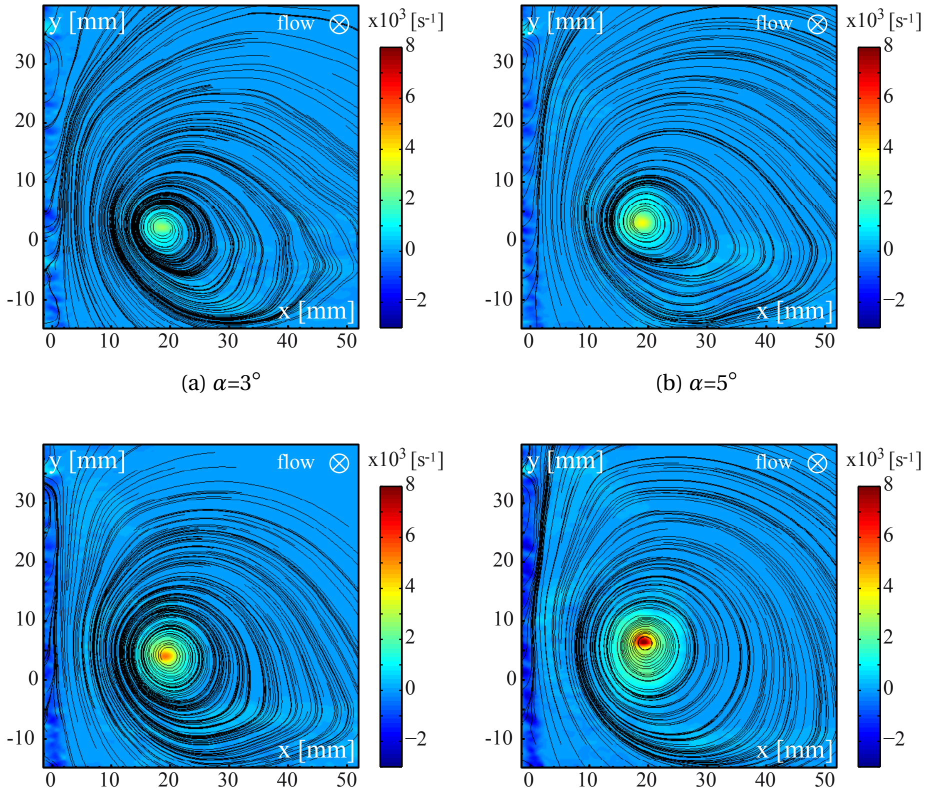

(a) α=3°

(b) α=5°

(c) α=7°

(d) α=10°

Figure 5.10: Streamlines and norm of the streamwise vorticity, rough hydrofoil, W_∞= 10 m/s, τ=1.5, z/c=1.

while the flow outside of it is almost irrotational. Small structures with negative vorticity are nonetheless produced in the boundary layer on the test section wall. The streamlines indicate that the vortex is not perfectly axisymmetric. The reason for this is twofold. Firstly, the test section wall alters the vortex symmetry by channeling the flow in the clearance. Secondly, the PIV measurement plane may be not perfectly orthogonal to the vortex axis, as visible in Figure 5.6. The inclination angles between the measurement plane and the vortex can be identified following a procedure similar to the one reported in [112], see Appendix A.1. The velocity fields can then be projected into the vortex coordinate system. However, it was observed that the vortex properties (circulation and viscous core radius) vary less than 1 % due to the vortex axis inclination. Consequently, and given that the identification of the inclination angles is subject to uncertainty, the analysis of the TLV is performed in the measurement plane reference frame.

The influence of the Re number is investigated by varying the inlet velocity with the fixed incidence α=5°. The evolution of the TLV circulation is illustrated in Figure 5.11. As predicted by the Kutta-Joukowski theorem, the vortex circulation follows a linear trend with the inlet velocity. Once again, smooth and rough hydrofoils generate a similar vortex circulation while the standard deviation increases with the vortex intensity. Furthermore, it was observed that an increase of the inlet velocity does not greatly influence the TLV structure or position.

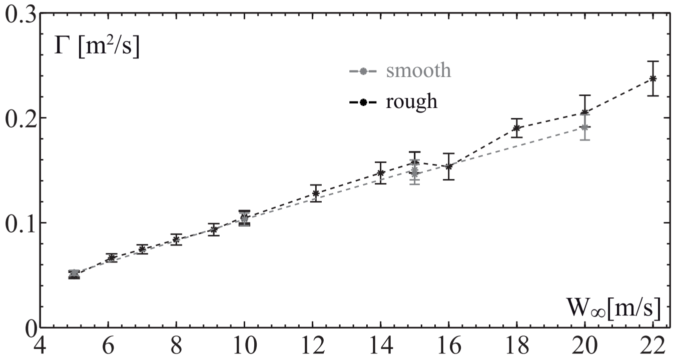

Figure 5.11: Evolution of the TLV circulation with the inlet velocity for the rough and smooth hydrofoils, α=5°, τ=1.5, z/c=1.

5.5.2 TLV axial flow

The evolution of the axial velocity in the vortex center with the incidence angle is represented in Figure 5.12. The results are normalized by the inlet velocity W_∞. It is observed that if the TLV features a velocity deficit at low incidence angles, the axial velocity in the vortex core increases monotonically with the incidence angle. As a consequence, the axial flow in the vortex core features a switchover angle for which it changes from wake-like to jet-like flow. Moreover, the axial velocity of the TLV generated by the smooth hydrofoil is systematically slightly higher than for the rough hydrofoil.

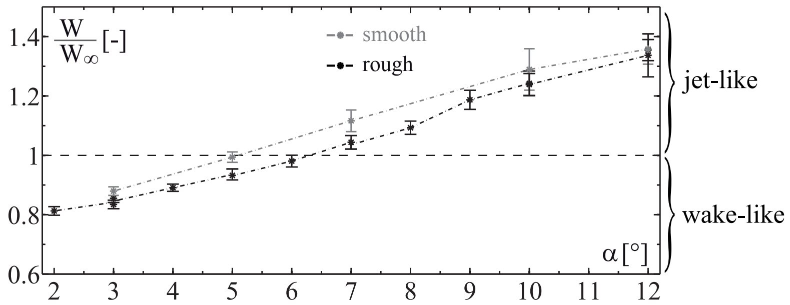

Figure 5.12: Axial velocity in the vortex center vs incidence angle for both the rough and smooth hydrofoils. W_∞=10 m/s, τ=1.5, z/c=1

The isocontours of the axial flow for the rough hydrofoil at four incidence angles (3°, 5°, 7° and 10°) are shown in Figure 5.13. The wall boundary-layer can be seen on the left-hand side of the subfigures, while the wake of the hydrofoil is visible as a horizontal region with a velocity deficit. The TLV tends to roll up the fluid layers in its vicinity, entraining the hydrofoil wake and resulting in a complex axial velocity field. Hence, a region with a deficit of velocity surrounds the TLV at 3° incidence, while for the 10° incidence, the vortex core axial flow is in contrast faster than the surrounding flow, despite the rolling up of the foil wake around its center. Moreover, the clockwise rotation of the TLV leads to an entrainment of the wall boundary-layer into the bulk flow. This phenomenon is all the more pronounced as the vortex intensity is high. Lee et al. [77] have reported that a jet-like axial flow is always present during the vortex formation but that interactions with the foil wake and shear layer are likely to change a jet-like axial flow to a wake-like axial flow for small incidence angles. For large incidence angles, they noticed that the vortex is surrounded by a shear layer, protecting it from outside disturbances. This roll up of the shear layer around the TLV is also observed in the present experiment, although additional measurements in the vortex formation region, i.e. over the hydrofoil, would be necessary to confirm their observations.

The nature of the axial flow can once again be interpreted in the light of Batchelor's eq. (4.3), which expresses the balance between an inviscid effect, which tends to accelerate the flow, and the momentum defect, originating from the rolling up of the foil boundary layer into the vortex core and resulting in a velocity deficit. With the assumption of constant dissipation and vortex core radius, Batchelor's equation states that an increase of the overall circulation results in a higher axial velocity in the vortex core. Given that the smooth foil generates a vortex with a smaller viscous core than the rough foil but a similar circulation (cf. Table. 5.2), a higher axial velocity is expected, explaining the trends in Figure 5.12. This is coherent with the fact that the switchover angle occurs around 5° for the smooth foil, compared to 6° for the rough foil.

For a better representation of the velocity field, Figure 5.14 illustrates the 3D streamlines with some fictive tracing particles for four different incidence angles (3°, 5°, 7° and 10°) at W_∞=10 m/s. Twenty-five streamlines are initiated in the measurement plane z/c=1 on a vertical line. Since the TLV properties vary little with the downstream distance, the velocity field is interpolated linearly between the three measurement planes. The pitch in the helix formed by

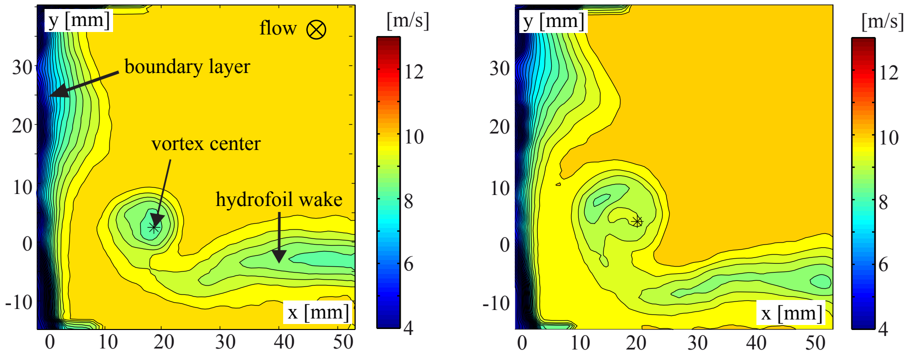

(a) α=3°

(b) α=5°

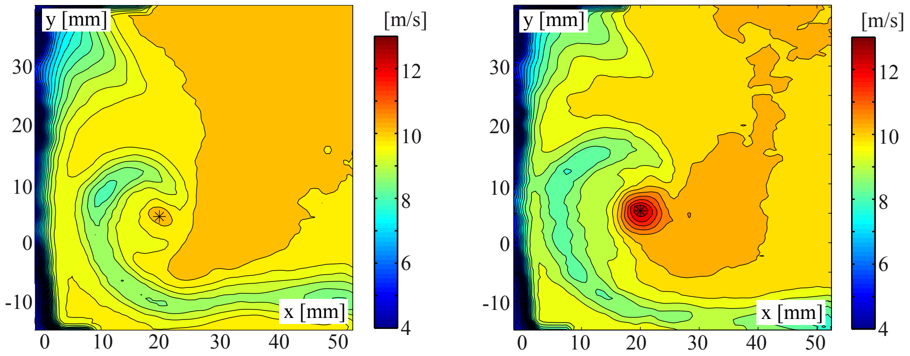

(c) α=7°

(d) α=10°

Figure 5.13: Isocontours of the axial flow, rough hydrofoil, W_∞= 10 m/s, τ=1.5, z/c=1.

the streamlines illustrates the vortex swirl number, i.e. the ratio between the circumferential and axial velocities. Higher incidence angles produce higher swirl in the flow. The tracing particles highlight the vortex core axial flow. Hence, for the 3° incidence angle in Figure 5.14a, the particles in the vortex center are following behind the outside particles due to the wake-like flow. For the 5° incidence angle in Figure 5.14b, the core axial velocity is almost the same as the inlet velocity and the particles stay in the same plane as they coil around the vortex. In contrast, for the 10° incidence angle in Figure 5.14d, the vortex core has a strong jet-like flow that deforms helically the pattern formed by the particles as they roll up into the vortex.

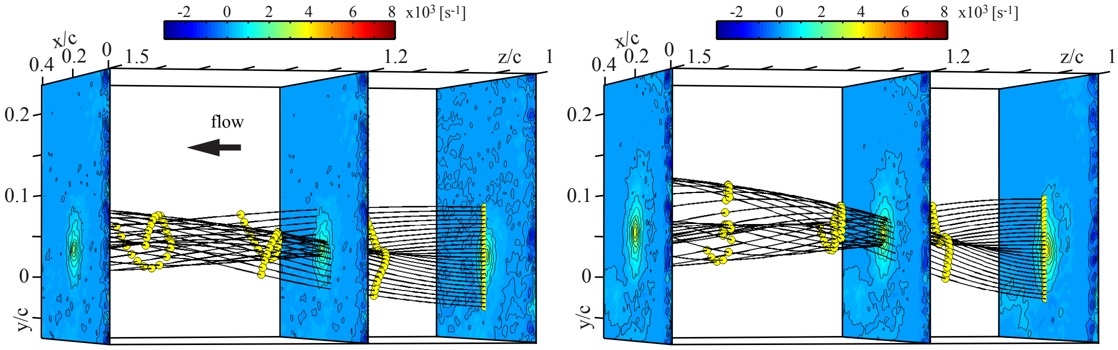

(a) α=3°

(b) α=5°

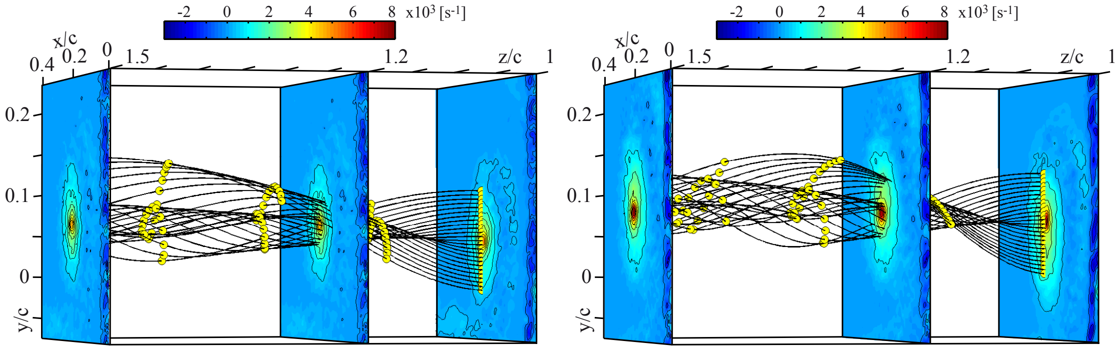

(c) α=7°

(d) α=10°

Figure 5.14: 3D streamlines with tracing particles in yellow showing the development of the TLV along the three measurement planes. The colors in the three measurement planes show the norm of the streamwise vorticity. Flow conditions: W_∞=10 m/s, τ=1.5, rough hydrofoil.

5.5.3 Influence of the tip geometry

The results presented so far were all obtained with the hydrofoil having the pressure side corner rounded with a 1 mm radius. In order to asses the potential effect of the tip geometry on the TLV as it evolves downstream of the hydrofoil, additional flow visualizations and SPIV measurements at the location z/c=1.2 are performed with a sharp tip hydrofoil. Figure 5.15 shows a comparison of the cavitating TLV for the rounded and sharp tip geometries at W_∞=15 m/s, α=5°, p_∞=0.9 bar and τ=0.5. It can be observed that the clearance cavitation is more pronounced for the sharp tip. The separation of the leakage flow is forced by the sharp edge, resulting into an increase of the number of vorticity filaments that merge with the primary vortex [56].

The evolution of the TLV circulation and core axial velocity with the foil incidence angle for the rounded tip and sharp tip hydrofoils is displayed in Figure 5.16. The data are obtained by SPIV in cavitation-free conditions at the normalized tip clearance τ=1.5 and the inlet velocity W_∞= 10 m/s. It can be observed that the sharp tip hydrofoil generates a TLV with an identical

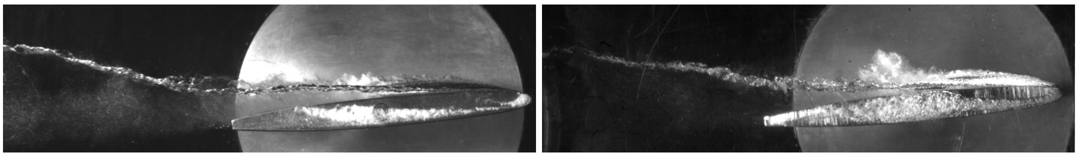
(a) Rounded tip (b) Sharp tip

Figure 5.15: Cavitating TLV generated by a *NACA 0009* for the rounded tip and sharp tip geometry. Flow conditions: W_∞=15 m/s, α=5°, p_∞=0.9 bar, τ=0.5.

circulation compared with the rounded tip hydrofoil. However, the axial velocity in the vortex core is slightly lower for the sharp tip hydrofoil compared with the rounded one. By referring to eq. (4.3) according to Batchelor, this implies that the sharp tip generates either higher losses ΔH and/or a vortex that is less concentrated than the one generated with the rounded tip.

The structure of the TLV generated by the rounded tip and sharp tip is presented in Figure 5.17 for the conditions W_∞= 10 m/s, α=7° and τ=1.5 at the measurement location z/c=1.2. The norm of the streamwise vorticity along with a number of streamlines is represented in the two subfigures at the top, while the two subfigures at the bottom display the average axial velocity contours. Both tip geometries produce a very similar TLV structure despite the multiple vorticity filaments produced by the sharp tip in the clearance region (cf. Figure 5.15). At the measurement location z/c=1.2, the merging of secondary vortical structures into the primary vortex is already completed and all the vorticity is concentrated in the vortex core. However, the sharp tip generates a slightly more diffuse vorticity distribution than the rounded tip. The axial flow maps are also very similar for the rounded tip and sharp tip. The wake sheet is clearly visible as a horizontal region of axial velocity deficit that rolls up around the TLV. For the rounded tip, a small region of axial velocity excess is visible near the vortex center. A local increase of the axial velocity around the center of the TLV is also visible for the sharp tip, but the maximal axial velocity remains lower than the free stream velocity.

In summary, while the tip geometry certainly affects the TLV structure in the early wake, at the location of the SPIV measurements the TLVs generated by the rounded tip and sharp tip are very similar and behave analogously. Larger differences are however expected, especially for the axial flow, if the rounding of the tip is more pronounced, as already reported by Giuni et al. [56] and Lee et al. [77].

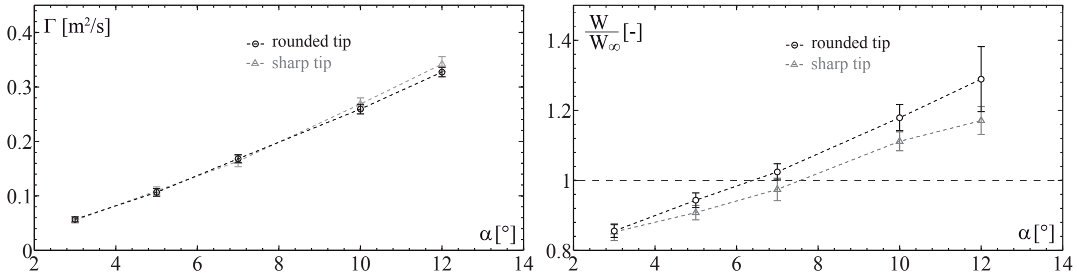

(a) Circulation

(b) Axial velocity

Figure 5.16: Evolution of the circulation and axial velocity vs incidence angle for the rounded tip and sharp tip hydrofoils. W_∞= 10 m/s, τ=1.5, z/c=1.2

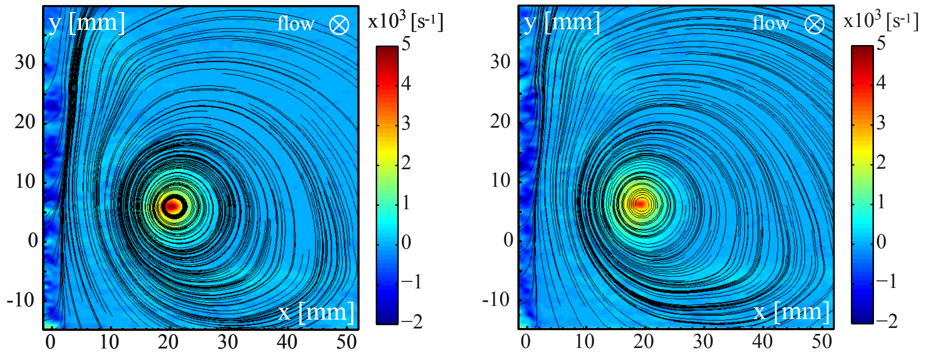

(a) Vorticity, rounded tip

(b) Vorticity, sharp tip

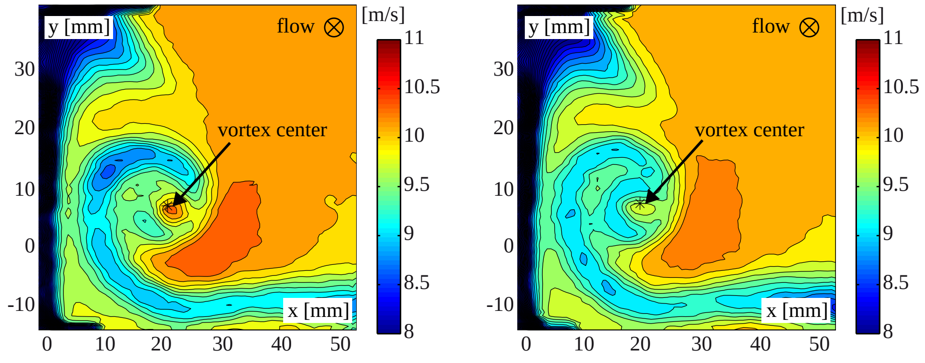

(c) Axial flow, rounded tip

(d) Axial flow, sharp tip

Figure 5.17: Comparison of the TLV generated by the rounded tip and sharp tip hydrofoils at W_∞= 10 m/s, α=7°, τ=1.5 and z/c=1.2. Top: streamlines and norm of the streamwise vorticity. Bottom: isocontours of the axial flow velocity.

5.6 TLV evolution with gap width

As the tip clearance is reduced, the characteristics of the TLV described in the previous section vary significantly. The main effects of the confinement are reported through changes in the vortex intensity, the core axial flow, the vortex center position and the wandering motion amplitude.

5.6.1 TLV intensity evolution

The main effects of the confinement on the vortex circulation are summarized in Figure 5.18. The figure is separated into four subplots, corresponding to the rough and smooth hydrofoils, at the downstream measurement locations z/c=1 and z/c=1.2. The evolution is depicted for the combination of the four inlet velocities (v=5, 10, 15 and 20 m/s) with four incidence angles (α =3, 5, 7, 10°). As discussed in Section 2.2.6, the pressure drop in a tip vortex is governed by the dimensionless circulation Γ^*, defined as the vortex circulation Γ divided by the viscous core radius r_c and the inlet velocity W_∞. The results are thus presented in terms of Γ^*, which merges the data into four groups according to their incidence angles, independently of their respective inlet velocity.

The evolution of Γ^* with the confinement is similar for all incidence angles and the existence of a specific gap width for which the vortex intensity reaches its maximum is clearly revealed. The

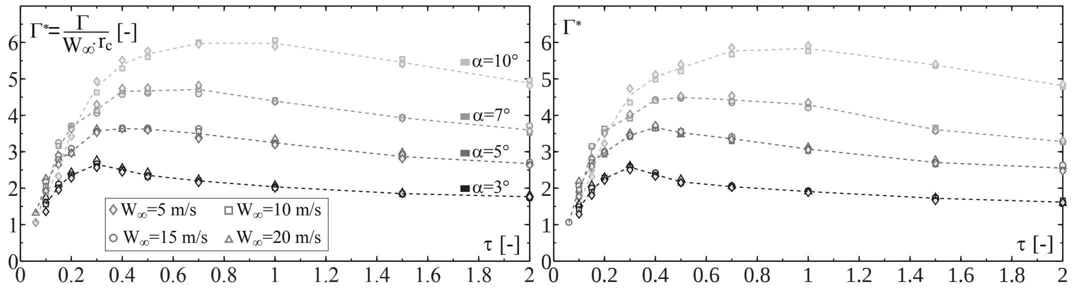

(a) Rough hydrofoil, z/c=1

(b) Rough hydrofoil, z/c=1.2

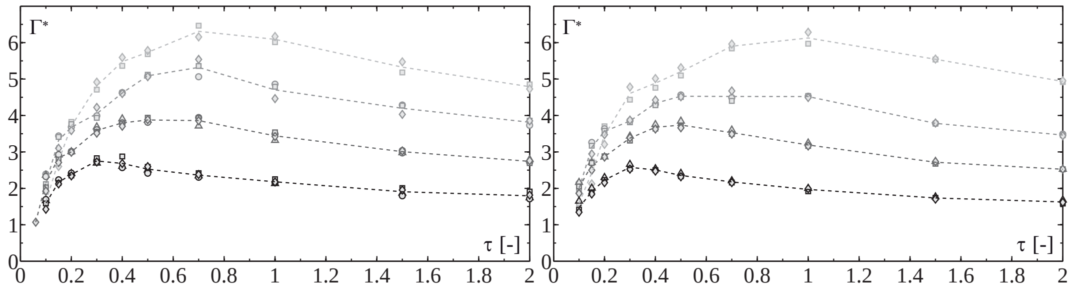

(c) Smooth hydrofoil, z/c=1

(d) Smooth hydrofoil, z/c=1.2

Figure 5.18: Evolution of the normalized circulation Γ^* with the normalized clearance τ. The dashed lines are the mean values for each incidence angle.

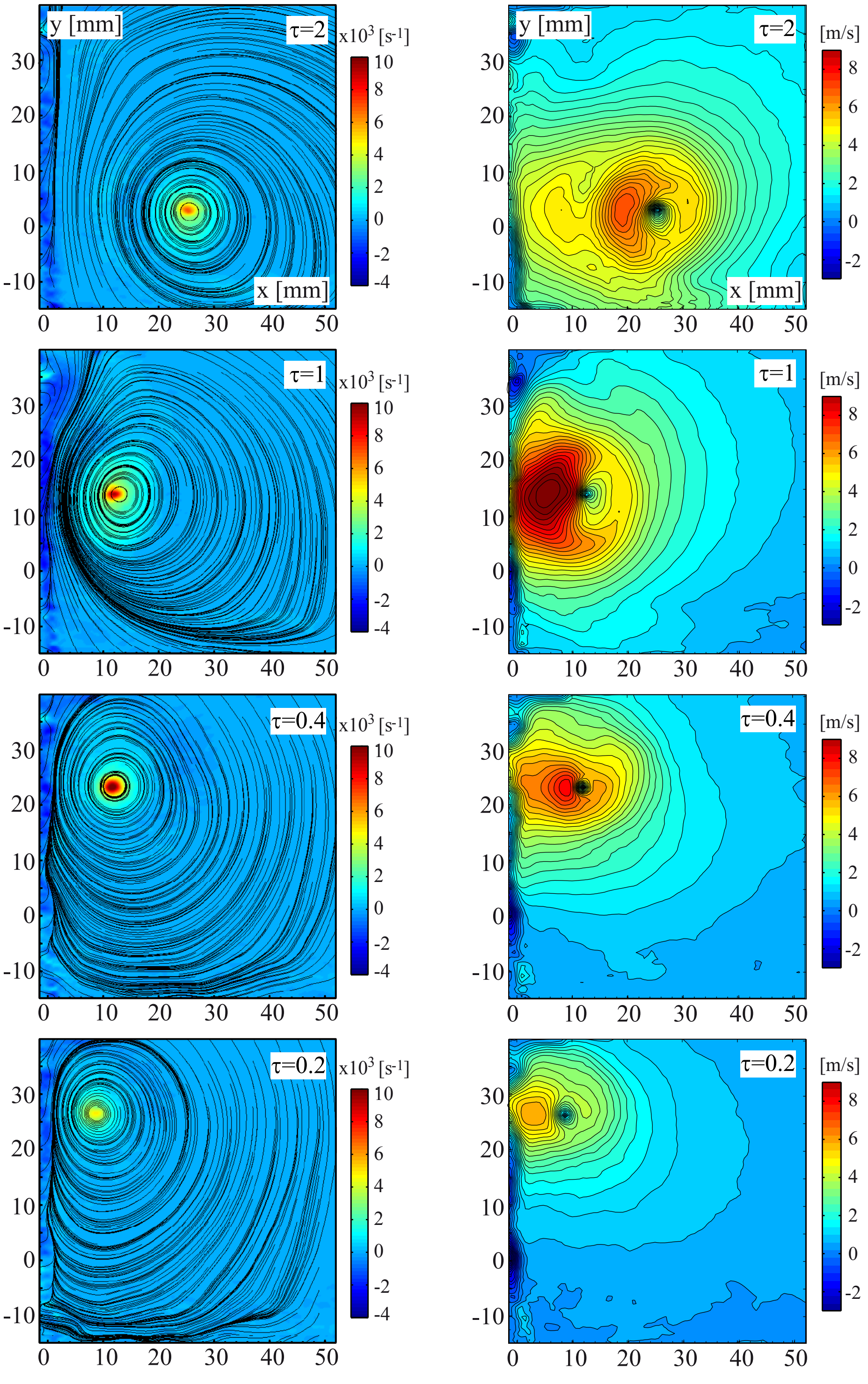

(a) Streamlines and vorticity (b) Circumferential velocity

Figure 5.19: 2D streamlines of the TLV with the norm of the streamwise vorticity (a) and isocontours of circumferential velocity (b) for various gap widths. Flow conditions: W_∞=10 m/s, α=10°, z/c=1, rough hydrofoil.

value of this specific gap width depends on the incidence angle. For instance, the maximum vortex intensity is obtained for a specific τ value of about 0.3, 0.4 and 0.5 for incidence angles of 3°, 5° and 7°, respectively. For the 10° incidence angle, the maximum value of Γ^* is reached for τ between 0.7 and 1, depending on the measurement location. Below those clearances, the vortex strength drops abruptly, whereas above them, it decreases slowly towards an asymptotic value for which the influence of the wall becomes negligible. The limit gap width for which the influence of the wall vanishes depends on the foil incidence angle. For instance, this condition is seemingly not yet reached for the 10° incidence angle at τ=2, since the vortex intensity seems to further decrease at higher clearances, as illustrated in Figure 5.18a. For the 3° incidence angle on the other hand, the asymptotic value is already reached at τ=1.5. This denotes a stronger vortex-wall interaction at high incidence angles. Finally, the evolution of the circulation for the 10° incidence angle is in agreement with the development of cavitation in the TLV as the confinement increases, as illustrated in Figures 5.6 and 5.7.

Figure 5.19a displays the vorticity map and the 2D streamlines for four different clearances, at an incidence angle of 10° and an inlet velocity of W_∞=10 m/s. Each subfigure represents an area of 50 × 50 mm surrounding the vortex. Outside the vortex core, the flow is irrotational except for the wall boundary layer region. For the τ=1 case, the leakage vortex induces flow separation on the test section wall, as visible on the upper left of the subfigure. The wall boundary layer with its negative vorticity is entrained by the nearby TLV, as also reported by Miorini et al. [86]. As the gap is reduced, the TLV is influenced by the neighboring wall and starts to migrate upward. The squeezing of the streamlines between the vortex center and the wall suggests a higher flow rate in this region. The inclination angle between the vortex axis and the measurement plane results in an apparent vortex asymmetry, as illustrated in Figure 5.19b, with the isocontours of the circumferential velocity around the TLV axis. The contours depict a crescent-shaped region of high circumferential velocity between the wall and the TLV center, particularly visible in the case of τ=1. As a consequence, the location of the maximum vorticity does not correspond exactly to the vortex swirl center of rotation. In contrast, the algorithm of Graftieaux [58] used for the identification of the vortex center (c.f. Section 3.7.2) is nearly unaffected by the vortex asymmetry.

5.6.2 Gap width influence on the TLV axial flow

The evolution of the axial velocity in the vortex core as a function of the normalized clearance τ is represented in Figure 5.20 with four subplots, corresponding to the rough and smooth hydrofoils at the measurement locations z/c=1 and z/c=1.2. Each subplot includes the axial velocity obtained with the incidence angles 3°, 5°, 7° and 10° at all the tested inlet velocities. The data are represented by the dimensionless ratio W/W_∞. Values smaller than one correspond to a wake-like profile, while values greater than one correspond to a jet-like behavior. Each incidence angle features a similar evolution of the core axial flow, with an increase in the first stage of the clearance reduction followed by an abrupt decline in the velocity magnitude in highly confined situations. For instance, the 5° incidence features a small axial velocity

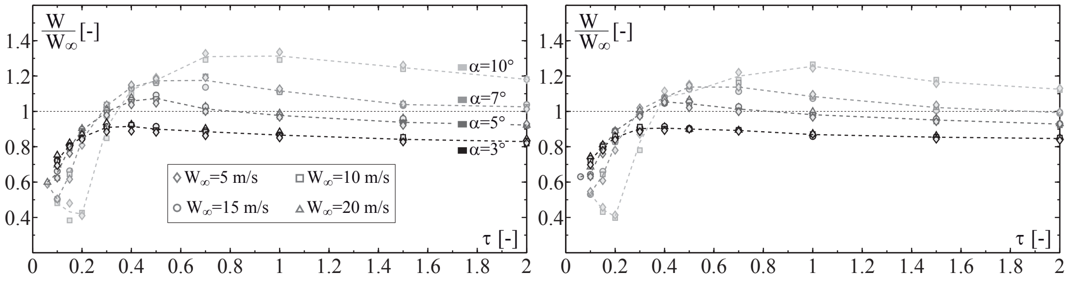

(a) Rough hydrofoil, z/c=1

(b) Rough hydrofoil, z/c=1.2

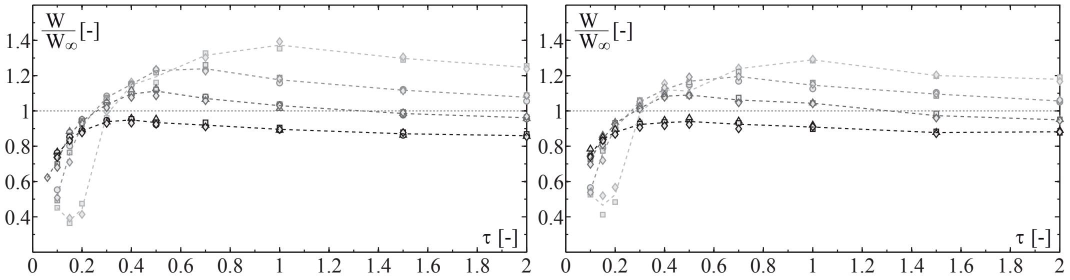

(c) Smooth hydrofoil, z/c=1

(d) Smooth hydrofoil, z/c=1.2

Figure 5.20: Evolution of axial velocity in the vortex core, normalized by the inlet velocity, with the normalized clearance τ. The dashed lines are the mean values for each incidence angle.

deficit at τ=2 which turns into a jet-like profile at τ=0.7 before resuming a wake-like profile at τ=0.3. As previously explained in Section 5.5.2, the vortex core axial flow is the resulting balance between an inviscid flow effect, which is linked to the vortex intensity and tends to accelerate the core flow, and the momentum deficit in the boundary layer that rolls up into the vortex core. It thus comes as no surprise that the evolution of the axial velocity follows the change of vortex intensity shown in Figure 5.18.

Figure 5.21 depicts the isocontours of the axial velocity for the 10° incidence at W_∞=10 m/s and illustrates the velocity evolution as the gap is reduced. The test section wall boundary layer is clearly visible on the left-hand side at $x = 0$ mm. With large clearance values, the TLV is surrounded by the foil wake that rolls up around the vortex axis. The velocity in the vortex center is a jet-like profile with a peak velocity 20 % higher than the inlet velocity. The vortex strength increases slightly as the clearance is reduced to τ=1 and the region in the TLV center with a velocity excess broadens, while the foil wake is squeezed between the wall boundary layer and the vortex center. At τ=0.4, the vortex starts to interact with the wall boundary-layer and a region of lower than the free stream velocity completely surrounds the TLV. A small region of high axial velocity remains nevertheless visible at the vortex center. The interaction with the wall boundary-layer escalates with the confinement, resulting in a large region of velocity deficit around the vortex at τ=0.3. At τ=0.2, the vortex intensity becomes very low and the momentum defects in the boundary layer overcome the core flow acceleration predicted by inviscid-flow theory. Consequently, a large wake-like region is present in the vortex core.

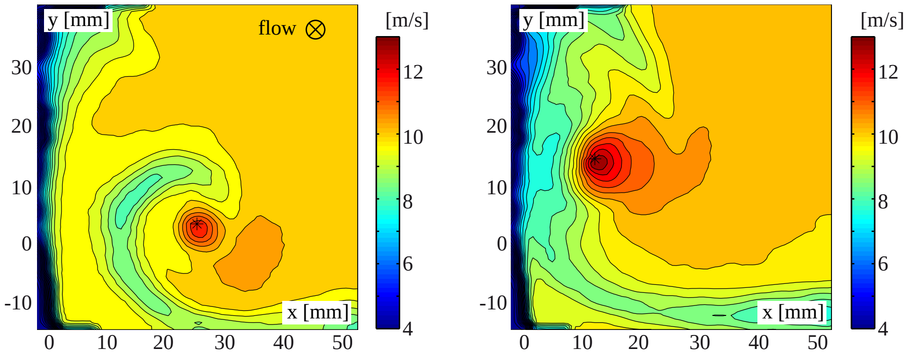

(a) τ=2 (b) τ=1

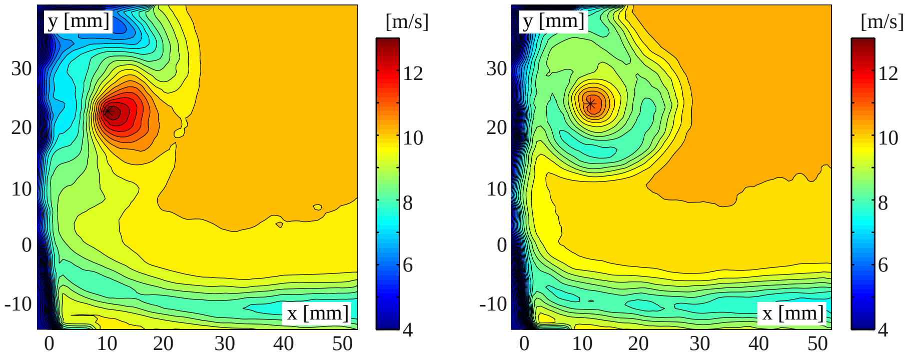

(c) τ=0.7 (d) τ=0.4

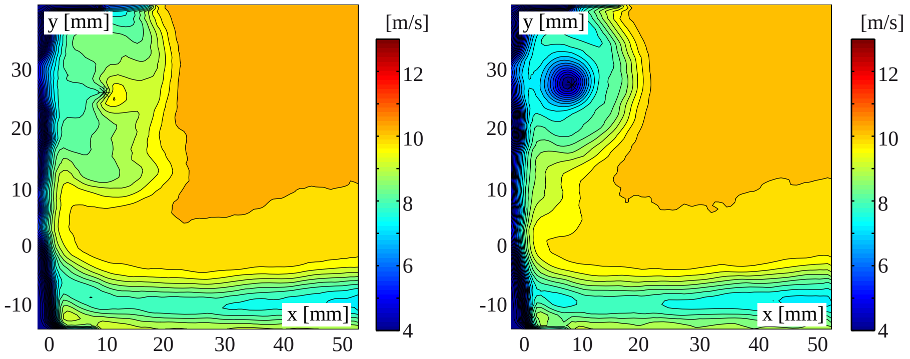

(e) τ=0.3 (f) τ=0.2

Figure 5.21: Isocontours of the axial velocity for different gap widths. Flow conditions: W_∞=10 m/s, α=10°, z/c=1, rough hydrofoil.

5.6.3 TLV position and wandering

As already pointed out in Section 5.4, the vortex trajectory is strongly influenced by the wall proximity. The position of the vortex center according to the SPIV measurements is shown in Figures 5.22a and 5.22b with the corresponding gap width. x_c represents the spanwise distance between the lateral wall and the vortex center, while y_c is the distance in the upward direction between the vortex center and the hydrofoil pitching axis, cf. Figure 5.1. As the clearance is reduced, the vortex naturally moves closer to the test section wall. However, a sudden increase in x_c is observed around the clearance corresponding to the maximum vortex intensity, i.e. τ=0.3, 0.4, 0.5 and 0.7 for the incidence angles of 3°, 5°, 7° and 10°, before the vortex center resumes its migration towards the wall. The wall proximity also affects the vortex vertical position, as depicted in Figure 5.22b. At large clearances, the vortex position is independent of the operating conditions, i.e. the incidence angle and the inlet velocity. As the confinement increases, the vortex migrates upwards. This displacement, which is more pronounced for high incidence angles, is characteristic of a vortex-wall interaction, modeled by an image vortex, as shown in Figure 5.8. The velocity induced by the image vortex depends both on the vortex strength and the proximity to the wall. Since the vortex strength diminishes at small clearances, this upward migration reaches a plateau, the value of which is linked to the foil incidence angle. The wandering amplitude in the x and y directions with respect to the gap width is depicted in Figures 5.22c and 5.22d, with the standard deviation of the mean vortex center location. It is observed that the wandering amplitude remains fairly constant for all the clearance values, except in the most confined situations where it becomes very large, especially in the y-direction.

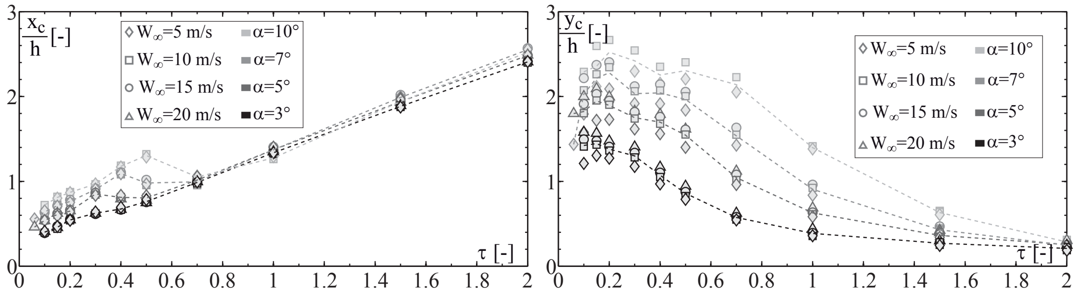

(a) x_c (b) y_c

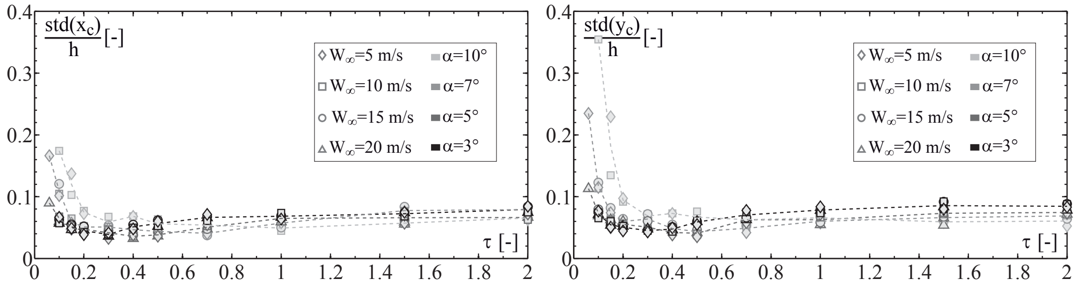

(c) std(x_c) (d) std(y_c)

Figure 5.22: Evolution of the mean vortex center position (x_c, y_c) and standard deviation (std(x_c), std(y_c)) with the normalized clearance τ for the rough hydrofoil at z/c=1. The dashed lines are the mean values for each incidence angle.

Flow visualizations show that the vortex moves away from the wall in the spanwise direction (x-direction) during its formation over the hydrofoil, but that downstream of the hydrofoil, the vortex center remains at a nearly constant distance from the wall, as also reported by Chen et al. [28]. To obtain a better understanding of the influence of the wall on the TLV position, Figure 5.23 illustrates the evolution of the TLV center position in the x-y plane with the x-coordinate corresponding to the position of the vortex relative to the foil tip, i.e x=$x_c - gap$. For readability, only the data of the rough hydrofoil measured at z/c=1 with W_∞=10 m/s are represented. Similar trends are however obtained for other operating conditions. As the confinement increases, the position of the TLV relative to the foil tip outlines a 'C' shape, the size of which depends on the incidence angle. This pattern can be interpreted in reference to the image system of the tip clearance vortex illustrated in Figure 5.8. At τ=2, the vortex location in the spanwise direction is between 4 and 5.5 mm away from the foil tip for all incidence angles. As the clearance is reduced, the vortex intensity increases (cf. Figure 5.18) as well as the induced velocity v_d (cf. Figure 5.8) which drives the vortex towards the foil tip. However, the vortex is also displaced upwards because of the induced velocity v_b, reducing at the same time the influence of the image vortex d. After reaching its peak value, the vortex intensity drops drastically with the confinement, resulting in a lower induced velocity v_d. Therefore, the vortex moves away from the foil tip in the x-direction. At low τ values, the vortex stabilizes finally in the vertical direction, while a small drift in the x-direction is still noticeable.

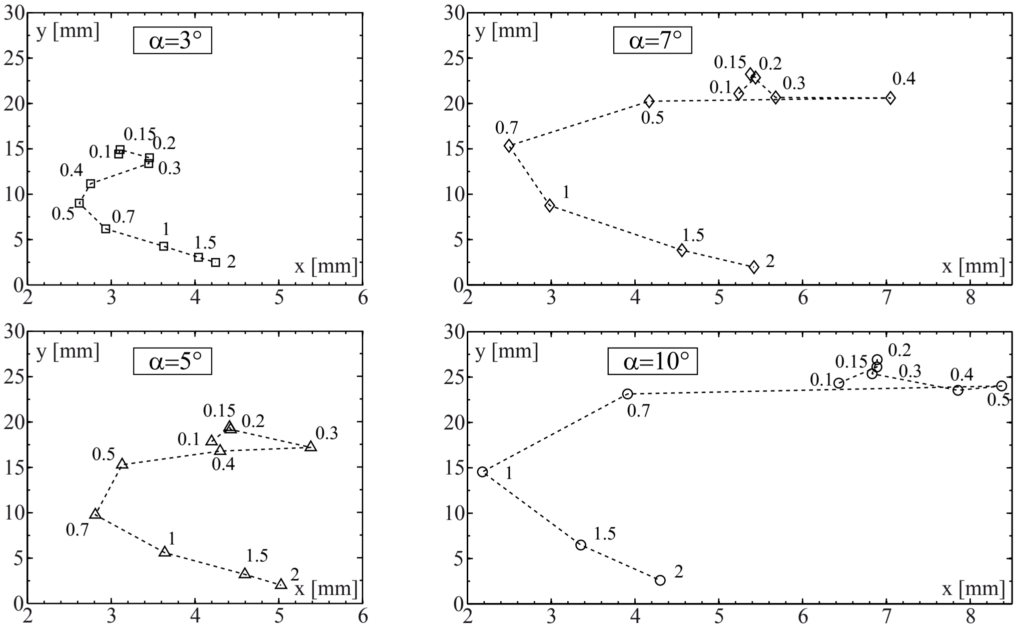

Figure 5.23: x-y position of the TLV for the rough hydrofoil at W_∞=10 m/s and z/c=1. The x-coordinate represents the distance relative to the foil tip: x=$x_c - gap$. The numbers next to the data points indicate the corresponding value of τ.

5.6.4 Particular case at high incidence angles

So far, all the analyses have been restricted to the incidence angles 3°, 5°, 7° and 10°, deliberately dismissing the case α=12°. In fact, a particular phenomenon, which deserves special attention, occurs at high incidence angles when the confinement increases. Figures 5.24a and 5.24b are basically the same as Figure 5.18 and Figure 5.20, but with the addition of the incidence α=12°. They depict the evolution of the dimensionless circulation Γ^* and the axial velocity in the vortex core as the clearance is reduced. During the first stage of clearance reduction ($1 \le \tau \le 2$), both the axial velocity and Γ^* increase similarly to the other angles of incidence. However, when the clearance is further reduced ($\tau < 1$), the axial velocity and Γ^* experience a considerably steeper decline for α=12° than for the lower incidence angles, suggesting a change of flow topology.

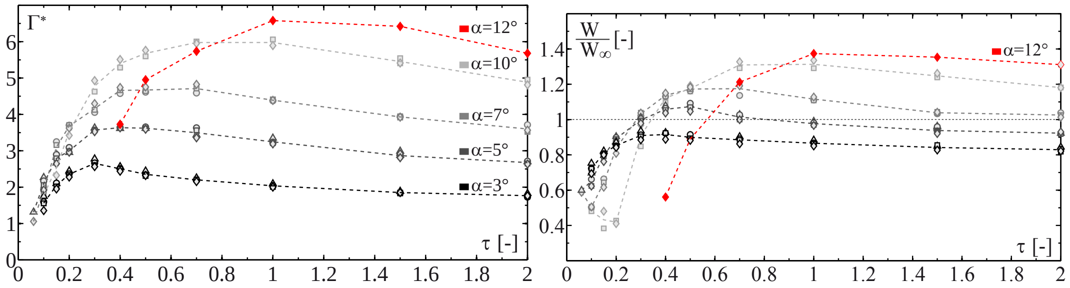

(a) Circulation

(b) Axial velocity

Figure 5.24: Same caption as Figure 5.18 and Figure 5.20 but with the particular case of α=12°. Rough hydrofoil, z/c=1.

To get an insight into the flow topology downstream of the hydrofoil, Figure 5.25 shows the instantaneous axial velocity fields and a number of planar streamlines at the operating conditions W_∞=10 m/s and α=12° for different values of τ. The streamlines highlight the instantaneous flow structures in the x-y plane. The TLV is readily identified as a swirling structure on the left-hand side of each subfigure. At $\tau = 1.5$ and $\tau = 1$, the TLV is very coherent and intense, as evidenced by the axial velocity excess in its center, while at $\tau = 0.1$ the TLV appears more disorganized and less intense. However, the striking feature of these instantaneous velocity streamlines is the evidence of unsteady secondary vortices at the bottom of each subfigure. Those vortices are characteristic of a separated flow region that occurs when the hydrofoil is close to stall condition. In fact, the critical stall angle is $\alpha \approx 13°$ for this hydrofoil. The wake of the separated flow region features a lower axial velocity than the free stream velocity and extends towards the foil tip as the confinement increases. For instance, at $\tau = 1.5$ the separation only starts around x=80 mm while at $\tau = 0.1$ the whole wingspan exhibits chaotic vortex shedding. For comparison purposes, Figure 5.26 shows the instantaneous streamlines obtained for $\tau = 1.5$ and $\tau = 0.1$ at the incidence angle α=10°. Apart from some small structures in the hydrofoil wake, no evidence of flow separation is visible in this case. An additional evidence of the separated flow is provided in Figure 5.27, which compares the mean axial velocity for the incidence $\alpha = 12°$ and $\alpha = 10°$ at two different values of the tip clearance.

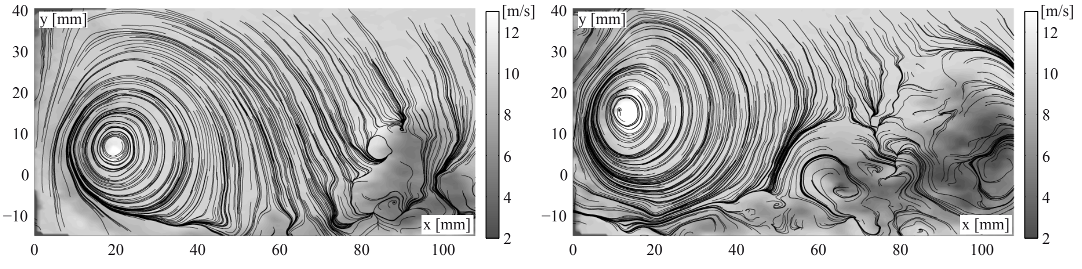

(a) $\tau = 1.5$ (b) $\tau = 1$

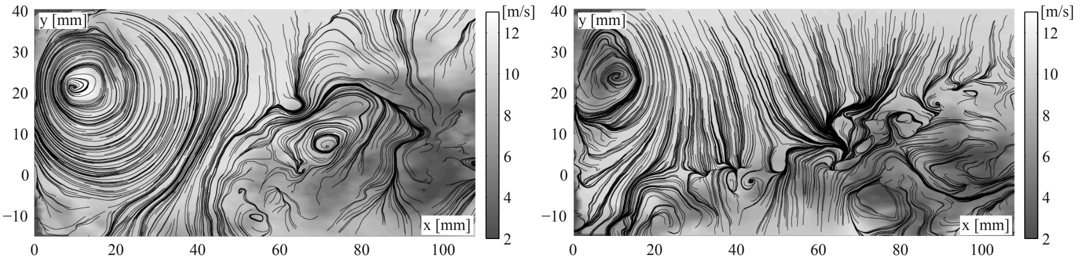

(c) $\tau = 0.7$ (d) $\tau = 0.1$

Figure 5.25: Instantaneous streamlines and axial velocity. Flow conditions: W_∞=10 m/s, α=12°, z/c=1, rough hydrofoil.

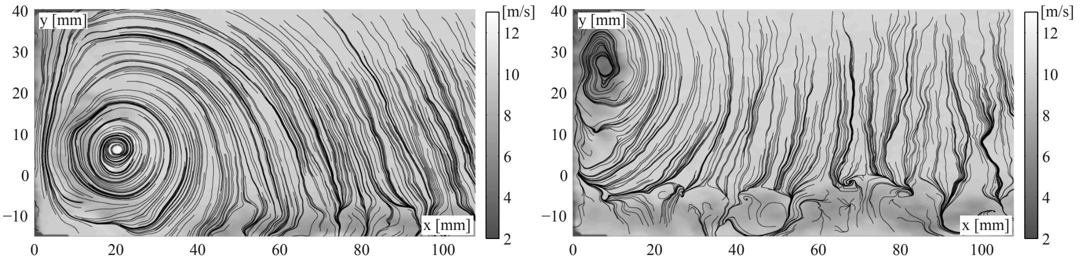

(a) $\tau = 1.5$ (b) $\tau = 0.1$

Figure 5.26: Instantaneous streamlines and axial velocity. Flow conditions: W_∞=10 m/s, α=10°, z/c=1, rough hydrofoil.

The wake of the separated flow is delimited by the region of velocity deficit that extends above the foil wake at $\alpha = 12°$, confirming that a higher confinement results in a larger separated flow region.

The flow separation clarifies the behavior observed in Figure 5.24. As the clearance is reduced, the separation moves closer to the foil tip and the violent and chaotic motions induced by secondary vortices destabilize the TLV, which therefore becomes less coherent, leading to a diminution of its intensity. Moreover, the extension of the separated flow region towards the foil tip as the confinement increases is directly related to the TLV dynamics: the clockwise rotation of the TLV induces a downwash motion of the fluid above the hydrofoil, as highlighted by the streamlines in Figures 5.25 and 5.26. The downwash motion in the vicinity of the TLV

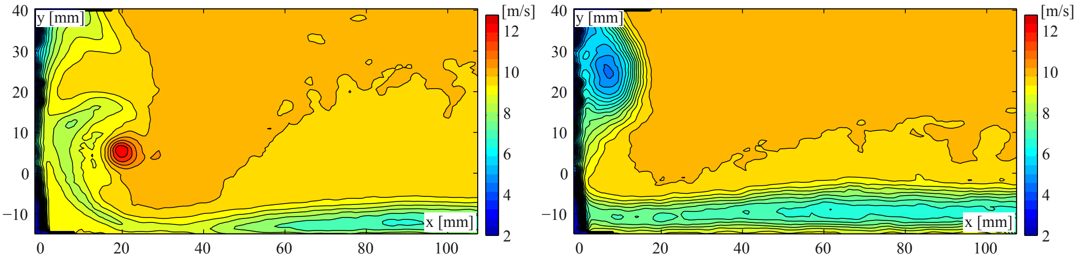

(a) α=10°, τ = 1.5 (b) α=10°, τ = 0.1

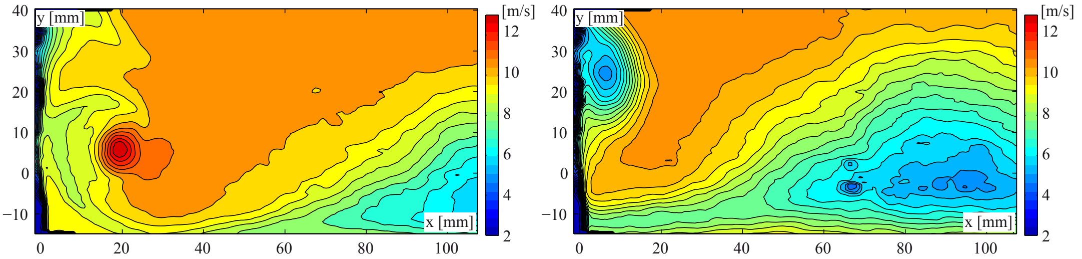

(c) α=12°, τ = 1.5 (d) α=12°, τ = 0.1

Figure 5.27: Comparison of the isocontours of the mean axial velocity for α=10° and α=12°. Rough hydrofoil, z/c=1.

delays the flow separation and associated vortex shedding, as reported by Prothin et al. [95]. This phenomenon explains the local reattachment of the flow near the foil tip observed in Figure 5.25a. As the clearance is reduced, the TLV tends to move away from the hydrofoil due to the wall influence, as explained in Section 5.6.3. As a consequence, the positive influence of the TLV on the flow separation is lessened for small clearances, and the separated flow region extends over the whole wingspan.

5.6.5 Effect of the wall boundary layer thickness

The influence of the wall boundary layer thickness on the TLV intensity evolution is investigated indirectly by varying the inlet velocity W_∞. The Figure 5.28a shows the change of boundary layer thickness δ with W_∞, at the location z/c=-1, i.e. one chord upstream of the hydrofoil. The boundary layer thickness shows a decreasing trend with increasing inlet velocity, as expected from typical Reynolds effects. The trend is in accordance with the theoretical law expressing the development of a turbulent boundary layer on a flat plate expressed by $\delta = 0.37\ x\ Re_x^{-1/5}$ [101]. The evolution of δ as a function of the downstream distance is depicted in Figure 5.28b. The corresponding measurements are obtained at W_∞= 10 m/s without a hydrofoil mounted in the test section, at the locations z/c=-1, 1, 1.2 and 1.5. Again, the evolution is consistent with the growth of a turbulent boundary layer on a flat plate.

In the range of velocities tested, no significant effect of the boundary layer thickness on the vortex intensity is observed, as evidenced by the overlapping of the data points corresponding to different values of W_∞ in Figure 5.18. It should be emphasized that Figures 5.28a and 5.28b display the wall boundary layer thickness without a hydrofoil mounted in the test section. In the clearance region, the boundary layer is however likely to be thinner than the values shown in Figures 5.28a and 5.28b, due to the local acceleration of the flow. Additional measurements would however be necessary to confirm this hypothesis.

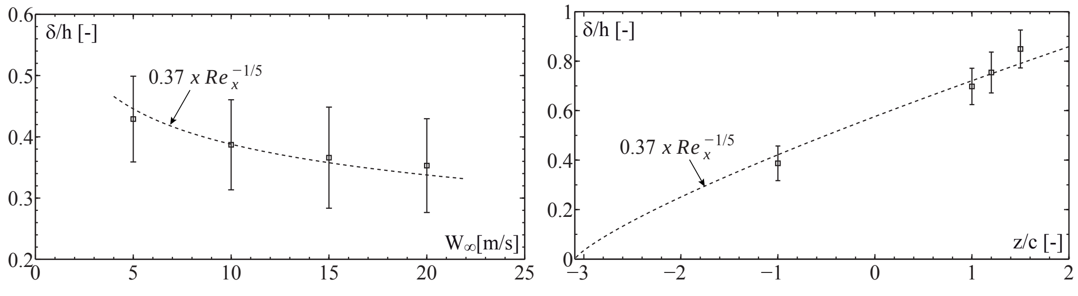

(a) δ vs W_∞ (b) δ vs z

Figure 5.28: (a) Boundary layer thickness vs inlet velocity at z/c=-1. (b) Boundary layer thickness vs downstream position at W_∞= 10 m/s. The dashed line is the best-fit of the theoretical law for a turbulent boundary layer on a flat plane [101]. No hydrofoil is mounted in the test section.

5.6.6 New scaling of the TLV intensity

One of the outcomes of the systematic measurements presented in Section 5.6.1 is the existence of a specific tip clearance for which the vortex intensity is maximum. However, the value of this specific gap increases monotonically with the foil incidence angle, because of a stronger vortex-wall interaction. In order to obtain an evolution of the TLV intensity with the gap width that is independent of the operating conditions, the dimensionless tip clearance τ is therefore scaled by the asymptotic value of the normalized circulation without confinement Γ^*_∞, corresponding to Γ^* at τ=2. Similarly, the vortex intensity Γ^* is normalized by Γ^*_∞. With this representation, all the results merge together on a similar pattern, as illustrated in Figure 5.29, which encompasses all the data measured for the rough and the smooth hydrofoils. The confinement produces a TLV peak intensity which is in average 45 (±10) % higher than the value away from the wall when the dimensionless coefficient τ/Γ^*_∞ equals approximately 0.2. Below this value, the vortex strength drops abruptly and quasi linearly towards zero, whereas for $\tau/\Gamma^*_\infty > 0.2$ it decreases slowly towards the value of the unconfined case.

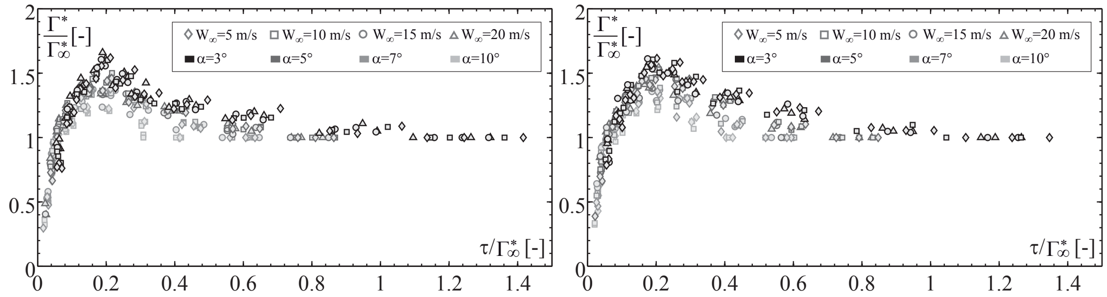

(a) Rough hydrofoil (b) Smooth hydrofoil

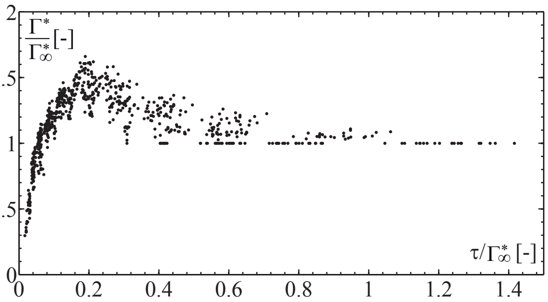

(c) Rough and smooth hydrofoils

Figure 5.29: General TLV intensity evolution obtained by normalizing Γ^* and τ by Γ^*_∞ (the non-dimensional circulation at τ=2). Data measured at z/c=1, 1.2 and 1.5.

5.7 Summary and discussion

This chapter investigates the influence of the clearance size on the TLV in a simplified case study. A total of 1,235 distinct flow configurations are tested by varying the inlet velocity, the incidence angle and the tip clearance. High-speed flow visualizations, with cavitation used as a tracer, have shown qualitatively that both the vortex trajectory and intensity are strongly influenced by the wall proximity. SPIV measurements confirmed that the smaller the clearance, the more the vortex is moved away from the hydrofoil. Moreover, the wake-like or jet-like nature of the axial flow in the vortex core was found to be related to the TLV intensity.

For each hydrofoil incidence angle, the systematic measurements clearly reveal the existence of a specific tip clearance for which the vortex intensity is maximum. By introducing a new dimensionless coefficient, it is established that the TLV circulation reaches a peak intensity for $\tau/\Gamma^*_\infty \approx 0.2$, the amplitude of which is in average 45 (±10) % higher than in the unconfined case, regardless of the operating conditions. Clearance values for which the TLV intensity is maximized should obviously be avoided in axial hydraulic machines, as they are the most prone to generating cavitation and leading to severe blade erosion. From a practical point of view, axial turbines are generally operated with the smallest possible clearance in order to minimize energy losses and the corresponding τ values are typically between 0.01 and 0.1. As suggested by Figure 5.18, the theoretical maximum TLV intensity is thus avoided. However, these operating clearances correspond to the region where the vortex intensity is very sensitive to the gap width and increases linearly with the latter. The IEC standard [66], which establishes the rules for reduced scale model testing, allows a gap that may deviate locally up to a factor of three between the prototype and a reduced scaled model (cf. Section 1.1.2). Hence, the non-dimensional TLV intensity Γ^* varies potentially by the same factor. Since the pressure drop in the vortex center depends on the squared value of Γ^* (cf. Section 2.2.6), this implies a change up to a factor of nine of the minimum pressure coefficient in the vortex. While the discrepancies in TLV cavitation occurrence between reduced scale models and prototypes are often explained by the non-similarity of nuclei content and Reynolds number, this result suggests that the gap width is probably the most important parameter that has to be taken into account.

The increase of the vortex strength during the first stage of the tip clearance reduction results essentially from a potential flow effect, since the maximum vortex intensity occurs at clearances larger than the boundary layer thickness displayed in Figure 5.28. This is in line with the findings of Boulon et al. [25], who link the increase of the vortex strength with clearance reduction to the modeling of the wall influence by an image vortex. The velocity induced by the image vortex leads to an increase of the effective incidence angle of the hydrofoil and consequently in vortex strength. In the case of a boundary layer larger than the specific tip clearance at which the vortex intensity is maximum, a viscous interaction would however certainly affect the vortex development.

It is worth mentioning that in the present study, the tip clearance is varied by changing the span of the hydrofoil, which also naturally affects the lift and thus the vortex strength. However, the change of span is limited to 15 % whereas the vortex circulation increases up to 60 %, as shown in Figure 5.29. Hence, the span variation does not account for the total change of vortex intensity and the potential effect prevails. Moreover, an increase of the vortex intensity with clearance reduction is also reported in the study of Boulon et al. [25], in which the tip vortex is generated by an elliptical foil and the confinement is achieved by a flat plate, without altering the span of the hydrofoil.

A particular phenomenon is observed when the hydrofoil is near the stall angle. At large clearances the TLV inhibits the flow separation in the vicinity of the foil tip, whereas the separated flow region extends over the whole wingspan when the confinement increases, due to the lower influence of the vortex. Although axial turbines generally do not operate at high incidence angles, this finding could have an implication in the case of ducted propellers. At high incidence angles, the confinement may potentially lead to a drop of hydraulic performances compared to the unconfined case.

6 Towards a control of the TLV in hydraulic turbines

6.1 Motivation and context

The erosion issue resulting from the TLV cavitation strongly motivates the development of tip leakage flow control strategies in hydraulic turbines. To the author's knowledge, the only industrially implemented solution in axial hydraulic turbines, such as Kaplan turbines and bulbs, is the 'anti-cavitation lip', which is a metallic piece attached to the tip of the blades. However, this remedy yields rather mixed results as cavitation is often not suppressed, but merely shifted on the anti-cavitation lip, as illustrated in Figure 6.1. Moreover, since there are no reliable guidelines for their design, the anti-cavitation lips are often ineffective to displace the TLV away from the blade, as reported by Roussopoulos & Monkewitz [99].

In the area of gas turbines and compressors, many passive or active control devices are used to increase the efficiency and/or the operating range by manipulating the flow in the tip clearance region [64, 84]. Active control strategies, such as mass flow ejection, boundary layer suction and synthetic jets [17], have the potential to adapt to various flow conditions, but are difficult and costly to implement. In contrast, passive control strategies rely rather on geo-

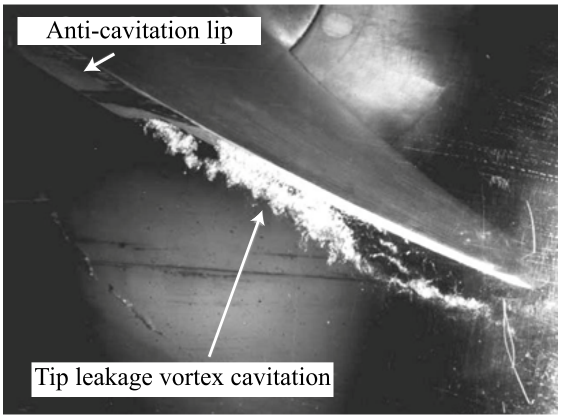

Figure 6.1: Anti-cavitation lip and cavitating tip leakage vortex in a reduced scale model.

metric alterations and are easier to implement. However, a parametric study of the geometric modifications is often required in order to optimize their effectiveness for a particular flow condition.

The use of casing treatments, such as circumferential or axial grooves, is an effective passive control strategy to increase the stall margin in axial gas compressors, with only a small impact on the overall efficiency [105]. The flow recirculations generated by the grooves appear to hinder the flow in the clearance region and alter the TLV formation. However, the physical mechanisms behind the effectiveness of casing treatments are still not understood. Kang et al. [69] interpret the working principle of the grooves by their ability to "trap" the TLV inside the cavity, while other studies mention the interaction between the grooves and the boundary layer as the dominant effect [63, 84]. Consequently, the design criteria of the grooves are mostly empirical and not well referenced. It is still unclear how the effectiveness of casing treatments is affected by the depth, the number, the spacing and the location of the grooves. The quest for the optimal grooves configuration is still an active subject of research in the field of compressors [63, 84, 89].

Recently, casing treatments were tested in space rocket inducers to suppress cavitation instabilities. Some promising results were obtained by controlling the tip leakage vortex trajectory with radial or circumferential grooves [32, 69, 103]. However, casing treatments have never been tested in axial hydraulic turbines. The grooves could be a simple and elegant solution to mitigate the TLV cavitation in hydraulic machines, provided they do not cause any penalty on the overall efficiency.

6.2 Case study and experimental setup

The alteration of the clearance geometry with grooves is tested in the same case study as described in Section 5.2.1. Based on flow visualizations using cavitation as a tracer, the TLV diameter at its origin, i.e. near the foil leading edge, is estimated to be roughly 1 mm, which is about the same order of magnitude as the wall boundary layer thickness (cf. Section 5.7). The dimensions of the rectangular grooves are therefore 1 mm, both in depth and width. A ridge of 2 mm separates two adjacent grooves, as shown in Figure 6.2c.

Figures 6.2a and 6.2b illustrate the implementation of the grooves in the test section of the cavitation tunnel. The grooves are machined on a 120 mm diameter Plexiglas cylinder, which is installed in the test section side window. The sealing between the two parts is ensured by an O-ring and the cylinder can be rotated to change the orientation of the grooves with respect to the flow. Half of the cylinder surface is covered with 20 grooves. The rotation axis of the cylinder is shifted by 7.7 mm in the y-direction compared to the hydrofoil pitch axis. In this manner, a variety of grooves configurations can be tested, as illustrated in Figure 6.3. When the angle between the grooves and the flow is set to 0°, the central groove is situated below the hydrofoil and the tip clearance geometry remains unaltered up to a foil incidence angle of $\alpha \approx 9°$. In contrast, at 180°, the grooves cover completely the clearance region and are aligned

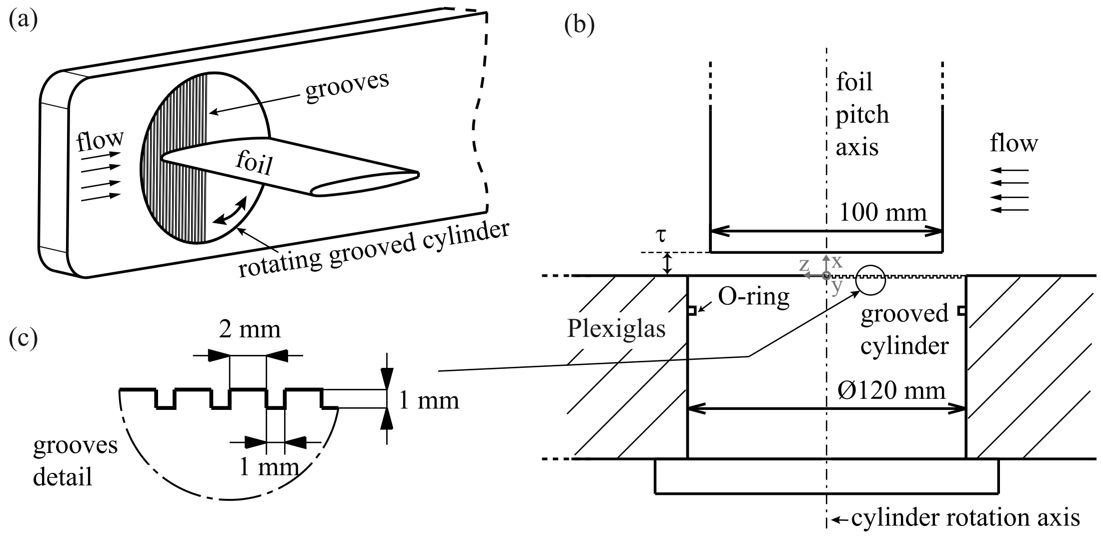
(a)
grooves
flow
foil
rotating grooved cylinder
(b)
foil
pitch
axis
flow
100 mm
τ
z
x
y
O-ring
Plexiglas
grooved
cylinder
Ø120 mm
cylinder rotation axis
(c)
2 mm
1 mm
grooves
detail
1 mm

Figure 6.2: Sketch of the grooves implementation. (a) Isometric view of the grooved cylinder and the hydrofoil. (b) Cross-section of the grooved cylinder. (c) Detail of the grooves geometry.

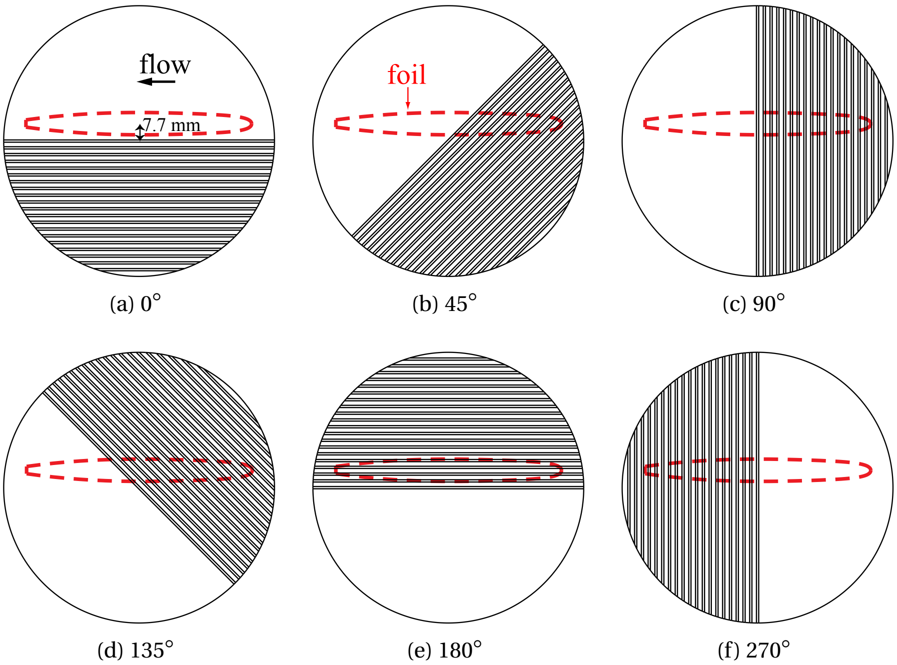
flow
7.7 mm
foil

(a) 0°

(b) 45°

(c) 90°

(d) 135°

(e) 180°

(f) 270°

Figure 6.3: Different grooves configurations in the test section.

with the incoming flow. At 90°, the grooves are perpendicular to the flow and cover the first half of the hydrofoil, while the second half is covered when the grooves are oriented at 270°. The configurations at 45° and 135° correspond to a forward, respectively backward, inclination of the grooves near the leading edge.

The effect of the grooves is assessed by performing high-speed flow visualizations, with cavitation used as a tracer, as well as lift and drag measurements. In order to limit the cavitation in the clearance region and on the foil leading edge, the TLV is generated by the smooth *NACA 0009* hydrofoil with the rounded tip. The tip clearance is varied during the visualizations with the help of the sliding support. The visualizations are limited to the incidence angles α=5° and α=7°, for which a coherent TLV is generated at small tip clearance values, representing an ideal situation to test the effectiveness of the grooves.

6.3 Results

6.3.1 Flow visualizations

Figure 6.4 compares the TLV generated without (smooth Plexiglas) and with the grooves at 0°, for the flow conditions α=5°, $\tau = 0.1$ and $\sigma = 1.2$. The left hand-side shows an instantaneous visualization of the TLV flow, as recorded by the high-speed camera. The right hand-side represents the summation of all the captured images, illustrating the mean TLV trajectory. To ensure an ideal optical access for the flow visualizations, the grooved cylinder is only maintained by the pressure difference between the inside and outside of the test section. Therefore, the tests with the grooves are always performed at flow conditions that involve a depressurization of the test section, e.g. W_∞=10 m/s and p_∞=0.62 bar in Figure 6.4, whereas the visualization without the grooves is performed at W_∞=15 m/s and p_∞=1.37 bar. However, the TLV structure does not depend significantly on the Reynolds number, as discussed in Section 5.5, and the cavitation development in the TLV is controlled solely by the σ value, which is identical for the two configurations in Figure 6.4.

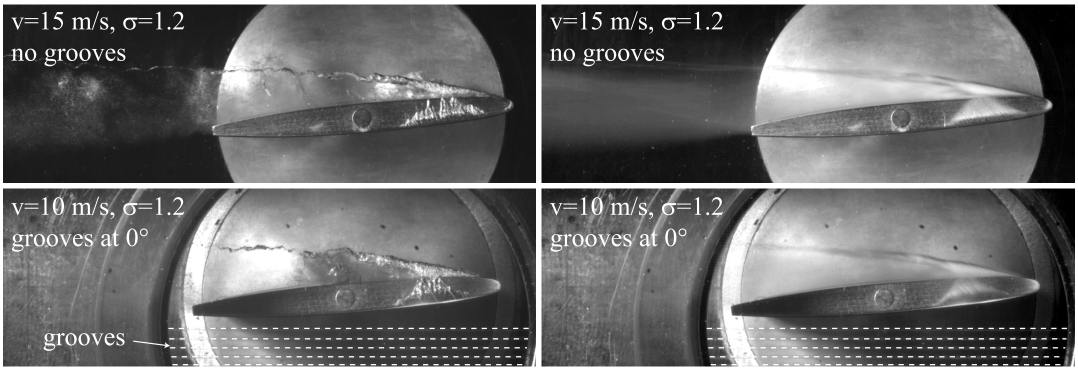

(a) Instantaneous (b) Average

Figure 6.4: Comparison of the cavitating TLV without grooves in the clearance (top) and with the grooves oriented at 0° (bottom). (a) Snapshots of the cavitating TLV (b) Average TLV trajectory obtained from the superposition of the captured images during 11 ms at 20,000 FPS. Flow conditions: α=5° and $\tau = 0.1$, $\sigma = 1.2$.

The cavitating TLV and the clearance cavitation observed in Figure 6.4 are equivalent without and with the grooves oriented at 0°. This indicates that, if the grooves are not situated directly in the clearance region, the TLV remains unaltered. The configuration with the grooves at 0° is therefore used as the reference case, representing the TLV in the absence of flow control.

The flow visualizations in Figures 6.5 to 6.8 evaluate the effect of the different grooves configurations sketched in Figure 6.3, for two incidence angles ($\alpha = 5°$ and $\alpha = 7°$) and two dimensionless clearances ($\tau = 0.1$ and $\tau = 0.2$), at the flow conditions W_∞=10 m/s, $\sigma = 1.2$ and $\sigma = 1.7$. A quick inspection of these visualizations reveals that the TLV cavitation is significantly altered when the grooves are oriented at 45° or 90°.

Figure 6.5 shows the case for α=5°, $\sigma = 1.2$ and $\tau = 0.1$. The reference case, i.e. the grooves oriented at 0°, features a cavitating TLV with an important vapor core, which is attached to the foil leading edge. The TLV cavitation is very intense near the leading edge, but diminishes towards the trailing edge, where the TLV becomes less coherent. A spot of clearance cavitation is also visible near the leading edge. When the grooves are oriented at 45°, the cavitating TLV nearly disappears and only a small cavitating vortex filament remains visible near the leading edge. Moreover, the clearance cavitation is suppressed. These effects are even enhanced with the grooves configuration at 90°, which suppresses totally the cavitation in the TLV and in the clearance. In contrast, when the orientation of the grooves is 135°, the TLV is cavitating intensively, similarly to the reference case with the grooves at 0°. When the grooves are oriented at 180°, the cavitation in the TLV is weaker than in the reference case and the clearance cavitation is suppressed. Moreover, the vortex trajectory follows more closely the foil than in the absence of control. Finally, the effect of the grooves on the TLV is almost negligible when the grooves are near the trailing edge, i.e. oriented at 270°. Surprisingly, the clearance cavitation is also suppressed with this configuration. However, experience shows that clearance cavitation is subject to a strong hysteresis: a slight increase and decrease of the foil incidence angle can trigger this cavitation at the same conditions for which it was not apparent before.

The influence of the grooves on the TLV is corroborated by the flow visualizations in Figure 6.5, in which the tip clearance ($\tau = 0.2$) is doubled compared to Figure 6.5. The larger tip clearance results in a stronger vortex (cf. Figure 5.18), as evidenced by the intense cavitating TLV in the reference case, with the grooves oriented at 0°. Since none of the grooves configurations completely suppresses the intense cavitation in the core of the TLV, a clear tracking of the vortex trajectory is possible. When the grooves are oriented at 45°, the clearance cavitation is suppressed and the amount of cavitation in the vortex core is reduced compared to the reference case. Moreover, the TLV trajectory is clearly altered and the vortex follows more closely the foil. When the grooves are oriented at 90°, the size of the cavitating TLV near the foil leading edge is slightly smaller than with the grooves at 45°. The TLV is pulled upwards during its passage over the hydrofoil and a small amount of cavitation is visible in the clearance. The configuration with the grooves at 135° does no affect the amount of cavitation in the TLV but alters its trajectory, which becomes almost straight. The orientation of the grooves at 180°

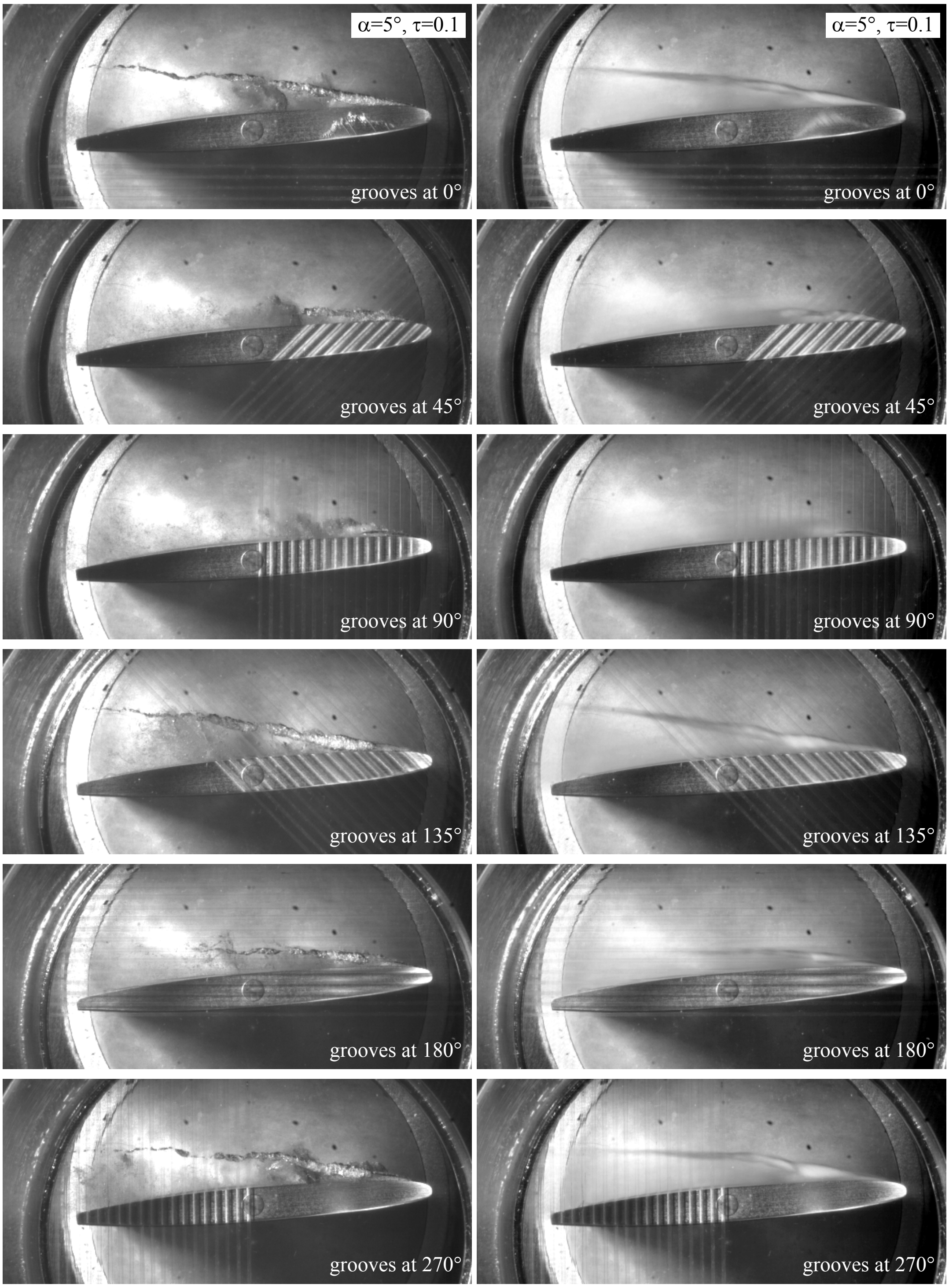
α=5°, τ=0.1
α=5°, τ=0.1
grooves at 0°
grooves at 0°
grooves at 45°
grooves at 45°
grooves at 90°
grooves at 90°
grooves at 135°
grooves at 135°
grooves at 180°
grooves at 180°
grooves at 270°
grooves at 270°

(a) Instantaneous

(b) Average

Figure 6.5: Effect of the grooves at W_∞=10 m/s, α=5°, $\tau = 0.1$, $\sigma = 1.2$. (a) Snapshots of the cavitating TLV (b) Average TLV trajectory obtained from the superposition of the captured images during 11 ms at 20,000 FPS.

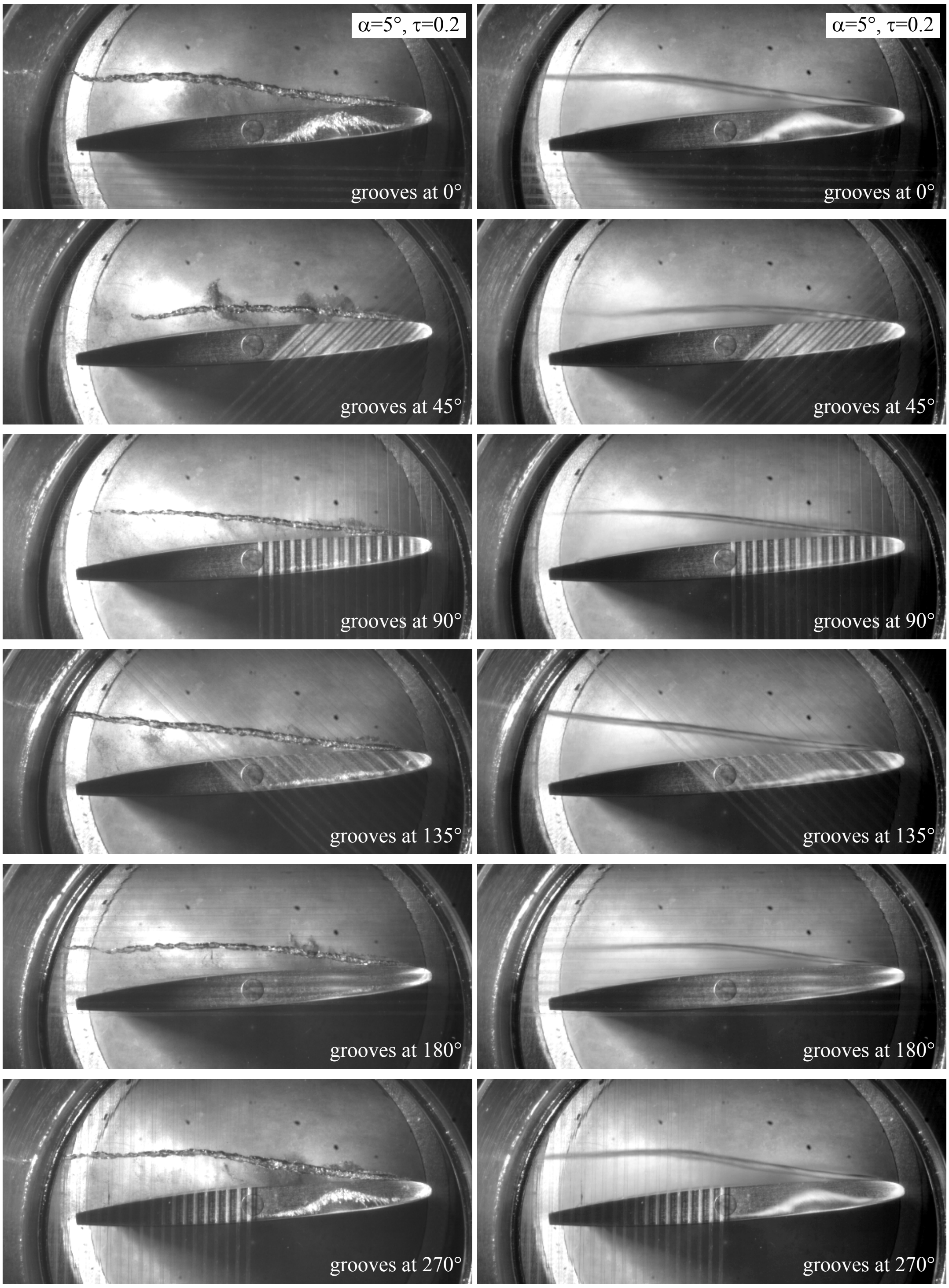
α=5°, τ=0.2
α=5°, τ=0.2
grooves at 0°
grooves at 0°
grooves at 45°
grooves at 45°
grooves at 90°
grooves at 90°
grooves at 135°
grooves at 135°
grooves at 180°
grooves at 180°
grooves at 270°
grooves at 270°

(a) Instantaneous (b) Average

Figure 6.6: Same caption as Figure 6.5 but for α=5°, $\tau = 0.2$ and $\sigma = 1.2$.

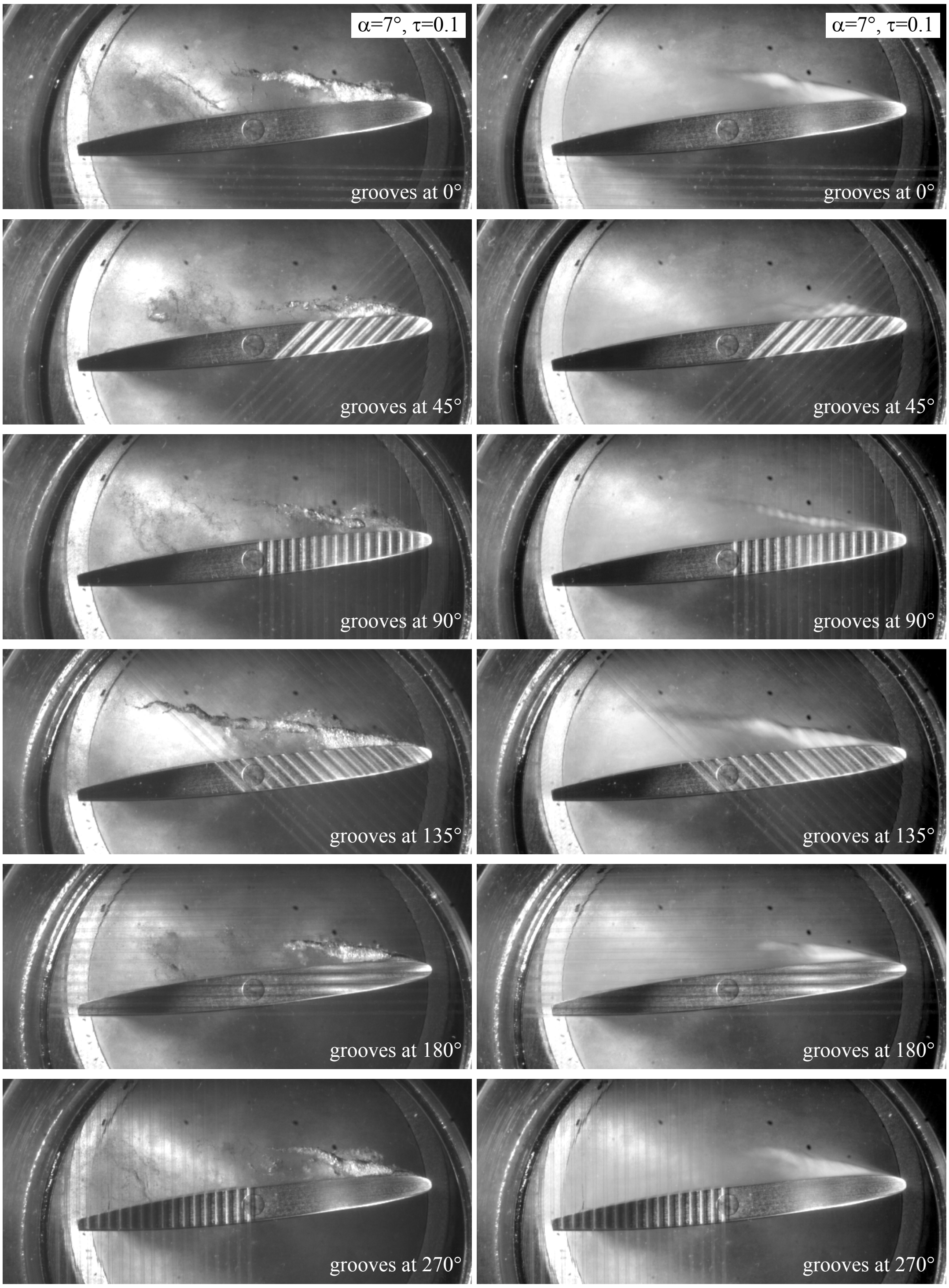
α=7°, τ=0.1
α=7°, τ=0.1
grooves at 0°
grooves at 0°
grooves at 45°
grooves at 45°
grooves at 90°
grooves at 90°
grooves at 135°
grooves at 135°
grooves at 180°
grooves at 180°
grooves at 270°
grooves at 270°

(a) Instantaneous (b) Average

Figure 6.7: Same caption as Figure 6.5 but for α=7°, $\tau = 0.1$ and $\sigma = 1.7$.

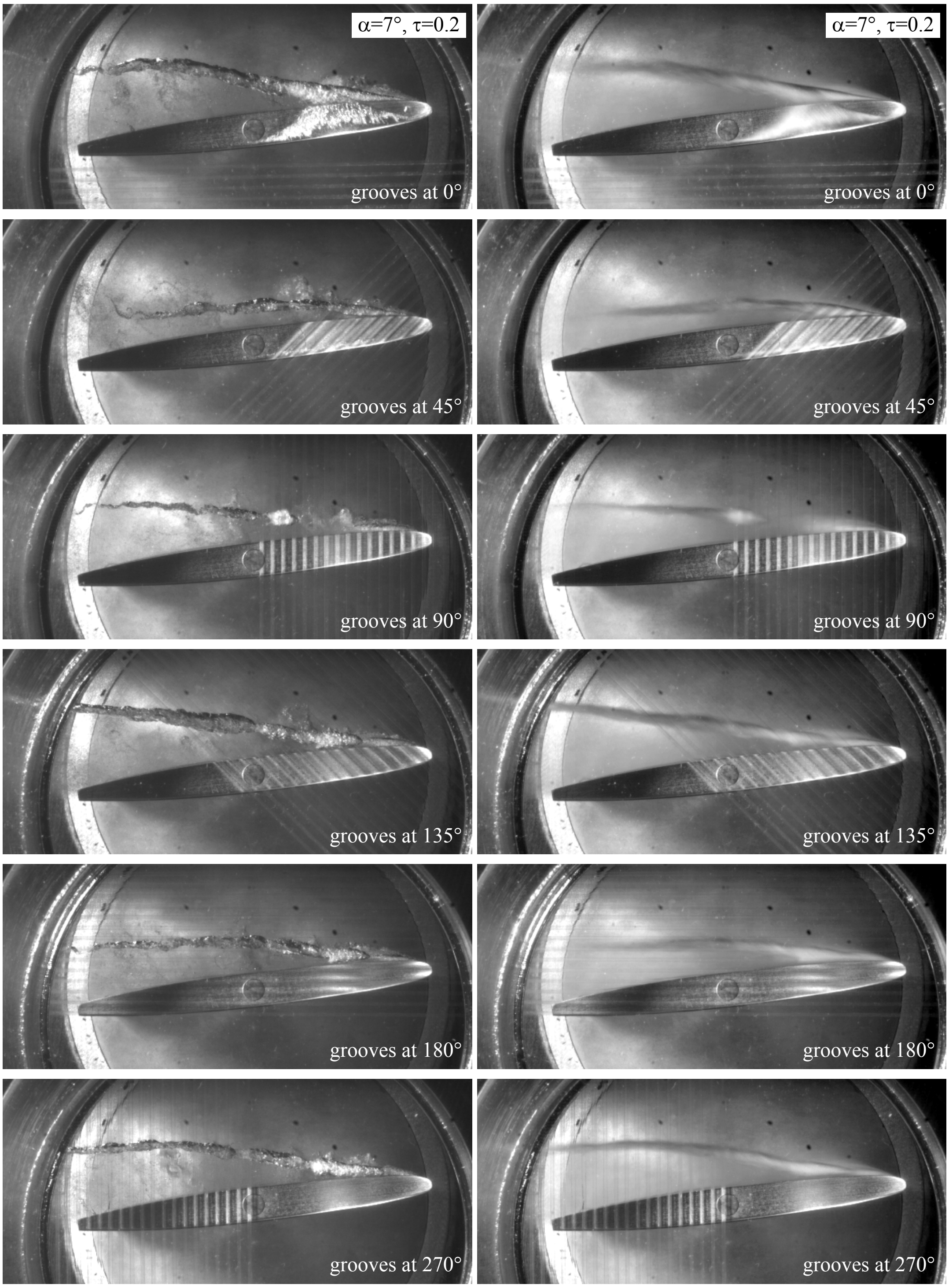
α=7°, τ=0.2
α=7°, τ=0.2
grooves at 0°
grooves at 0°
grooves at 45°
grooves at 45°
grooves at 90°
grooves at 90°
grooves at 135°
grooves at 135°
grooves at 180°
grooves at 180°
grooves at 270°
grooves at 270°

(a) Instantaneous (b) Average

Figure 6.8: Same caption as Figure 6.5 but for α=7°, $\tau = 0.2$ and $\sigma = 1.7$.

suppresses the clearance cavitation and reduces the intensity of the cavitating TLV compared to the reference case. The vortex remains also close to the hydrofoil during its development, although this effect is less pronounced than with the grooves at 45°. Lastly, the cavitation in the TLV and the clearance are identical when the grooves are oriented at 0° and 270°, which confirms the ineffectiveness of the configuration with the grooves situated near the foil trailing edge.

The effect of the grooves at the incidence angle α=7° is shown in Figures 6.7 and 6.8 for the dimensionless clearances $\tau = 0.1$ and $\tau = 0.2$ and a σ value of 1.7. The influence of the different grooves configurations on the TLV is generally similar to the case of α=5° (Figures 6.5 and Figures 6.6), with however a few differences. For the tip clearance $\tau = 0.1$ in Figure 6.6, the configuration with the grooves oriented at 45° is more effective than the grooves oriented at 90° to suppress the TLV cavitation. The amount of cavitation in the vortex core is still significantly reduced with the grooves at 90°, compared to the reference case with the grooves at 0°. For the tip clearance $\tau = 0.2$ in Figure 6.8, the clearance cavitation in the reference case reveals the merging of a secondary vortex and a primary vortex near the hydrofoil leading edge, resulting in an intense cavitating TLV over the hydrofoil. The configuration with the grooves at 45° seems to prevent this merging of vortices and the cavitating TLV intensity is diminished compared to the reference case. However, all the grooves configurations mitigate the clearance cavitation and it is not obvious if the secondary vortex is suppressed or simply not apparent in the visualizations. Finally, when the grooves are oriented at 90°, the cavitation in the TLV is not attached to the foil leading edge and makes a burst-like appearance roughly at mid-chord.

The effectiveness of the grooves decreases as the tip clearance increases. Flow visualizations at $\tau = 0.3$ and α=7° (not presented here) revealed that the grooves have only a limited impact on the TLV trajectory and the clearance cavitation.

6.3.2 Hydrodynamic performances

The hydrodynamic performances in terms of lift and drag are presented in Figure 6.9 for three incidence angles (3°, 5°, 7°). The two most effective grooves configurations (grooves at 45° and grooves at 90°) are compared to the case without grooves, obtained with the smooth Plexiglas. As evidenced by the overlapping of the data points, the grooves induce no significant alteration of the hydrodynamic performances. However, it is worth mentioning that the hydrodynamic load cell is designed to work with a fixed tip clearance of τ=0.1. It remains therefore to be confirmed that the hydrodynamic performances are unaltered at smaller τ values, where the relative size of the grooves compared to the tip clearance becomes more important.

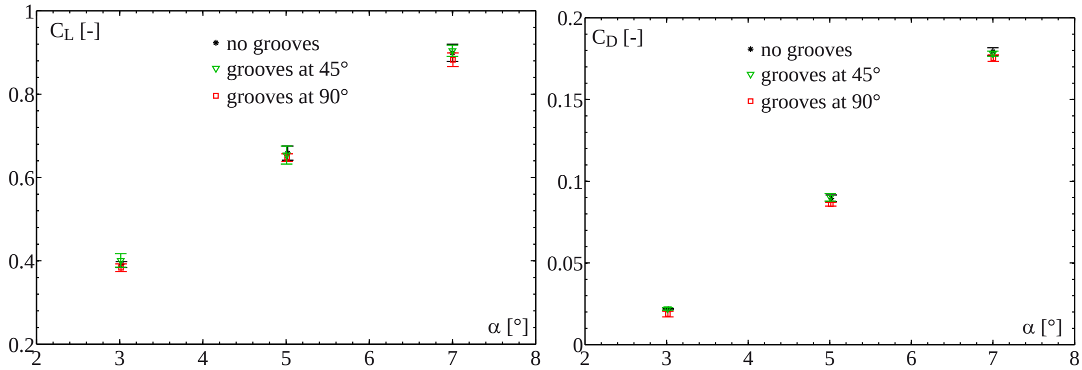

(a) Lift coefficient (b) Drag coefficient

Figure 6.9: Effect of the grooves on the lift and drag coefficients measured at $Re_c = 1 \times 10^6$

6.4 Discussion

The alteration of the clearance geometry with shallow grooves effectively influences the TLV trajectory and intensity, with no apparent penalty on the hydrodynamic performances. The most pronounced effects are achieved with the grooves located near the foil leading edge and oriented at 45° or 90° relative to the incoming flow. The mitigation of the clearance cavitation indicates that the flow disturbances induced by the grooves increase the local pressure. Moreover, by interfering with the leakage flow, the grooves result in a weaker TLV compared to the case with a smooth clearance geometry. It is assumed that the channeling of the flow by the grooves leads to a vorticity redistribution, so that the TLV is segmented into several weaker vortex filaments instead of a single coherent structure. The change of TLV intensity is evidenced by the modification of the vortex trajectory. According to the modeling of the wall influence by an image vortex discussed in Section 5.4 and sketched in Figure 5.8, a weaker TLV remains closer to the hydrofoil, since the velocity induced by the image vortex is lower.

These promising results suggest that the implementation of grooves on the casing of hydraulic turbines could be an effective solution to mitigate the TLV cavitation. The optimal geometry of the grooves remains yet to be established. It is likely that larger grooves will have a more pronounced impact on the leakage flow and resulting TLV. However, the alterations of the clearance geometry must remain small, in order to avoid any penalty on the overall efficiency of the machine. Furthermore, it is important to ensure that larger grooves do not act as nucleation sites, generating additional cavitation.

7 Conclusions and perspectives

7.1 Conclusions

The tip leakage vortex (TLV), which is a major issue in axial hydraulic machines, is investigated experimentally to better understand the underlying physics. In particular, the clearance size influence on the structure and the dynamics of the TLV is examined. To this end, two simplified case studies are addressed. In the first one, a rectangular *NACA 0009* hydrofoil is used as a generic blade in a water tunnel and the clearance between the blade tip and the wall is varied. The 3D velocity fields are measured using Stereo Particle Image Velocimetry (SPIV) in a total of 1,235 distinct flow configurations, by varying the inlet velocity, the foil incidence angle and the tip clearance. In the second case study, the effect of cavitation occurrence is investigated with the help of an elliptical hydrofoil, which generates a remarkably stable cavitating tip vortex. The velocity field around the cavitating vortex is measured by means of PIV using fluorescent seeding particles to cope with light reflections. Three cavitation numbers (non-cavitating, cavitation inception and developed cavitation) are tested in combination with two inlet velocities (10 and 15 m/s).

The results show that both the TLV trajectory and intensity are strongly influenced by the wall proximity. For each incidence angle, the measurements clearly reveal the existence of a specific tip clearance for which the vortex intensity is maximum. By introducing a new dimensionless coefficient, it is established that the TLV circulation reaches a peak intensity for $\tau/\Gamma^*_\infty \approx 0.2$, the amplitude of which is in average 45 (±10) % higher than in the unconfined case, regardless of the operating conditions. These clearance values for which the TLV intensity is maximized should obviously be avoided in hydraulic axial turbomachinery, as they are the most prone to generate cavitation and lead to severe blade erosion. Moreover, the TLV intensity proves to be very sensitive to the gap width in the range of tip clearances commonly used in axial turbines. While the discrepancies in TLV cavitation occurrence between reduced scale models and prototypes are often explained by the non-similarity of nuclei content and Reynolds number, the present work suggests that the gap width is probably the most important parameter that has to be taken into account. In other words, mind the gap!

Velocity measurements around a cavitating vortex reveal that the vortex circulation is unaltered by the cavitation inception. Far from the cavity, the tangential velocity distribution of the cavitating vortex is identical to the non-cavitating vortex. In contrast, near the cavity, the tangential velocity is lower than in cavitation-free conditions. The fluid is in solid body rotation in the vicinity of the cavity and it can be inferred that the shear stress at the liquid-gas interface is zero. Moreover, the location of the peak tangential velocity is shifted further away from the vortex center when the vortex is cavitating. To the author's knowledge, it is the first time that experimental data on the flow structure around a cavitating vortex are reported. The results obtained may help in developing a better physical model of cavitating vortices.

Finally, in an attempt to mitigate the tip leakage vortex cavitation, we have tested several configurations (location and orientation) of shallow grooves to control the flow in the clearance region. It is clearly observed that the TLV trajectory and intensity may be influenced, with no penalty on the hydrodynamic performances. The cavitation in the TLV and in the clearance region is significantly reduced with grooves located near the foil leading edge and oriented at 45° or 90° relative to the incoming flow. These preliminary results pave the way for further investigations and may ultimately lead to a practical solution for TLV cavitation mitigation in axial turbines.

7.2 Perspectives

Besides the fact that the experimental results form an extensive database for the validation and development of analytical and numerical flow models, it also allows for better design of further experimentations, as summarized hereafter.

Vortex cavitation

The change in the vortex structure due to cavitation can be further documented with additional measurements at different ratios of the cavity size relative to the vortex core size. Furthermore, measurements of the three components of the velocity field by means of a stereo-PIV setup would produce a clearer picture of the flow structure around the cavitating vortex. However, the spatial resolution of the measurements has to be high enough to accurately capture the velocity gradients near the vortex center. To overcome the resolution limitation of the setup used in the present work, measurements around a larger cavitating vortex might be performed, such as the vortex rope observed in the draft tube of a hydraulic machine. These measurements would help to understand the underlying physics of vortex cavitation, in order to develop an analytical model of the phenomenon.

Tip leakage vortex

In the present work, all the velocity measurements were obtained downstream of the hydrofoil. Measurements in the clearance region could be performed in order to better understand the mechanisms of the TLV formation. In addition, similar experiments with other hydrofoil geometries are suggested, in order to verify the scaling of the TLV intensity by the dimensionless tip clearance. In actual axial turbines, the wake of the guide vanes is highly suspected to modulate the TLV cavitation, leading to strong and repetitive collapses. The effect of the unsteadiness of the flow field on the TLV could be addressed in the cavitation tunnel by forcing the oscillation of the hydrofoil, in order to simulate the effect of the rotor-stator interaction with a periodic change of the incidence angle.

Control of the tip leakage vortex

Promising results were obtained with shallow grooves to mitigate the TLV cavitation in the simplified case study. However, the optimal geometry and configuration of the grooves remains yet to be established. The effectiveness of various grooves geometries could be quickly assessed by means of flow visualizations using cavitation as a tracer. A better understanding of the physical mechanisms involved would also help to determine the most effective grooves geometry. It is therefore suggested to perform velocity measurements in the vicinity of the grooves. In addition, alternative modifications of the clearance geometry can be tested, including the alteration of the blade tip geometry. Any modification which leads to a redistribution of the vorticity shed by the leakage flow could be considered to mitigate the TLV cavitation. It is however essential to ensure that the proposed solutions do not result in a decrease of the hydrodynamic performances.

A Appendices

A.1 Identification of the inclination angles between the vortex axis and the measurement plane

If the vortex axis is not orthogonal to the measurement plane, two rotations are required for the transformation from the measurement coordinates (x_{piv}, y_{piv}, z_{piv}) to the vortex coordinates (x_v, y_v, z_v), as illustrated in Figure A.1. The angle β is the elevation angle between the vortex axis and the x_{piv}-z_{piv} plane, and the angle α is the rotation angle around the y_{piv}-axis. The transformation from the measurement coordinates to the vortex coordinates is written as:

$$\begin{pmatrix} x_{piv} \\ y_{piv} \\ z_{piv} \end{pmatrix} = \begin{bmatrix} cos(\alpha) & 0 & sin(\alpha) \\ 0 & 1 & 0 \\ -sin(\alpha) & 0 & cos(\alpha) \end{bmatrix} \begin{bmatrix} 1 & 0 & 0 \\ 0 & cos(\beta) & sin(\beta) \\ 0 & -sin(\beta) & cos(\beta) \end{bmatrix} \begin{pmatrix} x_v \\ y_v \\ z_v \end{pmatrix} \tag{A.1}$$

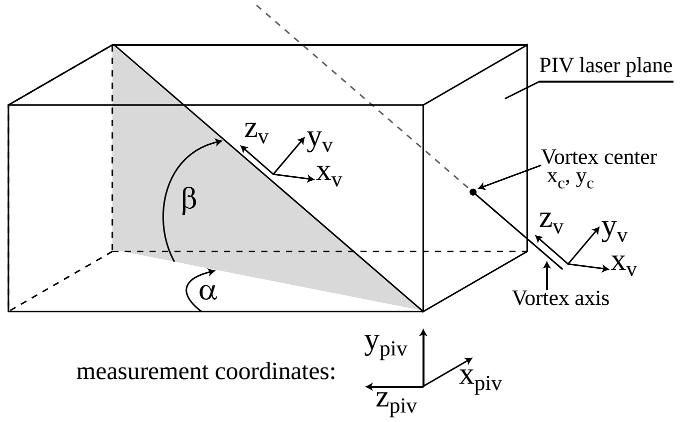
PIV laser plane
z_v
y_v
x_v
Vortex center
x_c, y_c
β
z_v
y_v
x_v
α
Vortex axis
y_{piv}
measurement coordinates:
x_{piv}
z_{piv}

Figure A.1: Inclination of the vortex axis relative to the measurement plane.

The origin of the two coordinate systems are both situated at the vortex center (x_c, y_c). Based on the assumption that in the vortex coordinates the axial velocity w_v is axisymmetric, van der Wall [113] proposed the following method to identify the angles α and β. First, the velocity components in the measurement plane $(u_{piv}, v_{piv}, w_{piv})$ are expressed as a function of their counterparts in the vortex coordinates (u_v, v_v, w_v). Using eq. (A.1), the projection of the velocities in the x_v-y_v plane along the y_v-axis $(v_v = 0)$ reads:

$$\begin{pmatrix} u_{piv} \\ v_{piv} \\ w_{piv} \end{pmatrix} = \begin{pmatrix} u_v cos(\alpha) + w_v cos(\beta) sin(\alpha) \\ w_v sin(\beta) \\ -u_v sin(\alpha) + w_v cos(\beta) cos(\alpha) \end{pmatrix} \tag{A.2}$$

Considering next the velocities obtained at the core radius below (subscript '$_-$') and above (subscript '$_+$') the center of the vortex, the assumption that w_v is axisymmetric gives the equality $w_v-=w_v+$. Using eq. (A.2), we can write:

$$\begin{aligned} u_{piv+} - u_{piv-} &= cos(\alpha)\,(u_{v+} - u_{v-}) \\ w_{piv+} - w_{piv-} &= -sin(\alpha)\,(u_{v+} - u_{v-}) \end{aligned} \tag{A.3}$$

and the angle α is given by:

$$\alpha = -\arctan\left(\frac{w_{piv+} - w_{piv-}}{u_{piv+} - u_{piv-}}\right) \tag{A.4}$$

The angle β is identified in a similar approach by extracting the velocities u_v, v_v and w_v along the x_v-axis, so that $u_v = 0$. The corresponding velocities in the measurement coordinates reads:

$$\begin{pmatrix} u_{piv} \\ v_{piv} \\ w_{piv} \end{pmatrix} = \begin{pmatrix} -v_v sin(\beta) sin(\alpha) + w_v cos(\beta) sin(\alpha) \\ v_v cos(\beta) + w_v sin(\beta) \\ -v_v cos(\alpha) sin(\beta) + w_v cos(\beta) cos(\alpha) \end{pmatrix} \tag{A.5}$$

As previously, by considering the velocities obtained at the core radius to the left (subscript '$_L$') and to the right (subscript '$_R$') of the center of the vortex, we can write:

$$\begin{aligned} v_{pivL} - v_{pivR} &= cos(\beta)\,(v_{vL} - v_{vR}) \\ w_{pivL} - w_{pivR} &= -cos(\alpha) sin(\alpha)\,(v_{vL} - v_{vR}) \end{aligned} \tag{A.6}$$

and the angle β is given by the following equation:

$$\beta = -\arctan\left(\frac{1}{\cos(\alpha)}\left(\frac{w_{pivL} - w_{pivR}}{v_{pivL} - v_{pivR}}\right)\right) \tag{A.7}$$

A.2 LDV measurement volume dimensions

The dimensions of the LDV measurement volume depend on the optical configuration and the used optical lens, which determine the crossing angle of the beams and their thickness at the focal point, as illustrated in Figure A.2. The laser beam thickness prior to the lens (D_L) and the distance 2d between the two laser beams are configured to be a fixed value, specific to each LDV system. The measurement volume is created at the focal point, which coincides with the position of the laser beam waist, i.e. the minimum thickness w_0 of a gaussian beam [127].

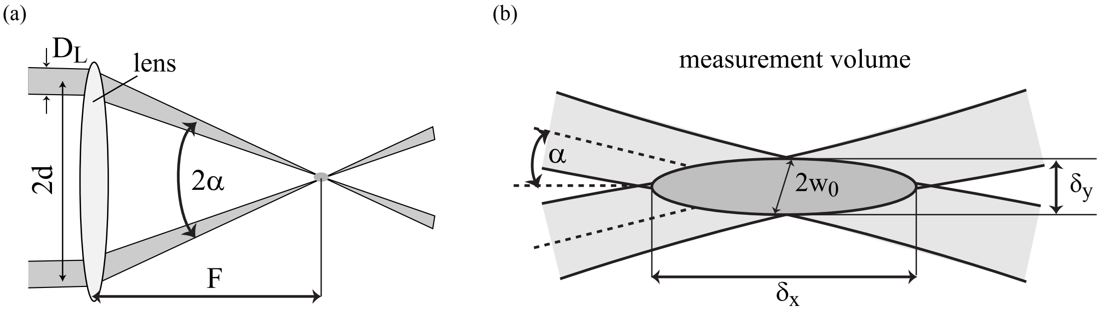

Figure A.2: (a) LDV configuration forming the measurement volume. (b) specification of the measurement volume size.

The shape of the measurement volume can be approximated by an ellipsoid, with a Gaussian intensity distribution in all 3 dimensions. The thickness δ_y and length δ_x of the measurement volume are given by the projection of the beam waist, while the dimension δ_z (cf. Figure 3.7) is equal to $2w_0$:

$$\delta_x = \frac{2w_0}{sin(\alpha)} \qquad \delta_y = \frac{2w_0}{cos(\alpha)} \qquad \delta_z = 2w_0 \tag{A.8}$$

The angle α is the half intersection angle between the two laser beams. It can be shown (see [127]) that the beam waist thickness is linked to the beam thickness prior to the lens D_L:

$$w_0 = \frac{2F\lambda}{\pi D_L} \tag{A.9}$$

where F is the focal length and λ is the laser wavelength. The dimensions of the measurement volume can be computed as follows:

$$\delta_x = \frac{4\mathrm{F}\lambda}{\pi \mathrm{D_L} \sin(\alpha)} \qquad \delta_y = \frac{4\mathrm{F}\lambda}{\pi \mathrm{D_L} \cos(\alpha)} \qquad \delta_z = \frac{4\mathrm{F}\lambda}{\pi \mathrm{D_L}} \tag{A.10}$$

If the measurement volume is formed in the water, the laser wavelength λ, the focal length F, and the intersection angle α are changed due to the light refraction. The wavelengths in air λ_1 and in water λ_2 are related via Snell's law:

$$n_1 \lambda_1 = n_2 \lambda_2 \tag{A.11}$$

where n_1 and n_2 are the refractive indices in air and in water, respectively. Similarly, the beams intersection angles in air α_1 and in water α_2 are linked by:

$$n_1 sin(\alpha_1) = n_2 sin(\alpha_2) \tag{A.12}$$

Finally, the focal length in water F_2 is easily computed with the geometry of the system sketched in Figure A.2:

$$\mathrm{F}_2 = \frac{d}{tan(\alpha_2)} \tag{A.13}$$

Bibliography

[1] Runner of kaplan turbine unit for guangxi dahua 110mw hydropower plant. (Online; accessed 28-January-2015), URL: http://www.tbhic.cn/en/productview.asp?id=65.

[2] R. J. Adrian. Particle-imaging techniques for experimental fluid mechanics. *Annual review of fluid mechanics*, 23(1):261–304, 1991.

[3] R. J. Adrian, K. T. Christensen, and Z.-C. Liu. Analysis and interpretation of instantaneous turbulent velocity fields. *Experiments in fluids*, 29(3):275–290, 2000.

[4] E. A. Anderson and T. A. Lawton. Correlation between vortex strength and axial velocity in a trailing vortex. *Journal of aircraft*, 40(4):699–704, 2003.

[5] J. D. Anderson. *Fundamentals of aerodynamics*. McGraw-Hill, Boston, 2001.

[6] V. H. Arakeri, H. Higuchi, and R. E. A. Arndt. A model for predicting tip vortex cavitation characteristics. *Journal of Fluids Engineering*, 110(2):190–193, June 1988.

[7] R. E. Arndt. Cavitation in vortical flows. *Annual Review of Fluid Mechanics*, 34(1):143–175, 2002.

[8] R. E. Arndt and A. P. Keller. Water quality effects on cavitation inception in a trailing vortex. *Journal of fluids engineering*, 114(3):430–438, 1992.

[9] R. E. Arndt and B. H. Maines. Viscous effects in tip vortex cavitation and nucleation. 1994.

[10] R. E. Arndt and B. H. Maines. Nucleation and bubble dynamics in vortical flows. *Journal of fluids engineering*, 122(3):488–493, 2000.

[11] R. E. A. Arndt. Vortex cavitation. In *Fluid Vortices*, pages 731–782. Springer, 1995.

[12] R. E. A. Arndt, V. H. Arakeri, and H. Higuchi. Some observations of tip-vortex cavitation. *Journal of Fluid Mechanics*, 229:269–289, 1991.

[13] J.-A. Astolfi, D. H. Fruman, and J.-Y. Billard. A model for tip vortex roll-up in the near field region of three-dimensional foils and the prediction of cavitation onset. *European Journal of Mechanics-B/Fluids*, 18(4):757–775, 1999.

[14] P. Ausoni. *Turbulent vortex shedding from a blunt trailing edge hydrofoil*. PhD thesis, EPFL, 2009.

[15] P. Ausoni, A. Zobeiri, F. Avellan, and M. Farhat. The Effects of a Tripped Turbulent Boundary Layer on Vortex Shedding from a Blunt Trailing Edge Hydrofoil. *Journal of Fluids Engineering*, 134(5):051207–051207, May 2012.

[16] F. Avellan, P. Henry, and I. Rhyming. A new high speed cavitation tunnel for cavitation studies in hydraulic machinery. *ASME Winter Annual Meeting*, 57:49–60, 1987.

[17] J. Bae, K. S. Breuer, and C. S. Tan. Control of tip clearance flows in axial compressors. *AIAA paper*, 2233:2000, 2000.

[18] G. K. Batchelor. Axial flow in trailing line vortices. *Journal of Fluid Mechanics*, 20:645–658, 11 1964.

[19] G. K. Batchelor. *An Introduction to Fluid Dynamics*. Cambridge University Press, Feb. 2000.

[20] M. J. Bhagwat and J. G. Leishman. Generalized viscous vortex model for application to free-vortex wake and aeroacoustic calculations. In *Annual Forum Proceedings-American Helicopter Society*, volume 58, pages 2042–2057. AMERICAN HELICOPTER SOCIETY, INC, 2002.

[21] M. J. Bhagwat and M. Ramasamy. Effect of tip vortex aperiodicity on measurement uncertainty. *Experiments in fluids*, 53(5):1191–1202, 2012.

[22] P. Billant, J. CHOMAZ, and P. Huerre. Experimental study of vortex breakdown in swirling jets. *Journal of Fluid Mechanics*, 376:183–219, 1998.

[23] D. M. Birch. Self-similarity of trailing vortices. *Physics of Fluids*, 24(2):025105, 2012.

[24] J. Bosschers. Modeling and analysis of a cavitating vortex in 2d unsteady viscous flow. In *7th international symposium on cavitation, CAV2009, Ann Arbor, Michigan, USA*, 2009.

[25] O. Boulon, M. Callenaere, J.-P. Franc, and J.-M. Michel. An experimental insight into the effect of confinement on tip vortex cavitation of an elliptical hydrofoil. *Journal of Fluid Mechanics*, 390:1–23, 1999.

[26] C. E. Brennen. *Cavitation and bubble dynamics*. Cambridge University Press, 2013.

[27] P. Chakraborty, S. Balachandar, and R. J. Adrian. On the relationships between local vortex identification schemes. *Journal of Fluid Mechanics*, 535:189–214, 2005.

[28] G. Chen, F. Marble, E. Greitzer, and C. Tan. Similarity analysis of compressor tip clearance flow structure. *Journal of Turbomachinery*, 113(2):260–269, 1991.

[29] G.-T. Chen. *Vortical structures in turbomachinery tip clearance flows*. Thesis, Massachusetts Institute of Technology, 1991. Thesis (Ph. D.)–Massachusetts Institute of Technology, Dept. of Aeronautics and Astronautics, 1991.

[30] J. Choi and S. L. Ceccio. Dynamics and noise emission of vortex cavitation bubbles. *Journal of Fluid Mechanics*, 575:1, Mar. 2007.

[31] J. Choi, C.-T. Hsiao, G. Chahine, and S. Ceccio. Growth, oscillation and collapse of vortex cavitation bubbles. *Journal of Fluid Mechanics*, 624:255, Apr. 2009.

[32] Y.-D. Choi, J. Kurokawa, and H. Imamura. Suppression of Cavitation in Inducers by J-Grooves. *Journal of Fluids Engineering*, 129(1):15, 2007.

[33] M. S. Chong, A. E. Perry, and B. J. Cantwell. A general classification of three-dimensional flow fields. *Physics of Fluids A: Fluid Dynamics (1989-1993)*, 2(5):765–777, May 1990.

[34] J. S. Chow, G. G. Zilliac, and P. Bradshaw. Mean and turbulence measurements in the near field of a wingtip vortex. *AIAA journal*, 35(10):1561–1567, 1997.

[35] C. del Pino, L. Parras, and R. Felli, M. Fernandez-Feria. Structure of trailing vortices: Comparison between particle image velocimetry measurements and theoretical models. *Phys. Fluids*, 23:013602, 2011.

[36] I. Delbende, J. CHOMAZ, and P. Huerre. Absolute/convective instabilities in the batchelor vortex: a numerical study of the linear impulse response. *Journal of Fluid Mechanics*, 355:229–254, 1998.

[37] J. D. Denton. The 1993 IGTI scholar lecture: Loss mechanisms in turbomachines. *Journal of Turbomachinery*, 115(4):621–656, Oct. 1993.

[38] W. J. Devenport, M. C. Rife, S. I. Liapis, and G. J. Follin. The structure and development of a wing-tip vortex. *Journal of Fluid Mechanics*, 312:67–106, 3 1996.

[39] T. Doligalski, C. Smith, and J. Walker. Vortex interactions with walls. *Annual Review of Fluid Mechanics*, 26(1):573–616, 1994.

[40] P. Dörfler, M. Sick, and A. Coutu. *Flow-Induced Pulsation and Vibration in Hydroelectric Machinery*. Springer, 2013.

[41] P. Dupont. *Etude de la dynamique d'une poche de cavitation partielle en vue de la prédiction de l'érosion dans les turbomachines hydrauliques*. PhD thesis, EPFL/LMH, 1993.

[42] M. V. Dyke. *An Album of Fluid Motion*. Parabolic Press, Inc., Stanford, Calif., 14th edition edition, June 1982.

[43] D. Fabre. *Instabilité et instationnarités dans les tourbillons: Application aux sillages d'avions*. PhD thesis, 2002.

[44] D. Fabre, J. Fontane, P. Brancher, S. Le Dizes, C. Roy, T. Leweke, R. Fernandez-Feria, L. Parras, and C. del Pino. Synthesis on vortex meandering. Technical report, STREP project no. AST4-CT-2005-012238, mai 2008.

[45] D. Fabre and L. Jacquin. Short-wave cooperative instabilities in representative aircraft vortices. *Physics of Fluids*, 16(5):1366, 2004.

[46] D. Fabre and L. Jacquin. Viscous instabilities in trailing vortices at large swirl numbers. *Journal of Fluid Mechanics*, 500:239–262, Jan. 2004.

[47] J. A. C. Falcão de Campos. Laser-doppler velocity measurements on tip vortices in non-cavitating and cavitating conditions. *ASME FED*, 135, 1992.

[48] M. Farhat, A. Chakravarty, and J. E. Field. Luminescence from hydrodynamic cavitation. *Proceedings of the Royal Society of London A: Mathematical, Physical and Engineering Sciences*, 467(2126):591–606, Feb. 2011.

[49] K. Farrell and M. Billet. A correlation of leakage vortex cavitation in axial-flow pumps. *Journal of fluids engineering*, 116(3):551–557, 1994.

[50] J. Feys and S. A. Maslowe. Linear stability of the moore-saffman model for a trailing wingtip vortex. *Physics of Fluids*, 26(2):024108, Feb. 2014.

[51] J.-P. Franc and J.-M. Michel. *Fundamentals of cavitation*, volume 76. Springer, 2006.

[52] J.-P. D. Franc, F. Avellan, and J.-L. Kueny. *La cavitation : mécanismes physiques et aspects industriels.* Presses universitaires de Grenoble PUG, 1995.

[53] D. H. Fruman, P. Cerrutti, T. Pichon, and P. Dupont. Effect of hydrofoil planform on tip vortex roll-up and cavitation. *Journal of fluids engineering*, 117(1):162–169, 1995.

[54] M. Giuni. *Formation and early development of wingtip vortices.* PhD thesis, University of Glasgow, 2013.

[55] M. Giuni and E. Benard. Analytical/experimental comparison of the axial velocity in trailing vortices. In *49th AIAA Aerospace Sciences Meeting. Orlando, FL*, 2011.

[56] M. Giuni and R. B. Green. Vortex formation on squared and rounded tip. *Aerospace Science and Technology*, 29(1):191–199, Aug. 2013.

[57] S. Gopalan, J. Katz, and H. L. Liu. Effect of gap size on tip leakage cavitation inception, associated noise and flow structure. *Journal of fluids engineering*, 124(4):994–1004, 2002.

[58] L. Graftieaux, M. Michard, and N. Grosjean. Combining PIV, POD and vortex identification algorithms for the study of unsteady turbulent swirling flows. *Meas. Sci. Technol.*, 12:1422–1429, 2001.

[59] S. Green. Wing tip vortices. In S. Green, editor, *Fluid Vortices*, pages 427–469. Springer Netherlands, 1995.

[60] S. I. Green. *Fluid Vortices: Fluid Mechanics and Its Applications*, volume 30. Springer, 1995.

[61] S. I. Green. Introduction to vorticity. In S. I. Green, editor, *Fluid Vortices*, number 30 in Fluid Mechanics and Its Applications, pages 1–34. Springer Netherlands, 1995.

[62] S. I. Green and A. J. Acosta. Unsteady flow in trailing vortices. *Journal of Fluid Mechanics*, 227:107–134, 5 1991.

[63] C. Hah. Toward optimum configuration of circumferential groove casing treatment in transonic compressor rotors. In *ASME-JSME-KSME 2011 Joint Fluids Engineering Conference*, pages 1823–1832. American Society of Mechanical Engineers, 2011.

[64] M. D. Hathaway. Passive endwall treatments for enhancing stability. 2007.

[65] F. J. G. Heyes, H. P. Hodson, and G. M. Dailey. The effect of blade tip geometry on the tip leakage flow in axial turbine cascades. *Journal of turbomachinery*, 114(3):643–651, 1992.

[66] IEC standards. 60193: Hydraulic Turbines, Storage Pumps and Pump-Turbines - Model Acceptance Tests, International Electrotechnic Commission, 2nd Edition, 1999.

[67] G. Iungo, P. Skinner, and G. Buresti. Correction of wandering smoothing effects on static measurements of a wing-tip vortex. *Experiments in Fluids*, 46(3):435–452, 2009.

[68] J. Jeong and F. Hussain. On the identification of a vortex. *Journal of Fluid Mechanics*, 285:69–94, 1995.

[69] D.-H. Kang, Y. Arimoto, K. Yonezawa, H. Horiguchi, Y. Kawata, C. Hah, and Y. Tsujimoto. Suppression of cavitation instabilities in an inducer by circumferential groove and explanation of higher frequency components. *International Journal of Fluid Machinery and Systems*, 3(2):137–149, 2010.

[70] S. Kang and C. Hirsch. Experimental study on the three-dimensional flow within a compressor cascade with tip clearance: Part i—velocity and pressure fields. *Journal of turbomachinery*, 115(3):435–443, 1993.

[71] S. Kang and C. Hirsch. Tip leakage flow in linear compressor cascade. *Journal of turbomachinery*, 116(4):657–664, 1994.

[72] S. Kang and C. H. Hirsch. Experimental study on the three-dimensional flow within a compressor cascade with tip clearance: Part II—the tip leakage vortex. *Journal of turbomachinery*, 115(3):444–450, 1993.

[73] R. D. Keane and R. J. Adrian. Theory of cross-correlation analysis of PIV images. *Applied Scientific Research*, 49(3):191–215, July 1992.

[74] R. Laborde, M. Mory, and P. Chantrel. Tip clearance and tip vortex cavitation in an axial flow pump. *Journal of fluids engineering*, 119(3):680–685, 1997.

[75] H. Lamb. *Hydrodynamics*. Cambridge university press, 1993.

[76] A. Le Guen, X. Viot, J. Y. Billard, and D. Fruman. Fluctuations des vitesses et biais spatial dans le tourbillon marginal. *Sixièmes Journées de l'Hydrodynamique*, pages 317–328, 1997.

[77] T. Lee and J. Pereira. Nature of wakelike and jetlike axial tip vortex flows. *Journal of Aircraft*, 47(6):1946–1954, 2010.

[78] W. F. Lindsey, D. B. Stevenson, and B. N. Daley. *Aerodynamic characteristics of 24 NACA 16-series airfoils at Mach numbers between 0.3 and 0.8.* National Advisory Committee for Aeronautics, 1948.

[79] O. Lucca-Negro and T. O'doherty. Vortex breakdown: a review. *Progress in energy and combustion science*, 27(4):431–481, 2001.

[80] R. Mailach, I. Lehmann, and K. Vogeler. Rotating instabilities in an axial compressor originating from the fluctuating blade tip vortex. *Journal of Turbomachinery*, 123(3):453, 2001.

[81] B. Maines and R. E. A. Arndt. The case of the singing vortex. *Journal of fluids engineering*, 119(2):271–276, 1997.

[82] B. H. Maines and R. E. A. Arndt. Viscous effects on tip vortex cavitation. *ASME-PUBLICATIONS-FED*, 177:125–125, 1993.

[83] Martin, P. B. ; Leishman, J. G. ; Pugliese, G. J. ; Anderson, S. L. Stereoscopic PIV measurement in the wake of a hovering rotorpdf. In *Annual Forum Proceedings-American Helicopter Society*, volume 56, pages 402–420. American Helicopter Society, 2000.

[84] J. Marty, L. Castillon, J. C. Boniface, S. Burguburu, and A. Godard. Numerical and experimental investigations of flow control in axial compressors. *AerospaceLab Journal*, 6(09):1–13, 2013.

[85] B. McCormick. On cavitation produced by a vortex trailing from a lifting surface. *Journal of Fluids Engineering*, 84(3):369–378, 1962.

[86] R. L. Miorini, H. Wu, and J. Katz. The internal structure of the tip leakage vortex within the rotor of an axial waterjet pump. *Journal of Turbomachinery*, 134(3):031018, 2012.

[87] D. W. Moore and P. G. Saffman. Axial Flow in Laminar Trailing Vortices. *Proceedings of the Royal Society of London. Series A, Mathematical and Physical Sciences*, 333(1595):pp. 491–508, 1973.

[88] A. Müller, M. Dreyer, N. Andreini, and F. Avellan. Draft tube discharge fluctuation during self-sustained pressure surge: fluorescent particle image velocimetry in two-phase flow. *Experiments in Fluids*, 54(4):1–11, 2013.

[89] M. W. Muller, H.-P. Schiffer, and C. Hah. Effect of circumferential grooves on the aerodynamic performance of an axial single-stage transonic compressor. In *Turbo Expo 2007: Power for Land, Sea, and Air*, pages 115–124. American Society of Mechanical Engineers, 2007.

[90] C. Muthanna and W. J. Devenport. Wake of a compressor cascade with tip gap, part 1: Mean flow and turbulence structure. *AIAA Journal*, 42(11):2320–2331, Nov. 2004.

[91] L. Nennemann and C. V. U. Thi. Kaplan turbine blade and discharge ring cavitation prediction using unsteady CFD. In *2nd IAHR international meeting of the workgroup on cavitation and dynamic problems in hydraulic machinery and systems. Timisoara, Romania*, 2007.

[92] B. G. Newman. Flow in a viscous trailing vortex. *The aeronautical quarterly*, 1:167–188, 1959.

[93] S. Pasche, F. Gallaire, M. Dreyer, and M. Farhat. Obstacle-induced spiral vortex breakdown. *Experiments in Fluids*, 55(8):1–11, 2014.

[94] A. K. Prasad. Stereoscopic particle image velocimetry. *Experiments in Fluids*, 29(2):103–116, Aug. 2000.

[95] S. Prothin, H. Djeridi, and J.-Y. Billard. Coherent and turbulent process analysis of the effects of a longitudinal vortex on boundary layer detachment on a NACA0015 foil. *Journal of Fluids and Structures*, 47:2–20, May 2014.

[96] M. Raffel, C. E. Willert, S. T. Wereley, and J. Kompenhans. *Particle Image Velocimetry: A Practical Guide.* Springer Science & Business Media, Sept. 2007.

[97] D. A. Rains. *Tip clearance flows in axial flow compressors and pumps.* PhD thesis, California Institute of Technology, 1954.

[98] M. Reclari. Tip vortex cavitation suppression by water ejection from wing tip. Master's thesis, Ecole polytechnique fédérale de Lausanne (EPFL), Laboratory for Hydraulic Machines (LMH), 2009.

[99] K. Roussopoulos and P. A. Monkewitz. Measurements of tip vortex characteristics and the effect of an anti-cavitation lip on a model Kaplan turbine blade. *Flow, turbulence and combustion*, 64(2):119–144, 2000.

[100] P. G. Saffman. *Vortex dynamics.* Cambridge university press, 1992.

[101] H. Schlichting, K. Gersten, and K. Gersten. *Boundary-Layer Theory.* Springer Science & Business Media, 2000.

[102] C. Schram, P. Rambaud, and M. L. Riethmuller. Wavelet based eddy structure eduction from a backward facing step flow investigated using particle image velocimetry. *Experiments in Fluids*, 36(2):233–245, Feb. 2004.

[103] N. Shimiya, A. Fujii, H. Horiguchi, M. Uchiumi, J. Kurokawa, and Y. Tsujimoto. Suppression of Cavitation Instabilities in an Inducer by J Groove. *Journal of Fluids Engineering*, 130(2):021302, 2008.

[104] C. H. Sieverding. *Tip clearance effects in axial turbomachines: April 15-19, 1985*. Von Karman Institute for Fluid Dynamics, 1985.

[105] G. D. J. Smith and N. A. Cumpsty. Flow phenomena in compressor casing treatment. *Journal of Engineering for Gas Turbines and Power*, 106(3):532–541, 1984.

[106] S. J. Song and M. Martinez-Sanchez. Rotordynamic forces due to turbine tip leakage: Part i—blade scale effects. *Journal of turbomachinery*, 119(4):695–703, 1997.

[107] S. J. Song and M. Martinez-Sanchez. Rotordynamic forces due to turbine tip leakage: Part II—radius scale effects and experimental verification. *Journal of turbomachinery*, 119(4):704–713, 1997.

[108] P. R. Spalart. Airplane trailing vortices. *Annual Review of Fluid Mechanics*, 30(1):107–138, 1998.

[109] C. Tan, I. Day, S. Morris, and A. Wadia. Spike-type compressor stall inception, detection, and control. *Annual Review of Fluid Mechanics*, 42(1):275–300, 2010.

[110] E. Terpetschnig, Y. Povrozin, and J. Eichorst. Long-wavelength polarization standards. *Technical notes*.

[111] R. Theunissen, F. Scarano, and M. L. Riethmuller. Spatially adaptive PIV interrogation based on data ensemble. *Experiments in Fluids*, 48(5):875–887, May 2010.

[112] B. G. van der Wall and H. Richard. Analysis methodology for 3C-PIV data of rotary wing vortices. *Exp Fluids*, 40:798–812, 2006.

[113] B. G. van der Wall and H. Richard. Analysis methodology for 3c-PIV data of rotary wing vortices. *Experiments in Fluids*, 40(5):798–812, May 2006.

[114] G. H. Vatistas, V. Kozel, and W. Mih. A simpler model for concentrated vortices. *Experiments in Fluids*, 11(1):73–76, 1991.

[115] H. Vollmers. Detection of vortices and quantitative evaluation of their main parameters from experimental velocity data. *Measurement Science and Technology*, 12(8):1199, Aug. 2001.

[116] I. A. Waitz, E. M. Greitzer, and C. S. Tan. Vortices in aero-propulsion systems. In *Fluid Vortices*, pages 471–531. Springer, 1995.

[117] Y. Wang and W. J. Devenport. Wake of a compressor cascade with tip gap, part 2: effects of endwall motion. *AIAA journal*, 42(11):2332–2340, 2004.

[118] J. Westerweel. Fundamentals of digital particle image velocimetry. *Measurement Science and Technology*, 8(12):1379, 1997.

[119] J. Westerweel. Theoretical analysis of the measurement precision in particle image velocimetry. *Experiments in Fluids*, 29(1):S003–S012, Dec. 2000.

[120] J. Westerweel and F. Scarano. Universal outlier detection for PIV data. *Experiments in Fluids*, 39(6):1096–1100, Dec. 2005.

[121] B. Wieneke and K. Pfeiffer. Adaptive PIV with variable interrogation window size and shape. 2010.

[122] H. Wu, D. Tan, R. L. Miorini, and J. Katz. Three-dimensional flow structures and associated turbulence in the tip region of a waterjet pump rotor blade. *Experiments in Fluids*, 51(6):1721–1737, Dec. 2011.

[123] J.-Z. Wu, H.-Y. Ma, and M.-D. Zhou. *Vorticity and vortex dynamics*. Springer-Verlag, Berlin, 2006.

[124] X. Xiao, A. A. McCarter, and B. Lakshminarayana. Tip clearance effects in a turbine rotor: Part i—pressure field and loss. *Journal of Turbomachinery*, 123(2):296, 2001.

[125] D. You, M. Wang, P. Moin, and R. Mittal. Effects of tip-gap size on the tip-leakage flow in a turbomachinery cascade. *Physics of Fluids*, 18(10):105102, 2006.

[126] D. You, M. Wang, P. Moin, and R. Mittal. Large-eddy simulation analysis of mechanisms for viscous losses in a turbomachinery tip-clearance flow. *Journal of Fluid Mechanics*, 586:177, Sept. 2007.

[127] Z. Zhang. *LDA Application Methods*. Springer Berlin Heidelberg, Berlin, Heidelberg, 2010.

Curriculum Vitae

Matthieu Dreyer

Rue Marcello 3
1700 Fribourg
Switzerland
matthieu.dreyer@a3.epfl.ch

22.01.1985
single
Swiss

Education

2011 - 2015	**PhD** École Polytechnique Fédérale de Lausanne (EPFL), Switzerland
2008 - 2010	**Master of Science, MSc** in mechanical engineering École Polytechnique Fédérale de Lausanne (EPFL), Switzerland
2005 – 2008	**Bachelor of Science, BSc** in mechanical engineering École Polytechnique Fédérale de Lausanne (EPFL), Switzerland
2000 – 2005	**Federal Maturity** in Science Collège St-Michel, Fribourg, Switzerland

Professional experience

2011-2015	**Doctoral assistant -** EPFL, Laboratory for Hydraulic Machines Experimental investigation of the tip leakage vortex via: • Velocity field measurements with stereo-PIV and LDV • High-speed visualizations Participation in teaching activities Supervision of semester projects and master theses Writing of scientific publications and participation in conferences

Languages

French:	Native speaker
English:	Professional working proficiency
German:	Elementary proficiency

Extracurricular activity

Music, guitarist in the band *Get in the Car Simone* (http://www.getinthecarsimone.ch/)

Journal papers

M. Dreyer, J. Decaix, C. Münch-Alligné, and M. Farhat (2014) Mind the Gap: A New Insight into the Tip Leakage Vortex Using Stereo-PIV. *Experiments in Fluids*, volume 55, issue 11, pages 1–13.

J. Decaix, G. Balarac, M. Dreyer, M. Farhat, and C. Münch (2015) RANS and LES Computations of the Tip-Leakage Vortex for Different Gap Widths. *Journal of Turbulence*, volume 16, issue 4, pages 309–341.

Z. Yao, F. Wang, M. Dreyer, and M. Farhat (2014) Effect of Trailing Edge Shape on Hydrodynamic Damping for a Hydrofoil. *Journal of Fluids and Structures*, volume 51, pages 189-198.

S. Pasche, F. Gallaire, M. Dreyer, and M. Farhat (2014) Obstacle-Induced Spiral Vortex Breakdown. *Experiments in Fluids*, volume 55, issue 8, pages 1–11.

M. Reclari, M. Dreyer, S. Tissot, D. Obreschkow, F. M. Wurm, and M. Farhat (2014) Surface Wave Dynamics in Orbital Shaken Cylindrical Containers. *Physics of Fluids (1994-Present)*, volume 26, issue 5, pages 052104.

A. Müller, M. Dreyer, N. Andreini, and F. Avellan (2013) Draft Tube Discharge Fluctuation during Self-Sustained Pressure Surge: Fluorescent Particle Image Velocimetry in Two-Phase Flow. *Experiments in Fluids*, volume 54, issue 4, pages 1–11.

S. Tissot, A. Oberbek, M. Reclari, M. Dreyer, D. L. Hacker, L. Baldi, M. Farhat, and F. M. Wurm (2011) Efficient and Reproducible Mammalian Cell Bioprocesses without Probes and Controllers? *New Biotechnology*, volume 28, issue 4, pages 382–90.

Conference papers

M. Dreyer, J. Decaix, C. Münch-Alligné, and M. Farhat (2014) Mind the Gap - Tip Leakage Vortex in Axial Turbines. *IOP Conference Series: Earth and Environmental* Science, volume 22, pages 052023

A. Müller, A. Bullani, M. Dreyer, S. Roth, A. Favrel, C. Landry, and F. Avellan (2012) Interaction of a Pulsating Vortex Rope with the Local Velocity Field in a Francis Turbine Draft Tube. *IOP Conference Series: Earth and Environmental Science*, volume 15, pages 032040.